Microstructure, Optical and Electrical Properties of Ultra-thin Nanostructured AgI and $Ag_{1-X}Cu_XI$ (x= 0.05, 0.1 and 0.2) Films Fabricated by Vacuum Thermal Evaporation and RF Magnetron Sputtering and Iodization

A thesis submitted for the degree of

DOCTOR OF PHILOSOPHY

In

PHYSICS

By

M. Gnanavel
(04PHPH14)

SCHOOL OF PHYSICS
UNIVERSITY OF HYDERABAD
CENTRAL UNIVERSITY P.O.
HYDERABAD 500 046

February 2010

DECLARATION

I here by declare that the matter embodied in this thesis titled **"Microstructure, Optical and Electrical Properties of Ultra-thin Nanostructured AgI and $Ag_{1-X}Cu_XI$ (x= 0.05, 0.1 and 0.2) Films Fabricated by Vacuum Thermal Evaporation and RF Magnetron Sputtering and Iodization"** submitted to University of Hyderabad for the award of **Doctor of Philosophy** in **Physics** is a record of original research work carried out by me under the supervision of **Prof. C. S. Sunandana**, School of Physics, University of Hyderabad. To the best of my knowledge, the thesis is not submitted for any degree in any University or institute.

Place: Hyderabad (M. Gnanavel)

Date:

SCHOOL OF PHYSICS
UNIVERSITY OF HYDERABAD
CENTRAL UNIVERSITY P. O.
HYDERABAD 500 046

CERTIFICATE

This is to certify that the research work presented in this thesis titled "**Microstructure, Optical and Electrical Properties of Ultra-thin Nanostructured AgI and $Ag_{1-X}Cu_XI$ (x= 0.05, 0.1 and 0.2) Films Fabricated by Vacuum Thermal Evaporation and RF Magnetron Sputtering and Iodization"** for the award of **DOCTOR OF PHILOSOPHY** is an original work carried out by **Mr. M. Gnanavel** under my supervision at School of physics, University of Hyderabad, Hyderabad. This thesis work has not been submitted to this or any other university partially or fully for the award of any degree or diploma.

Date: Prof. C. S. Sunandana

Place: Thesis Supervisor

Dean

School of Physics

ACKNOWLEDGEMENTS

It's my pleasure to write this part of my thesis and express my gratitude to one and all for helping me in a long run. It's time to bring them to stage since, most of them were behind the screen. I thank all of them who are involved directly or indirectly for the successful completion of this thesis.

I am deeply indebted to Prof. C. S. Sunandana, for the many way in which he has influenced me during my cherished research period with him. His guidance has brought about this thesis, a small extension of the vast store of knowledge achieved by standing over shoulder of giants like him. Thesis is but a small part of the result of his major influence on me. I thank him for moulding me to become a successful future researcher. I thank him for opening my eyes to all the noble qualities of not just a researcher, but also of a wonderful human being, shown to me not by explanation, but by exemplification, His kind words, constant goading, punctuality and his warm personality has never ceased to impress me.

As a voracious reader, his exotic but sensible thinking on material aspects incubated me to do things on a broader perspective. And add to it the enlightening discussion that we had about science, society and life in general. I wish to carry on the legacy of this warm, avuncular, brilliant and inquisitive person forever.

I thank Mrs. Praba Sunandana, whom I had very good interaction while having discussion with Prof. C. S. Sunandana at his home. She treated me as a one of her family member.

My bountiful and sincere thanks to Prof. S. P. Tewari, Director, ACRHEM, for his valuable discussions, support and encouragement.

I am deeply indebted to Prof. Anil K Bhatnagar. Who helped me to join with Prof. C. S. Sunandana.

I would like to express my heartfelt note of deep gratitude to Dr. M. Ghanashyam Krishna, doctoral committee member for his valuable discussion and advice throughout my research.

I thank the Dean, School of physics Prof. C. Bansal and former Deans, Prof. Vipin Srivastava, Prof. V. S. Sastry, Prof. S. N. Kaul, for providing me the facilities for the successful completion of my work. Also I would like to thank all the faculty members who have helped me throughout my stay here at the University of Hyderabad. I gratefully remember my other teachers who taught me in school as well as the faculty member at Department of Physics, Pondicherry University.

I am thankful to Prof. D. Narayana Rao for extending the Non-Linear optical facility for the Z- Scan measurement.

I thank Dr. K. C. James Raju for extending Impedance measurement facility at his lab.

I thank Prof. R. Shingh for extending the sputtering facility for thin film preparation.

I am thankful to Prof. T. P. Radhakrishnan, School of Chemistry, UoH, for extending Fluorescence spectrophotometer facility at his lab.

I am very grateful to Prof. N. Satyanarayana, for his inspirational guidance during my M. Sc and M. Phil project at Pondicherry University.

I would like to thank all the faculty members of ACRHEM for their valuable discussions.

I am thankful to Mr. Abraham, Offics Assistant, and School of Physics for his timely help. Mrs. Saramma, Mr. Purnachandra Rao, Mr. Anantha Rao of School of Physics, Mr. Rajeshwar and Mr. Nagaraj of ACRHEM are also acknowledged for their help.

I would like to thank my lab seniors Dr. P. Balaya, Dr. Y. Srinivasa Rao, P. Senthil Kumar, Dr. D. Barathi Mohan, Dr. Y. Sundarayya, Dr. Venkateswar Rao for their timely help and valuable discussions.

I thank all the scholars in School of Physics for helping me directly or indirectly. Abhilash, Shinto, Yuhender, Ravi Kumar, Manoj, Ramudu, Devendra, Srinivas, Rambabu, Vasu, Arun, Devaraj, Sekhar (thambudu), Ballu, Aali, Sulthan, Sandhiya, venkaiah, Sai Priya, Yashaswini, Rejina, Suresh, Partha, senthil and Raj Kumar for their timely help.

It's my pleasure to acknowledge my lovable friends, P. Manimaran, S. Dhamodaran, N. Sathish, K. Venkat, Sudhindaran, K. M. Ajith, Rizwan, Bari, Sai Preethi, Rajeeb, Juby, Laskhmi, Joji, Rajeshwari, Ashutosh, Trivikram, Ballu (mama), Vairam (mama), Madthu, Padthu, Prakesh, Venkatesh, Arumugam, Francis, Selva, Vijayan (gajaa), Sakthivel, Kannapiran, Arun babu, Vijayan (kapali), Naveen, Viji, Vignesh, Santhan Raj, Prabu, Ganesh, Ramesh and all my NRS Tamil friends who made my stay here pleasant and provided friendly atmosphere.

My sincere thanks to the staff of the CIL, ACRHEM and Nanocentre for the technical support they provided.

I thank G. V. Ramesh, Rajesh K, Abhijith, Guptha, Hari, Prasad and Manohar for timely helping. I owe special thanks for giving me a helping hand towards submission.

It's my pleasure to acknowledge the encouragement and support from my M. Sc classmates Balakrishnan, Sankar, Jayaraman, Rajesh, Geetha, Devi priya, Hariharan and Sathish.

It's my pleasure to thank the Tamil Cultural activity members, players of Sunday cricket team and members of DSPs for providing lively atmosphere during my stay in UoH.

I thank ACRHEM, UoH for providing Fellowship and also for the travel support to attend Global Photonics-2008 at Singapore. I thank university of Hyderabad for providing financial support under UPE grant for attending International and National conferences within India.

Above all it is the endless sacrifice, support and motivation from my Father and Mother which has brought me to the position where I am. I thank my Brother and all my relatives for their moral support.

Dedicated to
My Family
and
My Teachers

Preface

This thesis deals with the experimental research work carried out by the author on the fabrication of ultrathin (≤ 15 nm thick) silver and silver-copper alloy films by vacuum thermal (co) evaporation and (co) sputtering and their systematic iodization to produce zincblende AgI based nanostructures. A systematic characterization of these thin films has focused on the crystal structure microstructure and optical properties (optical absorption and photoluminescence) besides a preliminary study of the thin film electrical conductivity through impedance spectroscopy as AgI undergoes the superionic phase transition at 420 K.

The simple but effective means of iodization of Ag foils and thin films developed in our laboratory for about a decade and recognized and adopted by peer groups worldwide has helped investigate nanostructure development, thin film formation mechanism and such novel issues as plasmon-exciton transition in Ag and Ag-Cu 'alloy' films. This effort represents a logical continuation of a decade-long research programme on the semiconducting aspects of I-VII compounds of which AgI, CuBr and CuI are members. These are generally referred to as superionic conductors or solid electrolytes (ionic conductivities ~ 0.1 S/cm at or near ambient). They possess crystal structures with a large concentration of cationic Frenkel defects based on the partially covalent Ag-I/Cu-Br/Cu-I bond resulting in wurtzite/zincblende crystal structures (like III-V and II-VI compound semiconductors and also like ZnO) that eventually results in transitioned phases alpha AgI (bcc) and alpha CuBr/CuI(fcc) in which the metal cations form a kind of fluid of mobile ions. The physics of the wurtzite/zincblende phase transition though quite interesting is incompletely understood. The unusual nature of the Ag-I bond and the defects and disorder associated with the crystal structure play a crucial role in optical and electrical properties of both bulk and thin film forms of AgI and other superionic conductors.

This effort has thrown up such novel results as the development of core-shell type Ag@AgI nanoparticles and Cu-enhanced excitonic photoluminescence in Cu-doped AgI zincblende structured films. PVA polymer films have emerged as a very attractive active platform/matrix to look at shape-evolution of AgI nanoparticles that could be monitored by TEM and SAED techniques.

An impedance spectroscopy study on AgI and Cu-doped AgI thin films has revealed the superionic phase transition in AgI at 420 K in dc conductivity and the effect of Cu in controlling phase transition and overall conductivity reduction. This preliminary study has opened up a window on the study of ion diffusion in 2D systems.

This PhD thesis has probably helped understand basic concepts in solid state physics such as nature of quasiparticles (plasmons and excitons) and electronic energy band structure development in a direct gap semiconductor such as AgI besides providing recipes for fabricating optimal ultrathin nanostructures that could lead to device development. The novel plasmon-exciton transition reported here needs to be formulated and solved as a basic problem in condensed mater physics.

CONTENTS

DECLARATION

CERTIFICATE

ACKNOWLEDGMENTS

PREFACE

1. Introduction, Motivation and Thesis overview

1.1 Introduction 1

1.2 Nature of the Ag-I Bond, Defects, Clusters and Crystal Structure 4

1.3 Crystal Structure of AgI 8

1.4 Critical Ionicity, Structural Instability and Phase Transitions in AgI 10

1.5 Quasiparticles and Energy Band Structure 14

1.5.1 Surface Plasmons and Surface Plasmon Resonance

1.5.2 Excitons in Semiconductors

1.5.3 Band Structure of AgI

1.6 Motivation and Scope of the Present Work 24

References 31

2. Thin Film Fabrication and Characterization Methodology

2.1 Introduction 36

2.2 Bottom up approach 37

2.3 Thin Film Fabrication Techniques 38

2.3.1 Vacuum Thermal Evaporation

2.3.2 Sputtering Technique 41

2.3.3 RF sputtering 45

2.3.4 Magnetron sputtering 47

2.3.5 Thin film deposition by RF magnetron sputtering 48

2.3.6 Nucleation and Growth 50

2.4 Material characterization 52

2.4.1 Thickness measurement 52

2. 4.2 X-Ray diffraction 52

2.4.3 Scanning Probe Microscopy 55

2.4.4 Electron Microscopy 57

2.4.5 Electron diffraction (ED) 61

2.4.6 Optical Characterization 63
2.4.6.1 Ultra Violet-Visible Spectrophotometer
2.4.6.2 Photoluminescence
2.4.8 Electrical Characterization 67
2.4.8.1 Impedance spectroscopy
2.5 Summary 70
References 71
3. Surface plasmon-exciton transition in ultra thin silver and silver iodide films deposited on glass substrates by vacuum thermal evaporation
3.1 Introduction 73
3.2 Preparation of Ag and AgI thin films 74
3.3 Crystal Structure of iodized Ag films 75
3.4 Surface Morphology 78
3.5 Optical Properties 81
3.5.1 Surface plasmon to exciton transition
3.5.2 Excitons formation in iodized Ag thin film
3.6 Photoluminescence Studies of Ultra thin AgI Films 90
3.7 Summary 94
References 94
4. Thickness and composition dependent Plasmon-Exciton transition and Photoluminescence study of cation stabilized Co-Evaporated Ag-Cu nanostructured thin films iodized at ambient
4.1 Introduction 99
4.2 Deposition of Ag and Ag-Cu thin films 100
4.3 Structural Characterization 101
4.3.1 Crystal Structure of γ and β-AgI, Vegard's Law and crystallites sizes
4.3.2 Strain Analysis
4.3.3. Composition analysis
4.4. Surface microstructure characterization of Cu doped AgI thin films 107
4.5. Optical properties 113
4.5.1 Surface plasmon-exciton transition in progressively iodized Cu doped Ag thin films
4.6. Photoluminescence study of Vacuum Evaporated nanostructured AgI thin films 122
4.6.1 Room temperature photoluminescence study of Cu doped AgI thin films

4.7 Summary 128

References 129

5. Cu enhanced quasi–free excitonic photoluminescence in Co-Sputtered $Ag_{1-x}Cu_X$ (x= 0.05, 0.1 and 0.2) thin films grown on fused quartz substrates iodized at ambient

5.1 Introduction 132

5.2 Deposition of Ag-Cu thin films 133

5.3 Structural characterization of γ-AgI films deposited on fused silica substrates 135

5.3.1 Lattice parameter and iodization time dependent strain measurement

5.4 Surface microstructure characterization of AgI thin films grown on fused silica substrates 140

5.5. Optical properties of RF Sputtered Ag and AgI thin films 148

5.5.1 Surface plasmon resonance of Ag and Ag-Cu alloy films

5.6 Exciton formation in Undoped and Cu doped AgI thin films 151

5.6.1. Exciton formation in AgI thin films:

5.6.2 Cation stabilized exciton formation of Cu doped AgI thin films

5.7 Photoluminescence study of nanostructured Silver iodide thin films 161

5.7.1 Thickness and iodization time dependent band structure development of AgI thin films

5.7.2 Room temperature photoluminescence study of Cu doped AgI thin films deposited on fused silica substrates

5.8 Summary 169

References 170

6. Iodization time dependent Surface plasmon to exciton transition and Photoluminescence study of Core shell Silver Iodide thin films sputtered On PVA substrates

6.1 Introduction 175

6.2 Experimental detail 176

6.2.1 AgI thin film fabrication

6.2.2 PVA substrate preparation

6.2.3 TEM sample preparation

6.3 Spectroscopic and TEM Monitoring of Growth process 177

6.4 Quantum Confinement Effect 181

6.5 Grain growth and structural analysis of AgI nanoparticles 183

6.6 Iodine induces AgI nano particle growth 184

6.7 Photoluminescence studies of partially iodized Ag thin films 190
6.8 Summary 193
References 194
7. Superionic phase transition in AgI and (Ag-Cu) I thin films: A Preliminary Impedance Spectral Study
7.1 Introduction 197
7.2 Deposition of Ag and Ag-Cu films on Pt/Si single crystal substrates 198
7.3 Structural characterization of Ag and Ag-Cu alloy films deposited on Pt/Si substrates 198
7.4 Surface morphology 199
7.5 Impedance measurement 201
7.5.1 Fabrication of M-I-M structure
7.6 DC Conductivity 205
References 206
8. Conclusions and Suggestions for Future Work 208

List of Publications

Chapter I

Introduction, Motivation and Thesis overview

1.1 Introduction

This thesis deals with the fabrication and study of ultrathin (≤ 10 nm thick) silver and silver-copper 'alloy' films by vacuum thermal co-evaporation and RF co-sputtering and their systematic iodization to produce zincblende AgI based nanostructures. The crystal structure microstructure and optical properties(absorption and photoluminescence) and electrical conductivity have been systematically investigated. The simple but effective means of iodization of thin films developed in our laboratory has helped investigate nanostructure development, film formation mechanism and such novel issues as plasmon-exciton transition in Ag and Ag-Cu alloy films [1-2]. This iodization strategy is actually two-pronged. While it enables us to develop and investigate nanostructures it also provides a window to look at thin film formation a very basic thermodynamic process. Figure 1.1 illustrates a fundamental schematic model for iodization.

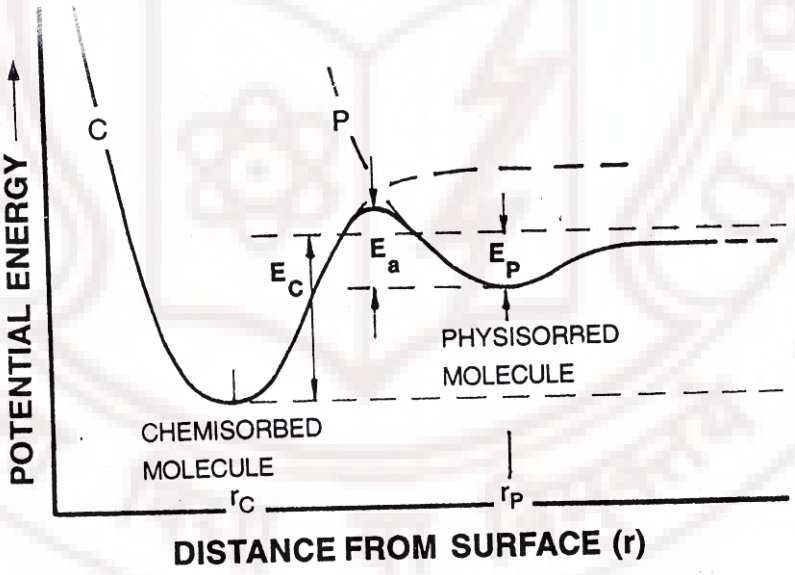

Figure 1.1: Model for iodization of silver films thermally evaporated/RF sputtered on glass substrates. Iodine molecules could be physisorbed or chemisorbed on silver surfaces to retain their identity or to dissociate into two nascent iodine atoms to form Ag-I bonds that subsequently form AgI nanoparticles [3].

To appreciate the importance of AgI and also CuI it is appropriate to mention that these two iodides occur as rarest of rare minerals containing iodine. Known by the names Iodargyrite (AgI) and Marshite (CuI) they grow either as micron-sized inclusions in other

minerals or by themselves as hexagonal platelets (beta AgI) or as triangular tablets (gamma CuI) (figure 1.2) [4]. It is very interesting to note that the habit of marshite (figure 1.2(d)) is exactly the one adopted by the nuclei of gamma AgI that grow on PVA substrates (Chapter 6).

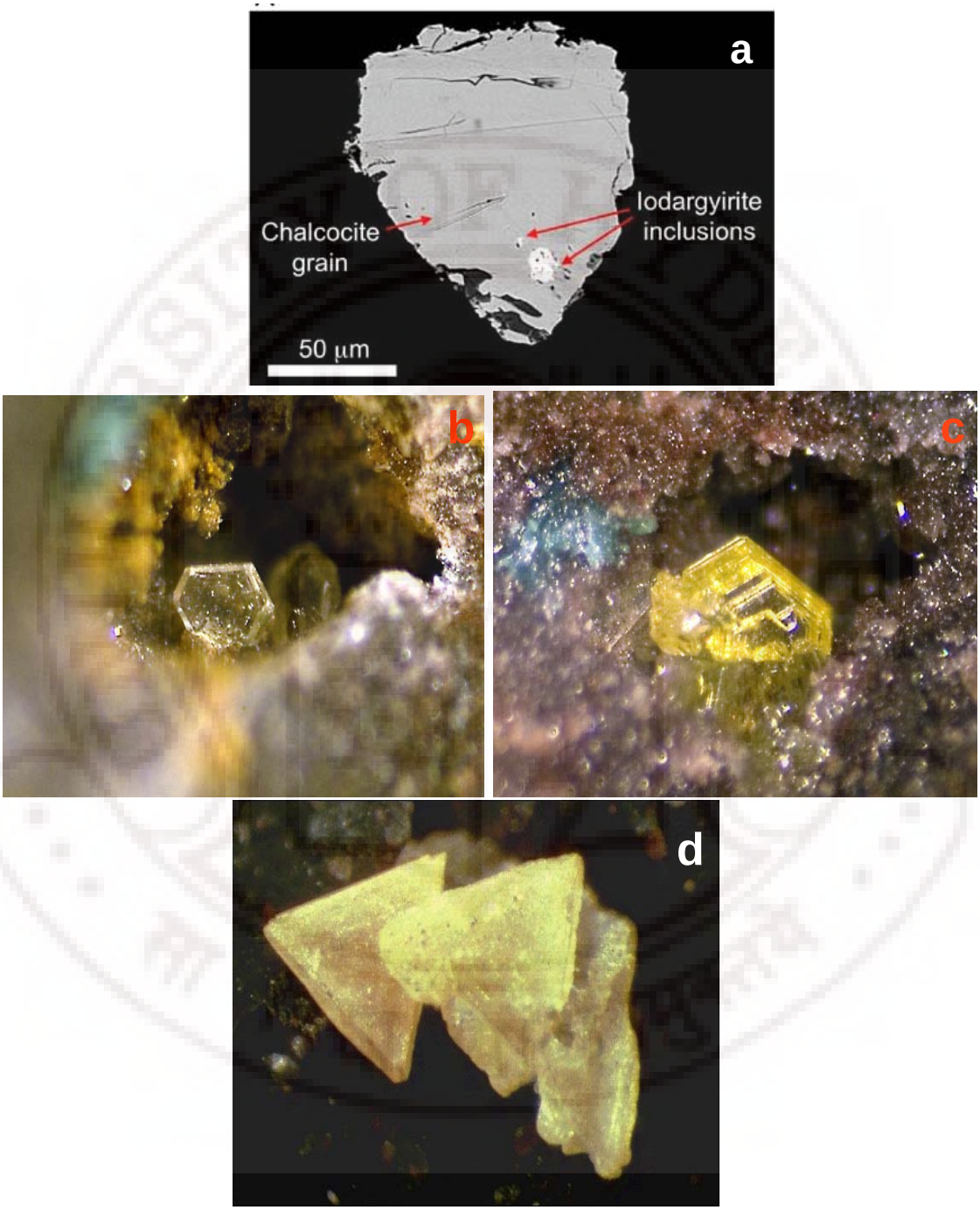

Figure 1.2: Photographs of (a) micron-size AgI (Iodargyrite) inclusions in mineral chalcocite grain (b) A natural crystal of AgI (c) A macrocrystal of beta AgI showing hexagonal platelets stuck together (d)Triangular prisms of mineral marshite (CuI). Note that this is the shape of the AgI zincblende nuclei that form and grow as γ-AgI nanostructure on PVA substrate (Chapter6)) (www.mineralatlas.com) [4].

The current effort represents a logical continuation of a research programme on the semiconducting aspects of I-VII compounds of which AgI, CuBr and CuI are members [5-8]. These are generally referred to as superionic conductors or solid electrolytes (ionic conductivities ~ 0.1 S/cm at or near ambient) [9-18]. They possess crystal structures with a large concentration of cationic Frenkel defects based on the partially covalent Ag-I/Cu-Br/Cu-I bond resulting in wurtzite/zincblende crystal structures (like III-V and II-VI compound semiconductors and also like ZnO) that eventually results in transitioned phases α-AgI (bcc) and α-CuBr/CuI(fcc) in which the metal cations form a kind of fluid of mobile ions [5-8,20]. It thus turns out that AgI (& also CuBr, CuI) are *Janus-faced*: excellent cation superionic (Frenkel defect) conductors [21-23] and I-VII semiconductors by virtue of tetrahedral metal-halogen bond. In fact, CuI is a p-type semiconductor from 300 K to 580 K and Cu^+ ion superionic conductor for T>600 K. AgI possesses zincblende (metastable)/wurtzite structure and direct band gap of 2.82 eV (γ-AgI) at room temperature [24-34].

Nanoscale halides of I-VII materials are more and more appealing as they are useful in optoelectronics, solid-state semiconductor battery [11,35] industrial catalysis [36] composite conductive fiber and gas sensing [37]. It is a pity that the applications of them are significantly limited because of the lag of their synthesis. Developing appropriate techniques to produce 1D I-VII materials are of practical importance.

Ag and Ag-alloy thin (a few tens of nm thick) films support surface plasmons (could carry laser light). When iodized they gradually convert to nanostructured zincblende AgI [38-46]. Excitons develop *ab initio* in AgI band structure [31]. What if we make $Ag_{1-x}Cu_x$ (x=0, 0.1, 0.2, 0.3) and iodize them systematically (monitored by XRD) in a bid to (a) use Cu as a particle growth kinetic controller (AFM) and zincblende structure stabilizer and (b) see how plasmons of metal/alloy transition to zincblende excitons as seen by optical absorption and photoluminescence spectroscopy and look at excitonic photoluminescence in AgI in the presence of Cu? The present thesis attempts to find answers to these questions by focusing on the stabilization of γ-AgI thin films. The fundamental importance and technological potential of AgI, CuBr and CuI is due to the fact that these materials combine strongly coupled ionic and electronic subsystems such that crystal structure, defects and microstructure as well as electronic band structure

nontrivially dictate their physics and application potential. To appreciate this, it is necessary to review briefly the basic physics of these materials including chemical bonding, crystal structure, structural phase transitions and electronic band structure.

1.2 Nature of the Ag-I Bond, Defects, Clusters and Crystal Structure

Quantum chemistry of the Ag-I bond has been discussed on the basis of Density functional theory (DFT) based electronegativity in connection with phase formation, phase transition and superionic conductor [46a]. The Ag-I bond in AgI appears to be a unique chemical bond simply because of the nature of the atomic constituents Ag (Z=47, $1s^2 2s^2 2p^6 3s^2 3p^6 3d^{10} 4s^2 4p^6 4d^{10} 5s^1$) and I(Z=53, The$1s^2 2s^2 2p^6 3s^2 3p^6 3d^{10} 4s^2 4p^6 4d^{10} 5s^2 5p^5$). Their atomic/ionic sizes, electronic structure and the proximity of *4d*-band to the *5s* band in Ag and the presence of a sizeable quadrupole moment of I (0.67 barn) [47,48] (which makes it a highly polarizable ion and deformable too) ensure that the Ag-I bond is probably made up of a combination of four components: ionic, covalent, van der Waals and 'hydrogen"-like bonds so that one could write for fractional bond strengths (f)

$$f_i + f_c + f_{vdW} + f_H = 1 \qquad (1.1)$$

The physics of the Ag-I bond could be understood if all the four components are estimated. Philips critical ionicity concept (see later) considers only the first two components.

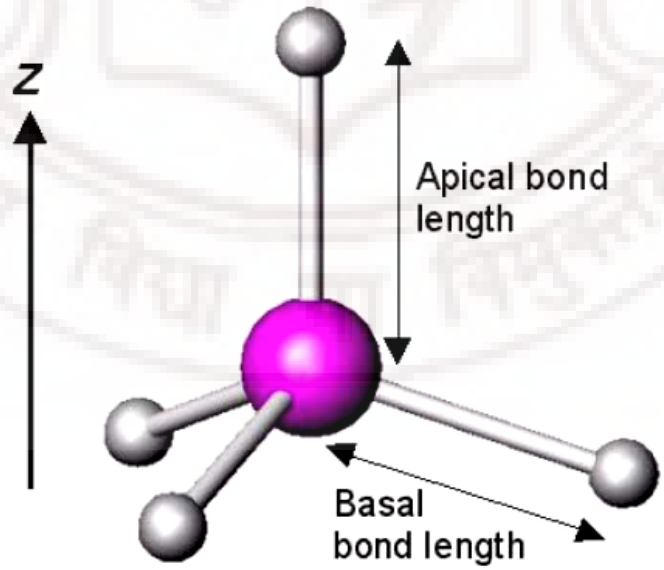

Figure 1.3: Ag_4I tetrahedron form wurtzite-type, b-AgI [55].

It is instructive to look at the Ag-I bond in the light of the superionic phase transition of AgI from wurtzite (β) phase to bcc (α) phase at 420 K. The nature of the β-α phase change in silver iodide has been studied in some depth [49,50-54]. Buhrer and Bruesch [50] postulate that the phase change is driven by entropy (an order–disorder transition). However, there is an energy cost for the creation of cationic Frenkel defects, effectively limiting the increase in entropy. Transformation into the α-AgI phase results in many more vacant sites and a statistical distribution of silver ions across them. However, Yoshiasa and co-workers propose that the aforementioned low-lying TO mode is responsible not only for large Ag ion movements, but also for small I^- ion displacements which lead directly into the phase transformation (displacive transition) [52]. Basically the silver iodide system is highly anharmonic. Anharmonicities in atom vibrations increase as the temperature approaches the phase transition. The low energy TO modes are primarily bending modes, with apical Ag–I bond angles changing significantly. This movement is accompanied by small changes in the apical Ag–I bond length, see figure 3. At temperatures significantly lower than Tc, the apical Ag–I bond is observed to be longer than the ideal structure would suggest, owing to a large covalent component in the bonding. This bond length becomes equal to the basal bond lengths on heating and as the phase transition is approached the apical Ag–I distance becomes shorter whilst the three basal Ag–I distances become slightly larger [55]. This structure change can be explained by anharmonicity in the atomic thermal vibrations, especially for the iodine atom, as demonstrated by Yoshiasa [52]. As the anharmonic effect increases, it is observed that the magnitudes of iodine displacement are greater in the three antibonding directions. This makes the structure closer to the bcc arrangement of α-AgI. Hence, the increase in anharmonic thermal motion is consistent with a further transformation to the superionic α-phase. The phonon density of states has been calculated by Buhrer and Bruesch for the wurtzite-type, β-phase of silver iodide, are in good agreement with experimental results [50]. Their calculated phonon dispersion curves show that the phonon spectrum is dominated by strong anharmonic effects [50] and that there are several low-lying transverse optic (TO) modes which behave as largely decoupled from the remainder of the phonon spectrum. These modes give the major contribution to the thermal motion because they have a high density of states and are easily thermally activated due to the low energy of around 500 MHz. In terms of microwave heating, this low-lying band of closely related TO modes should allow facile multi-phonon interactions with the

microwave field. Thus the temperature-resolved, in-situ powder X-ray diffraction of silver iodide under microwave irradiation assumes a fundamental significance (Robb et al) [55]. Furthermore, owing to the large separation between TO and higher frequency bands it is a more difficult process to redistribute this energy quickly. This may result in a non-classical distribution of energies within the phonon spectrum. Silver ion performs most of the movement in these low-energy modes. Though lighter, the silver atom is smaller and it is this movement which leads to the formation of Frenkel defects in the structure and allows ionic conduction of the silver ions to take place. As the anharmonic effect increases which is responsible for negative thermal expansion of AgI (see section 1.6), it is observed that the magnitudes of iodine displacement are greater in the three antibonding directions. This makes the structure closer to the bcc arrangement of α-AgI. Hence, the increase in anharmonic thermal motion is consistent with a further transformation to the superionic α-AgI phase. The hypothesis is that microwave energy interacts directly with low-lying TO modes via a multi-phonon process. Redistribution of this energy is slow with respect to the rate at which energy goes into the system from the microwave field, and a non-classical distribution of internal energies is the result. The phase transition occurs when enough energy is in the relevant mode to promote the structural change (be that through the creation of sufficient interstitial Ag ions, or through displacement of I^- ions). However, the average internal energy in the system is lower than at the equivalent point during conventional heating [56].

Frenkel defects in AgI-an Ag^+ vacancy and an Ag^+ interstitial-basically arise from the unique Ag *(4d)-I (5p)* hybridization. First principles molecular orbital calculations of [57] on an interstitial Ag in AgBr and AgI, using the discrete variational (DV)-Xα method have shown that although AgI is considered to be an ionic crystal, Ag-4*d* orbitals are well admixed with anion-*p* orbitals in their valence band. In the presence of an interstitial Ag (Ag_i), an interstitial level appears within the band gap. The interstitial orbital is found to be less delocalized around the Ag_i in AgI than in AgBr. As a result, the Ag_i-Ag covalent bond in AgI is much weaker than the Ag-I bond at normal sites. Since the formation of strong Ag_i-Ag bond is essential for the agglomeration of Ag atoms, an Ag cluster can be formed easier in AgBr than in AgI. This last observation is very relevant to the present work where AgI cluster formation is effectively controlled through programmed iodization.

The electronic states of silver iodide were calculated by the DV-Xα cluster method to get more microscopic evidence for the *p–d* hybridization in noble metal halides [58]. The calculations carried out for the $Ag_{13}I_{14}$ clusters indicate that both components of anti-bonding and bonding exist in the diagram of overlap population (DOP) for AgI and these two components are made up of the 4*d* band of Ag^+ and the *p* band of halogen ion, which form the *p–d* hybridization. In sharp contrast, the DOP of nonsuperionic conducting sodium iodide is occupied by almost only bonding component. The significant inference is that the origin of AgI type superionic conductor is in the weakness of *p–d* hybridization.

The bonding nature of the superionic material AgI has been studied by using a pseudo potential theory [59]. In comparison with that for GaAs, which is a well-known semiconductor. It is found that the real space valence electron distribution between these compounds differs qualitatively, and that the bonding in AgI is determined mainly by the iodine. The local electronic excitations from the bonding to the antibonding orbitals can trigger the migration of the mobile species, thus initiating in this way the superionic transport. Thus the unique iono-covalent nature Ag-I bond is important for defect production and superionic conductivity as well as phase transitions. Indeed the weakly hybridized *p-d* bond (energy) in AgI is temperature dependent, exhibiting a sudden drop at wurtzite/zincblende to bcc phase transition at 420 K in AgI establishing the importance of bonding and anti-bonding states in AgI [60].

Apart from the cationic Frenkel defects electronic defects (due to non-stiochiometry and existence of dangling-bond type defects are also prevalent in AgI (and CuI) and these electronic defects give characteristic signatures of the 420 K phase transition. An early investigation has clearly established an anomaly in the electronic conductivity at 420 K (figure 1.4) when n-type beta AgI turns p-type α-AgI. Mechanochemical reaction stabilized AgI and AgI-CuI exhibit similar electronic signatures (see Sec.1.5) [47].

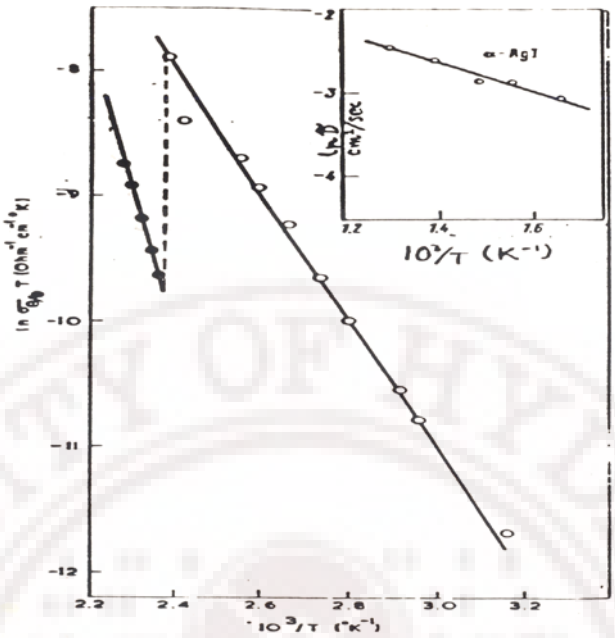

Figure 1.4: Electronic conductivity versus reciprocal temperature for AgI. Dashed vertical line depicts the ~ 2 order sudden drop in electronic conductivity as beta AgI changes over to alpha AgI with a corresponding change in band gap from 2.8 eV to 2.5 eV and the change in the position of the Fermi level w.r.t the top of the valence band from 1.6 to 1.1 eV [60].

1.3 Crystal Structure of AgI

The weakly covalent tetrahedral Ag-I bond admits many stacking sequences including …ABCABC… and …ABAB… just as covalent semiconductors resulting in polymorphism in AgI. Three crystal structures are commonly encountered (figure 1.5 (a) Zincblende or γ-AgI with …ABAB… stacking (b) Wurtzite or β-AgI …ABCABC… stacking) and (c) α-AgI. The high-temperature bcc or alpha AgI which is the Ag^+ superionic conducting phase attained through a first order structural phase transition (as seen in our impedance spectroscopy measurements on AgI thin films to be described in Chapter 7).

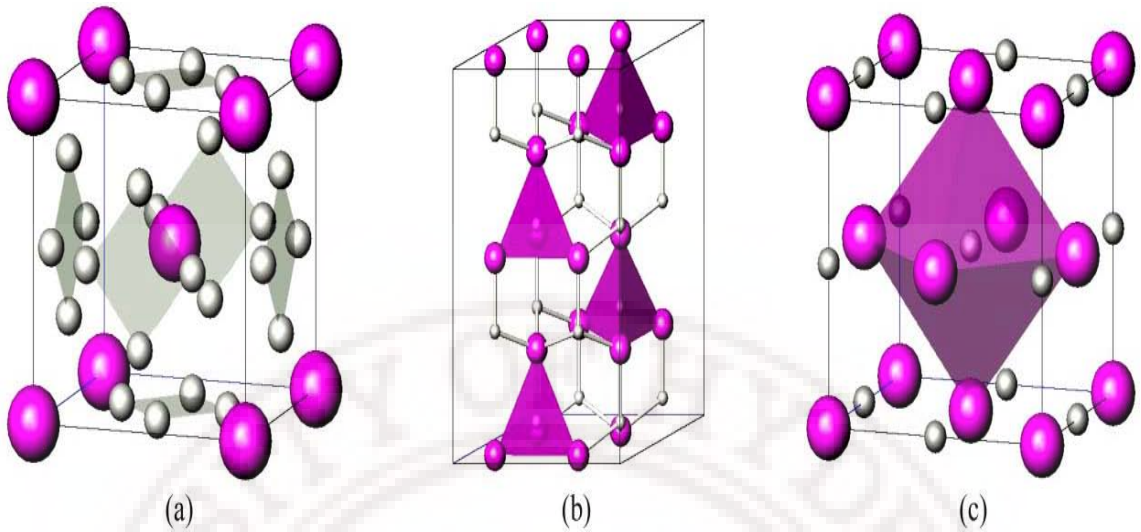

Figure 1.5: Structures of silver iodide (Ag = grey, I = magenta). (a) Superionic, α-AgI: silver sites are 1/6 occupied. (b) Wurtzite-type, β-AgI. (c) Metastable, zinc-blend type, γ-AgI. Click images or (a)–(c) to access 3D representations [55].

An important study of the structural properties of silver halides based on Density Functional theoretical calculations by Palomino-Rojas et al has among other things focused on the stability of the zincblende phase of AgI [61]. Their calculations for AgI correctly predict the ground state structure to be zincblende/wurtzite, and predict a transition to a rocksalt structure the application of pressure. The calculated transition pressure is 0.67 GPa using local density approximation, and 2.32 GPa using the generalized gradient approximation.

Figure 1.6 shows the total energy *vs* volume plots for the relative stability of AgI in NaCl, CsCl. Wurtzite and zincblende phases while figure 1.7 shows the total density of states vs energy with contribution from I (5p) electrons and the Ag (4d) states.

These features are in line with the abovementioned discussion of p-d hybridization [62]. Thus the band structure of AgI and the associated optical properties especially the GaAs-like gamma AgI may be expected to be determined by *p-d* hybridization and a discussion of band structure of AgI is in order- as will be done in section 1.4.

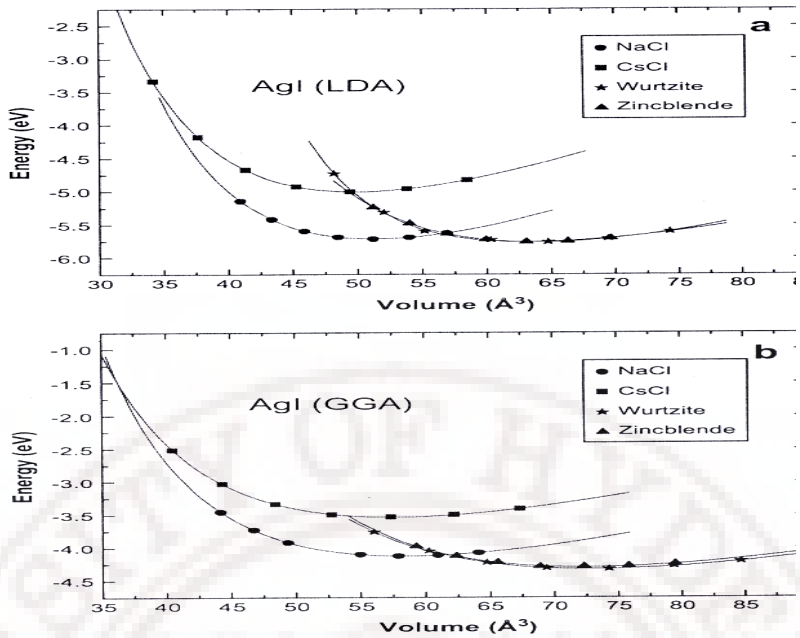

Figure 1.6: Total energy of AgI in its NaCl, CsCl, Wurtzite and Zincblende phases in (a) LDA approximation (b) GGA approximation of DFT.

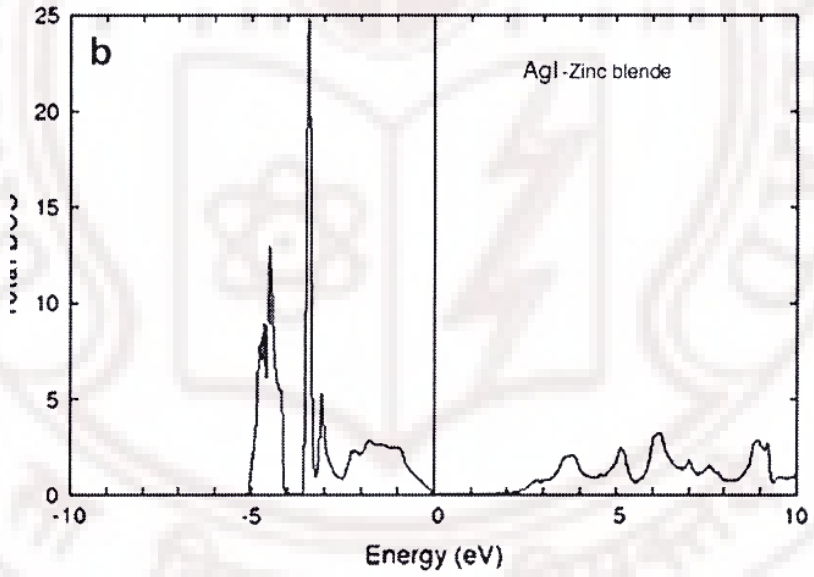

Figure 1.7: Calculated total density of states of zincblende AgI using LDA It is seen from figure that there is an energy region from nearly -5eV to -2.5 eV Consisting of I (5p) and Ag (4d) states. Closer to the Fermi level there is a region.

1.4 Critical Ionicity, Structural Instability and Phase Transitions in AgI

Fast ion transport requires mobile ions of small-enough mass physically moving from cathode across the electrolyte to the anode in an electrochemical cell. Plenty of

mobile ions in crystalline electrolytes have to move across rather easy barriers created by a small number of counter ions that possess a specific geometry-faces of tetrahedra for example. Four coordinated rather than six-coordinated structures often favour fast ion transport. Such structures also incorporate a substantial concentration of Frenkel defects and the mobile ion sub-lattice is liquid-like while the immobile ions form a supporting structure. In structural superionic conductors (such as AgI, CuI and CuBr) one finds that the Debye-Waller factor that is crucial to ion dynamics is controlled by ionicity [63]. A critical ionicity was found by Phillips for the occurrence of a structural instability and superionic conductivity which corresponds to the borderline between 4 and 6-coordinated compounds. This number (number line in fact) 0.785 lies just to the right of AgI making it a generic or canonical superionic conductor with a structural phase transition to the superionic phase at 420 K. Unlike AgCl and AgBr Ag sits in a tetrahedral cage of I^- ions and vice versa. A good correlation exists between Debye-Waller factor and ionicity which diverges at 0.785 for tetrahedrally coordinated compounds figure 1.8. This divergence is characteristic of structural instability which when controlled would yield good superionic conductors. Even metastable phases of AgI such as zincblende or gamma AgI when stabilized by marginal additions of monovalent cations such as Cu could arrest instability and optimize conductivity over an extended range of temperatures.

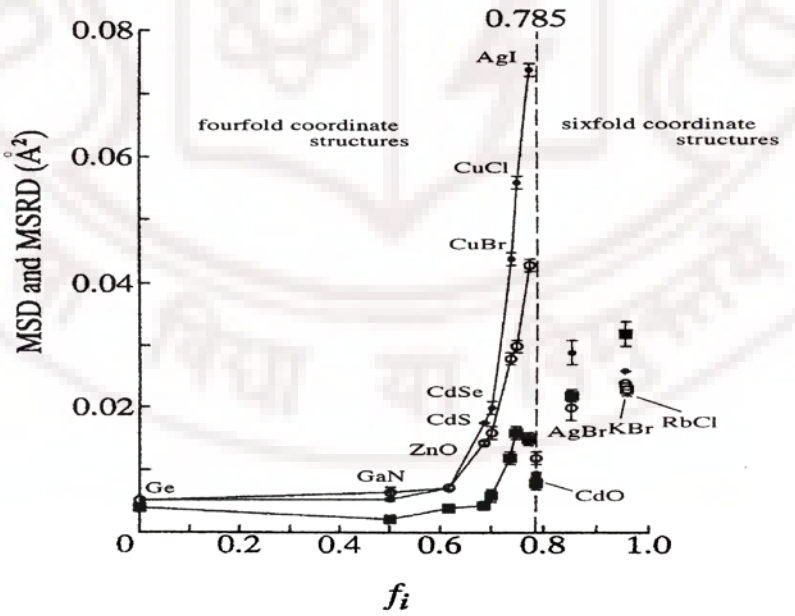

Figure 1.8: Ionicity (f_i) dependence of Debye-Waller factors mean square relative displacements (MSRD) derived from EXAFS experiments (■) and mean-square displacements for cations (●) and anions (o) derived from diffraction experiments [63]. MSRD and MSD correlate well with coordination number and ionicity. MSRD's of 4-coordinated materials show a gradual approach

to those of 6-coordinated ones as the ionicity increases. A diverging curve towards F_i=0.785 is observed for the MSD in the 4-coordinated materials indicating lattice instability.

Several models have been proposed for the superionic phase transition in AgI as it transforms to the normal conducting wurtzite/zincblende phase to the fast-ionic Ag^+ conducting bcc phase at 420 K [64]. This unsual first order phase transition that violates the Landau-Lifshitz criterion [6], involves mobile-ion centred clusters, phonons, and the distortions that the clusters induce in a dynamic way. This complex nonlinear problem has been tackled in the cluster-induced distortion model by Ishii and Kamishima [65]. The main results of this model are displayed in figure 1.9. Note that the order parameter and pair probability as well as the mean displacement of mobile ions besides the phonon energies all show a discontinuous jump at the phase transition temperature, in tune with many experimental observations including heat capacity, ionic/electronic conductivity, lattice parameter, thermal expansion, EPR susceptibility associated with paramagnetic centres stabilized in AgI and Ag *(4d)-I (6p)* hybridization energy and Debye temperature, among others.

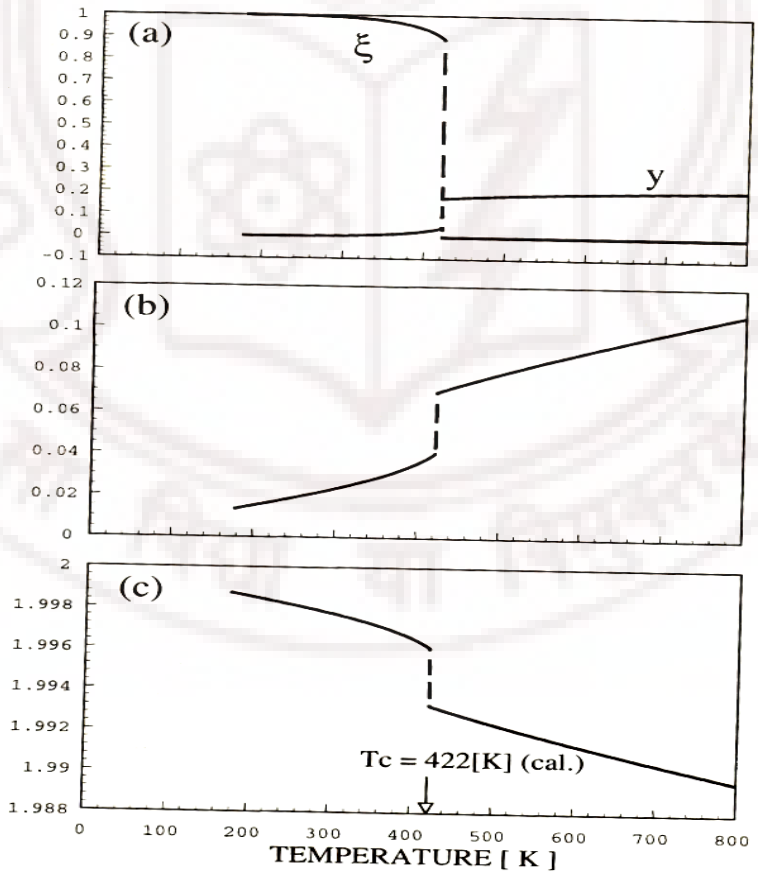

Figure 1.9: T-dependences of (a) order parameter ξ and pair probability (b) mean displacement and (c) phonon energy in AgI according to the cluster induced distortion model for the superionic phase transition [65].

Because of the highly asymmetric potential in which Ag^+ ions move in the AgI lattice, the lattice vibrations are highly anharmonic (the interatomic restoring forces are weak), as directly reflected in thermal expansion studies through the phase transition. This aspect has been studied at a microscopic level by monitoring the temperature dependence of the attenuation of longitudinal ultrasonic waves propagated through AgI as done by Page and Prieur [66]. Figure 1.10 which dramatically depicts the changes in attenuation behaviour near the phase transition temperature highlights the anharmonic contribution to the elastic constants besides shedding light on the nature of the Ag^+ conductivity relaxation.

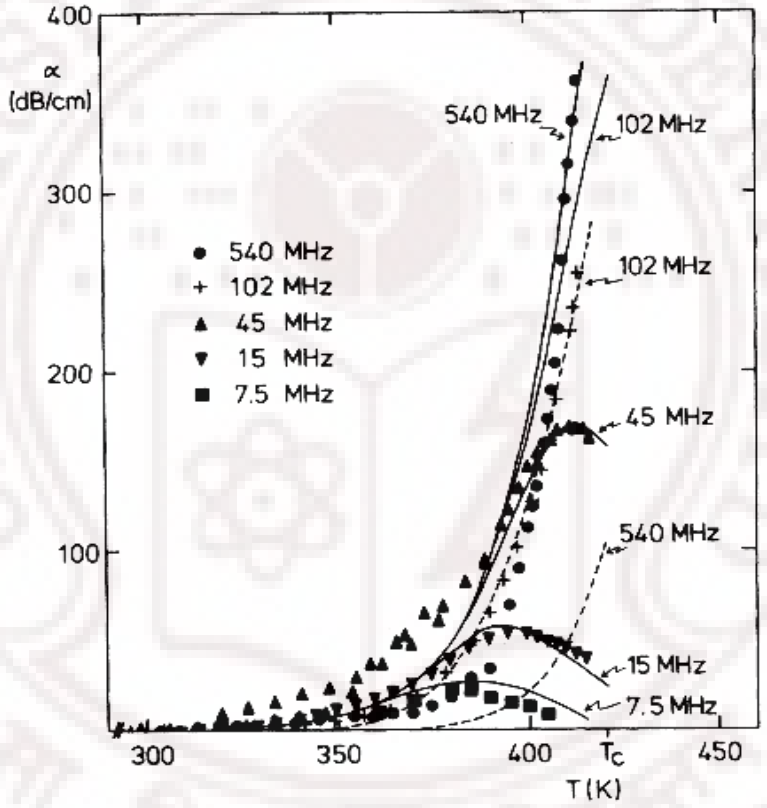

Figure 1.10: Temperature dependence of the attenuation of longitudinal ultrasonic waves (α) propagating along the c-axis in β-AgI. While points represent experimental data, solid lines represent the equation $\alpha=\kappa^2/v_s[\omega^2\tau_c/(1+\omega^2\tau_c^2)]$ where $\kappa^2=\eta^2/\varepsilon\ \varepsilon_0 c_A$,η=piezoelectric tensor element, ε=dielectric constant, ε_0= vacuum permittivity, c_A= an-harmonic contribution to elastic constant, v_s=velocity of sound ,τ_c=conductivity relaxation time and ω=frequency of the ultrasonic wave) Dashed curves are given by $\alpha=\kappa^2/v_s\ [\omega^2\tau_c/\{\omega^2\tau_c+(1+\omega^2\tau_c\tau)^2\}]$ taking into account of screening and T-dependent Ag^+ conductivity relaxation. The atomic nature of Ag and I_2 in AgI are highlighted in properties such as Debye temperature which impact thermal physics of these materials [66].

In a unique neutron resonance absorption study, Kaneko et al [67] have looked at the temperature dependence of the Debye temperature of AgI (figure 1.11) through the

phase transition. Their results along with appropriate calculations of Debye temperatures have convincingly demonstrated that the beta-alpha phase transition anomaly actually results from the change of the dynamical property of the Ag ion as seen through the temperature dependence of Debye temperature of the Ag atom but not of the I atom.

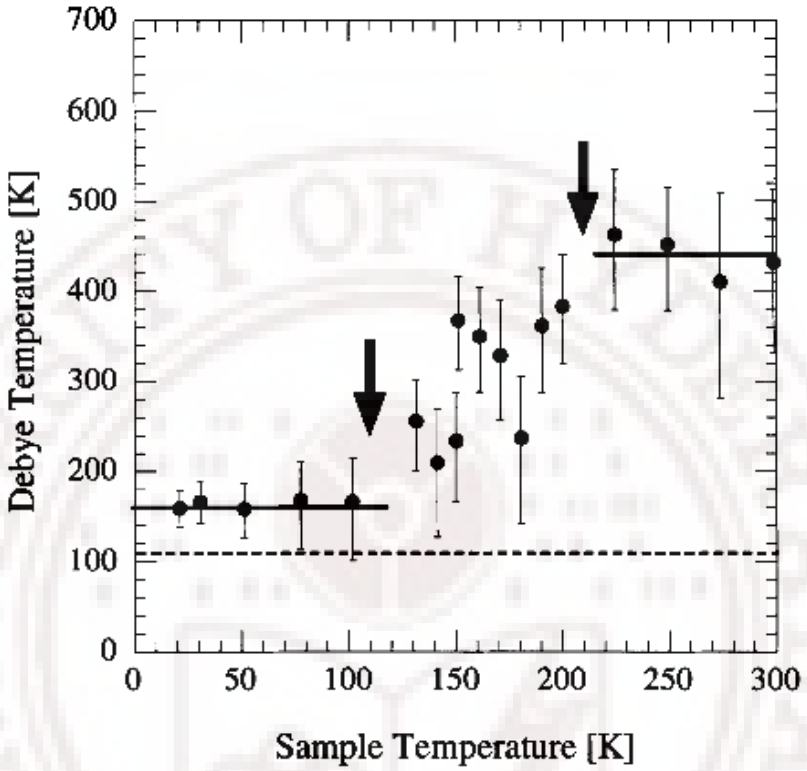

Figure 1.11: T-dependence of the Debye temperature of Ag atom and I atom in AgI determined from neutron resonance absorption spectroscopy. Broken line: calculated value for I atom with Debye temperature 106 K. Solid lines are calculated values for Ag atom with Debye temperature of 160K and 440K. Gradual change of Debye temperature of Ag atom occurs in the region 120-210 K below 120 K Debye temperature of Ag ≈ Debye temperature of I_2. The β-α superionic phase transition anomaly thus results from the change of the dynamical property of the Ag atom [67].

1.5 Quasiparticles and Energy Band Structure

Fabrication of Ag and Ag-Cu alloy ultrathin films and their systematic iodization provides a unique opportunity to study two important quasiparticles in condensed matter (1) Plasmons in Ag and (2) Excitons in γ-AgI zincblende structure; both these are very important components of the energy band structure of Ag and AgI. Most interestingly, gradual iodization of ultrathin Ag films involves transformation of Ag plasmons into excitons of AgI [24-30,38-46,68].

1.5.1 Surface Plasmons and Surface Plasmon Resonance

Free carriers or conduction electrons (charge q, concentration n, effective mass m*) in noble metals (eg. 5s electrons in Ag) especially in the form of submicron thick films exhibit a special kind of absorption due to the collective action of carriers known as plasma resonance absorption [69-81]. The classical dynamics of a collection of free electrons displaced a distance ξ due to an applied electric field $E = 4\pi nq\xi$ can be described by the equation [80]

$$nm^*d^2\xi/dt^2 = -nq\,E = -4\pi nq^2\,\xi \quad (1.2)$$

which corresponds to a simple system with natural frequency ω_p:

$$d^2\xi/dt^2 + \omega_p\,\xi = 0 \quad (1.3)$$

where ω_p is the plasma resonance frequency

$$\omega_p = (4\pi nq^2/m^*)^{1/2} \quad (1.4)$$

strong absorption occurs when the incident radiation frequency incident on a metal thin film sample matches ω_p whose value depends essentially on n. For a metal with $n=10^{22}$ conduction electrons per cc plasma resonance absorption occurs in the UV region at 330 nm. As n continuously decreases as in thinner and thinner noble metal ultrathin films employed in this work, ω_p shows a progressive shift to the visible.

How does the thin metallic film behave optically for $\omega \approx \omega_p$ i.e., $\omega \leq \omega_p$ or $\omega \geq \omega_p$? A 1D equation of motion with $E = E_x\exp(-j\omega t)$, a mean relaxation time τ for scattering of electrons by interaction with lattice waves and charged imperfections among others (which damps electron motion, damping α velocity component/τ)

$$d^2x/dt^2 + (1/\tau)dx/dt = -(q/m^*)\,E_x\exp(-j\omega t) \quad (1.5)$$

If $x\ \alpha \exp(-j\omega t)$ then

$$(-\omega^2 - i\omega/\tau)\,x = -(q/m^*)E_x \quad (1.6)$$

As the electric field polarizes the medium with polarization $P^* = -nqx$,

$$P^* = -(nq^2/m^*)/((\omega^2 + i\omega/\tau)\,Ex \quad (1.7)$$

but relative dielectric constant

$$\varepsilon^*_r = 1 + P^*/E_x \quad (1.8)$$

So

$$\varepsilon^*_r = 1 - 4\pi (nq^2/m^*)/(\omega^2 + i\omega/\tau) \quad (1.9)$$

for large τ, $i\omega/\tau$ is negligible so that ε^*_r is positive and refractive index is real if $\omega \geq \omega_p$. ε_r^* is negative and refractive index complex if $\omega \leq \omega_p$. Propagation of electromagnetic waves through the medium is allowed for $\omega \geq \omega_p$ but for $\omega \leq \omega_p$ there is no propagation but strong absorption and reflection. Oscillations of electric charge involved in plasma resonance have their associated quanta of energy called plasmons with energy $(h/2\pi)\ \omega_p$. Plasmons can me observed directly by measuring energy loss of electrons penetrating a thin metal foil or indirectly by conventional UV/visible optical spectra measured after absorption by/reflection from thin films as is done in the present work. Charge oscillations occurring at the surface of a metal thin film constitute surface plasmons while those characteristic of the bulk metal are volume plasmons. Interfacial plasmons can occur at the boundary between a dielectric substrate and a metal film [80-81]. A possible coupling between optical photons and the surface plasmons leads to applications in holography planar light source, enhanced Raman scattering and submicron electronic circuitry. Current research efforts have focused on building a surface plasmon laser also called “spaser”. Surface plasmons of much interest in the context of plasmon-exciton transition observed in our work is a realization of the fact that a bounded electron gas can support natural oscillation in the electron density at its surface. To look briefly at the physics of the surface plasmon, the electron density fluctuations (in space and time) $\delta n(\mathbf{r},t)$ associated with the volume plasmon of wave vector $\mathbf{k}$ in a free electron gas must be considered:

$$\delta n(\mathbf{r},t) = \delta n_0 \exp[i(\mathbf{k}.\mathbf{r} - \omega_{\mathbf{k}} t) \quad (1.10)$$

where

$$\omega_k \approx (\omega p^2 + (3/5)\ v_F^2\ k^2)^{1/2} \quad (1.11)$$

is the eigen frequency of the wave and v_F is the Fermi velocity in the electron gas. Note that in homogeneous isotropic systems these fluctuations are completely longitudinal.

Introduce a surface. Symmetry of the system is broken whereby **k** may assume complex values corresponding to the density fluctuations bound to the surface, the motion itself likely to acquire a transverse character. These may be written as

$$\delta n(x,y) \approx \exp\{i[k_y-\omega_s(\kappa)t\}\exp(-ik_s x), \quad (1.12)$$

κ being the wave number of the oscillatory motion along the surface, $\omega_s(\kappa)$ its eigenfrequency, and $1/k_s$ is ~ Thomas Fermi screening length, ~ 1 A^o in metals.

A wave of this kind has an eigen frequency ω_s (κ=0) ≡ ω_{s0}= $\omega_p/\sqrt{2}$ for very long wavelengths. This frequency is less than the volume plasma frequency due to the depolarizing effect of the surface. If the long wavelength dielectric constant of the plasma system is ε (ω) and if the dielectric constant of the material in the half space x<0 is constant at ε_0, then oscillations occur when $\varepsilon(\omega) + \varepsilon_0 = 0$. Using the form $\varepsilon(\omega) = 1-(\omega_p/\omega)^2$, we have for the surface plasmon, $\omega_{s0}= \omega_p/(1+\varepsilon_0)^{1/2}$.

The analysis of surface plasmon dispersion given above assumes that (a) light speed is infinite (b) all interactions are instantaneous and the surface oscillation is entirely longitudinal and (c) phase velocity of the wave >> velocity of light *c*. What if $\omega_s(\kappa)/\kappa \sim c$? A fundamentally and applicably important change occurs namely the wave acquires a transverse character in that the coupling with the radiation field becomes important. The equation to be solved, for a plane-bounded electron gas taking full transversality of the fields in the hydrodynamic model, is

$$\omega_s(\kappa)/\kappa\,[\nu+\nu_0]\,\eta = \omega_p^2[\kappa^2 c\beta + \nu_0\,\eta] \quad (1.13)$$

Here $\beta^2=3v_F^2/5$ so as to obtain the correct volume plasmon dispersion relation. Also

$$\nu^2 = \kappa^2c^2 + \omega_p^2 - \omega_s^2(\kappa) \quad (1.14a)$$

$$\nu_0^2 = \nu^2 - \omega_s^2, \text{ and.} \quad (1.14b)$$

$$\eta^2 = \kappa^2\beta^2 + \omega_p^2 - \omega_s^2(\kappa). \quad (1.14c)$$

Taking $\beta \rightarrow 0$ one gets the dispersion relation for surface plasmons as

$$\omega_s^2(\kappa)=(1/2)\,\omega_p^2 + \kappa^2c^2 - [(1/4)\,\omega_p^4 + \kappa^4c^4]^{1/2} \quad (1.15)$$

A plot of ω / ω_p versus cK/ω_p K being the wave vector parallel to the bounding surface is presented in figure 1.12 of particular relevance to the work to be presented in this thesis is the case of the surface plasmon in non-ideal geometries. Structural non-uniformities such as existing in ultrathin films that are fairly rough facilitate conversion of a photon to a surface plasmon mediated by the rough surface. Here the momentum necessary for the creation of the surface plasmon comes from the surface structure. Thus

a roughness measurement can be used at least for qualitatively correlating the surface plasmon results to microstructure and optical properties.

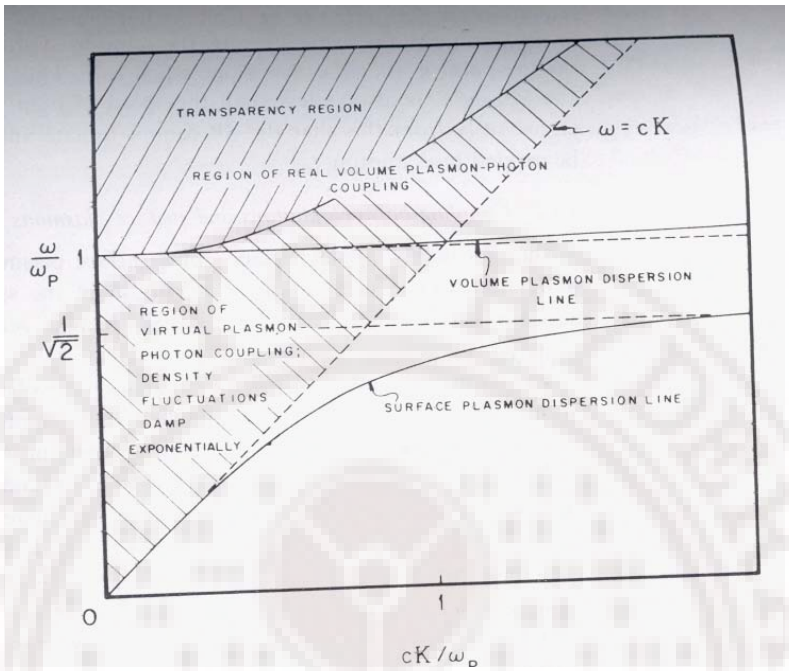

Figure 1.12: A schematic plot of the surface plasmon dispersion appropriate to a semi-infinite plane-bounded electron gas. K is the wave vector parallel with the bounding surface. The 'volume plasmon dispersion line' refers to the case of a volume plasmon with zero momentum normal to the surface. The surface plasmon dispersion line is sketched asymptotic to the frequency $\omega = \omega_p/\sqrt{2}$ [80].

1.5.2 Excitons in Semiconductors

An exciton in a semiconductor such as GaAs or CdS or AgI is a bound electron-hole pair held together by a weak coulomb interaction [82-92]. Excitons in AgI arise *'ab initio'* when an ultrathin-film of Ag is iodized. As the intensity of plasmon absorption of Ag slowly diminishes upon even a few minutes of iodization excitons appear as weak, barely detectable shoulder on the broad plasmon absorption peak signaling the formation of AgI nanoparticles on the composite Ag-AgI thin film in the manner of a plasmon-exciton transition [38-46]. Excitons in direct gap semiconductors such as AgI offer the possibility of realizing intense photoluminescence upon photo-excitation in the fundamental band edge region through direct electron-hole recombination. A high point of the present work is the realization of such excitonic photoluminescence in Cu-stabilized γ-AgI at room temperature [38,46]. An exciton is properly represented in a two-particle picture as in figure 1.13.

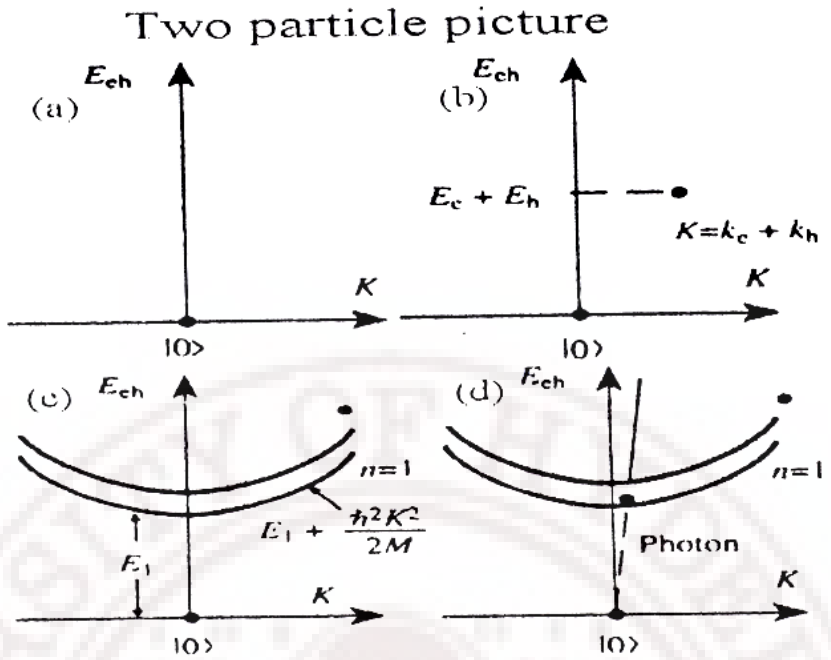

Figure 1.13: Two-particle representation of exciton states in a typical semiconductor. (a) Ground state (b) Excited state (c) Correlated exciton (d) Optical absorption. E's are energies, M = reduced mass, K= momentum [7].

A vivid picture of exciton formation is as follows: a photon enters a semiconductor, exciting an electron from the valence band into the conduction band. The missing electron in the valence band leaves a hole behind, of opposite electric charge, to which it is attracted by the Coulomb force because the electron and hole stay so close to each other (less than Debye length) [7]. The exciton results from the binding of the electron with its hole; as a result, the exciton has slightly less energy than the unbound electron and hole. Excitons are the simplest manifestations of many-body elementary excitations in covalent/iono-covalent crystalline semiconductors namely III-V (GaAs, GaN), II-VI (CdTe) and I-VII (AgI,CuI) [7,34,38,82-92].

In this work we focus on the last group of noble metal iodides and that too AgI which is characterized by mutual tetrahedral bonding between Ag and I/I and Ag leading to an open 3D zincblende structure. A healthy mix of ionic and covalent bonding (77%-23%) ensures a large concentration of Frenkel defects while proximity of Ag *4d* and *4s* bands and possibility of hybridization of *4d*- orbitals with *5p* orbitals of I^- along with symmetry breaking leads to a direct gap semiconductors with characteristic zincblende exciton signatures in their optical spectra-perhaps the most sensitive indictors of nanostructure formation and band structure development in AgI upon iodization. Being bound states of an electron-hole system excitons are stabilized by a Coulomb interaction

more like in positronium than in hydrogen which too exhibits the so-called Balmer, Paschen etc series [7,84-85]. In a way AgI excitons too are atom like. The processes of creation, stabilization and recombination of excitons in ultrathin AgI (and also in CuI and CuBr gotten through iodization, and bromination of Cu thin films) obtained by iodization of Ag film precursors could will be conveniently investigated through ambient temperature optical absorption and photoluminescence [24-30,34,38,93-94].

Interestingly the formation of excitons in nanoparticles stabilized in thin films a basic cluster formation process in thin film physics-leads to the creation of quantum dots that is, quasi-zero dimensional structures that confine carriers in all three spatial dimensions thereby enhancing applicable phenomena such as blue light emission and pollutant gas sensing. Two quantities namely Bohr radius (a_B) and binding (ground state) energy (E_{ex}) characterize excitons in a semiconductor. For AgI these numbers are 6 A^0 and 80 meV respectively. The dielectric constant (ε) of the semiconductor 'stabilizes' these two quantities as obtained in a hydrogenic model with a Coulomb potential 'normalized' by ε, within the framework of the effective mass approximation [7]:

$$a_B = (h^2/4\pi^2e^2)\,\varepsilon \qquad (1.16)$$

$$E_{ex} = 4\pi^2 m_r\, e^4/2\,\varepsilon^2 h^2 \qquad (1.17)$$

where m_r is the reduced mass of the electron-hole pair: $m_e m_h/(m_e + m_h)$.Exciton binding energies increase with increasing energy gap. According to k.p perturbation theory a larger gap is correlated with a larger effective mass which in turn results in a larger exciton binding energy. The energy spectra predicted by the hydrogenic model is a series of sharp and discrete levels right up to the continuum i.e. the conduction band. Generally the spatial extent of an exciton in state n (eq 1.16) corresponds to the ground state) is given by

$$a_n^* = \varepsilon(m_0/m_r)\, a_B\, n \qquad (1.18)$$

where a_B= 52.9 pm is the Bohr radius of the hydrogen atom. For AgI a_B= 6 A^o, E_x= 80meV. A comparison of a_n^* with the unit cell dimension decides the nature of exciton confinement in nanoparticles. In this picture AgI excitons (and also CuI excitons) in nanoparticles and structures are apparently weakly confined real exciton spectra, however, have a finite, temperature dependent width (and line shape) and the peak positions are a function of the size of the "quantum dot". This is the consequence of the finiteness of the nanocrystal (a macroscopic crystal is infinite) whose boundaries present a potential barrier for the motion of the carrier and whose size could be of the order of a_B.

These quantum size effects as well as the confinement of carriers (either together or separately) are the basic phenomena, the consequences of which are to be understood and exploited in excitonics.

In the two-particle picture (figure 13), the optical absorption by excitons involves the conversion of a photon into an exciton, the absorption occurring at a place where phonon dispersion curve intersects the exciton dispersion curve, meeting conservation criteria. Photoluminescence involves conversion of external photos by the medium into coupled exciton-photon states. Photoluminescence could be due to the radiative annihilation (or recombination) of excitons to produce a free exciton peak or due to recombination of an exciton bound to a donor or acceptor impurity (neutral or charged) in the semiconductor [95-96]. The free exciton spectrum generally represents the product of the polariton distribution function and the transmission coefficient of polaritons at the sample surface. Bound exciton emission involves interaction between bound charges and phonons, leading to the appearance of phonon side bands. The above-mentioned electronic properties exhibit quantum size effect in the nanometric size regime when the crystallite size becomes comparable to the Bohr radius a_B. The basic physics of this effect is contained in the equation for confinement energy [96-98],

$$E_x \cong E_g + \frac{\hbar^2\pi^2}{2R^2}\left[\frac{1}{m^*_e} + \frac{1}{m^*_h}\right] - \frac{1.8e^2}{4\pi\varepsilon\varepsilon_\circ R} \qquad (1.19)$$

where R is the nanoparticle radius. As excitons are just part of the electronic energy band structure, it is appropriate to discuss briefly the band structure of zincblende AgI *vis a vis* wurtzite AgI.

1.5.3 Band Structure of AgI

Victora, et al, [31] has done ab initio electronic structure calculations, β-AgI, and γ-AgI. The full-potential linear augmented-Slater-type-orbital implementation of the local-density approximation is employed. Theoretical predictions for most observed features, such as bandwidths and the location of band gaps are in good agreement with experiment. Although band-gap magnitudes are underestimated, the relative ordering of the direct gaps is correctly predicted. The beta polymorph is the ground state of AgI at room temperature. It has hexagonal symmetry with I atoms located at

$$r = ahx\hat{} + ak((1/2)x\hat{} + \sqrt{3/2}y\hat{}) + clz\hat{} \quad (1.20)$$

and

$$r = a(h + 1/3)x\hat{} + a(k + 1/3)(\frac{1}{2}x\hat{} + \sqrt{3/2}y\hat{}) + c(l + 1/2)z\hat{}. \quad (1.21)$$

The Ag lattice is displaced by 3c/8z^. The value of c is taken to be $(8/3)^{1/2}$ a, and the experimental value of a=4.58Å is used. This structure has point-group symmetry C_{6v}, although only point operations of the subgroup C_{3v} have primitive translations associated with them. Unlike the other silver halides discussed in this paper, β-AgI has four atoms per unit cell. The band structure, therefore, has twice the number of bands as revealed in figure 1.14b. The I s electrons form a narrow band 12–13 eV below the upper edge of the valence band. Theory correctly predicts a direct band gap at Γ that is slightly larger than that of α-AgI. This is consistent with experiment. As usual, the actual value is underpredicted relative to experiment. Gamma-AgI is the fcc counterpart of β-AgI. The Ag atoms are located at

$$r = (a/2)[(h + l)x\hat{} + (h + k)y\hat{} + (k + l)z\hat{}]. \quad (1.22)$$

The I lattice is displaced by (a/4) (x^+1y^+1z^) where the lattice constant a is given by the experimental value of 6.473 Å. The point-symmetry group is T_d. γ-AgI is not the experimental ground state. Theoretically, the energy is found to be 0.08 eV per formula unit above that of β-AgI. The band structure of β-AgI, and γ-AgI shown in figure 1.14(b) and (c). However the difference in stacking sequence between fcc and hcp structures typically changes energies by less than one-tenth of an eV. Comparison is most easily made from the band gap (Δ≈ 0.07 eV, the binding energies of the s electrons, and the energies beginning at the Γ point and extending toward the L point. Both Γ and L correspond to the point in β-AgI. The midpoint of the line Γ-L corresponds to the symmetry point A in the β polymorph. The average change in the band energies, between these structures evaluated at equivalent wave vectors, is only 0.02 eV.

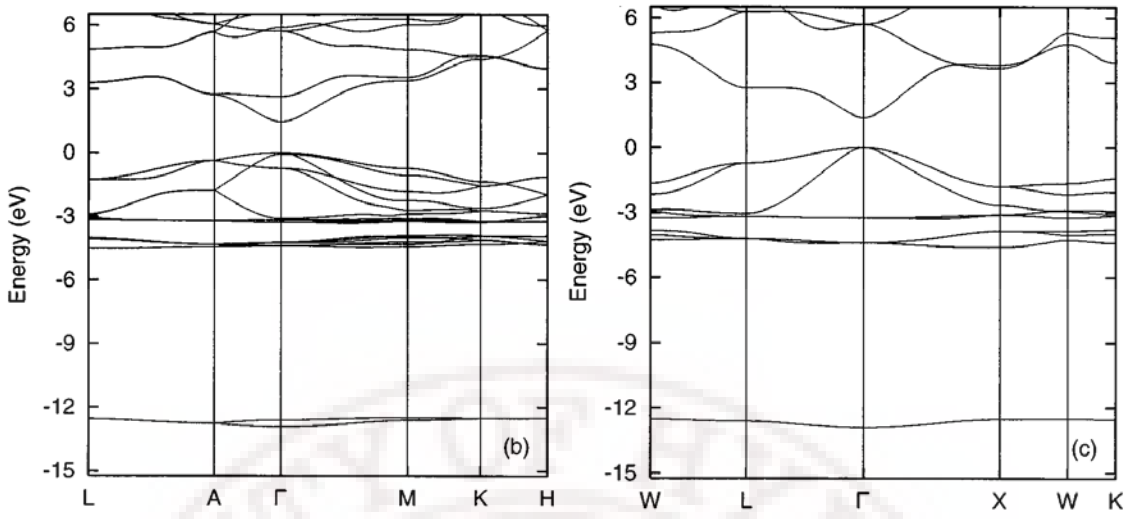

Figure 1.14: Band structure of (b) β-AgI and (c) γ-AgI [31].

Optical absorption and photoluminescence experiments enable determination of certain important features of band structure notably the band gap and allowed states within the forbidden gap including impurity and surface states and excitonic states. Many of these are involved in the recombination of photo-excited electron across the gap. As is true with other properties such as electronic conductivity the band gap of AgI and Cu-doped AgI also exhibit the beta to alpha phase transition as demonstrated by Suri et al [34]. In figure 1.15 and 1.16 one sees an abrupt drop in Eg (β-AgI) from ~2.7 eV just below the phase transition temperature to ~2.35 eV in the alpha phase. 8% Cu doping not only reduces the band gap of beta phase but also increases the transition temperature by ~10 K. Such band gap changes have been observed (w r t AgI) in the present work on the optical absorption of Cu-doped Ag thin films upon iodization.

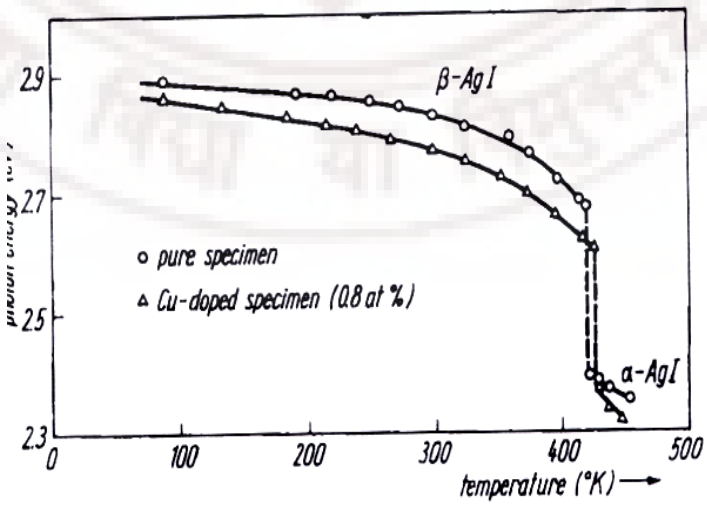

Figure 1.15: Temperature dependent of the optical absorption edge for pure and Cu-doped AgI crystals [34].

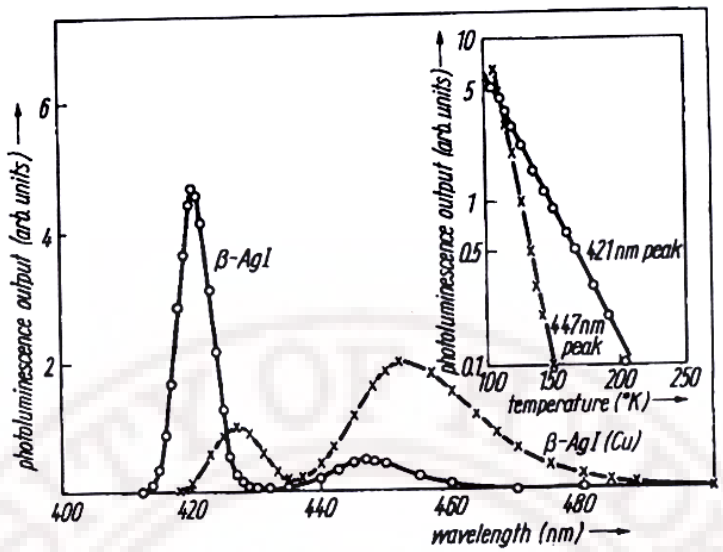

Figure 1.16: Photoluminescence spectra for pure and Cu-doped β-AgI crystals at 100° K. Exciting radiation: 365.8 nm. Inset: Temperature dependence of photoluminescence; pure β-AgI [34].

1.6 Motivation and Scope of the Present Work

Structurally metastable condensed matter holds much interest for fundamental investigators and much promise for those who seek applications for example sensing and energy-conversion technologies. People have always sought input-saving synthesis techniques to stabilize optimize and exploit such structures that often arise-thermodynamically speaking- as a result of a non-negligible covalency in the metal-nonmetal bond. Examples include chalcogenides such as ZnS,CdS,CdSe and CdTe and oxides such as Fe_2O_3 and ZnO. AgI (and CuBr ,CuI) fall into this group [7,82-92]. A general strategy of stabilizing such structures (γ-AgI zincblende or wurtzite ZnO or γ-Fe_2O_3) could be termed oxidation. When carried out at ambient temperature such 'oxidation' offers many variables to control the process and conveniently investigate the metastable formation process and the physics of the realized product. For over a decade we have used this strategy to develop three simple fabrication techniques; (1) Iodization of commercial Ag (10 micrometer thick) foils or lab-fabricated Ag or Cu metal/Ag-Cu/Ag-Sb/Ag-Al/Ag-Sn alloy thin films through closed light-tight space sublimation (2) Grinding of metal(s) powder and iodine flakes in an agate mortar and (3) Surfactant-assisted solution-based precipitation reactions.

The physics of the resulting materials- nanostructured (ultra) thin films and nano-powders have been investigated through micro-structural, electrical, thermal and optical probes to harvest a fairly rich body of phenomenology. A brief summary of this follows to set the stage for the present investigation.

1. Innovative experiments on iodization of commercial as-received and thermally annealed Ag foils yield wurztite AgI while chemically etched Ag foils yielded the expected zincblende AgI which over a week at ambient transforms into wurtzite phase, necessitating alloying of Ag as a mandatory strategy to obtain zincblende AgI [40].

2. Stabilization of the metastable zincblende structure of AgI using Cu and Sb as 'dopants', in the form of nanoparticles on glass-backed precursor (Ag-Cu and Ag-Sb) films obtained by vacuum thermal evaporation and subjected to systematic iodization in a closed cylindrical camber in a novel matrix-free approach was a high point in the investigation; Cu and Sb control effectively the AgI nanostructure growth kinetics effectively and sensitively monitored by optical absorption. The AgI film formation (> 10 nm thick) is satisfactorily accounted for by a dynamic sandwich layer model [38-39].

3. The observation of photoluminescence due to quasi-free excitonic recombination in Cu-stabilized AgI thin films and due to donor-acceptor recombination in Sb-stabilized AgI films at room temperature has seeds of quantum dot physics with new lines of investigation and application potential [38-39].

4. Ag^+ conductivity (figure 1.17) and phase transition in AgI partially substituted by Cu (obtained as nanopowders from controlled precipitation reactions) find explanation in terms of enhanced covalency effects of the Ag-I bond induced by Cu via *I(6p)-Cu(3d)* hybridization reflected directly in reduced lattice parameter and increased zincblende-bcc structural transition temperature [99].

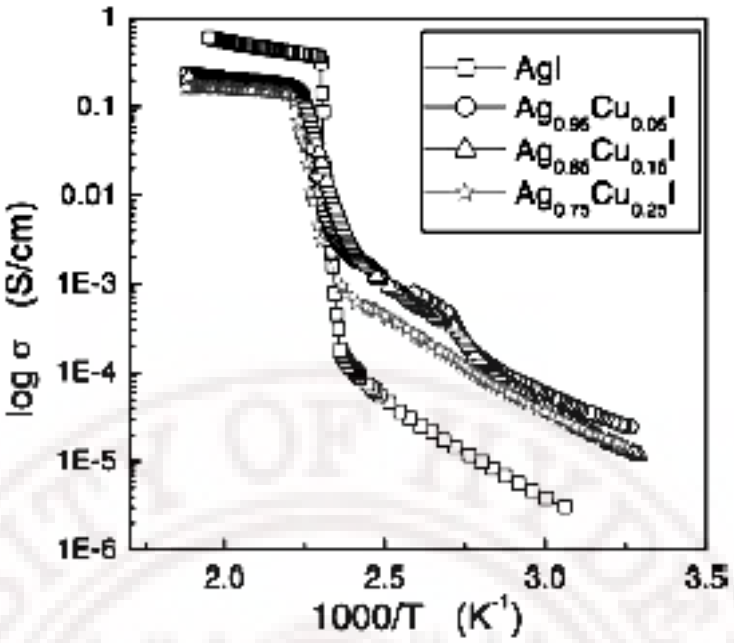

Figure 1.17: Arrhenius plots of ionic conductivity of Ag-rich solid solutions x=0, 0.05, 0.15, and 0.25 showing mixed phase regions for x>0 [99].

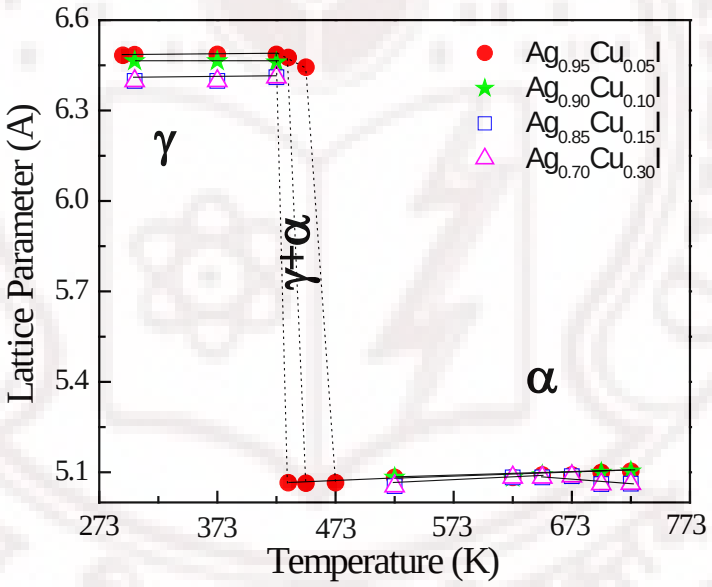

Figure 1.18: A Temperature dependence of lattice parameter values for the Ag-rich AgI-CuI solid solutions. The data points in the mixed phase (γ +α) region [100-101].

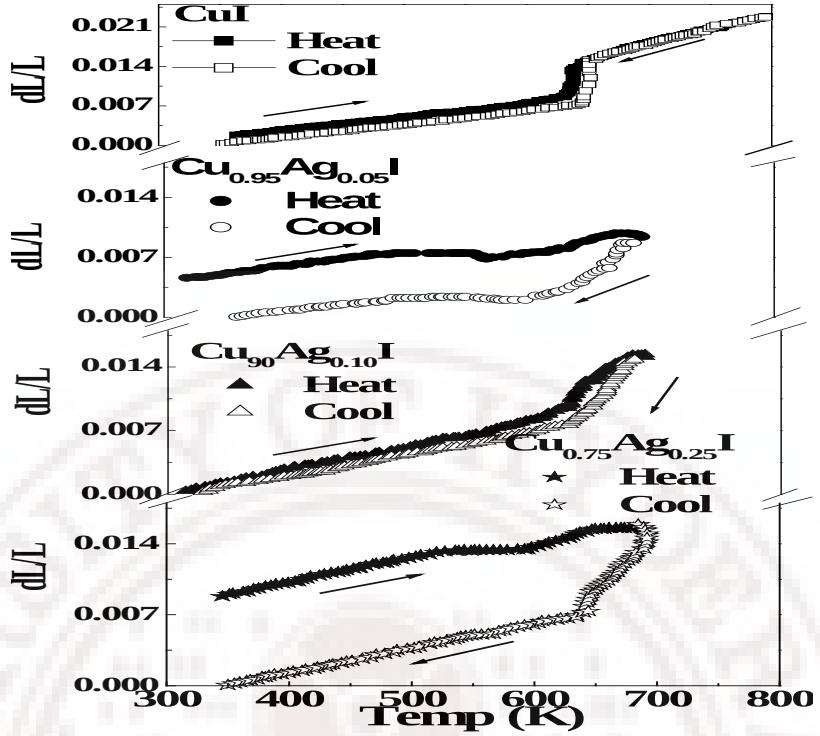

Figure 1.19: Dilatometry plots for Cu-rich solid solutions x=0, 0.05, 0.10, and 0.25 showing mixed phase regions for x>0 [100].

5. High-temperature XRD (figure 1.18) and dilatometry measurements (figures 1.19) on $Ag_{1-x}Cu_xI$ the former seeking to establish the partial phase diagram (T-x) of AgI-CuI system and the latter searching for a zero expansion material (AgI is a negative thermal expansion (thermal contraction) material while CuI is a positive thermal expansion material) have demonstrated that defects, disorder and anharmonic phonons have made these phenomena highly nonlinear (figure 1.19) [100]. This aspect remains a theoretical challenge and these experiments offer the possibility of verifying formulation of suitable models and property computations thereof. Thermal and electrical studies point to mesoscopic order emerging in this system at high temperatures.

6. It was soon realized that RF sputtering offers a convenient and controllable way of obtaining disordered (amorphous) metal films of Ag and alloys with thickness control so that better control of iodization could be achieved. Microstrucural control such as surface roughness could also enable plasmons- especially surface plasmons-to be excited in Ag films [42]. And optical absorption could be monitored carefully as the films are iodized

so that one could look at the iodization physics in a radically new perspective. One could then compare the results obtained from thermally evaporated and RF sputtered films.

7. Equally it was realized that soft mechano-chemical reactions(MCR) easily effected by a prolonged patient grinding of precursor charges in a agate mortar could yield nanoscale solid solution phases between AgI and CuI. This offered an ingenious way of investigating the phase diagrams and more importantly looks for unusual probes to look at structure-bound paramagnetic defects, possible formation of nanoscale p-n junctions and investigate thermodynamics of superionic phase transitions in AgI modified by isostructural CuI [43]. From a practical viewpoint these MCR-derived powders could be used without further processing as prime movers to develop gas sensor technologies for pollution monitoring and control.

(i). The 50-50 composition $Ag_{0.50}Cu_{0.50}I$ is characterized by ~17nm diameter spherical monodisperse crystallites with a lattice parameter a=626 pm is a potential sensor material. Thus Cu is seen to induce beneficial modification in cation disorder and strengthen the Ag-I bond in AgI-CuI binary.

(ii). The MCR process has in an unusual and spectacular manner helped create electron-hole based complementary structural/electronic paramagnetic defects in AgI and its alloys with CuI that act as microscopic probes to monitor the zincblende-bcc superionic phase transition in AgI through the EPR technique. Thus X-band EPR detected a Ag^{++} based hole centre with an average g of 2.21025 shows an abrupt rise in reciprocal EPR susceptibility at 423+/-1 K (figure 1.20a) [102].

(iii). An electron centre such as Ag^{0} in AgI nano powders obtained by MCR characterized by a narrow EPR line (10 G wide peak to peak) with a g=2.0019 again shows a rise in reciprocal EPR susceptibility at the phase transition (figure 1.20b). AgI-CuI 'alloy' compositions show very similar results except at higher transition temperatures extended by the Cu-enhanced covalency of the Ag-I bond [102]. The differential cw microwave power saturation characteristics set these two paramagnetic centres apart.

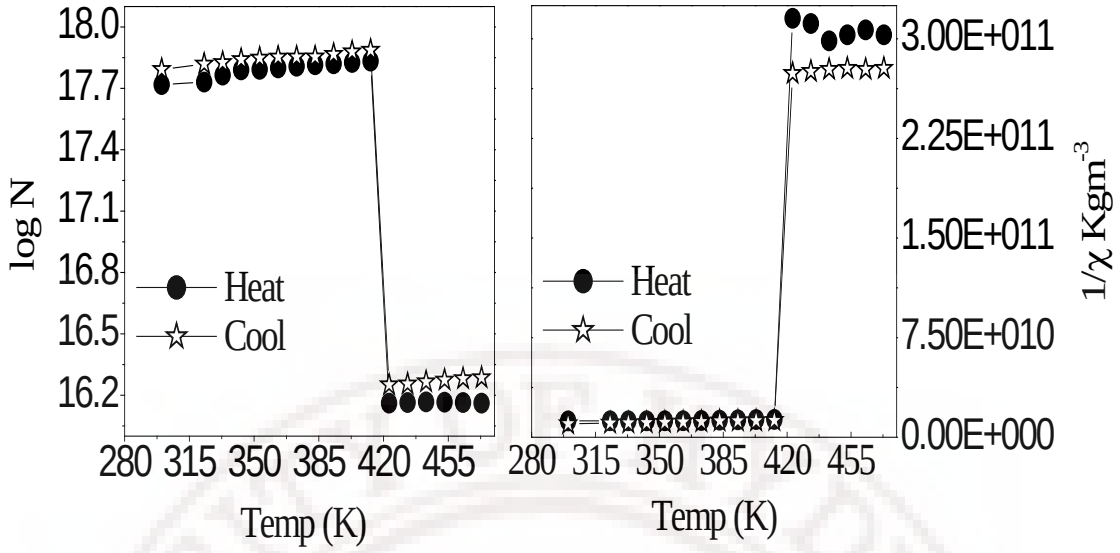

Figure 1.20 a, b: Temperature-dependence of the number of paramagnetic centres (N) and reciprocal susceptibility ($1/\chi$) corresponding to signal a in MCR-synthesized AgI. Note the abrupt changes at the phase transition temperature [102].

8. Nonohmic behaviour (diode-like) seen in the I-V characteristics of the AgI and AgI-CuI nanopowders arising from the formation of nanoscale p-n junctions yielding forward currents ranging from nanoamp to microamp underscore the role of electronic defects created by MCR and neatly corroborate the EPR results. Furthermore they could also arise in partially iodized Ag and Ag-Cu ultrathin films to be discussed in this thesis and connect well with impedance spectra measured on these thin films. These defects are thermally activated with activation barriers of 0.48, 0.60, 0.74 and 1.01 eV for AgI, $Ag_{0.95}Cu_{0.05}I$, $Ag_{0.80}Cu_{0.20}I$ and $Ag_{0.85}Cu_{0.15}I$ respectively. Hole injection and drastic depletion of Ag^+ Frenkel defects push the transition temperatures higher and higher upon Cu doping into AgI [103].

9. Aliovalent cations (Al and Sn) introduced into β and γ-AgI modifies the crystal structure, microstructure and exciton dynamics of AgI; they (i) enhance ionic conductivity and (ii) usefully modify optical properties (UV-Visible absorption and photo luminescence) through particle-size reduction and retarded/enhanced nanostructure development. Thermodynamically speaking, ambient temperature and slight iodine over pressure (above atmospheric pressure) appear to be an attractive strategy for controlled AgI nanoparticle growth [43,104]. While Sn-doped Ag films fabricated by thermal evaporation have Sn-induced disorder in the wurtzite structure developing upon

iodization , with (i) removal of UV-absorption in Ag, (ii) occurrence of red plasmon-type absorption and (iii) reduction of particle size in >10 nm film but increased particle size in 40 nm film, Al-doped Ag films and Ag films produced by RF sputtering show similar results in $Z_{1,2}$ and Z_3 exciton development, blue shift, particle size reduction and creation of donors and acceptors for recombination of electrons and holes.

10. Sputtered Ag films when systematically iodized exhibit surface plasmon resonance due to Ag colloidal particles co-existing with excitons absorbing at 420 nm and 330 nm due to $Z_{1,2}$ and Z_3 excitons respectively [42]. Plasmons 'decay' to excitons. There is in addition a thickness-induced gamma to beta structural 'transition'. The question naturally arises as to what kind of mechanism accounts for the nanoparticle formation? What kind of nanoparticles are these? Can one control the process locally by alloying Ag with Cu and making ultrathin (<10 nm) films? Such questions motivate us to develop this theme as is done in the present thesis.

11. Ag /Sn bilayers produced by RF sputtering have yielded upon iodization beta AgI nanorods whose lengths seem to increase with Sn layer thickness. These are characterized by wurtzite-type excitons and show promise for applications such as bio sensing when suitably embedded in say carbon tubes [104].

General theme of present thesis deals with preparation of cation (Cu) stabilized γ and β-AgI nanostructure thin films by using vacuum thermal evaporation and RF magnetron sputtering techniques and their studies of crystal structure, morphology, UV/visible optical absorption, photoluminescence and Superionic phase transition in AgI and $(Ag_{1-X}Cu_X)I$ thin films using a preliminary Impedance Spectral Study. This brief but comprehensive introduction, followed by a Thin Film Fabrication and Characterization Methodology chapter. The results of work carried out in this PhD project described in Chapters 3-7 are outlined as follows:

1. Surface plasmon-exciton transition in ultra thin silver and silver iodide films deposited on glass substrates by vacuum thermal evaporation.
2. Thickness and composition dependent Plasmon-Exciton transition and Photoluminescence study of cation stabilized Co-Evaporated Ag-Cu nanostructured thin films iodized at ambient.

3. Cu enhanced quasi–free excitonic photoluminescence in Co-Sputtered $Ag_{1-x}Cu_X$ (x= 0.05, 0.1 and 0.2) thin films grown on fused quartz substrates iodized at ambient.
4. Iodization time dependent Surface plasmon to exciton transition and Photoluminescence study of Core shell Silver Iodide thin films sputtered on PVA substrates.
5. Superionic phase transition in AgI and (Ag-Cu) I thin films: A Preliminary Impedance Spectral Study.

The thesis concludes with a Summary Chapter including a few suggestions for further investigation. The experimental results reported in this thesis are completely new and the thesis represents first efforts to understand them.

References

1. P. Senthil Kumar, *"Ionic and Mesoscopic Aspects of Cation Stabilized Silver Iodide"*, Ph. D Thesis, University of Hyderabad, Hyderabad, (2002), India.
2. D. Bharathi Mohan, *"Synthesis and Studies of Cation and Disorder stabilized AgI nanostructured Materials"*, Ph.D Thesis, University of Hyderabad, (2002), Hyderabad, India.
3. Milton Ohring, *Material Science of Thin Films, deposition and structure*, second edition, Acadamic press, 1900, San diego, California, USA-92101-4495.
4. Martin Reich, *Mineralium. Deposita*, **44,** 719 (2009).
5. S. Chandra, *Superionic Solids: Principles and Applications*, Amsterdam, North Holland (1981).
6. M.B. Salamon (ed), *Physics of Superionic Conductors*, Springer verlag, Berlin, 1979.
7. H. T. Grahn, *"Introduction to semiconductor physics"* World Scientific Publishing Co. Pte. Ltd, Singapore, 1999.
8. S. Hull, Superionics: Crystal structures and conduction process, *Rep. Prog. Phys*, **67,** 1233 (2004).
9. J. Maier, *Solid State Ionics*, **291**, 154-155 (2002).
10. J. S. Lee, S. Adams, J. Maier, *J. Phys. Chem. Solids*, **61,** 1607 (2000).
11. Hirotoshi Yamada, Aninda J. Bhattacharyya and Joachim Maier, *Adv. Funct. Mater*, **16**, 525–530 (2006).
12. Yu-Guo Guo, Jong-sool Lee, and Joachim Maier, *Adv. Matter*, **17**, 2815 (2005).
13. Aimin Hao, Chunxiao Gao Ming Li, Chunyuan He, Xiaowei Huang, Guangtian Zou, Yongjun Tian, and Yanzhang Ma, *J. Appl. Phys*, **101**, 53701 (2007).

14. Li-Feng Liu, Seung-Woo Lee, Jing-Bo Li4, MarinAlexe, Guang-Hui Rao, Wei-Ya Zhou, Jae-Jong Lee, Woo Lee and Ulrich Gosele, *Nanotechnology*, **19**, 495706 (2008).
15. Yuxia Wang, Liang Huang, Haiping He, Ming Li, *Physica B*, **325**, 357 (2003).
16. R. Makiura, Takayuki Yonemura, Teppei Yamada, Miho Yamauchi, Ryuichi lkeda Hiroshi Kitagawa, Henichi Kato and Masaki Takata, *Nature Materials*, **8**, 476 (2009).
17. K. Terabe, T. Hasegawa, T. Nakayama, M. Aono, *Nature*, **47**, 433 (2005).
18. Rahima Khaton, Shin-ichiro Kashiwagi, Toshifumi limori and Nobuhiro Ohta, *Appl. Phys. Lett*. **93,** 234102 (2008).
19. J. Maier, *Z. Anorg. Allg. Chem*, **426**, 264 (2000).
20. S. Mochizuki, *Physica B*, **308–310**, 1042 (2001).
21. D. A. Keen, S. Hull, A. C. Barnes, P. Berastegui, W. A. Crichton, P. A. Madden, M. G. Tucker, and M. Wilson, *Phys. Rev B,* **68**, 14117 (2003).
22. Chaok Seok and David W. Oxtoby, *Phys. Rev. B*, **56(18)**, 11485 (1997).
23. Raymond S. Eachus, Alfred P. Marchetti, and Annabel A. Muenter, *Annu. Rev. Phys. Chem*, **50**. 117 (1999).
24. P. Marchetti, J. C. Hansen, S. Chen, M. Irving, R. Baetzold, and B. R. Sever, *Phys. Rev B,* **69**, 094107(2004).
25. Michal Ilana Freedhoff, Alfred P. Marchetti, George L. Mclendon *J. Luminescence*, **70**, 400 (1996).
26. Shosuke Mochizuki and Kouta Umezawa, *Physics Letters A*, **228**, 111(1997).
27. R. Berry, *Phys. Rev*, **161(3)**, 848 (1967).
28. S. Mochizuki and Fumito Fujishiro, *J. Phys.: Condens. Matter*. **16,** 3239 (2004).
29. Manuel Caradona, *Phys. Rev,* **129(1)**, 69 (1963).
30. S. Kondo, T. Itoh, and T. Saito, *Phys. Rev. B,* **57(20)**, 13235 (1998).
31. R. H. Victora, *Phys. Rev. B,* **56 (8)**, 4417 (1997).
32. T. H. Wei, C. W. Chen, L.C. H. Wang, P. L. Tu, T, C. Wen, *Journal of Luminescence*, **128**, 161 (2008).
33. O. Husberg, H. Vogelsang, W. Von der Osten, *J. Luminescence,* **96**, 155 (2002).
34. S.K. Suri and H. K. Henisch, *Phys, Stat. Sol. (b),* **44**, 627 (1971).
35. V. Perera and K. Tennakone, *Sol. Energ. Mat. Sol. C*, **79**, 249 (2003).
36. B. Wang, B. Lu, Y. W. Jiang, Y. H. Zhang, D.W. Ma, *Org. Lett*, **10**, 2761(2008).
37. M. Bendahan, P. Lauque, J. Seguin, L. Aguir, K. Knauth, P. Sens. *Actuator B-Chem*, **95** (2003).
38. P.Senthil Kumar and C. S. Sunandana, *Nano Letters*, **2(4),** 431 (2002).
39. P.Senthil Kumar and C. S. Sunandana, *Nano Letters*, **2(4),** 975 (2002).
40. P. Senthil Kumar and C. S. Sunandana, *Thin Solid Films*, **323**, 110 (1998).

41. P. Senthil Kumar, P. Babu Dayal and C.S. Sunandana, *Thin Solid Films*, **357**, 111 (1998).
42. D. Bharathi Mohan and C.S.Sunandana, *J. Appl. Phys*, **100**, 064314 (2006).
43. D. Bharathi Mohan, C.S. Sunandana, *J. Phys. Chem. Solids*, **65**, 1669 (2004).
44. D. B. Mohan, V. S. Reddy and C. S. Sunandana, *Appl. Phys. A*, **86**, 73 (2007).
45. M.Gnanavel, D. Bharathi Mohan, C. S. Sunandana, *Thin Solid Films*, **517**, 1058 (2008).
46. M.Gnanavel and C. S. Sunandana, *Proc. SPIE*, **7394**, 73942D (2009).

    46 (a) C. S. Sunandana, *J. Phys. Chem. Solids*, **58,** 1359 (1997).
47. K. Barn, Murakawa, *J. Pjhys. Soc. Japan*, **13,** 484 (1985).
48. J. Bieron, *Phys. Rev. A*, **64,** 52507 (2001).
49. J. E. Maskasky, *Phys. Rev. B: Condens. Matter Mater. Phys*, **43(7)**, 5769 (1991).
50. W. Buhrer, R. M. Nicklow and P. Bruesch, *Phys. Rev. B: Condens. Matter Mater. Phys*, **17(8)**, 3362 (1978).
51. R. J. Cava and E. A. Rietman, *Phys. Rev. B: Condens. Matter Mater. Phys*, **30(12)**, 6896 (1984).
52. Yoshiasa, K. Koto, F. Kanamaru, S. Emura and H. Horiuchi, *Acta Crystallogr. Sect. B: Struct. Sci* **.43**, 434 (1987).
53. Rains and J. R. Ray, *Phys. Rev. B: Condens. Matter Mater. Phys*, **44(17)**, 9228 (1991).
54. J. L. Tallon, *Phys. Rev. B: Condens. Matter Mater. Phys*, **38(13)**, 9069 (1988).
55. G. R. Robb, A. Harrison and A. G. Whittaker, *Phys Chem Comm*, **5(19)**, 135 (2002).
56. Katsuyuki Matsunaga, Isao Tanaka and Hirohiko Adachi, *J. Phys. Soc. Jpn.* **67**, 2027 (1998).
57. S Ono, K Kobayashi, *J. Phys. Soc. Jpn*. **74**, 648-652 (2005).
58. M Aniya, *J. Phys. Soc. Jpn*. **61**, 4474, (1992).
59. D Mazumdar, P A Govindacharyulu and D N Bose, *J. Phys. Chem.Soilds*, **43**, 933 (1982).
60. Yu. Ya. Gurevich and A K Ivanov Shitz, *Semiconductors and Semimetals*, **26**, 229 (1998).
61. L A Palomino-Rojas, *Solid State Sciences*, **10**, 1228 (2008).
62. S. Ono, M. Kobayashi, H. Iyetomi, T. Tomoyose, *Solid State Ionics*, **139**, 249 (2001).
63. A Yoshiasa, K Koto, H Maeda and T Ishii, *Japanese. J. Appl.Phys*, **781**, 3636 (1997).
64. S. Sunandana and P. S. Kumar, *Bull. Mater. Sci*, **27**, 1 (2004).
65. T. Ishii and O Kamishima, *J. Physical Society of Japan*, **70**, 159 (2001).
66. J H Page and J-Y Prieur, *Phys. Rev. Lett.* **42**, 1684 (1979).

67. K. Kaneko, T. Kamiyama, Y. Kiyanagi, T. Sakuma and S. Iked, *J. Phys. Chem. Solids*, **60**, 1499 (1999).
68. David B. Pedersen and Shiliang Wang, *J. Phys. Chem. C*, **111**, 1261 (2007).
69. R H Bube, *Electrons in Solids*, Chap-8, Academic Press, San Diego, 3rd edition, (1992).
70. F. Bohren and D. R. Huffman, *Absorption and Scattering of Light by Small Particles*, Wiley, New York (1983).
71. G. Mie, *Ann. Phys*. **25**, 377 (1908).
72. Cecilia Noguez, *Optical Materials*, **27**, 1204 (2005).
73. Stephan Link and Mostafa A. El-Sayed. *J. Phys. Chem. B* **103**, 8410-8426 (1999).
74. P. B. Johnson and R.W. Christy, *Phys. Rev. B*, **6(12)**, (1972) 4370.
75. Stefan A. Maier, "Plasmonics: *Fundamentals and Applications*", Springer, United Kingdom.
76. W. P. Halperin, *Rev. Mod. Phys*, **5**(3), 533-607 (1986).
77. Kreibig, U.; Vollmer, M. *"Optical properties of metal cluster"*; Springer: Berlin, 1995.
78. N. Economou, "Surface Plasmon in Thin Films". *Phys. Rev.* **182(2)**, 539-554 (1969).
79. Josette Rivory, *Phys. Rev B,* **15(6)**, 3119(1977).
80. R H Ritchie, *Plasmons in Solids, Surface Science,* **34**, 1 (1973).
81. J. L. Pautrat, J. M. Gerard, E. Bustarret, D. Cassagne, E. Hadji and C. Seassal, *Optronics*, chapter-**16**, page-169, Nanoscience, Springer 2007.
82. H. Haug and S. W. Koch. *Quantum theory of the optical electronic and properties of semiconductors*, World Scientific Publishing, year 2005, Singapore -596224.
83. C. D. Reynolds and T. C. Collins, *Excitons, Semiconductor*, Encyclo. Modern. Phys, RA Meyers (Ed), AP 1990.
84. C. Kittle. *Introduction to solid state physics*, 7th edition, *Wiley*, 1996.
85. Yu. Ya Gurevich and A.K Ivanov-shits. *'Semiconductor properties of Superionic Materials, Semiconductor and semimetals*, Academic Press, New York, 26, 230, 1988.
86. L. A. Swafford, L. A. Weigand, M. J. Bowers, J. R. McBride, J. L. Rapaport, T. L. Watt, K. Sriram, D. Leonard C. Feldman, and J. Sandra. Rosenthal, *J. Amer. Chem. Soc*. **128**, 12299-12306 (2006).
87. S. A. Ivanov, A. Piryatinski, Jagjit Nanda, Sergei Tretiak, K. R. Zavadil, W. O. Wallace, Don Werder, and V. I. Klimov *J. Am. Chem. Soc.* **129,** 11708 (2007).
88. H.Y. Xu. Z.Liu, Y. Liang, Y. Y. Rao, X.T. Zhang, and S. K. Hark. *Appl. Phys. Latt*, **95**, 133108 (2009).
89. K. Suzuki, H. Kondo, M. Inoguchi, N. Tanaka, K. Kageyama and H. Takagi, *App. Phys. Lett*, **94**, 223103 (2009).

90. C. Y. Wang, Jeongho Kim, P. Sreekumari Nair, M. C. Nagy and G. D. Scholes, *J. Phys. Chem. C*, **113**, 795 (2009).
91. B. Enright and D. Fitzmaurice, *J. Phys. Chem*, **100**, 1027 (1996).
92. N. Pikhtin and H. H. Hegazy, *Semiconductors*, **43(10)**, 1259 (2009).
93. A.P. Marchetti, J. C. Hansen, S. Chen, M. Irving, R. Baetzold and B. R. Sever, *Phys. Rev. B,* **69**, 94107 (2004).
94. S-H Ciou, Yi-Wei Cao, H-C Huang, De-Yan Su, and V. L. Huang, *J. Phys. Chem. C,* **113**, 9520 (2009).
95. Bernard Valeur, *Molecular Fluorescence Principles and Applications*, Wiley, 2002.
96. Timothy H. Gfroerer, '*Photoluminescence in Analysis of Surfaces and Interfaces'*, *Encyclopedia of Analytical Chemistry*, R.A. Meyers (Ed.) pp. 9209–923, Wiley, 2000.
97. L. E. Brus, J. Chem. Phys. 80(9), 4403 (1984).
98. Tito Trindade, Paul O'Brien and Nigel L. Pickett, *Chem. Mater.* **13**, 3843 (2001).
99. P. S. Kumar, P. Balaya P. S. Goyal and C. S. Sunanada, *J. Phys. Chem. Solids*, **64**, 961 (2003).
100. P. Senthil Kumar, A. K. Tyagi and C. S. Sunandana, *J. Phys. Chem. Solids*, **67**, 1809 (2006).
101. J. Kimura, T. Ida, M. Mizuno, K. Endo, M. Suhara, K. Kihara, *J. Mol. Struct*, **522**, 61 (2000).
102. Bharathi Mohan and C. S. Sunandana, *J. Phys. Chem. B*, **110**, 4569 (2006).
103. D. Bharathi Mohan and C. S. Sunandana, *Pramana*, **67,** 331 (2006).
104. D. Bharathi Mohan and C. S. Sunandana, *J. Naosci. Nanotech*, **5**, 1-5 (2005).

Chapter II

Thin Film Fabrication and Characterization Methodology

2.1 Introduction

In this chapter, we outline thin film fabrication and characterization techniques used in the present study. We have tried to grow semiconducting nanoparticles by bottom up method (iodization of Ag and Ag-Cu thin films at ambient using a special jig developed in house). The precursor thin films were fabricated by vacuum thermal evaporation and RF Magnetron sputtering. The techniques involve stylus profilometry for thickness measurements and X-ray diffraction for examining crystals, crystallite size and orientation. Dynamic Force Microscopy (DFM) and Atomic Force Microscopy (AFM) were used for surface topography and surface roughness determination. Transmission electron microscopy (TEM) and selected area electron diffraction (SAED) were used for investigation of crystal structure, particle size, shape and growth of the nanoparticles determination. UV-Vis spectrophotometry was used to obtain optical absorption curves from which the optical constants such as absorption coefficient and optical band gap were determined. UV-Visible fluorolog-3Model FL3-22 spectrophotometer was used for Photoluminescence study of AgI and Cu doped AgI thin films to determine formation of band structure and band gap. The impedance measurement spectroscopy studies of AgI were carried out using an impedance analyzer using Metal-Insulator-Metal (MIM) structures.

2.2 Bottom up approach

In the 'bottom up' approach [1], the 'sublime physics' of a 'ridiculously simple' additive chemical reaction namely

$2Ag\ (solid) + I_2\ (vapour) \rightarrow 2\ AgI\ (solid)$

could be explored Ex-situ.

In this approach low density I_2 vapours hit sputtered/thermal evaporated pure Ag, Ag-Cu alloy films. These films may be stressed/stress free depending upon mechanism of growth. A new '8' shape glass chamber was made for iodization shown in figure 2.1. Films of thermally evaporated and RF sputtered were iodized for periods ranging from 5 minutes to 24 hr using this setup at ambient temperature. 1 mm diameter hole made at the center of the chamber controls the iodization rate throughout the process, serving as a 'flux/limiter' of I_2 vapour molecules. Chamber is made up of glass with dimensions of length and diameter being 25 cm and 4 cm respectively.

Two major factors control the process namely

1. Substrate-film 'interfacial stress' (thickness effect)
2. Microstructure of the films

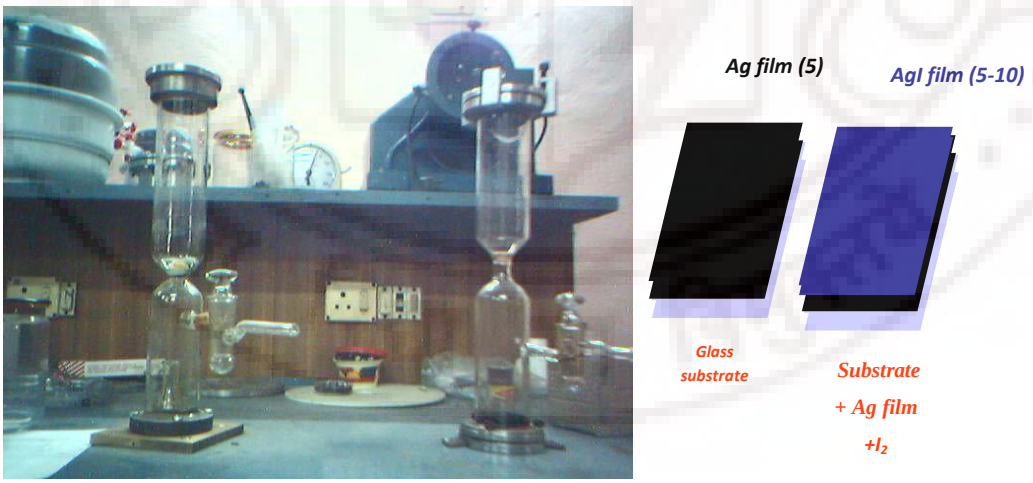

Figure 2.1: shows that an 8 shape glass chamber holds iodine at bottom sublimating at room temperature. The iodization rate is controlled through a 1 mm hole and it is finally reacted with thin film kept at the top portion of the chamber.

Ag and Ag-Cu thin films upon controlled iodization following the procedure described above reveal

1. Quasiparticle formation,
2. Band structure development, and,
3. Various traps level formation.

2.3 Thin Film Fabrication Techniques

We used two different experimental techniques to fabricate Ag and $Ag_{1-x}Cu_X$ (x= 5, 10, 15 and 20 at wt %) metal and alloy thin [2-4] films thickness of 5 and 15 nm (and occasionally 40 nm) on glass, fused silica and polymer substrates, namely,

1. Vacuum Thermal Evaporation
2. RF magnetron sputtering

2.3.1 Vacuum Thermal Evaporation

In present study we have used the vacuum thermal evaporation method to deposit Ag and Ag-Cu alloy thin films thickness of 5-15 nm. Vacuum thermal evaporation is one of the most commonly used metal vapor deposition methods [2-4]. A solid material is evaporated by heating it to sufficiently high temperature and re-condensed onto a cooled substance to form a thin film. As the name implies, the heating (Joule heating effect) is carried out by passing a large current through a filament container which has a finite electrical resistance. Once the metal is evaporated, its vapour undergoes collisions with the surrounding gas molecules inside the evaporation chamber. As a result a fraction is scattered within a given distance during their transfer through the ambient gas. The mean free path for air at 25^oC is approximately 45 and 4500 cm at pressure of $1x10^{-4}$ and $1x10^{-6}$ Torr, respectively. Therefore, pressures lower than $1x10^{-5}$ Torr is required to ensure a straight line path for most of the evaporated species and a substrate- to- source distance of approximately 10 to 25 nm in a vacuum chamber is usually employed

Figure 2.2 shows schematic representation of the vacuum unit ('HINDHIVAC' vacuum coating unit, model No.12A4) along with all the components is shown in the figure 2.2 Essentially, it includes a bell jar made up of metal, with two quartz view posts, connected to a rotary pump, a diffusion pump (DP), a roughing valve (connecting the rotary pump to the chamber), a backing valve (connecting the rotary pump to the

diffusion pump), a high vacuum valve (baffle, which connects the diffusion pump to chamber).

In the present study, prior to evaporation, a portion of highly pure Ag (99.999%) and Cu (99.999%) purchased from (Aldrich USA) were ground thoroughly in an agate mortar, to form a fairly homogenous physical mixture of Ag and Cu of desired compositions e.g. 5, 10, 15 and 20% of Cu (by atomic weight). The powder was placed in a molybdenum boat and thermally evaporated on to the substrates kept at an ambient temperature. These compositions were deposited using thermal evaporation technique by following the same procedure mentioned above.

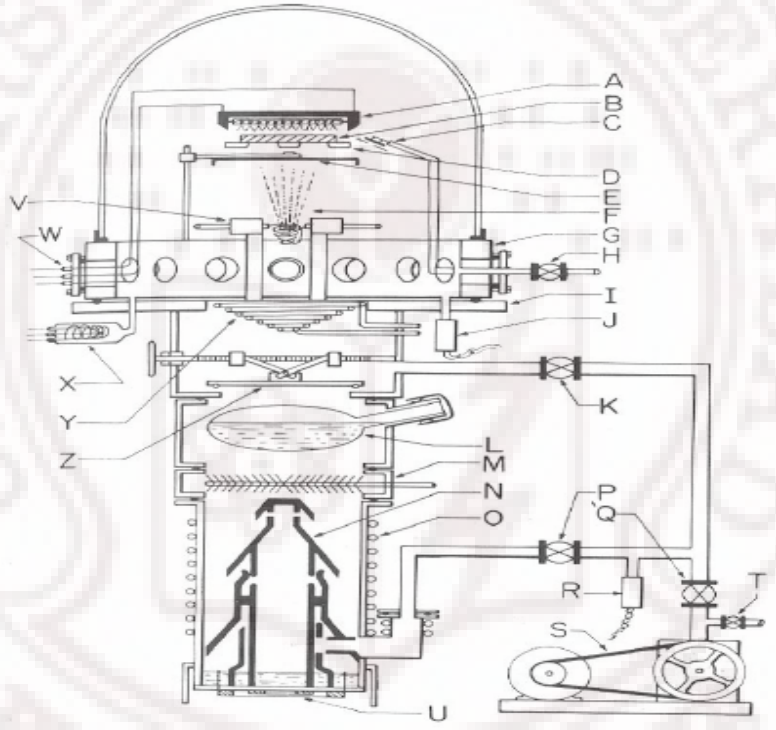

Figure 2.2: A schematic representation of thermal evaporation unit. Different parts of Vacuum unit:

A- Quartz iodine lamp heater
B- Substrate
C- Quartz crystal rate controller and deposition monitor
D- Substrate mask
E- Shutter (Mechanical or Electromagnetic)

F- Vapours from evaporation source
G- Adapter collar between the bell jar and the pump baseplate flange
H- Air-inlet valve
I- Baseplate flange

J- Pirani or thermocouple gauge
K- Roughing valve
L- Liquid-air trap
M- Cooled chevron baffles
N- Diffusion pump
O- Cooling coils
P & Q- backing valves
R- Pirani gauge
S- Forepump with air-inlet valve T
U- diffusion-pump heater
V- Filament holders
W- Multiple feed through
X- Ionisation gauge
Y- Meisner trap
Z- Baffle valve.

The optical parameters and the microstructure of our thin film samples are expected to be sensitive to thickness making thickness measurements mandatory. So a Digital Thickness Monitor (DTM) (Model No. DTM-101) was used which improved manual control of the vacuum film deposition process by providing a direct display of film thickness and deposition rate during the coating. In a DTM, the physical basis of the thickness measurement is the oscillation of a piezo- electric quartz crystal. The frequency of the crystal, as the film deposits on it, simultaneously as it does on the substrate, decreases.

The thickness is given by

$t = -df/C_{fo} \times \rho_{film}$

Where, df is the frequency difference, ρ_{film} is the density of the film, c_{fa} is the elastic constant of the quartz crystal. The input parameters required for displaying the accurate thickness and rate of deposition is

(i) Tooling Factor Correction = Distance between the sample and the quartz crystal/ distance between the sample and the substrate
(ii) Density of the sample
(iii) Acoustic impedance of the sample

By utilizing the tooling factor correction, the DTM can calculate and display the deposition rate and thus the thickness of the film coated on the substrate rather than on the crystal sensor itself. The density and acoustic impedance mismatch between the quartz crystal and the film material has to be taken into account in order to display the thickness

accurately. If not corrected, enormous errors result as the film thickness increases. In all our thickness measurements using this DTM-101, the resolution of the film thickness were of the order of ±1 A^0.

2.3.2 Sputtering Technique

The term sputtering comes from the Dutch word "sputteren" meaning "to spit out in small particles and with a characteristic explosive sound". Sputtering was first observed by Groves in 1852 with Plücker first to suggest, in 1858, that this discovery be used as a tool to produce metallic films. Sputtering is a physical vapor deposition (PVD) process where material is physically removed from a target due to momentum transfer between the target atoms and the impinging energetic ion [5]. The sputtered atoms ejected into the gas phase are not in their thermodynamic equilibrium state, and tend to deposit on all surfaces in the vacuum chamber. A substrate (such as a wafer) placed in the chamber will be coated with a thin film. Sputtering usually uses argon plasma. Sputtering process has proved to be advantageous due to high deposition rates, low sputtering pressure, good composition control, ability to deposit on large area and this process is industrially and economically feasible [2-6].

Four main processes occur during sputter deposition: plasma generation, ion bombardment, atomic transport, and nucleation and growth at the substrate surface. These are individually discussed, as each one of them influences thin film growth.

2.3.2.1 Plasma Generation

Plasma is defined as a quasi neutral gas of charged and neutral atoms and clusters [7]. In a thin film deposition unit such as sputtering, an airtight chamber is evacuated using a system of vacuum pumps, to pressures on the order of 10^{-6} - 10^{-10} Torr, and backfilled with a high pure gas (Ar, 99.9%) to relatively low pressures, usually in the mTorr range.

A planar diode sputtering system in its basic form consists of two opposing, flat electrodes in an evacuated chamber. A variety of power supplies (dc and rf) are available for plasma generation. In dc sputtering a potential difference of several hundred volts is generated between the two plates creating an intense electric field between them. The electric field E is given by [8-9]:

$$\mathbf{E = \frac{V}{d}} \qquad \mathbf{(2.1)}$$

where V is the applied voltage and d is the separation between the two electrodes.

A generated free electron placed near the cathode will be accelerated in the direction of the applied field. As the electron is propelled toward the anode it will encounter gas atoms contained between the electrodes. This is generally a high purity noble gas such as argon at a reduced pressure. The impact of the high-energy electron with a gas atom will ionize the atom by removing a weekly bound outer shell electron. The ejected electron is subjected to the same field and will also be accelerated toward the anode. This avalanche effect of electrons is responsible for the breakdown of the gas molecules and provides self sustaining plasma. There are four important processes that occur within the plasma in order to sustain a quasi-neutral gas of charged particles: Ionization, Excitation, Relaxation and Recombination. The most prevalent of these is electron impact ionization described by the reaction [6]

$$e^- + Ar^o \rightarrow Ar^+ + 2e^- \qquad (2.2)$$

According to the eq (2.2) and (2.3) (below) a single electron collision with a gas molecule produces two electrons and an ion. As the process continues, the generation of two electrons from a single electron impact leads to an avalanche effect (discharge) which leads to sustained plasma. Excitation is a process of electron promotion to a higher energy state, which is short, lived due to recombination and photon generation.

$$e^- + Ar \rightarrow Ar^* + e^- \qquad (2.3)$$

Relaxation occurs as the electron relaxes from an excited state to its ground state. As the electron relaxes a photon is given off with an energy corresponding to an energy difference that is elementally specific. It is this process that is a function of all plasmas and responsible for the term glow discharges. Recombination occurs as ions and electrons within the plasma recombine to form neutral molecules.

2.3.2.2 Ion Bombardment

The modern theory of sputtering, based on the momentum transfer theory caused by a collision cascade, states that at low kinetic energies, or the "sub-threshold region", where E = 0-50 electron volts (eV), the ion does not have enough energy to dislodge target atoms. At moderate energies or the "knock-on sputtering regime", where E = 50-1000 eV, ions impact and dislodge "knock-on" atoms into the target. These knock on atoms impact and dislodge *other* target atoms. This results in a collision cascade that ejects atoms, ions, electrons and neutrals from the first 10 to 50Å of surface of a target. Several researchers have shown that the energy of ions must exceed four times the binding energy of the target atoms to induce sputtering, which is what most of the practical PVD techniques offer. At high energy, where E = 1-50 keV, impacting ions penetrate into the lattice and are successfully implanted. At very high energies, E >50 keV, ions penetrate deep into the lattice and are implanted within the bulk. While these latter two processes are used for material doping and implantation, they are virtually irrelevant to the present context of sputtering.

Ions located near the edge of the plasma are accelerated towards the anode. Momentum transferred from ion impact to target atoms will drive the atoms on the surface into the target. Thus the sputtering process can be likened to a break in a game of "atomic" billiards. The excited ions, representing the cue ball, strikes the atomic array of the target-the neatly arranged pack-scattering them in all directions. Some of these will be ejected in the direction of the original approaching ion i.e. normal the target surface. It is this ejected particle which is useful for deposition on the surface of the substrate. Hence the sputter process essentially involves *knocking an atom or molecule out of the surface of a target.* Under the right conditions, the sputtered species will travel through space until it strikes and condenses on the surface of the substrate. *Sputtering, therefore, requires a sequence of collisions.* A collision cascade arises from multiple interactions of bombarding ions with target atoms, as the ions impart their energy over a distance within the surface of the target [7].

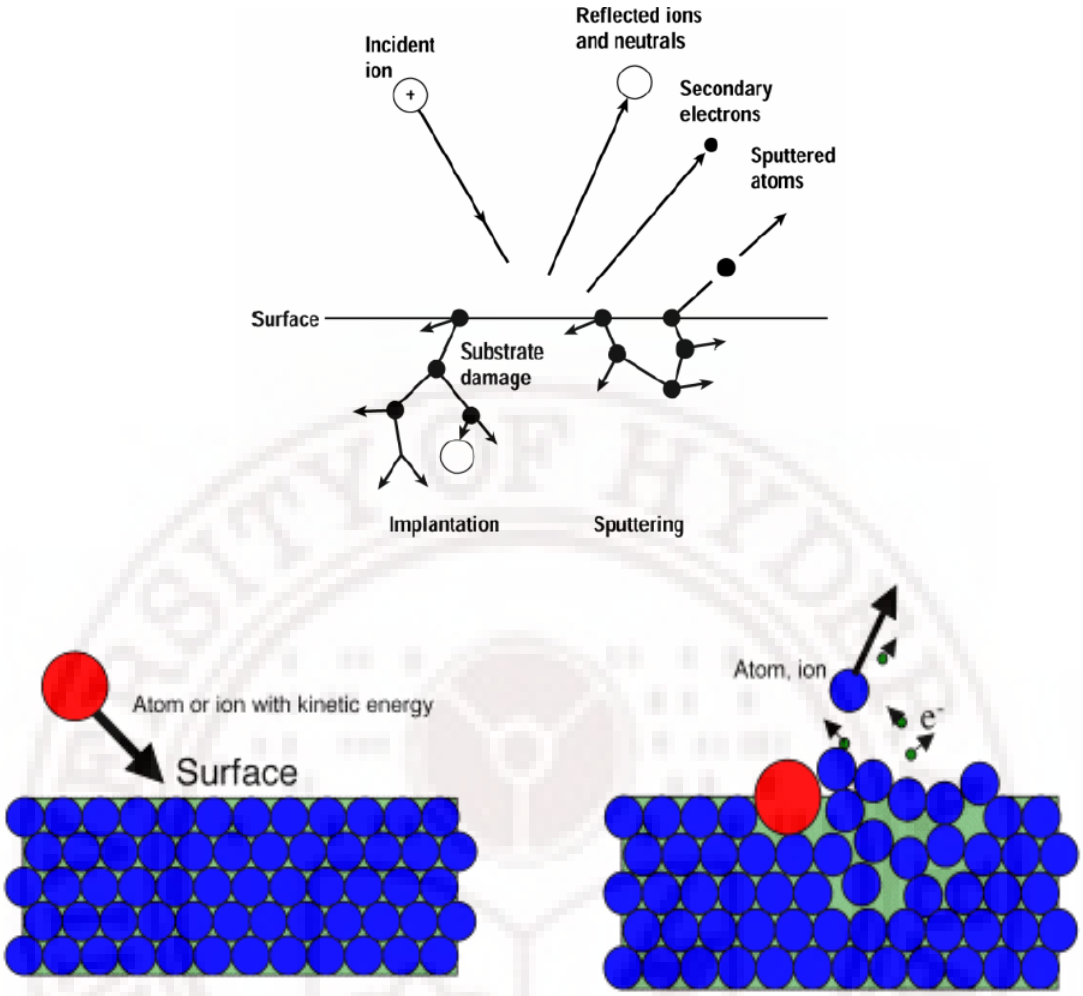

Figure 2.3: Ion bombardment of an atom out of the surface of target

2.3.2.3 Atomic Transport

In sputtering, target atoms originate from the solid phase. These particles are then subject to aspects of the plasma before reaching the substrate. The transport mechanism is largely dependent upon the sputtering pressure utilized. Sputtered atoms traversing the distance between cathode and anode have a statistical probability of collision with gas atoms, known as the collision cross-section. The mean distance a gas molecule can travel before collision with another gas molecule is known as the "mean free path" (*l*) and is given by:

$$\mathbf{l} = \frac{\mathbf{1}}{\sqrt{\mathbf{2}}\boldsymbol{\pi}\mathbf{d}^{\mathbf{2}}\mathbf{n}_{\mathbf{v}}} \qquad \mathbf{(2.4)}$$

where n_v is the number of molecules per unit volume (molecules/m^3) and d is the diameter of the molecule [3].

At a pressure of about 100 mTorr, the mean free path is roughly 5 mm. At low pressures, or longer *l*, sputtered particles will have few gas phase collision and arrive at the substrate with their initial kinetic energy. These energetic bombarding species can have beneficial or deleterious effects upon the substrate and the growing film. At higher pressures, or shorter *l*, sputtered atoms collide with gas atoms and transfer energy through elastic collisions, thereby thermalizing with the gas, the outcome of which is a decrease in sputtered atom energy as a function of increasing pressure or increasing distance between cathode and anode. This type of transport is referred to as diffusive transport.

2.3.3 RF sputtering

It is well known that dc sputtering is a versatile technique for deposition of metallic films from a metallic target. But, sputtering of insulating compounds does not permit the use of dc power because of the immediate buildup of surface charge of positive ions on the front side of the insulating target [2-6]. This then prevents any further ion bombardment and/or lead to an arcing event. Arcing is detrimental to the growth of high quality films as it results in macro-molecule ejection of target species which will be incorporated into the growing film. To sputter insulating material by dc power requires a practically impossible power of 10^{12} volts. In principle, there are many methods to overcome this issue out of which use of high frequency power supplies allows the sputtering of insulating, conducting, or semi-conducting material by defeating the buildup of charge on the surface of the target.

The Federal Communications Commission (FCC) has assigned a radio frequency of 13.56 MHz for industrial, educational and medical uses, and is one of the frequencies typically utilized for RF sputtering. Sputtering in the RF discharge was observed by Robertson and Clapp in 1933 [10]. They found that the glass surface of the discharge tube was sputtered during the RF-discharge. Presently the RF-sputtering system holds an important position in the field of thin film deposition. A typical RF-sputtering system is shown in figure 2.4.

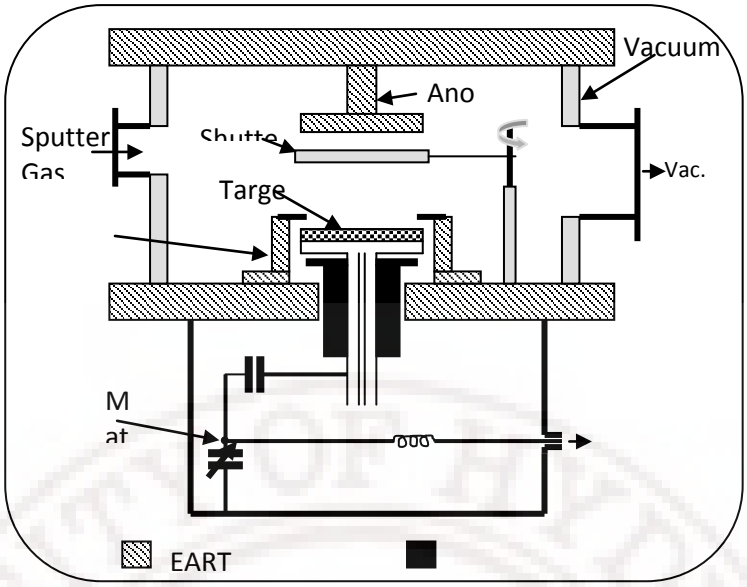

Figure 2.4: RF magnetron sputtering system

The RF diode sputtering system requires an impedance-matching network between the power supply and discharge chamber. A typical network for impedance matching is shown in figure 2.5. The impedance of the RF-power supply is almost always 50Ω. The impedance of the glow discharge is of the order of 1 to 10kΩ.

In RF diode sputtering, the target current density, i_s, is given by,

$$i_s \cong C\frac{dV}{dt} \qquad (2.5)$$

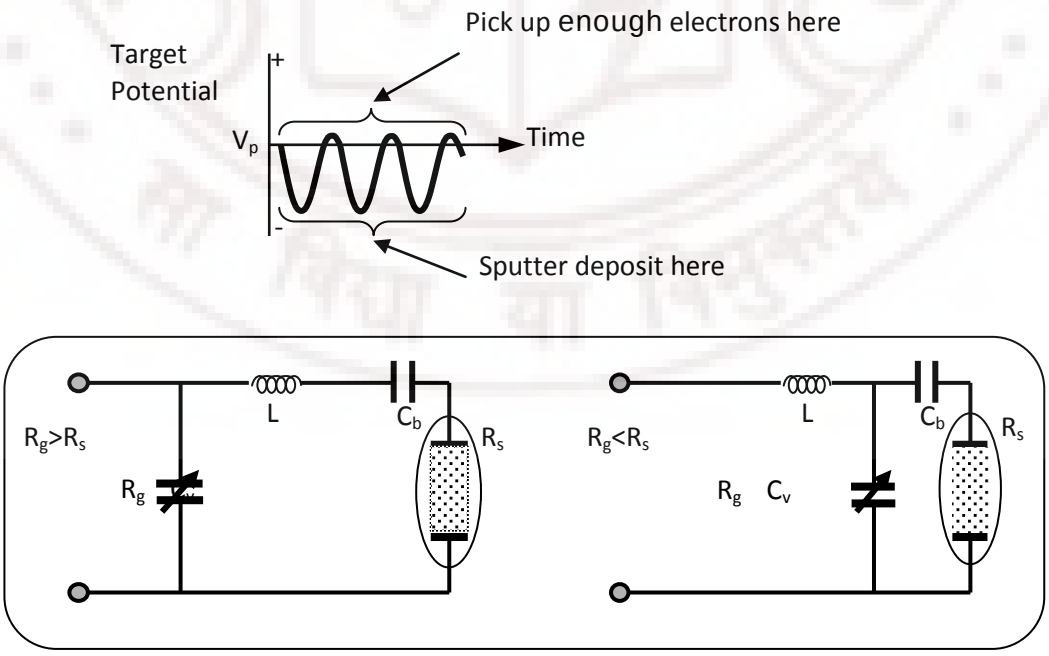

Figure 2.5: Impedance matching networks for RF-sputtering system

$$X_L = \sqrt{R_s R_g - R_s}, \qquad X_c = \frac{R_s R_g}{X_L} \qquad X_c = R_s \sqrt{\frac{R_g}{(R_s - R_g)}}, \qquad X_L = \frac{R_s R_g}{X_c}$$

R_g: Impedance of RF-generator, C_v: variable capacitor

R_s: Impedance of RF-discharge, C_v: blocking capacitor

where *C* is the capacitance between the discharge plasma and the target, $\frac{dV}{dt}$ denotes the time variations of the target surface potential [10]. Therefore the increase of frequency increases the target ion currents. In the RF discharge system the operating pressure is lowered to as low as 1 mTorr, since the RF electrical field in the discharge chamber increases the collision probability between the secondary electrons and the gas molecules. In the RF sputtering system, a blocking capacitor is connected between the matching network and the target. The target area is much smaller than the grounded anode and the chamber wall. This asymmetric electrode configuration induces a negative dc bias on the target, and this causes sputtering in the RF system.

2.3.4 Magnetron sputtering

In magnetron sputtering, a magnetic field is superposed on the cathode and glow discharge, which is parallel to the cathode surface. The electrons in the glow discharge show helical motion and the center of the orbit drifts in the direction of **E** x **B** with the drift velocity of E/B, where **E** and **B** denotes the electric field in the discharge and the superposed transverse magnetic field, respectively. The magnetic field is oriented such that these drift paths for electrons form a closed loop. This electron trapping effect increases the collision rate between the electrons and the sputtering gas molecules [11]. This enables one to lower the working gas pressures as low as 10^{-5} to 10^{-3} Torr. Magnetron sputtering can be done either using a dc or rf power supply. In magnetron sputtering, the magnetic field increases the plasma density which leads to increase in the current density at the cathode/ target. Due to low working pressure of the gas, the sputtered particles traverse the discharge space without collision, which results in high rates of deposition. The other advantage of magnetron sputtering is that, most of the electrons are confined near the cathode and hence fewer electrons reach substrate, which reduces substrate heating due to electron bombardment.

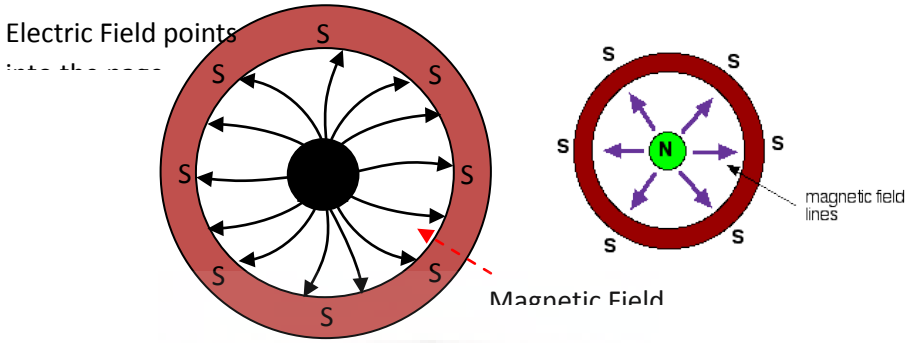

Figure 2.6: Cross-sectional view of the planar magnetron sputtering

2.3.5 Thin film deposition by RF magnetron sputtering

The schematic of the RF magnetron sputtering system used in this work is shown in figure 2.7. It consists of a 60 liter stainless steel vacuum chamber (VC) which houses 3 cathodes and a substrate holder. Out of the 3 cathodes, 2 are RF powered while the other one is dc powered. One of the RF powered cathodes was used for the deposition of Ag and Ag-Cu alloy thin films. During deposition of thin films, the vacuum chamber is continuously cooled by flow of water through the water cooling jackets fitted on the exterior to the vacuum chamber. The vacuum chamber is evacuated through the electro-pneumatic roughing valve (RV) from atmospheric pressure to $\leq 2 \times 10^{-3}$ Torr using a rotary vane mechanical pump (RP, DS-102, Varian, Italy), with an approximate pumping speed of 6.84 m^3h^{-1}. The vacuum chamber is isolated from the turbo molecular pump (TMP, Turbo-V 301, Varian, Italy) through a mechanical screw driven gate valve (GV) which is attached to the VC by a 6" conflate flange with copper gasket. The pumping speed of the TMP is about 15 $m^3\ h^{-1}$. Once the chamber pressure reaches$\leq 2 \times 10^{-3}$ Torr, the RV is closed and the TMP is evacuated through electro-pneumatic backing valve (BV). As the fore-line pressure reaches$\leq 2 \times 10^{-3}$ Torr, the TMP is switched on and the GV is opened. The pressure in the vacuum chamber can now be brought into the high vacuum regime. The pressure is monitored using a cold cathode gauge (Pfeiffer vacuum, Germany). A base pressure of $2x\ 10^{-6}$ Torr can be achieved in about 2 hrs. Two mass flow controllers (MFC, Bronckhurst Hi-tech, Ruurlo-Holland) which can independently control flows of argon (Ar, 99.9% purity) and molecular oxygen (O_2, 99.999% purity) are connected to the VC through a solenoid valve. The use of a gas mixture of inert argon and reactive oxygen helps to achieve the same stoichiometry as that of the target in the film.

The working pressure during sputtering is controlled partly by adjusting the total input gas flow and by reducing the throughput of the TMP by partially closing the manual gate valve. The working pressure is monitored by a capacitance manometer (CMM, Inficon, USA). Once the predetermined working pressure and deposition temperature is achieved, the sputter deposition process is started by initiating the plasma using the RF power generator (RF VII Inc, USA) coupled with the matching network. The VC walls and substrate holding stage form the grounded electrode.

Figure 2.7: Photograph of (a) the sputtering system, (b) inner view of the vacuum chamber and (c) RF plasma generated during Ag and Ag-Cu alloy deposition. (supplied by M/s APT Ltd, Pune).

The substrate holding stage is placed on the top plate of the VC and is capable of rotating on its own axis and at the same time allows the deposition of metal films at temperatures ranging from room temperature up to 600^{o}C. Prior to every sputter deposition, the target was conditioned by pre-sputtering for an hour by closing the shutter. The system is vented to atmosphere after closing all valves to isolate the pumps from the VC. The photographs of the sputter deposition unit, inner view of the vacuum chamber and RF plasma generated during sputtering of Ag and Ag-Cu are shown in figure 2.7.

2.3.6 Nucleation and Growth

This process is at the heart of the thin film processing sequence because the thin films form through nucleation and growth. The process begins as the sputtered atoms and molecules (or the sputtered species) arriving at the substrate surface become physically absorbed, after which they often diffuse to some distance before becoming incorporated into the film. The diffusion length or the mobility of the sputtered species depends upon the binding energy of the species to the substrate and the temperature of the substrate. Higher the substrate temperature and lower the binding energy, the greater is the mobility of the species upon the surface. The initial aggregation of the film material is called nucleation. Nucleation generally leads to clustering of particles. Those clusters of particles which are not thermodynamically stable will get desorbed from the surface and the thermodynamically stable clusters overcome the nucleation barrier and will begin to grow. These nuclei grow across the surface of the substrate by surface diffusion until islands grow large enough to touch and continue until the film reaches continuity. The islands start to coalesce to reduce the overall surface area of the growing film. This process of coalition to form larger islands is known as agglomeration and during this process the film transforms from a discontinuous islands type to a porous network type. This type of growth will continue until all islands have grown together and will result in a continuous film. As the film grows, it develops a structure, or morphology, which includes both topography (surface morphology and roughness) and crystallography.

Depending upon the deposition condition of thin films on a foreign substrate, the initial nucleation and growth stages are strongly influenced by the free energy, γ at the substrate. Here, we need to consider the γ of both the substrate free surface, γ_s, and of the substrate-film- interface, γ_i, relative to that of the film free surface, γ_f. All the three γ values will generally depend on crystallographic orientation, among other factors. Assume that there is enough surface diffusion so that the depositing material can rearrange itself to minimize γ, that is, assume that the nucleation is not kinetically limited and can approach equilibrium. For this, the diffusion length, Λ must be much greater than the hopping distance of the atoms, a, i.e., $\Lambda >> a$. In the opposite case, i.e., when $\Lambda < a$, the atoms stick where they land, and the growth behavior is “quenched”. With our assumption of $\Lambda >> a$, there are two nucleation and growth situations on the bare substrate, as shown in figure 2.8. The film spreads across or “wets” the substrate because [6, 12],

$$\gamma_f + \gamma_i < \gamma_s \qquad (2.6)$$

That is, the total surface energy is lower for the wetted substrate than for the bare one. This leads to smooth growth, atomic layer by layer, which is sometimes referred to as Frank-van der Merwe growth mode. For this mode to occur there must be strong enough bonding between film and substrate to reduce γ_i to where equation (2.6) holds. If there were no such bonding at all, we would have $\gamma_i=\gamma_f+\gamma s$, so spreading the film across the substrate would always increase total surface energy by $2\gamma_f$. Thus, with insufficient substrate bonding, equation (2.6) ceases to hold, and the film does not wet the substrate but instead forms three-dimensional (3D) islands, shown in figure 2.8(b) and sometimes referred to as the Volmer-Weber growth mode. There is a third growth mode, Stranski-Krastanov, shown in figure 2.8(c), in which the growth changes from layer to island after a monolayer or two due to change in the energy situation with successive mono-layers. This mode is associated with epitaxy.

In general, Frank-van der Merwe growth occurs when lattice mismatch is small and the binding energy of sputtered atoms is equal to or less than the binding energy of sputtered atoms to the substrate. Volmer-Weber occurs when sputtered atoms are bound more tightly to each other than the substrate, such as in the growth of metal films on insulators. Those that grow by a mixture of the two are called Stranski-Krastanov type [6].

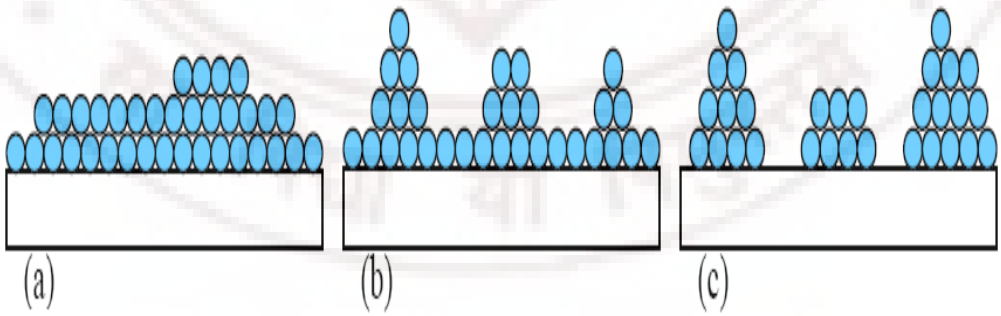

Figure 2.8**:** Initial growth stages in the sputter deposition process [12].

In the present studies a hybrid growth process layer plus island growth is apparently involved in sputtered Ag and Ag-Cu films while only island growth is favoured in vacuum evaporated Ag and Ag-Cu films.

2.4 Material characterization

2.4.1 Thickness measurement

The thickness of all the samples were measured using stylus profiler (also known as profilometer) (Model XP-1, Ambios Technology, USA). Surface profilometry is a direct, simple and fast measurement technique for determining the physical thickness of thin films [13]. The only requirement is the existence of a step as shown in figure 2.9. In this study, the step was made by covering a part of the substrate using a thin stainless steel shadow mask during deposition. This method involves loading a stylus (generally a diamond stylus) slightly in contact with the film surface and gently dragging it across the step as shown in figure 2.9. The vertical deflection measures the change in step height (film thickness) and the trace is recorded with high accuracy. Film thickness was also estimated from the spectral transmittance curves as described later.

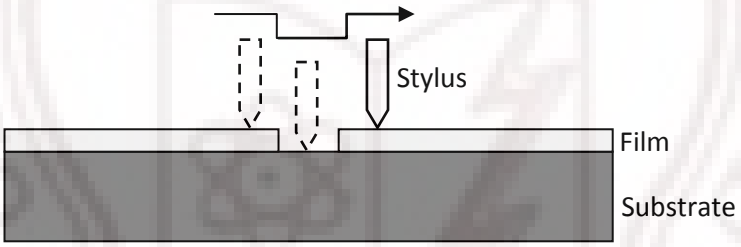

Figure 2.9: Illustration of stylus profillometry to measure film thickness.

2. 4.2 X-Ray diffraction

X-ray diffraction is a well-known technique for characterizing the crystal structure of materials. X-rays have a wavelength of the order of Angstroms (10^{-10} m), which is comparable to the inter-atomic spacing in crystalline solids. Therefore, a diffraction pattern can be observed when a beam of x-rays is directed on a crystalline material (where the atoms are arranged periodically). This diffraction pattern is directly related to the crystal structure of the material under observation. The diffraction of x-rays by a crystalline material is illustrated in figure 2.10.

In the present work, two types of X-ray diffractometers with different x-ray source were used to characterize the samples. One was equipped with Co Kα (λ=1.788Å)

radiation in a wide angled powder X-ray diffractometer (INEL Model CPS120) and a position sensitive detector while the other one was a conventional X-ray diffractometer operating in the Bragg-Brentano geometry with Cu K_α (λ=1.54056 Å) radiation (Philips PW 1830 diffractometer). Calibration using a Si standard was done to account for the instrumental line broadening and the value was approximately 0.05^0 for the former and 0.10 for the later. The patterns were compared with standard patterns (JCPDS) and the phases and degree of crystallinity was determined. A slow scanning rate of 0.5°/min was used to extract data for the measurement of crystallite size. These results gave important information regarding the variation in the films' orientation, lattice constants, crystallite size, strain etc. as a function of processing conditions.

2.4.2.1 Calculation of crystallite sizes from x-ray diffraction patterns

***Bragg's Law*:**

In figure 2.10 below, consider rays 1 and 1a in the incident beam. They strike atoms K and P in the first plane of atoms and are scattered in all directions. Only in the directions 1' and 1a', the scattered beams are completely in phase (because QK – PR = PK Cos θ - PK Cos θ = 0) and are capable of reinforcing one another.

This relationship is true of all the planes separately, and we have to find the condition for reinforcement of rays scattered by atoms in different planes. Let us take rays 1 and 2 scattered by atoms K and L, and the path difference for rays 1K1' and 2L2' is

$$ML + LN = d\sin\theta + d\sin\theta \qquad (2.7)$$

If this path difference is equal to a whole number n of wavelengths,

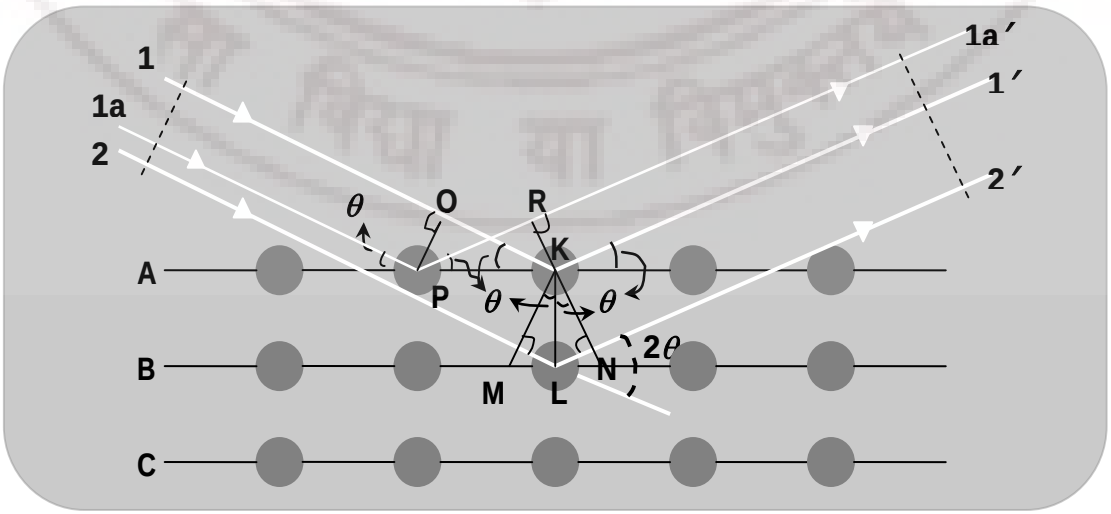

Figure 2.10: Diffraction of X -rays by periodically arranged atoms in a crystalline material.

$n\lambda = 2d \sin\theta$ (2.8)

where, θ is the diffraction angle, λ is wavelength of the X-ray and n is the order of reflection, which may take any integral value consistent with sinθ but not exceeding unity.

This relation was first formulated by W. L. Bragg and is known as the Bragg law [14]

$$\frac{n\lambda}{2d} = \sin\theta < 1 \quad (2.9)$$

i.e., nλ must be less than 2d. For n =1 the condition for diffraction at any observable angle 2θ is λ < 2d.

For most sets of crystal planes d is of the order of 3 Å or less, which means that λ cannot exceed about 6 Å.

Scherrer's formula is used to estimate the crystallite size, *t* given by,

$$t = \frac{0.93\lambda}{\beta \cos\theta_\beta} \quad (2.10)$$

$$\beta = \frac{1}{2}(2\theta_1 - 2\theta_2)$$

where, β is angular width, in terms of 2θ and is measured in radian at an intensity equal to half the maximum intensity and is called full width at half maximum (FWHM) (shown in figure 2.11 below)

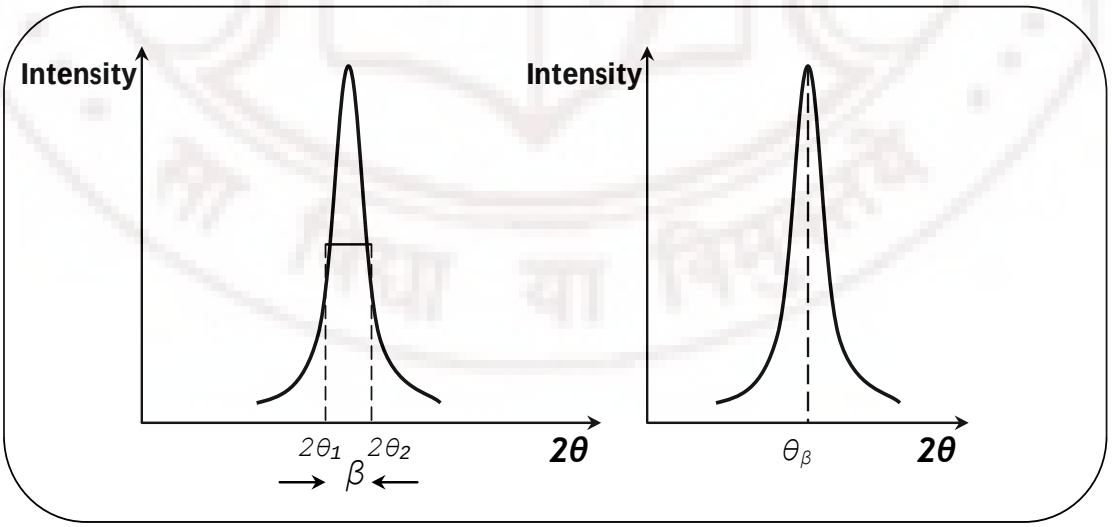

Figure 2.11: Graphs show the FWHM.

2.4.3 Scanning Probe Microscopy

Scanning probe microscopy (SPM) covers several related technologies for imaging and measuring surfaces on a fine scale, down to the level of molecules and groups of atoms. SPM technologies share the concept of scanning an extremely sharp tip (3-50 nm radius of curvature) across the sample surface. The tip is mounted on a flexible cantilever, allowing the tip to follow the surface profile.

When the tip moves in proximity to the investigated object, forces of interaction between the tip and the surface influence the movement of the cantilever [15]. These movements are detected by selective sensors. Various interactions can be studied depending on the mechanics of the probe. Our interest is in the atomic force microscope (AFM). The atomic force microscope (AFM) probes the surface of a sample with a sharp tip (often less than 100A^{o} in diameter). The tip is located at the free end of a cantilever that is 100 to 200μm long. Forces between the tip and the sample surface cause the cantilever to bend, or deflect. A detector measures cantilever deflections as the tip is scanned over the sample, or the sample is scanned under the tip. The measured cantilever deflection is mapped as the surface topography [16]. AFM can be used for insulator and semiconductor as well as electrical conductors [17]. The schematic diagram of AFM is shown in figure 2.12.

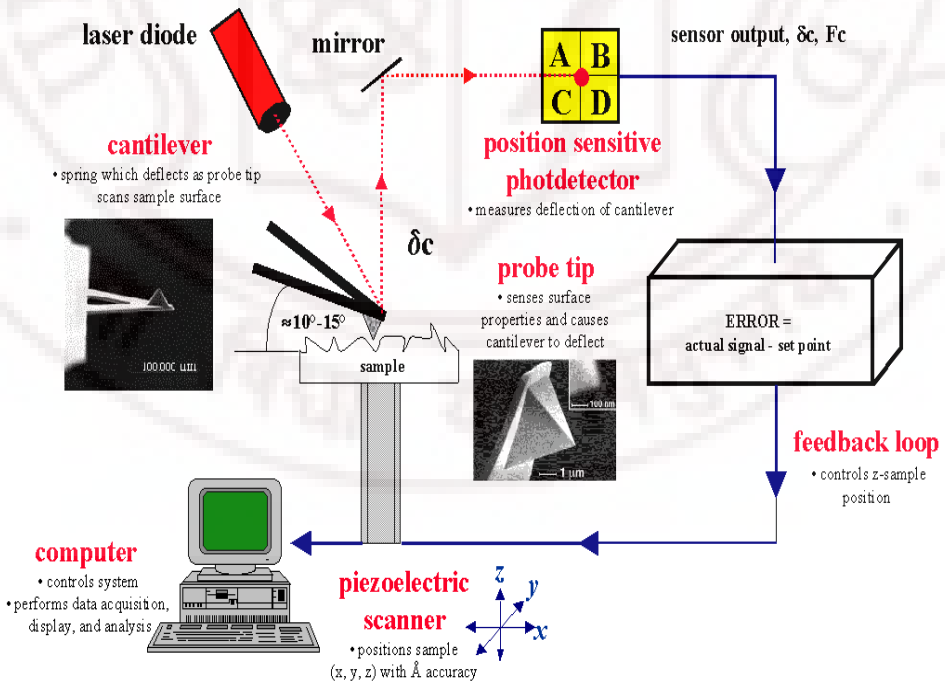

Figure 2.12: Schematic diagram of atomic force microscopy (AFM) [18].

Several forces contribute to the deflection of an AFM cantilever. The force most commonly associated with atomic force microscopy is an inter-atomic force called the Van der Waals force depending upon the distance between tip and sample as shown in figure 2.13.

Two distance regimes are labeled in figure 2.13 the contact regime and the non-contact regime. In the contact regime, the cantilever is held less than a few angstroms above the sample surface and the interatomic force between the cantilever and sample is repulsive [19]. In the non-contact regime, the cantilever is held about tens to hundreds of angstroms away from its attractive regime (largely a result of the long-range Van der Waals interactions).

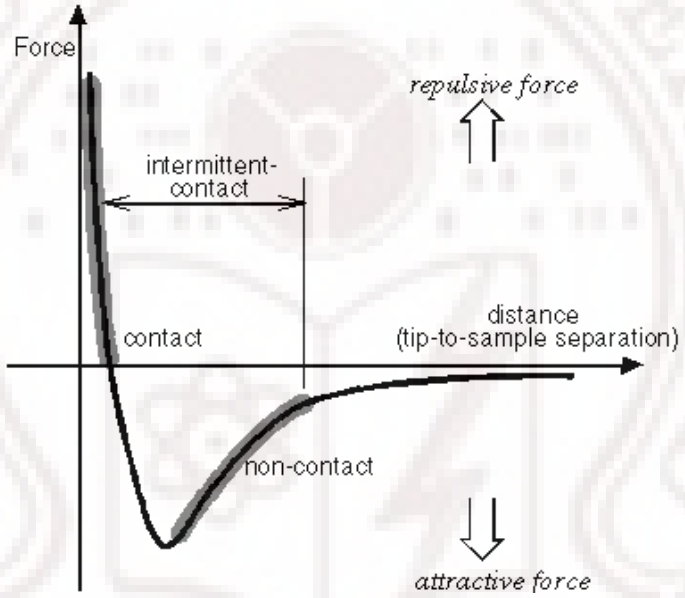

Figure 2.13: Nature of forces in the Contact and Non-contact mode of AFM operation.

2.4.3.1 Non-contact AFM

Non-contact AFM (NC-AFM, otherwise known as dynamic force microscope, DFM) is one of the modes of operation in AFM, where the cantilever is vibrated near the surface of the sample. The spacing between the tip and sample for DFM is of the order of tens to hundreds of angstroms. This spacing is indicated in the Van der Waal force curve in figure 2.13 as the non-contact regime.

DFM is desirable because it provides a means for measuring sample topography with little or no contact between the tip and sample. Similar to contact-AFM, DFM can also be used to measure the topography of the insulator and semiconductors as well as electrical conductors. The total force between the tip and sample is very low, generally

10^{-12}N. Since the force between tip and sample in the non-contact regime is low, it is more difficult to measure this region than in the contact regime. In addition, the cantilever used in DFM is stiffer than those used for contact AFM because soft cantilevers can be pulled easily onto the sample surface. Hence, both these factors make the DFM signal difficult to measure. Thus, a sensitive, AC detection scheme is used in this operation. In the non-contact mode, the system vibrates a stiff cantilever near its resonant frequency (typically from 100 to 400 kHz). Then, it detects the changes in the resonant frequency or vibration amplitude as the tip comes near the sample surface. The sensitivity of this detection scheme provides sub-angstrom vertical resolution in the image, as with contact AFM.

The relationship between the resonant frequency of the cantilever and variations in sample topography can be explained as follows. The resonant frequency of a cantilever varies as the square root of its spring constant. In addition, the spring constant of the cantilever varies with the force gradient experienced by the cantilever. Finally, the force gradient, which is the derivative of the force Vs distance curve changes with the tip-to-sample separation. Thus, change in the resonant frequency of the cantilever can be used as a measure of change in the force gradient, which changes with the tip-to-sample spacing, or sample topography. DFM does not suffer from the tip or sample degradation effects that are sometimes observed after taking numerous scans with contact AFM. As mentioned above, DFM is preferable to contact AFM for measuring soft samples. In the case of rigid samples, contact and non-contact AFM for images may look the same. In the present study Seiko SPA-400 scanning probe microscope was used in the DFM mode to obtain the surface morphology of Ag, Ag-Cu and AgI thin film samples.

2.4.4 Electron Microscopy

Electron microscopes use electron beams to provide images of nanoscale objects. In transmission electron microscopy (TEM), the specimen is illuminated with an electron beam. The electron beam that transmits through the specimen produces a transmitted, optical image, much like conventional optical microscopy. The wavelength of electron is much smaller than that of light, therefore the optimal resolution attainable for TEM image is several orders of magnitude higher than that for a light microscope. Not all the electrons are transmitted through the sample, some are also scattered or diffracted. The scattered and diffracted electrons form the image contrast as denser or thicker parts of the

sample scatter as well as absorb, more electrons, thus appearing as darker areas in the image [20-21].

In the present work we have used Transmission electron microscope (model: FEI TECNAI 20 G2) to investigate nano particle nucleation and growth and to determine crystal structure of iodization time dependent 5 nm Ag thin (free standing) films sputtered on PVA polymer.

2.4.4.1 Imaging Modes of a TEM

The imaging system of a TEM consists of at least three lenses (Figure. 2.14): the objective lens, the intermediate lens (or lenses), and the projector lens. The intermediate lens can magnify the first intermediate image, which is formed just in front of this lens, or the first diffraction pattern, which is formed in the focal plane of the objective lens, by reducing the excitation [20]. In many microscopes, an additional diffraction lens is inserted between the objective and intermediate lenses to image the diffraction pattern and to enable the magnification to be varied in the range 102 to 106. The *bright-field mode* (BF) with a centered objective diaphragm is the typical TEM mode, with which scattering contrast and diffraction contrast can be produced with objective apertures α_o between 5 and 20 mrad. For high-resolution phase contrast, the aperture should be larger ($\alpha_o \geq 20$ mrad) to transfer high spatial frequencies. The only purpose of the diaphragm in this mode is to decrease the background by absorbing electrons scattered at very large angles. The resolution is limited by the attenuation of the contrast-transfer function (CTF) caused by chromatic aberration and not by the objective aperture α_o. Normally, the specimen is irradiated with small illumination apertures $\alpha_i \leq 1$ mrad. For high resolution, an even smaller aperture $\alpha_i \leq 0.1$ mrad is necessary to avoid additional attenuation of the CTF by partial spatial coherence. When unconventional types of contrast transfer are desired, it is often necessary to change the illumination condition by tilting the beam or using hollow-cone illumination, for example.

In the *dark-field mode* (DF), the primary beam is intercepted in the focal plane of the objective lens. Different ways of producing dark-field conditions are in use. The shifted-diaphragm method (Fig. 2.15 b) has the disadvantage that the scattered electrons pass through the objective lens on off-axis trajectories, which worsens the chromatic

aberration. The most common mode is therefore that in which the primary beam is tilted (Fig. 2.15 c) so that the axis strikes the centered diaphragm. The image is produced by electrons scattered into an on-axis cone of aperture α_o. This mode has the advantage that off-axis aberrations are avoided. There is thus no increase of chromatic error.

Asymmetries in the dark-field image can be avoided by swiveling the direction of tilt around a cone, or conical illumination can be produced by introducing an annular diaphragm in the condenser lens. Another possibility is to use a central beam stop that intercepts the primary beam in the back focal plane for this, a thin wire stretched across a circular diaphragm may be employed (Fig. 2.15 d). DF micrographs need a longer exposure time because there are fewer scattered electrons. For high resolution, the contrast-transfer function (CTF) of DF is nonlinear, whereas the CTF of the BF mode is linear for weak-phase specimens. The DF mode can also be employed to image crystalline specimens with selected Bragg-diffraction spots.

Increasing the objective aperture in the BF mode allows us to transfer the primary and one Bragg-reflected beam through the diaphragm [20]. These beams can interfere in the final image. The fringe pattern is then an image of the crystal-lattice planes. Optimum results are obtained for this mode when the primary beam is tilted by the Bragg angle $+\theta_B$. The Bragg-reflected beam that is deflected by $2\theta_B$ passes through the objective lens with an angle $-\theta_B$ relative to the axis.

In the *crystal-lattice imaging mode*, more than one Bragg reflection and the primary beam form a lattice image that consists of crossed lattice fringes or an image of the lattice and its unit cells if a large number of Bragg reflections are used. This mode is most successful for the imaging of large unit cells, which produce diffraction spots at low Bragg angles so that the phase shifts produced by spherical aberration and defocusing are not sufficiently different to cause imaging artifacts. Further operating modes of a TEM are described in other sections: scanning transmission mode, Lorentz microscopy and the analytical modes of x-ray microanalysis, electron energy-loss spectroscopy, and electron diffraction [20]. The Photograph of TEM used in this work is given in figure 2.16.

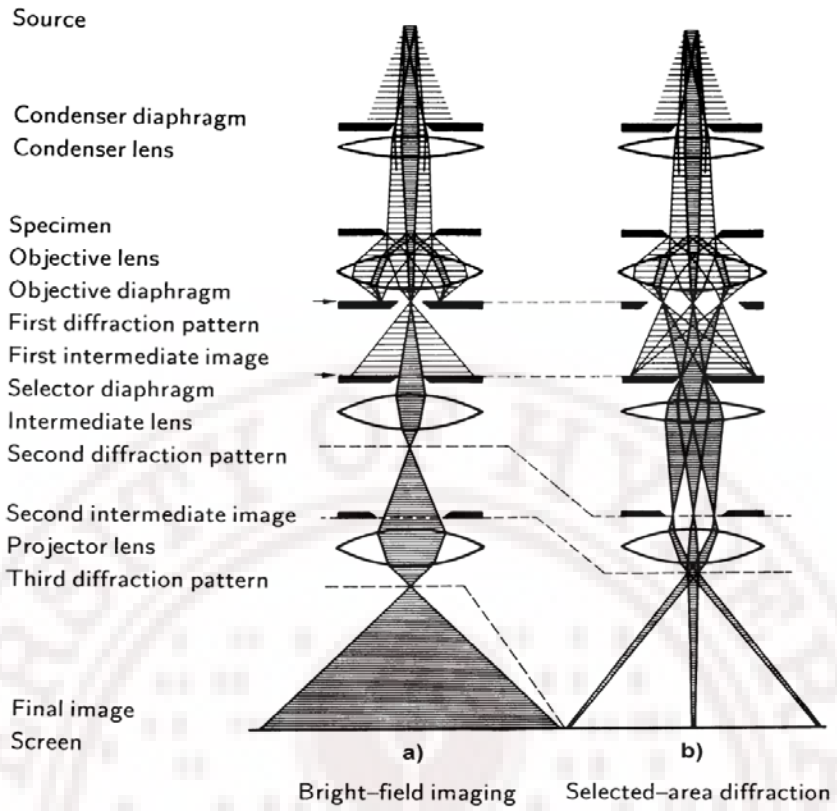

Figure 2.14: Ray diagrams for a TEM in (**a**) the bright-field mode and (**b**) selected area electron diffraction (SAED) mode [20].

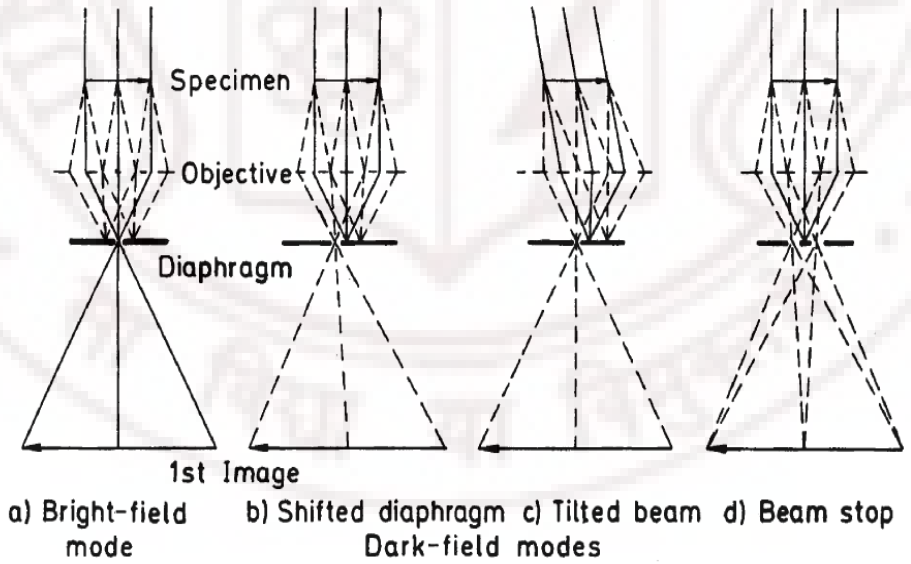

Figure 2.15: (a) Bright-field mode with a centered objective diaphragm and production of a dark-field mode by (b) a shifted diaphragm, (c) a tilted beam, and (d) a central beam stop [20].

2.4.5 Electron diffraction (ED).

Electron-diffraction methods are employed for the identification of substances by measuring the lattice-plane spacing and for the determination of crystal orientations in polycrystalline films (texture) or single-crystal foils. Extra spots and streaks, caused by antiphase structures or plate-like precipitates, for example, may also be observed when imaging a selected area. The selected-area diffraction technique, in which an area of the order of 0.1–1 μm across is selected by a diaphragm in the first intermediate image, is a standard method [20].

2.4.5.1 Selected-Area Electron Diffraction (SAED)

The cone of diffracted electrons with an aperture of the order of a few tens of milli radians (mrad) can pass through the small pole piece bores of the final lenses only if the back focal plane of the objective lens that contains the first diffraction pattern is focused on the screen. Figure 2.14(b) shows the ray diagram of this technique. A selector diaphragm of diameter *d* situated in the intermediate image plane (magnification M ≈20−50) in front of the intermediate or diffraction lens selects an area of the specimen of diameter d/M. This area can be chosen in the normal bright-field mode (figure. 2.14 a), in which the primary beam passes through the objective diaphragm. When the excitation of the intermediate lens is decreased, its focal length is increased and the diffraction pattern in the focal plane of the objective lens can be focused on the final screen after removing the objective diaphragm (figure. 2.14 b). The excitations of the later projector lenses are unchanged. These lenses magnify either the intermediate image or the diffraction pattern behind the intermediate lens. The diameter of the area selected cannot be decreased below 0.1–1 μm owing to the spherical aberration of the objective lens. The intermediate images of the Bragg reflections (dark-field images) are shifted relative to the bright-field image by a distance [20]

$$\Delta s = (Cs\theta^3 g - \Delta z \theta g)\, M, \qquad (2.11)$$

which depends on the defocusing Δz and the constant Cs ($\theta g = 2\theta_B$ and θ_B is the Bragg angle). It is of course possible to compensate for the shift by a suitable choice of the defocus Δz, but only for one Bragg reflection, not for the whole diffraction pattern simultaneously. The consequence is that Bragg reflections of high order with large θg do

not come from the area that was selected in the bright-field mode. Thus, for $2\theta_B$ = 50 mrad and *C*s = 1 mm, the shift is 0.125 μm. The diffraction angle θg decreases linearly with λ as the electron energy is increased. A further selection error can result if the position of the intermediate image is shifted when the intermediate lens changes over from the imaging to the diffraction mode.

Figure 2.16: Photograph of the Transmission electron microscope (model: FEI TECNAI 20 G2) (established at CFN, UoH) to obtaining the nano particle growth and crystal structure of free standing AgI thin films.

Diffraction patterns from smaller areas can only be obtained by using the rocking-beam technique or by producing a small electron probe. The resolution d/Δd of an SAED pattern can be defined in terms of the smallest lattice-spacing difference Δd that can be resolved and may be estimated from the ratio Δr/r. Here r denotes the distance from a diffraction spot to the center of the diffraction pattern in the focal plane of the objective lens, $r = 2\theta_B f = \lambda f/d$ (*f*: focal length), and Δr is the diameter of the spot, which is equal to the diameter $2\alpha_i f$ of the primary beam (α_i: illumination aperture):

$$d/\Delta d = r/\Delta r = \lambda/2\alpha_i d \qquad (2.12)$$

Thus, for λ = 3.7 pm (100 keV), d = 0.1 nm, and α_i = 0.1 mrad, we find d/Δd = 200. The resolution can be increased only by reducing α_i, but this reduces the pattern intensity. The

spherical aberration of the objective lens can cause barrel and spiral distortion of the SAED pattern but this is, however, smaller than 1%; an elliptic distortion can arise due to astigmatism of the intermediate lens. The most severe distortion is caused by the projector lens. For the accurate determination of lattice spacing *d*, the diffraction (camera) length *L*) must be calibrated by using a diffraction standard [20].

2.4.6 Optical Characterization

2.4.6.1 Ultra Violet-Visible Spectrophotometer

Optical properties of the AgI thins were studied using a JASCO V-570 UV-VIS-NIR double beam Spectrophotometer. The optical studies of thin films are mainly concerned with basic optical phenomena including absorption, reflection and transmission and also the interaction of photon energy with mater and consequent changes in electronic states [22]. The important parameters that can be obtained from the measured spectral absorption data include absorption coefficient and optical band gap of AgI thin films were measured. In the present study we have focused on the quantitative determination of surface plasmon to exciton transition in thin Ag and AgI films. The data was collected in the range of 300 to 800 nm at 300 K.

The Ultra Violet -Visible-Near Infrared (UV-VIS-NIR) spectrophotometer uses two light sources, a deuterium (D_2) lamp for ultraviolet region and a halogen lamp for visible and NIR region. The light from the source lamp gets reflected from mirror 1 and beam passes through slit 1 and hits a diffraction grating. The grating can be rotated allowing for a specific wavelength to be selected. At any specific orientation of the grating, only monochromatic (single wavelength) beam successfully passes through slit 2. A filter is used to remove unwanted higher order diffracted beam. The light beam hits a second mirror before it gets split by a half mirror (half of the light is reflected, the other half gets transmitted). One of the beams is allowed to pass through a reference sample (air in the present case), the other passes through the film coated substrate. The intensities of the light beams are then measured at the end as shown in figure 2.17. The photometer (not shown) computes the ratio of the sample signal to reference signal (I/I_0) to obtain the transmittance.

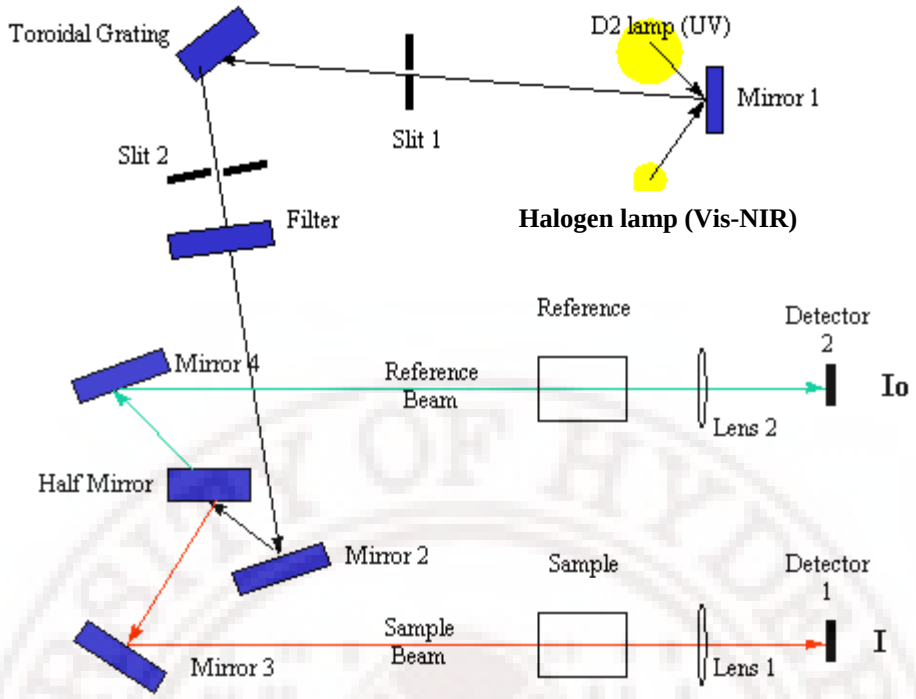

Figure 2.17: Schematic diagram of UV-VIS-NIR spectrophotometer.

An electronic transition consists of the promotion of an electron from an orbital of a molecule in ground state to an unoccupied orbital by absorption of a photon. The molecule is then said to be in an excited state. Experimentally, the efficiency of light absorption at a wavelength λ by an absorbing medium is characterized by the absorbance A(λ) or the transmittance T(λ), defined as [23]

$$A(\lambda) = \log_{10} I_\lambda^0 / I_\lambda = -\log T(\lambda) \qquad (2.13)$$

$$T(\lambda) = \frac{I_\lambda}{I_\lambda^0}$$

where I_λ^0 and I_λ are the light intensities of the beams and entering and leaving the absorbing medium, respectively

Usually the absorbance of a sample follows the Beer-Lambert law

$$A(\lambda) = \log_{10} \frac{I_\lambda^0}{I_\lambda} = \varepsilon(\lambda) l c \qquad (2.14)$$

where A is the measured absorbance, I_0 is the intensity of the incident light at a given wavelength, I is the transmitted intensity, L the path length through the sample, and c the concentration of the absorbing species. For each species and wavelength, ε is a constant known as the molar absorptivity or extinction coefficient. This constant is a fundamental

molecular property in a given solvent, at a particular temperature and pressure, and has units of 1 / *M* * *cm* or often *AU* / *M* **cm*..

The absorption spectra give the fundamental absorption. This refers to the band-to band absorption i.e. the excitations of electrons from the valence band to the conduction band of a semiconductor. A simple analysis of the absorption process yields a fundamental relation for the absorption coefficient, $\alpha \propto (h_\gamma - E_g)^{1/2}$ and $\alpha \propto (h_\gamma - E_g)^{3/2}$ for direct and indirect band gap materials respectively. Here, E_g is the energy band gap of the material. Conventionally for inorganic semiconductors, electrons can be excited from the valence band to the conduction band by absorption of incident radiant energy only if this energy is equal to or larger than E_g, the band gap of the system. Thus, absorption of light occurs when a quantum of energy ($h\gamma$) equals E_g;

$$Eg = h\gamma_g = hc/\lambda_{g\,(nm)} = (1240/\lambda_g)\ eV \qquad (2.15)$$

As all our thin film samples show a semiconductor like behaviour, λ_g(nm) is determined at the point where there is an abrupt change in slope of the absorbance versus wavelength curve. Nevertheless, these obtained approximate energy gap values enormously helps in the realization of the band structure of the as-obtained thin films.

2.4.6.2 Photoluminescence

Optical transitions provide direct access to the energy level band development structure of a system. Photons of a particular energy that are absorbed or emitted by a sample provide evidence of electronic states differing by that energy within the material. Absorption is a good probe of the overall band structure of a system because bands have a relatively high density of states. PL emission, on the other hand, tends to favor sparse low-lying states because photoexcited carriers rapidly thermalize through bands and closely spaced states to within *kT* of the lowest available levels. This feature of PL makes it particularly effective in the analysis of interfaces where discrete defect and impurity states abound. If the state is radiative, it will generate unique peaks in the PL spectrum [23-25]. Thus, the PL measurement is a very sensitive and selective probe of such states. In addition to identifying discrete states, PL peak positions can be used to evaluate the composition of semiconductor alloys. Here, the energy of the band-edge emission is correlated with the composition dependent band gap of the alloy. Other features of the PL

spectrum, including linewidths and splittings, provide important information on thin films interfaces. These systems are very sensitive to interface roughness because fluctuations as small as one atomic monolayer can alter the carrier confinement energy considerably.

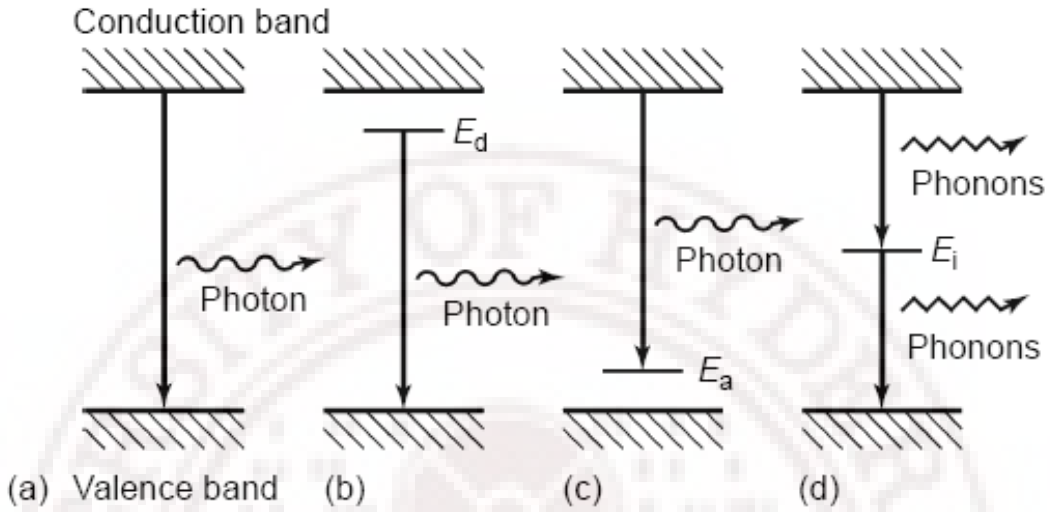

Figure 2.18: (a–c) Radiative recombination paths: (a) band-to-band; (b) donor to valence band; (c) conduction band to acceptor. (d) Non-radiative recombination via an intermediate state [24].

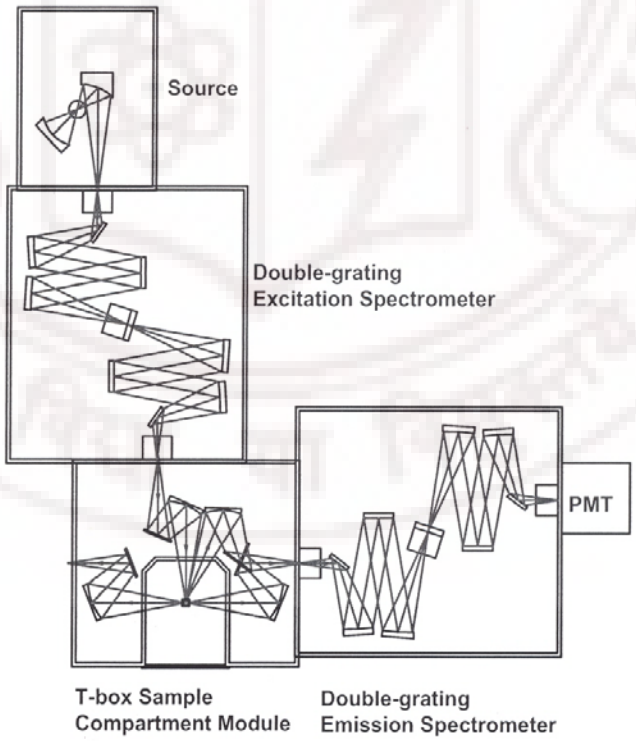

Figure.2.19: Schematic diagram of Fluorolog-3 Spectroflurometer.

We recorded the Photoluminescence (PL) and the excitation spectra (at 300 K) of thin pristine and Cu doped AgI films thickness of 5 and 15 nm deposited on fused silica and polymer substrates by using Fluorolog-3 spectroflurometer at different excitation wavelengths.

In the setup of Figure.2.19 the light sources used inlude 150-W Xe lamp (Oriel 6333 lamp in Oriel 66881 housing with an Oriel F/0.85 pyrex Condenser and an Oriel 68938 constant power supply) in the visible region, (B) a high pressure 500W Xe-arc lamp in the near ultraviolet region. The higher power of the Xe lamp compared to the halogen lamp makes it particularly suitable for fluorescence measurements, where intense light is an advantage. However, the light intensity of the Xe lamp fluctuates with time at fixed wavelength and its spectrum contains some intense and very narrow peaks. The latter makes it unsuitable for excitation measurements. Light was dispersed through a 0.22 mm pathlength monochromator. Bandwidth and light intensity were controlled with two slits. Parabolic mirrors focused the beam on the sample. A resolution of 2 nm was used for the excitation monochromator. Photoluminescence spectra were collected at an angle of 90^{o} (front page) relative to the excitation beam through another 0.22 m pathlength monochromator, with a resolution of 4 nm during emission scans, and 2 nm during excitation scans. The thin films spectra were taken with an optical density below 0.5 at excitation wavelengths. A Hamamatsu R 928 photomultiplier tube was used to measure the luminescence photons. In an excitation spectrum, the intensity of an emission band is recorded as a function of the excitation wavelength. Excitation spectra provide a link between the absorption and emission spectra, and can be used to distinguish between emission bands due to different species. Since the intensity of the emitted light depends on the number of absorbed photons (in some cases the samples have a very weak absorption or scatter strongly), excitation spectra can also substitute the very difficult absorption measurements, as the detection of fluorescence is background free and is made very efficient by the use of intense laser light for excitation.

2.4.8 Electrical Characterization

The electrical Dc conductivity of pure and copper doped AgI thin films were extracted from impedance spectroscopy measurements. The test structures used for electrical characterization are M-I-M capacitance structure is shown in figure 2.22. In the present study, we have used shadow mask capacitance structure. The top electrode (gold) layer was fabricated using a RF magnetron sputtering techniques. The frequency and

temperature dependent AC impedance measurements were carried out on mixed conducting AgI and $Ag_{1-x}Cu_X$ films grown on Pt/Si substrates. It is to be noted that electrical conductivity of such films cannot easily be measured using DC techniques. The measurements were carried out from 40 Hz to 1 MHz using an Agilent 4294A impedance analyzer (shown in figure 2.21 and 2.22).

The top and bottom electrodes of the M-I-M (Au/AgI//PtSi) structures were connected to the impedance analyzer through two tungsten probes connected to their respective micropositioners in the probe station (LMS 2709), which in turn is connected with the impedance analyzer.

2.4.8.1 Impedance spectroscopy

The electrical properties of a material are unique and can be discovered by utilizing the frequency dependence of its constituent components. In addition the study of frequency related phenomena as a function of applied bias or temperature is often essential in the performance testing of materials. Virtually every electrochemical system is able to pass the current when a voltage is applied to it. If a variable (ac) voltage is applied to the cell, the ratio of voltage changes in a way that provides valuable insights in to its physical and chemical properties. AC techniques also use low perturbation signals (mV) that do not disturb the system under test, unlike dc techniques that generally require large perturbation signals.

The advantages of impedance measurement over other techniques include:

1. Rapid acquisition of data
2. Accurate, repeatable measurements
3. Effective in low conductivity media
4. Non-destructive nature
5. High adaptability to a wide variety of different applications

In general, impedance spectroscopy models the electrical behavior of the electrochemical cell in terms of an equivalent circuit of resistors and capacitors for the various applied voltages. It also calculates the electric field distribution with in the cell. The impedance at any frequency is a complex number represented by [26-27],

$$Z(\omega, V_0) = \delta V(\omega) / \delta I(\omega) \qquad (2.16)$$

because $\delta I(\omega)$ contains phase information as well as the magnitude- the AC current may have a phase lag θ with respect to the AC voltage. Thus, if we apply,

$V = V_0 + |\delta V| \times \cos(\omega t)$ (2.17)

and measure

$I = I_0 + |\delta I| \times \cos(\omega t - \theta)$ (2.18)

Then,

$Z(\omega, V_0) = (\delta V / \delta I) \times \{\cos(\theta) + i\sin(\theta)\}$ (2.19)

where $i^2 = -1$ and both magnitude and phase of the impedance $|Z|$ and θ vary with ω. Usually, the real and imaginary parts of $Z(\omega)$ are plotted in a complex plane (Argand diagram) and is known as the Cole-Cole plot [27].

$Re\{Z\} = |Z(\omega)| \times \cos[\theta(\omega)]$ (2.20)

$Re\{Z\} = |Z(\omega)| \times \sin[\theta(\omega)]$ (2.21)

The Cole-Cole plot describes a full or partial semicircle depicting the simple Debye type relaxation of ions in a semiconductor system represented by the RC network as shown in figure 2.20.

The diameter R of the semicircle corresponds to the resistance of the sample and the frequency at 90_0 corresponds to $1/\iota = 1/RC$ [27]. In the case of solid electrolytes, the presence of diffuse and disordered interfaces contributes to the depressed semicircles in the Cole-Cole plot. The resistance is used to calculate the grain boundary conductivity in all solid electrolyte samples, which follow an Arrhenius type behavior [28-29] represented by

$\sigma = \sigma_0 \exp(-E_a/kT)$ (2.22)

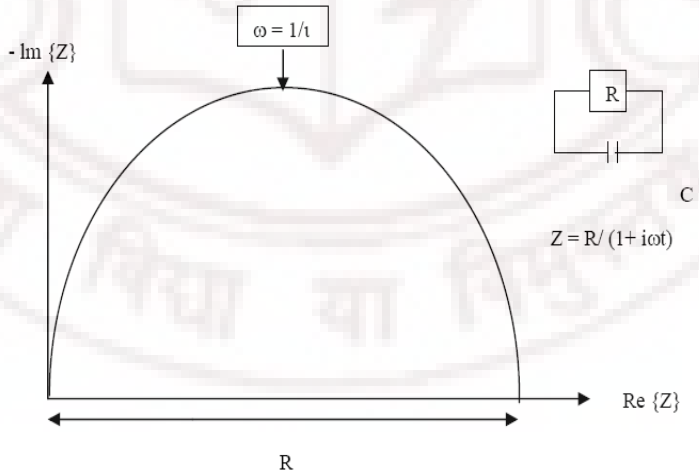

Figure 2.20: Cole-Cole plots showing the semicircle for a simple RC network circuit.

Figure 2.21: Photograph of the Agilent 4294A impedance analyzer.

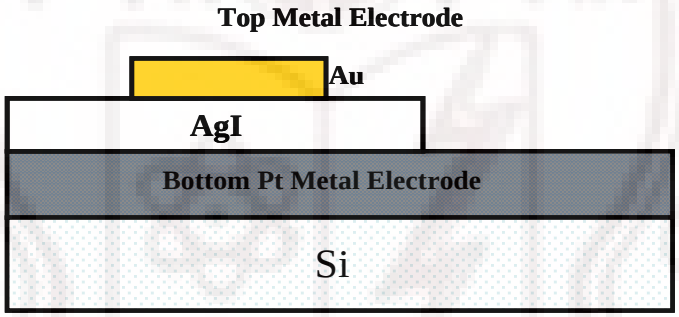

Figure 2.22: the schematic cross section view of the M-I-M structure fabricated on Pt/Si substrate.

2.5 Summary

In Summary, a brief description and scope of important and relevant characterization techniques such as surface profilometer, X-ray diffraction, Atomic Force microscope, Tunneling Electron microscope, UV-Vis-NIR spectrophotometer, Photoluminescence study and DC conductivity using Impedance analyzer used in the present work has been provided in this chapter.

The next chapter deals with the Surface plasmon-exciton transition in ultra thin silver and silver iodide films deposited on glass substrates by vacuum thermal evaporation method.

References

1. Jennifer A. Dahl, Bettye L. S. Maddux, and James E. Hutchison, '*Toward Greener Nanosynthesis*', Chem. Rev. **107**, 2228-2269 (2007).
2. Milton Ohring, '*Material Science of Thin Films, deposition and structure'*, 2nd edition, Acadamic press, 1900, San diego, California, USA-92101-4495.
3. D. L. Smith, *Thin films Deposition*. McGraw-Hill, New York, 1995.
4. L. Holland, *Vacuum Deposition of Thin Films*, Wiley, New York, 1956.
5. G. K. Wehner, G. S. Anderson, *Vacuum Technology, Thin Films, and Sputtering:* an Introduction, ed. R. V. Stuart, Academic Press, New York, 1983.
6. K. Wasa and S. Hayakawa, *Handbook of Sputter Deposition Technology: Principles, Technology and Applications*, Noyes, New Jersey, 1992.
7. B. Chapman, *Glow Discharge Processes*, John Wiley & Sons, Inc., New York, p. **177,** 1980.
8. J. A. Thornton, Deposition *Technologies for Films and Coatings: Development and Applications*, ed. R. F. Bunshah, Noyes Publications, NJ, 1982.
9. F. F. Chen, *Introduction to Plasma Physics and Controlled Fusion*, Plenum Press, New York, 1984.
10. L. l. Maissel and R. Glang, *Handbook of thin film Technology*, 4-35, NY, Mc Graw-Hill (1970).
11. S Swann, Magnetron Sputtering, *Phys. Technol*, **lS**, 67-75 (1988l).
12. B.A. Movchan and A.V. Demchishin, *Fiz. Metal. Metalloved*, **25**, 653 (1969).
13. K. Creath and A. Morales, *Contact and noncontact profilers in optical shop testing*, 2nd ed. Wiley, New york (1992).
14. B. D. Cullity, *X-ray Diffraction*, Addison-Wesley, Reading, MA (1956).
15. J. Giessibl Franz, *Review of Mod. Phys*., **75**, 949 (2003).
16. P. West, *Introduction to Atomic Force Microscopy: Theory, Practice and applications* www. AFMUniversity.org.
17. Q. Zhong, *Surf. Sci. Lett*., **290**, L688 (1993).
18. www.pscl.me.ntu.edu.tw
19. J.B. Hudson, *Surface Science-An introduction*, Wiley, New York (1998).

20. L. Reimer H. Kohl, '*Transmission Electron Microscopy Physics of Image Formation*', **5th** Ed, Springer, New York, 10013, USA (2008). TEM book

21. Z. L. Wang, Transmission Electron Microscopy of Shape-Controlled Nanocrystals and Their Assemblies, *J. Phys. Chem. B, **104,*** 1153-1175 (2000).

22. Olaf Stenzel, *The Physics of thin film Optical Spectra: an Introduction*, Springer Germany (1996).

23. Bernard Valeur, *Molecular Fluorescence Principles and Applications*, Wiley, 2002.

24. Timothy H. Gfroerer, '*Photoluminescence in Analysis of Surfaces and Interfaces', Encyclopedia of Analytical Chemistry,* R.A. Meyers (Ed.) pp. 9209–923, Wiley, 2000.

25. H. T. Grahn, "*Introduction to semiconductor physics*" World Scientific Publishing Co. Pte. Ltd, Singapore, 1999.

26. J. R. Macdonald (Ed.), *Impedance Spectroscopy: emphasizing solid materials and system,* Wiley-Inter-Science, NY, 1987.

27. A. K. Jonscher, *Dielectric Relaxation in solids,* Chelsa, London, 1994.

28. K. S. Cole and R.H. Cole, "Dispersion and Absorption in dielectrics I. Alternating Current Characteristics", *J. Chem. Phys.* **9** (1941) 341.

29. S. Chandra, *Superionic Solids: Principles and Applications*, North Holland, Amsterdam, 1981.

Chapter III

Surface plasmon-exciton transition in ultra thin silver and silver iodide films deposited on glass substrates by vacuum thermal evaporation

3.1 Introduction

As discussed in chapter 1, fabrication of γ-AgI zincblende structure. AgI thin films has received much attention for their potential applications in various electronic and optoelectronic devices. Crystalline γ-AgI thin films possess high ionic conductivity (~ 1 μS) at room temperature and excellent optical properties. As stated earlier AgI is a superionic conductor which exhibits three different polymorphs out of which α-AgI is a high temperature phase transition at 420 K where as β and γ-AgI are form < 420 K in which γ-AgI is a metastable at room temperature. AgI is a I-VII semiconductor direct band gap materials which gives luminescence in the blue region at 300 K.

In this chapter we discuss the deposition of thin Ag films thickness of 5, 10 and 15 nm deposited by vacuum thermal evaporation. We determine the thickness and iodization time dependent metastable γ-AgI zincblende structure development and look at their optical properties such as surface plasmon to exciton transition and photoluminescence at 300 K.

3.2 Preparation of Ag and AgI thin films

Thin Ag films were deposited on borosilicate glass substrates by Vacuum thermal evaporation method [1-5]. The precursor material namely highly pure Ag Powder (Aldrich, 99.999%) placed evaporation source (molybdenum boat) was thermally-evaporated on to the cleaned borosilicate glass substrate kept at an ambient temperature at a pressure of $5x10^{-6}$ Torr. The base pressure of the vacuum chamber was maintained at ~$3x10^{-6}$ Torr throughout the evaporation process. The amorphous glass substrates were kept at a distance of 20 cm from the source for deposition [6]. Thin films of pure Ag with thickness of 5-20 nm deposited at room temperature and the rate of deposition was maintained constant (0.1 A^o/sec) during the entire process. The above conditions were found favorable for the formation of uniform and homogeneous films. The thickness of the films was determined by using stylus profiler (Model XP-1, Ambios Technology, USA) profilometer.

Substrate: Prior to the deposition these substrates were cleaned as follows: substrates were first immersed boiling 10% soap solution with 90% water, rubbed with cotton in cold water to remove weathering, kept in chromic acid up to boiling point for removing organic contaminates, washed in cold water to remove surface contaminants followed by ultra-sonification in isopropyl alcohol for 5-10 min duration, and, finally these substrates were dried in air before loading in to the vacuum chamber for deposition.

Iodization: To iodize Ag films, an air/vacuum-tight figure of eight glass chamber was fabricated with dimensions of 10 cm height × 6 cm diameter. Iodine kept at the bottom of the lower half of the chamber sublimates at room temperature and slowly deposits on the Ag films kept at the top of the chamber shown in figure 3.1 [6-10]. Thus iodization was carried for selected durations in the range 5 minutes to 60 minutes. These films without any post-annealing treatment were characterized by XRD using a PHILLIPS X-ray powder diffractometer with Cu Kα (λ= 1.54056 A^o) radiation. To analyze the surface morphology, films were examined by SPA 400 Atomic Force Microscope (AFM) using non contact Dynamic Force Mode. JASCO V-570 UV-VIS-NIR double beam spectrophotometer has been used for optical absorption studies at 300K in the UV/visible range from 300 to 600 nm with scanning rate 4 nm per second. Fluorolog-3 Spectroflurometer has been used for Photoluminescence studies at 300K in the UV/Visible range from 300 to 800 nm with different excitation wavelength.

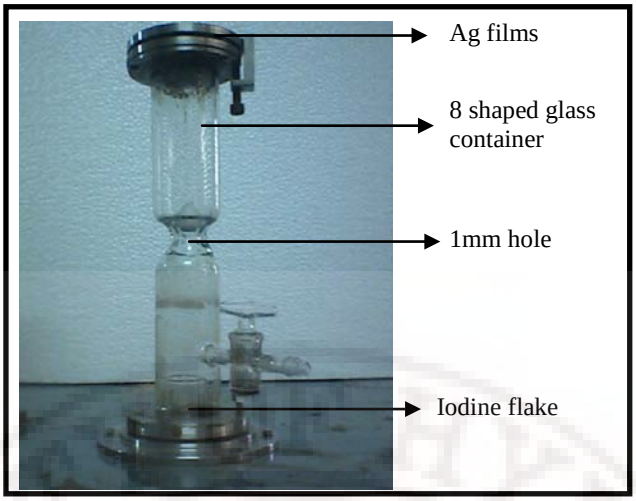

Figure 3.1: Iodization chamber

3.3 Crystal Structure of iodized Ag films

Ag films thickness of 5-20 nm deposited on silicate glass substrates at room temperature were characterized by XRD as shown in figure 3.2. Figure 3.2 shows the thickness dependent nanocrystalline formation of Ag thin film. Ag films thickness of <5 nm show the quasi amorphous island growth due to high surface to volume ratio. Vacuum thermal evaporation favors discontinuous island type growth due to high thermal energy during evaporation thus increasing the surface diffusion of Ag atoms responsible for the long range order development. The Ag film thickness > 5 nm show the formation of crystalline fcc structure with (111), (200) reflections. The low angle (111) Ag peaks is the most intense in the pattern, which implies a slight preferential orientation of the Ag grain along the (111) reflection [11-14]. Upon increased Ag film thickness, the X–ray intensity starts decreasing possibly due to decrease of surface to volume ratio of Ag particle. The (111) plane in Ag has lowest surface energy, and therefore, equilibrium growth condition leads to a (111) orientation. As the film thickness increases, the (111) reflection shifts to higher angles and FWHM reduces, which indicates that grain growth has occurred, resulting in the partial relief of intrinsic stress within the films. From the FWHM and peak position of the (111) peak, the grain size and the film stress are calculated. It shows that the grain sizes and the film stress are influenced by the film thickness [15-16]. With increasing film thickness, grain sizes increases and the absolute peak intensities decrease while film stress decreases. In the θ-2θ mode, only crystallites with lattice planes parallel to the surface are measured. Compressive stress parallel to the surface causes vertical

expansion of the film and leads to an increase of interplanar spacing, which is parallel to the surface. [17-20].

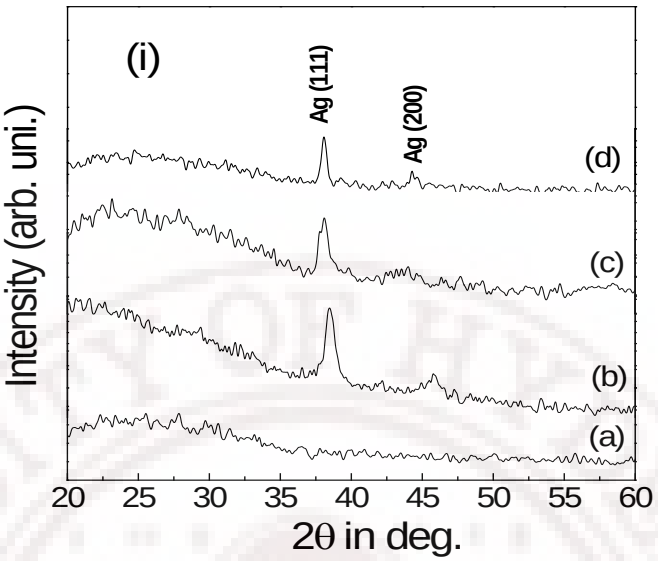

Figure 3.2: XRD pattern of as deposited Ag thin films (a) 10 nm (b) 15nm (c) 20 and (d) 25 nm thick deposited on amorphous borosilicate glass substrates at room temperature.

The grain sizes in Ag films were calculated according to the Scherrer formula [21]:

$$<D> = 0.098\lambda / \beta\cos\theta \qquad (3.1)$$

where λ is the X-ray wavelength (1.54186A^{o}), β is the full width at half maximum (FWHM) of (111) and (200) reflection as a function of 2θ, θ is the angle of incidence of the X-radiation measured for the sample surface and θ is the Bragg angle. The interplanar spacing d can be evaluated from the Bragg relation: $2d\sin\theta = n\lambda$ (n=1). The calculated average crystallite size was 20 nm.

How does the iodization of these silver films proceed? A controlled flux of molecular iodine vapours is realized in a figure of eight or hourglass jig (figure 3.1) with a 1 mm opening at the centre for brief durations ~ 5 to 60 minutes. Thus silver nanoparticles are gradually converted into AgI nanoparticles with predominant phase of γ-AgI (111) reflection (Zincblende structure) and small "impurity" of β-AgI (101) reflection (Wurtzite structure) perhaps due to local iodine excess [(Ag/I)<1] of silver iodide nanoparticles [6-11,22-25]. XRD pattern as shown in figure 3.3(a) reveal the change in structure of 5nm Ag films iodized at 60 min due to formation of "mixed phase" of AgI structure (transition from metal to semiconductor) due to very high surface to volume ratios. It can be seen that the good crystalline quality and oriented growth of all the AgI films are vey similar for all thicknesses with respect to iodization time [6-10]. Figure 3.3 (b) and (c) show XRD patterns of 60 min iodized thick Ag films, where the

development of intense low angle (111) peak of γ-AgI is highlighted. As mentioned earlier (111) direction in γ-AgI film has the lowest surface energy, therefore equilibrium growth conditions leads to a (111) orientation, whereas non-equilibrium condition give rise to other grain orientations detected as other XRD peaks such as (101). β-AgI as an inevitable impurity phase due to excess iodine present locally in the thin film system [5,9-11,22-25]. The percentage of β-phase is observed to increase with increasing film thickness. An enormous growth of γ-AgI phase is observed for 15 nm Ag films after 60 min of iodization. It consists of major peaks of γ-AgI which corresponds to the metastable zincblende structure [5,9]. Intensity increases dramatically with respect to iodization time something unusual and rare in ultra thin films. It has been observed that the very thin evaporated AgI films thickness < 2-10 nm show formation of metastable silver iodide. From these observations one may infer that the formation of γ-AgI nanoparticles are not reproducible on ultra thin films, suggesting that *both* zincblende and wurtzite crystal structure enhancement in the intensity are possible as these films are grown on discontinuous silver films involving especially very large surface to volume ratio. Two challenges of discontinuous films are desirable phase instability and poor reproducibility. Also note that the intensity of XRD peaks decrease with increasing film thickness probably due to a decrease in the surface area of Ag nanoparticles and randomization of (111) planes.

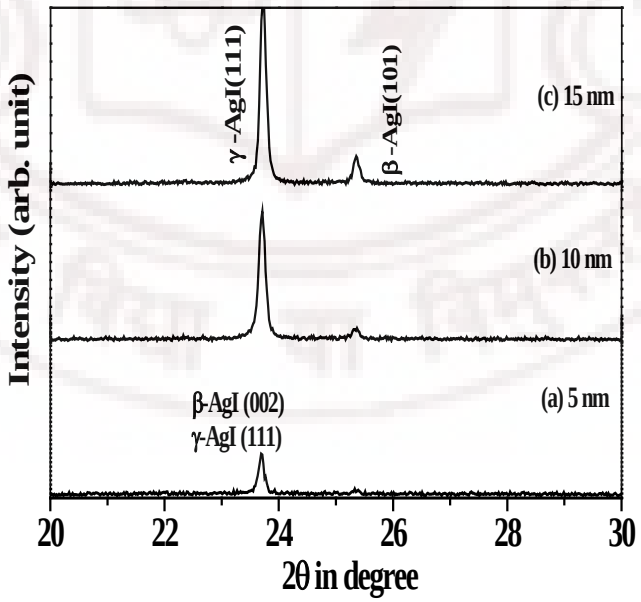

Figure 3.3: XRD pattern of as deposited Ag films5, 10 and 15 nm thick iodized for 60 minutes.

Iodization generally induces strain and defects (Frenkel defects etc) [30] in the AgI films making it hard to generalize about particle growth with respect to thickness induced stress particularly in AgI films grown on amorphous substrates. Compressive stress may be generated due to (i) differences in the expansion coefficients of film and substrate, (ii) incorporation of foreign atom or chemical reactions, (iii) variation of the inter-atomic spacing with crystal size, (iv) re-crystallization process, and (v) microscopic voids and dislocations. From the peak position shift in the XRD pattern one can calculate average strain (ε) using the following relation [9-10]:

$$\varepsilon = [(d_{obs} - d_{reference})/d_{reference}] \times 100\% \quad (3.2)$$

where d_{obs} and $d_{reference}$ for the interplanar spacing of γ-AgI(111) plane, β-AgI(101) plane and reference from JCPDS values. The calculated average strains are positive and high (1.9%) in 5-15 nm films iodized at 60 min. iodization suggesting the existence of compressive stress in the film at room temperature. The average strain decreases slowly with increasing iodization time [10,15,16,28] which shows that the strain relaxation (defect-free film) by iodization is generally dependent on the film stress, temperature, and iodization mechanism. These results are to be compared to the surface morphology studies by AFM technique where uniform size and shape of particles are observed upon increasing film thickness and iodization times [10,29].

3.4 Surface Morphology

The as-deposited Ag and subsequently iodized Ag films show well-defined surface morphologies as revealed by Atomic Force Microscope (AFM) show in figure 3.4 [6]. The iodization process induces AgI grain growth leading to a significant increase in lateral grain growth and a striking difference in the morphology between Ag-I bonds depending upon iodization time [6,9,10]. When compared with all subsequent iodized surfaces, the initial surface features are smoothened with larger grains. A set of DFM images with (0.5 μm×0.5 μm) field of view are shown in figure 3.5 for as deposited Ag of three different thicknesses 5, 10 and 15 nm films iodized for 60 min. A careful comparison of as deposited silver films (figure 3.4) reveals that the morphology of 5 nm thick silver films are characterized by loosely bound isolated uniform spherical silver nanoparticles with average particle diameter 27 nm and the film surface roughness (rms) 3.6 nm. With increasing film thickness a closely packed continuous film surface morphology develops on 10 nm and 15 nm thick films due to increased particle sizes

besides a decrease of surface to volume fraction of Ag metal particles, increased filling factor and decrease of inter particle distance [6-10,32]. Figure 3.5 displays surface microstructure of Ag films iodized at 15, 30 and 60 min for different thickness: (1) 5 nm (2) 10 nm and (3) 15 nm respectively. Short time (15 min) iodized Ag films to be passivated at the top by a thin I_2 layer and at the bottom by the unconsumed Ag layer.

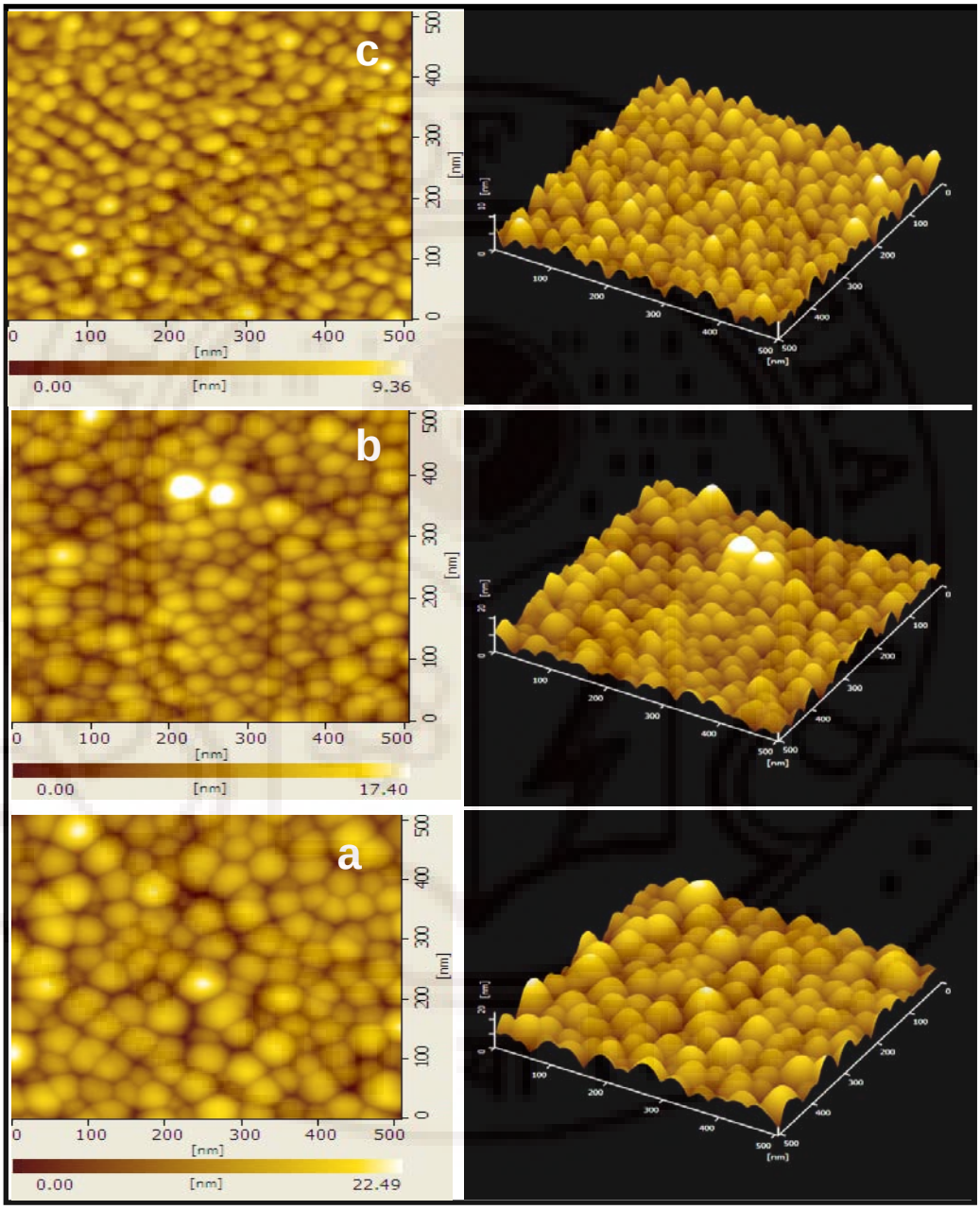

Figure 3.4: DFM surface micro structure (0.5 µm x 0.5 µm) of as deposited Ag films of thickness (a)5 nm (b)10 nm (c)15 nm. Particle sizes increases with increasing film thickness.

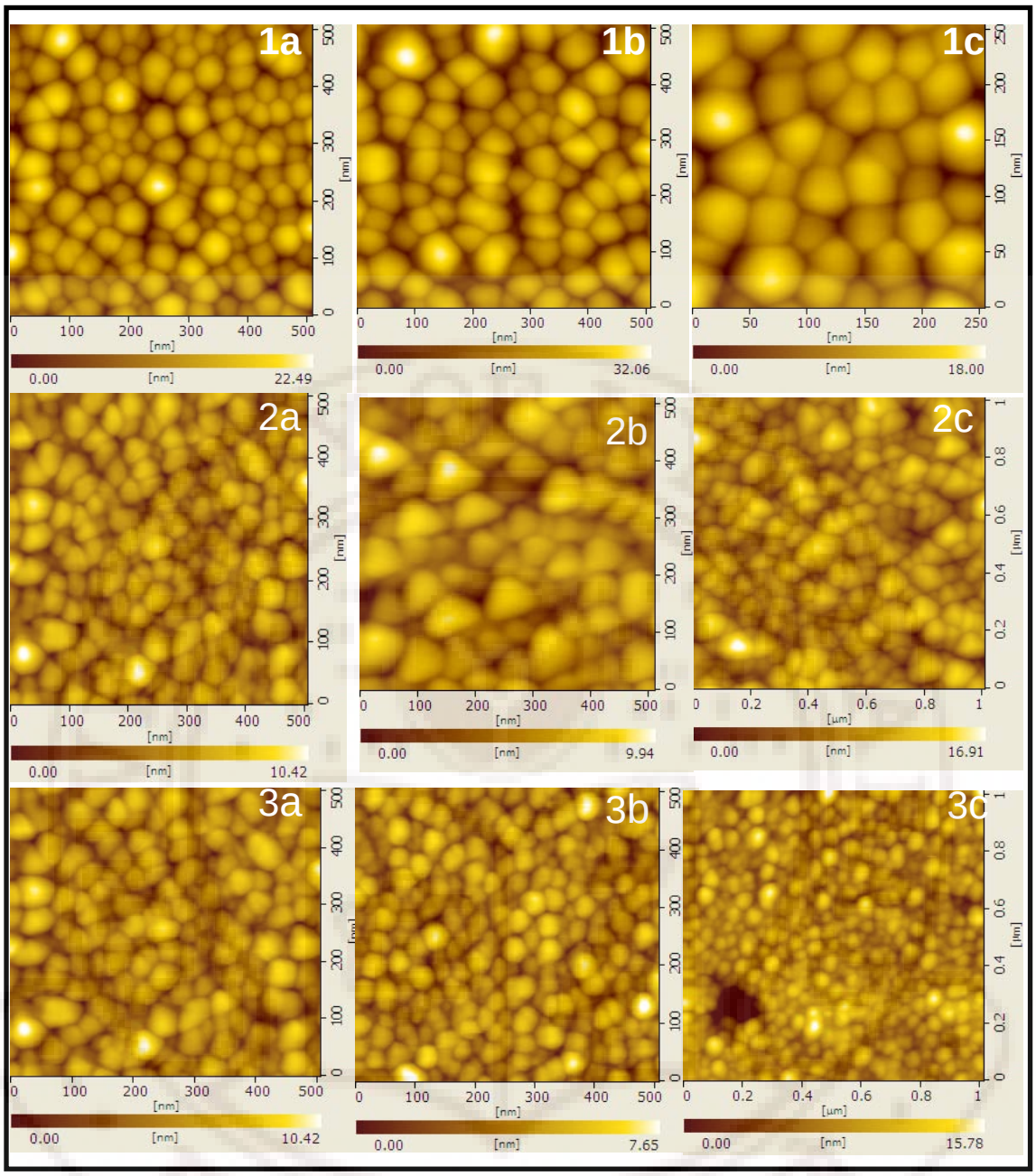

Figure 3.5: DFM surface micro structure (0.5 µm x 0.5 µm) of Ag thin films of thickness (1) 5nm (2) 10 nm (c) 15 nm: Iodized at (a) 15 min (b) 30 min (c) 60 min. Particle sizes and surface roughness increases with increasing iodization time and film thickness.

Typically, AgI particle size increases from 30 nm to 40nm with increasing iodization time as clearly seen in figure 3.5 [6-10]. (It is to be noted that due to the prevailing interatomic, intra-and intercluster forces that encourage agglomeration it is generally difficult to stabilize AgI nanoparticles less than this size unaided by impurity doping in a template-free approach as adopted in the present work). A 5nm Ag thin film was completely consumed by iodine molecules in a relatively short iodization time of 30 min to produce γ-AgI nanoparticles, which are homogeneously distributed with uniform

spherical shape and size ~30 nm on silicate glass substrates. Similarly surface roughness increases as a function of iodization time [9-10]. 5 nm thick films seem to be locally iodine rich systems because of the less packing density and filling factor. Vacuum evaporated thin films reveal island type growth of nanoparticles due to the high thermal strain and kinetic energy [1-5]. This type of growth is favored for short time iodization to form AgI nanoparticles in very thin films. Whereas in the case of RF sputtered Ag thin films (to be discussed in Chapter 5) disorder and stress present significantly modify the mechanism of film growth and particle growth kinetics even upon short time iodization. The complexity of the plasma environment and the effect of the working gas favor a kinetically stabilized film growth [9-10]. Upon increase of iodization time from 30 min to 60 min particle size does not change much but gets saturated due to iodine rich environment present in the systems resulting in the formation of Ag @ AgI core shell nanostructures [32-35].

It must be emphasized that despite the presence of locally iodine-rich regions, iodization does not result in beta AgI formation mainly because of the filling factor which does not apparently favor much lateral diffusion. This excess iodine very interestingly allows change of shape of the AgI nanoparticles; also surface trapped iodine molecules present in AgI surface create Frenkel defects and impurity centers in the system [29,30, 36]. A smooth surface of Ag film with thickness of 10 nm composed of higher volume fraction of metal particles apparently controls the size and yet preserves shape of AgI nanoparticles which could be the effect of film thickness. In case of 15 nm thick films iodine diffusion in the silver surface will be delayed due to the high volume fraction and packing density or low porosity. XRD patterns have shown thickness induced increases in peak intensity and changes of interplanar spacing due to compressive strain. However controlled iodization would possibly not impact the size and shape for thicker films because of their increased surface roughness [9,10].

3.5 Optical Properties

When a metal particle is excited by an electromagnetic (EM) field, its electrons start to oscillate with the same frequency as that of the incident EM field. The excited charges can transform energy of the incident EM wave into thermal energy in a so–called absorption process. However, the charges may also be accelerated such that they can radiate energy in any direction in a so-called scattering process. The sum of both effects leads to the eventual response namely light extinction [37-41]. Here we consider

nanoparticles large enough to use the classical theory for analysis but still enough small to observe the nature of dependence of its optical properties as a function of film thickness, particle size and shape. This means that the inhomogeneities of the particles are small compared to the wavelength of the incident field, such that, each point of the nanoparticles can be described in terms of its macroscopic behavior. To understand the range of the different processes as a function of the size of the particle, we study the thickness and iodization time dependent optical absorption of Ag and AgI thin films.

3.5.1 Surface plasmon to exciton transition

Figure 3.6 (i) show the optical absorption spectra of as deposited Ag films. Clearly resolved and broad maxima seen at 430, 439 and 457 nm for the films of thickness of 5, 10 and 15 nm respectively are identified as surface plasmon resonance absorption (SPR) which is a typical characteristic of Ag nano particles. According to classical Mie theory, the extinction coefficient for small cluster due to SPR [42-49] is given by

$$\sigma_{ext}(\omega) = 9V\frac{\omega}{c}\varepsilon_m^{3/2}\frac{\varepsilon_2(\omega)}{[\varepsilon_1(\omega)+2\varepsilon_m]^2+\varepsilon_2(\omega)^2} \qquad (3.3)$$

where V is the particle volume and $\varepsilon_1(\omega) = \varepsilon_1(\omega) + i\varepsilon_2(\omega)$ is the frequency dependent dielectric constant of the nanoparticles. The SPR maximum occurs at that frequency ω_s when $\varepsilon_1(\omega) + 2\varepsilon_m$ becomes zero, where ε_m is the dielectric constant of the host matrix assumed to be real. The SPR peak is size dependent because ω_s is given by $\omega_p/\sqrt{1+2\varepsilon_1}$, which is directly proportional to the number of the conduction band electron n_e through the equation $\omega_p^2 = 4\pi n_e e^2/m$, where e is the electric charge, m is the electronic mass, and ω_p is the plasma frequency of the metal. The broadening of the SPR band is due to chemical interface damping (CID) which is sub divided into two types: (1) static charge transfer (SCT) [50], whereby the electrons in the cluster will tunnel out from the cluster and fill up energy levels of the adsorbate atoms, which are at an equal or lower energy. This reduction of free electron density in the cluster will shift the plasmon oscillation frequency to the red end of the spectrum. For smaller clusters that are the smaller than 10-20 nm, the peak shift in frequency for an electron density change from n_1 to n_2 is given by

$$\Delta\omega_{\text{resonance}} \approx [(n_1)^{1/2} - (n_2)^{1/2}]\,(e^2/\varepsilon_0\, m_{\text{eff}})^{1/2}\,(2\varepsilon_m + 1) + \chi_{1\ \text{interband}})^{-1/2} \qquad (3.4)$$

where m_{eff} is the effective mass of the electron and $\chi_{1\text{intrband}}$ is the optical susceptibility for interband transition.

The second type of CID is known as the dynamic charge transfer (DCT) [51], or host dependent SPR broadening. In DCT, the cluster-host interface and the chemical properties of the host (which can be also be a functional group/ adsorbate atom) become important. Here, a temporary charge transfer will occur in a few femtoseconds. The back transferred electrons will undergo inelastic collision/ scattering with the electrons in the cluster, which oscillate coherently thereby broadening the spectrum. Apart from SCT, particle size increases will also show a red shift in the SPR band [42-49,51-58]. In the present case, at higher thickness, the peak position shows a red shift, as shown in the figure 3.6 (ii) which normally happens due to the nucleation and growth of clusters, interparticle distance and high filling factor in solid matrix surface. In addition to this, the surface plasmon band width or full width at half maximum (FWHM) decreases with the increase of film thickness, which also indicates the increase in size of nanoparticles. The SPR bandwidth depends on the size-shape parameters A and R (cluster radius) through the relation

$$\Gamma(A_{\text{size}}, R) \cong \Gamma_0 + (2\omega_p^2/\omega^2)\nu_{Fermi}[\partial\varepsilon_1/\partial\omega)^2 + (\partial\varepsilon_2/\partial w)^2]^{-1/2} A_{size}/R, \qquad (3.5)$$

where Γ_0 is the SPR bandwidth predicted by Mie's equation [43]. The 1/R dependence of Γ is the consequence of two effects: while the number of conduction band electrons participating in the collective excitation is proportional to R^3, the number of surrounding matrix molecules is only proportional to (R^2). This is the reason that smaller clusters show higher FWHM then the bigger particles. (The XRD pattern of a nanopowder also shows broader Bragg peaks than those of a micropowder). The average diameter of the cluster (d) can be obtained from FWHM of the SPR band, using the relation

$$d = \frac{\nu_f \lambda_p^2}{\pi c \Delta\lambda} \qquad (3.6)$$

where ν_f (1.39 x 108 cm s^{-1}) is the Fermi velocity of electron in bulk silver, c is the speed of light and λ_p and $\Delta\lambda$ are the characteristic wavelength and the FWHM of the surface plasmon resonance [59].

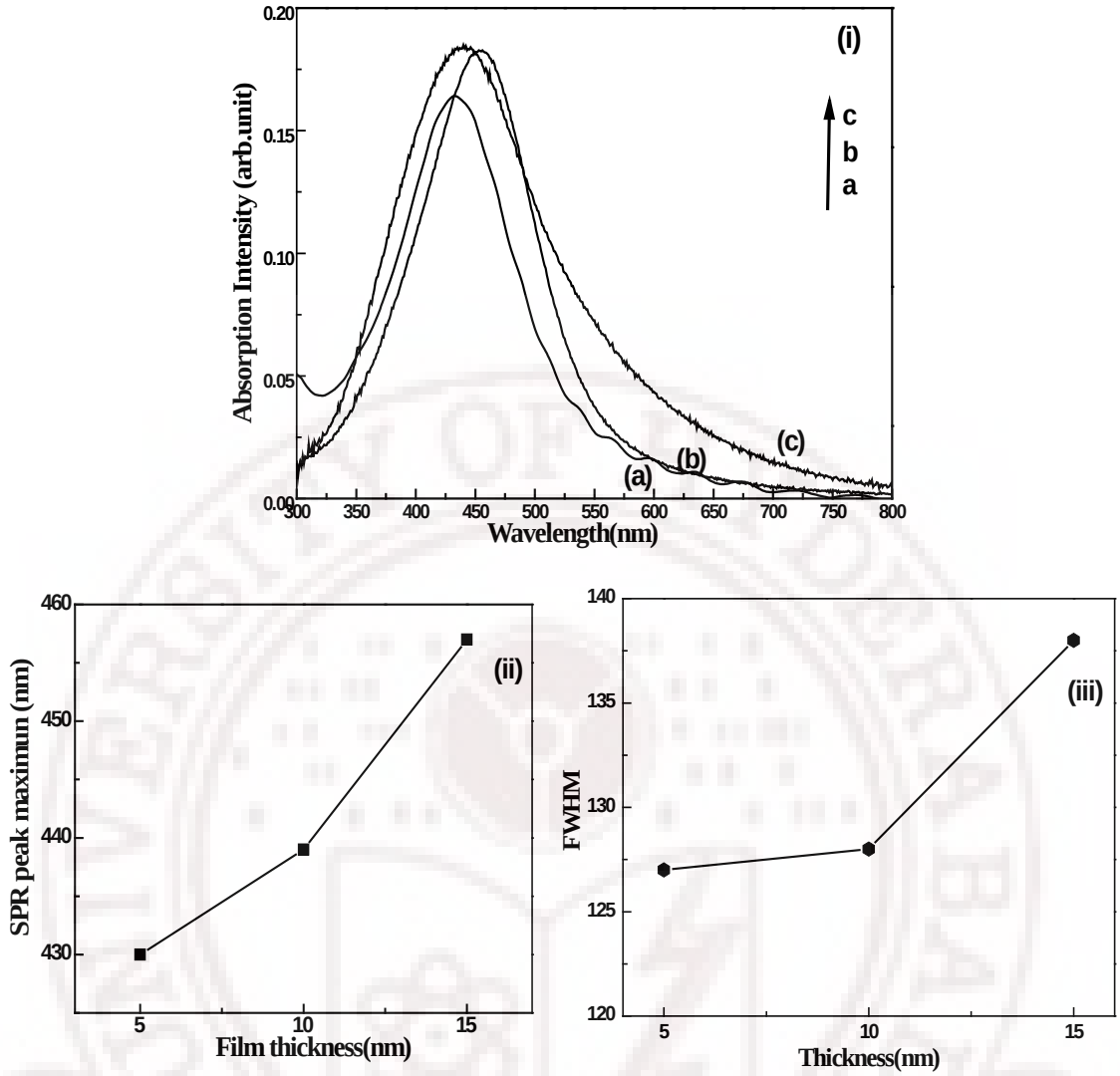

Figure 3.6: (i). UV/Visible Optical absorption spectra of as deposited Ag films of thickness (a) 5nm (b) 10 nm and (c) 15 nm. Thickness dependence of (ii) SPR peak maxima and (iii) FWHM are shown below.

In addition, cluster- matrix interaction can also contribute to the line width. For silver particles containing more than 150 atoms, the optical measurements of Charle et al show that the total line width of the plasmon peak scales with the inverse of the cluster diameter. In fact the 'composite' line width in such a case is the sum of several individual plasmon absorption peaks, belonging to clusters of different sizes. SPR is red shifted by 0.32 eV (from 2.81 to 2.49 eV) besides a doubled line width with increasing thickness of silver films. The above shift may be ascribed to an increased electromagnetic interaction between the Ag particles with the systematic decrease of the surface to volume ratio with increasing particle size and of surface roughness with increasing film thickness. Thus it is clearly a case of electromagnetic absorption by small metal particles stabilized in a dielectric matrix-the matrix (AgI in the present case). The intensity of the SPR

tremendously increases for the 5 nm thick film, suggesting that 5 nm could be a critical thickness with optimally matched dielectric and electronic properties of the substrate and the nanocomposite respectively. (It would be desirable to work with thin films less than 5 nm thick but they cannot be stabilized and characterized under the conditions employed in this work).

3.5.2 Excitons formation in iodized Ag thin film

Optical excitation creates the same number of electrons in the conduction band as holes in the valence band. Due to the Coulomb attraction between the electron and the hole, the energy necessary to create an electron-hole pair is slightly smaller than the energy gap. Neglecting exchange and correlation terms, the interactions take place only through the Coulomb interaction. The resulting correlated electron-hole pair is known as an exciton. Excitons are the simplest manifestation of the many body elementary excitations in crystalline solids. These are the bound state of an electron-hole system held by a coulomb attraction- not as strong as in a hydrogen atom but more like in positronium. The ground and excited states of an exciton are properly represented only in a two particle band picture [60-63].

Two quantities–Bohr radius (a_B) and binding (ground state) energy (E_{ext}) characterize exciton in semiconductors. The dielectric constant (ε) of the semiconductor stabilizes these two quantities through equation (3.7) and (3.8) derived in a Hydrogenic model with a coulomb potentials normalized by ε within framework of the effective mass approximation.

$$a_B = (h^2/ 4\pi^2 e^2)\, \varepsilon, \tag{3.7}$$

$$E_{ex} = 4\pi^2 m_r e^4 / 2 \varepsilon^2 h^2 \tag{3.8}$$

where m_r is the reduced mass of the electron-hole pair: $m_e m_h / m_e + m_h$

The charge carrier in a semiconductor can form a bound state when they approach each other in space. This bound electron-hole pair, known as a Wannier exciton, is delocalized within the crystal lattice and experiences a screened Coulombic interaction [64]. The Bohr radius of the bulk exciton is given by

$$a_B = \frac{\hbar^2 \varepsilon}{e^2}\left[\frac{1}{m_e^*} + \frac{1}{m_h^*}\right] \tag{3.9}$$

ε represents the bulk optical dielectric coefficient, e is the elementary charge, and m_e^* and m_h^* the effective mass of the electron and hole, respectively.

This process of creation, stabilization and recombination of excitons could be conveniently investigated through ambient optical absorption and photoluminescence in I-VII compounds [61]. Interestingly the formation of exciton in nanoparticles stabilized on thin films- a basic cluster formation process in the thin film physics-leads to the creation of quantum dots, i.e. quasi- zero dimensional structure that confines carriers in all the three spatial dimensions [64].

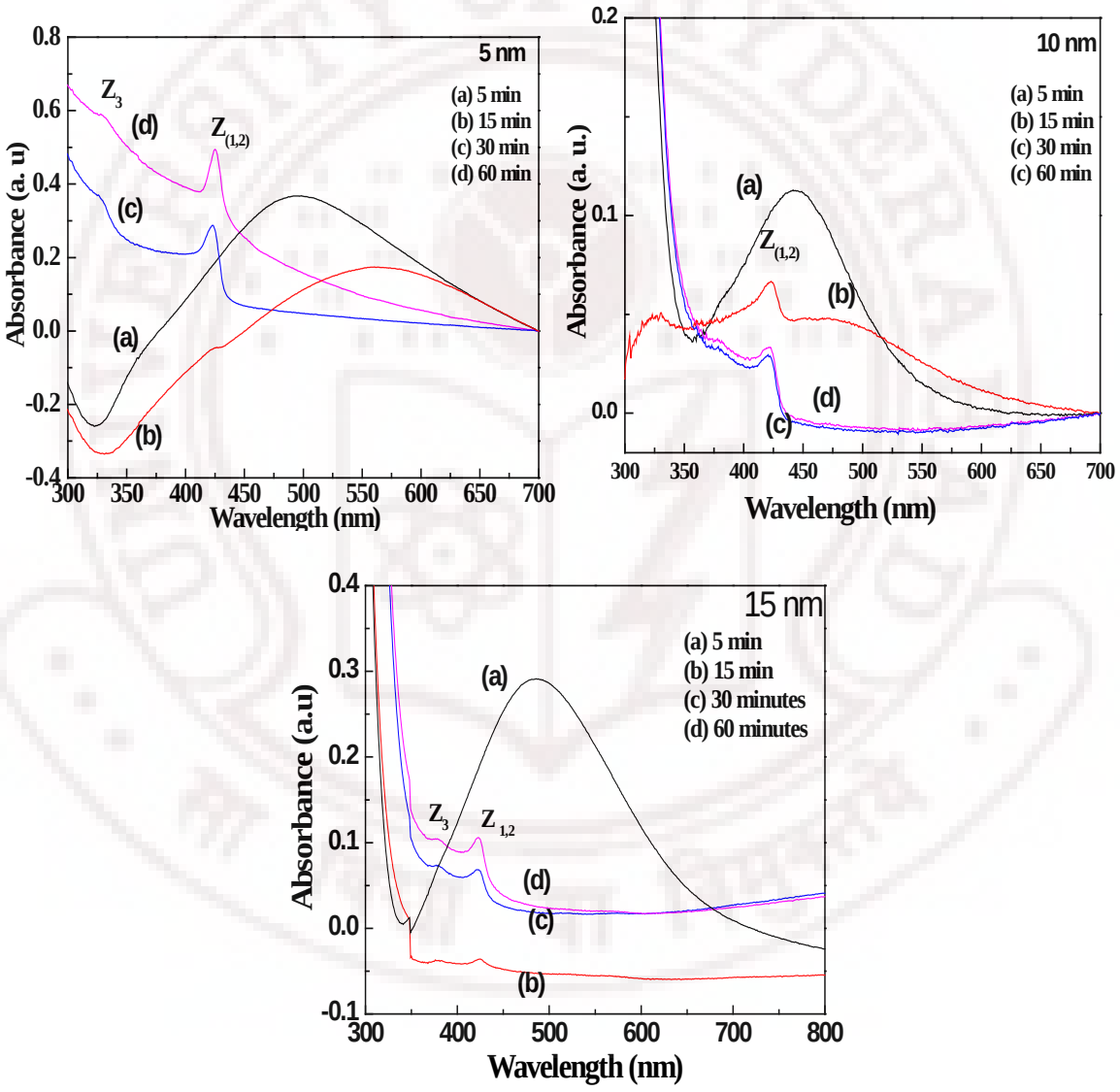

Figure 3.7: Optical absorption spectra of as deposited Ag films 5, 10 and 15 nm thick iodized for periods ranging from 5 minutes and 30 minutes at room temperature.

Mono-halides of copper and silver- especially CuCl, CuBr, CuI, AgI and AgBr belong to this class of I-VII's. The first four of the above materials are characterized by mutual tetrahedral bonding between metal and halogen leading to an open 3D structure namely Zincblende structure and direct electronic energy band gap similar to that of GaAs (111-V) and CdTe (II-VI) [61,62]. Unlike bonding in covalent semiconductor, there is healthy mix of ionic and covalent bonding in the manner of a weakly covalent structure in I-VII compounds. A large concentration of highly mobile Frenkel defects makes these materials supperionic conductors at fairly high temperatures. Thus the unique semiconductor-superionic conductor combination is crucial in understanding both ion and carrier (i.e electron and hole) dynamics and their recombination [60].

Upon controlled iodization, iodine vapor was deposited on the Ag surface and by the action of several processes initiated including surface diffusion at the gas-solid interface, silver nanoparticles surface are eventually iodized [6-10, 65-71]. As the silver iodide begins to grow on the surface at the early stage of iodization (5 minutes) the core still remains as silver constituting at Ag @ AgI core shell type of growth [29,32-35]. This type of growth mainly depends on the surface morphology of the film, rate of iodization, temperature at which iodization takes place and finally the film thickness. Figure 3.7a shows optical absorption of 5 nm thick silver film reveal a weak SPR1 with red shift after 5 minutes iodization. Additionally two new peaks at 420 nm (classified as $Z_{1,2}$ exciton) and 380 nm SPR 2 are due to the formation of silver iodide on the surface as a shell around uniodized silver core, respectively [9-10]. A core-shell type of growth is observed only by adopting the I_2 flux-controlled iodization technique. After 60 minutes iodization, SPR2 is completely diminished as the silver core is depleted ensuring that the silver iodide growth is completed. At this juncture it would be appropriate to focus on the coupling between the Ag and AgI nanocomposite features. Initially there are only Ag spherical nanoparticles. But upon iodization the conduction electrons of Ag are used to form AgI nuclei with I capturing an electron to form I^- and eventually the I^- MO's upto HOMO and the valence band. The formation could be visualized in the I/AgI/Ag two interface model [14]. Upon even a minute's exposure to I, AgI nanoparticles are nucleated on the surface which effectively depletes metal nanoparticle density besides decreasing the interparticle Ag-Ag distance whereby the plasmon resonance of Ag would start diminishing and an AgI/Ag diffusion barrier (a distribution of barriers is possible) would be established. The diffusion is controlled by (a) strength of the barrier, (b) surface

electron concentration on the Ag side and (c) the iodine concentration on the left side of the AgI shell. As the electrons are continually depleted, SPR intensity decreases and there is a corresponding buildup of excitons because the depleted Ag conduction electrons get transferred to nearby I atoms and initiates the crystal structure and valence band formation in AgI [65-67].

The evolution of optical absorption peak at 420 (due to the dipole forbidden $4d^{10}$-$4d^{9}5s$ transition in Ag, allowed by the tetrahedral symmetry of Ag^{+} ion in the Zincblende γ- AgI structure and the resultant p-d hybridization) has been attributed to $Z_{1,2}$ excitons [65-70]. The 420 nm exciton peak, the sharp rise in absorption below 330 nm (Z_3), and the long wavelength tail due to the intrinsic Frenkel disorder, all systematically characterize the very basic process of the band structure formation of AgI starting from the nanocluster level [71]. 5 and 10 nm (ultra thin) thick films exhibit exciton at 420 nm with larger intensity after 5 minutes iodization and however further iodization (15 and 60 minutes iodization) declining the intensity and red shifted perhaps due to larger size of silver iodide particles (figure 3.7a and 3.7b).

Ag film thickness of 10 and 15 nm iodized at 60 min exhibit a sharp rise in absorption below 330 nm due to effects of mixed exciton formation which is W_1 (below 320 nm) and Z_3 (330 nm) with increasing film thickness to 10 and 15 nm for longer time of iodization. After 60 minutes iodization, SPR 2 completely disappeared and meanwhile a new peak developed near 330 nm due to spin-orbit split Γ^{-} valence of the spin orbit interaction attributed to Z_3 exciton. The top of the valance band (Γ^{8}) is triply degenerate without spin-orbit interaction in the zincblende structure. This degeneracy is reduced by spin-orbit splitting resulting in a doubly degenerate state (Γ_7) and a singlet (Γ_9). The Γ_9 doublet gives the $Z_{1,2}$ peak whose degeneracy is lifted due to some strain field change at the crystallite surface (for example, surface reconstruction or surface defects) [65-67]. These results corroborate our earlier studies on RF sputtered films where the valence band degeneracy is lifted at room temperature for 20 and 30 nm thick films [9-10]. Optical absorption of vapor quenched metastable Ag-Cu thin films revealed that the strain induced size control by Cu helps in the confinement of excitons in AgI nanoparticles [7].

Mshvelidse et al studied excitonic absorption of silver iodide quantum dots in an aluminoborosilicate host network structure at 10K [72,73]. Mochizuki et al measured optical absorption of AgI at temperature from 7 K, through the superionic phase transition point T_c (419K), to 472K [68-69]. Band gap energy of the semiconductor with a direct band gap is,

$$(\alpha h\nu)^2 = B(h\nu - E_g), \qquad (3.10)$$

where α is the absorbance coefficient, $h\nu$ is the energy of incident light, B is the parameter that depends on the interband transition probability, and E_g is the energy gap. The plot of $(\alpha h\nu)^2$ vs incident photon energy $h\nu$ is found to be a straight line. The intercepts of the linear plots on the energy axis at $(\alpha h\nu)^2 = 0$ gave a band gap value determined for both $Z_{1,2}$ excitons. 5, 10 and 15 nm thick silver films show band gap 2.85, 2.82 and 2.82 eV after 60 minutes iodization respectively. Band gap decreases with increasing film thickness and iodization time indicating the effect of increasing particle size and correspondingly decreasing quantum confinement effects.

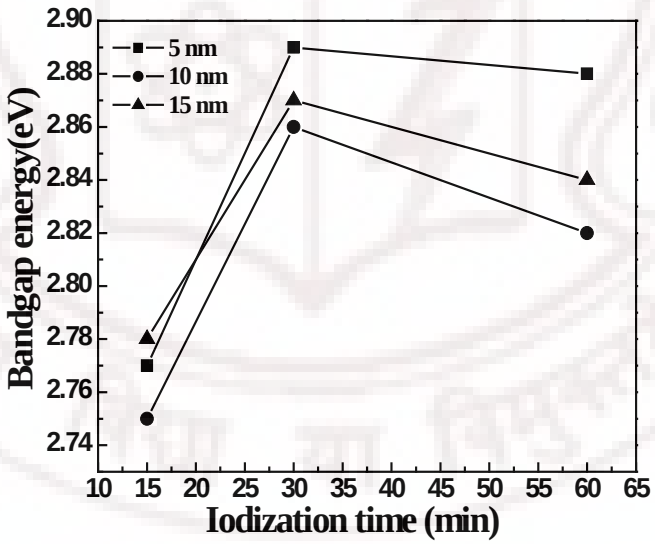

Figure 3.8: Band gap (Eg) as a function of iodization time for Ag films thickness (a) 5 nm (b) 10 nm and (c) 15 nm.

3.6 Photoluminescence Studies of Ultra thin AgI Films

Nanocrystalline semiconductors have two fundamental features both related to the size of individual nanocrystals distinguish their behaviour from the corresponding microcrystalline material. The first is the high dispersity (large surface to volume ratio) associated with the particles, with both the physical and chemical properties of the semiconductor being particularly sensitive to the surface structure. The second factor is the actual particle size, which can determine the electronic and physical properties of the materials. The absorption and scattering of incident light in larger colloidal particles is described by the Mie's theory; however the optical spectra of nanocrystalline compound semiconductors which show blue shifts in their absorption edge as the size of the particle decreases cannot be explained by the classical theory. Such size dependent optical properties are examples of the size quantization effect which occurs when the size of the nanoparticle is smaller than the bulk-exciton Bohr radius, a_B of the semiconductor [64].

$$l << R \leq a_B \qquad (3.11)$$

for a spherical crystalline radius *R*, the region of intermediate character between that of a molecule and that of the bulk materials and *l* is the lattice spacing.

Charge carriers in nanocrystalline semiconductor are spatially confined within three dimensions. In the case of ideal quantum confinement the wave function in eq (3.11) has to satisfy the boundary conditions of

$$\Psi(r \geq R) = 0 \qquad (3.12)$$

For nanoparticles the electron and hole are closer together than in the microcrystalline material, and as such the coulombic interaction between electron and hole cannot be neglected; they have higher kinetic energy than in the microcrystalline material. On the basis of the effective mass approximation, Brus [74] showed for CdE (E or Se) nanocrystalline that the size dependent on the energy of the first electronic transition of the exciton (or the band gap shift with respect to the typical bulk value) can be approximately calculated using [64,74]

$$E_x \cong E_g + \frac{\hbar^2\pi^2}{2R^2}\left[\frac{1}{m^*_e} + \frac{1}{m^*_h}\right] - \frac{1.8e^2}{4\pi\varepsilon\varepsilon_\circ R} \qquad (3.13)$$

where Eg≈2.82 eV; R is the cluster radius; m^*_e and m^*_h, the electron and hole effective masses, respectively; and $\varepsilon\varepsilon_o$, the dielectric constant. Using $m^*_e=0.26m_e$, $m^*_h= 0.7m_e$ [74], and $\varepsilon\varepsilon_o=4.0x$ ($8.85x10^{-12}C^2J^{-1}m^{-1}$), Ex is calculated on the basis of eq (3.13) is $E_x(eV) \approx 2.82+1.98/R^2(nm)-0.64/R(nm)$.

Figure 3.9 shows the photoluminescence (PL) spectra of AgI thin films thickness 5-15 nm on the glass substrate at room temperature. The γ-AgI like III-V semiconductor **(**GaAs for example**)**, has a direct band gap of 2.82 eV at room temperature [75], the observed PL spectra correlates well with the fact that strong visible luminescence at ambient temperature is possible in materials with Eg > 1.8 eV. Controlled growth of AgI films with thickness of (5-15 nm) and different iodization times also optimize the band gap for efficient radiative recombination, as evidenced by the enhanced luminescence PL intensity of γ-AgI [9-10,68-69,71].

The PL emission peak appears at the same wavelength as that of the $Z_{1,2}$ exciton bands as described in the absorption spectra. Thus the photo excited electron at the conduction band edge tends to recombine *directly* with holes at the valance band edge. This process results in the emission of a PL photon having energy *almost* equal to that of the band gap. It is well known that in silver halides interstitial silver atoms and clusters are produced under illumination. Such defects may act as shallow exciton traps and cause the multiphonon structure in the PL spectrum as observed [68-69,71]. It is to be noted that unlike in our earlier PL studies on iodized Ag-Cu alloy films [7] there is no major involvement of phonons in the present case which could imply weak exciton-phonon coupling and more free excitons stabilized by iodization. Intrinsic Frenkel defects and impurities could be involved in the formation of trapping stage for recombination [70]. The recombination rate is increased with increasing iodization time as seen from PL spectra figure 3.9(i). Even in direct band gap semiconductor materials such as AgI a typical electron-hole recombination takes place only in a few nano seconds. However the typical time for an electron or hole to undergo scattering with a photon is much shorter 0.1-10ps. Thus the PL linewidths are dominated by e-h recombination [76].

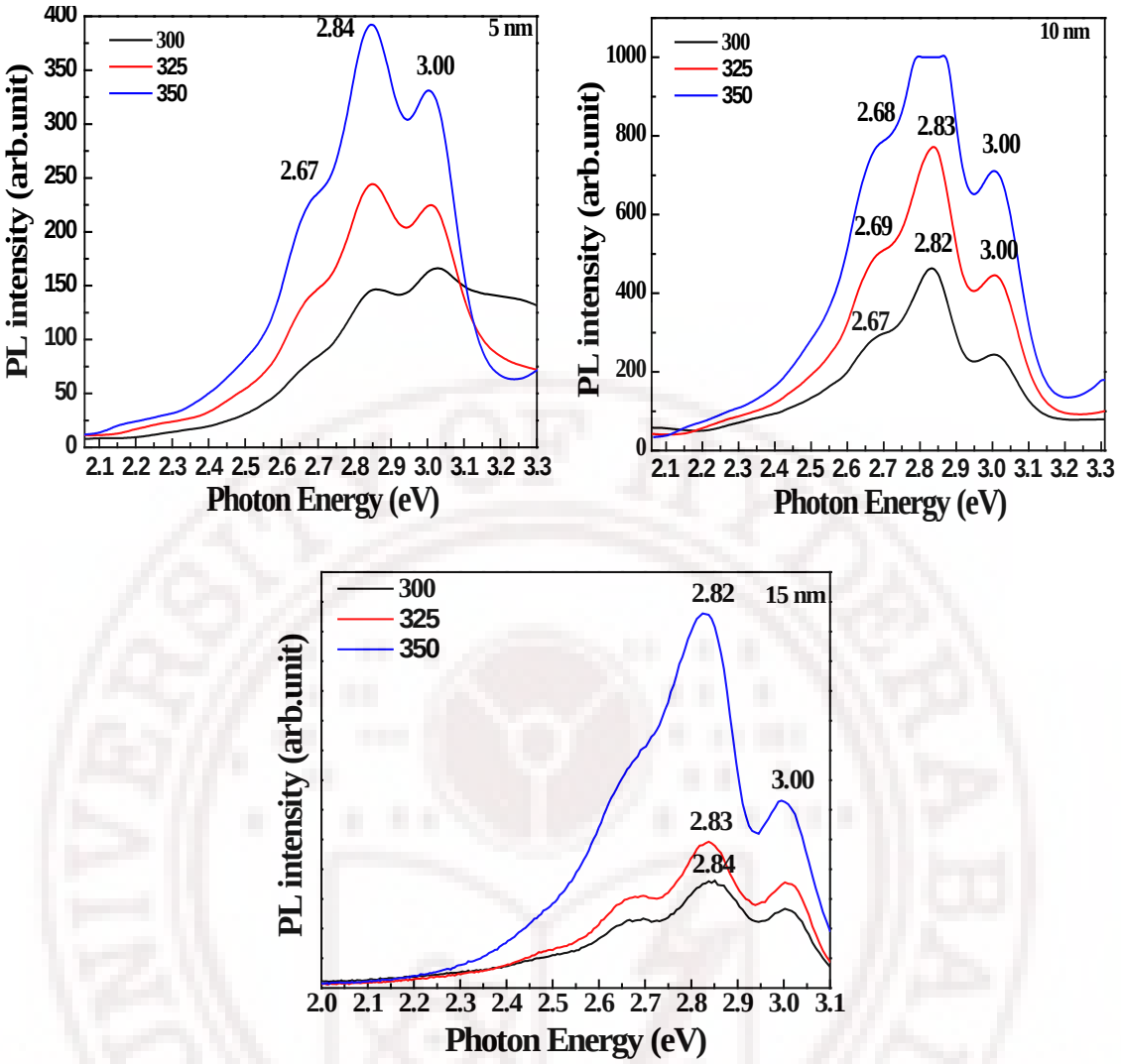

Figure 3.9: shows the PL spectra of 5, 10 and 15 nm thin Ag thin iodized at 60 min excited at wavelengths (a) 300 nm (b) 325 nm and (c) 350 nm.

It is interesting to find that the emission of AgI clusters is stronger than that of Ag clusters when excitation is at the absorption band of Ag clusters. The emission of Ag clusters is stronger by indirect excitation into the excited states of AgI clusters than that by direct excitation into the excited states of Ag clusters. Similarly, the emission of AgI clusters is stronger by indirect excitation into the excited states of Ag clusters than that by direct excitation into the excited states of AgI clusters. These possibilities indicate that energy transfer or carrier migration between Ag and AgI clusters is a dominant process in photo excitation. Details about the interaction and energy transfer between the two clusters are not very clear now, but they are probably related to the structure of the two clusters. These types of composite clusters each of which contain some Ag as well as AgI, may be formed upon short-time iodization. Each of these composite clusters may

have two domains with a sharp boundary separating Ag from AgI [77]. The structure of the composite AgI-Ag clusters is probably similar to that of mixed CdS-CdSe nanoparticles [78-80]. As silver and silver iodide clusters have different energy gaps there must be a potential difference between the Ag and the AgI clusters, and therefore the dominant mobile carrier is the electron in one and the hole in the other. Thus, under light stimulation, charge carrier migration or energy transfer between the two clusters can be expected. This is similar to the result observed in the Ag-AgI coupled composites [77].

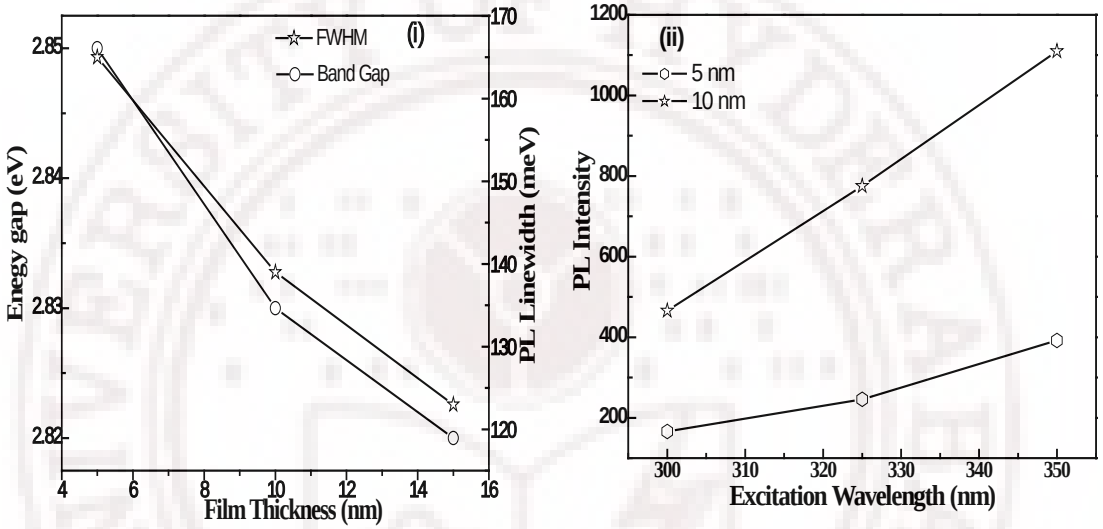

Figure 3.10: (i) Band gap and PL line width (meV) as a function of films thickness, iodized at 60 min and excited at 355 nm. (ii) The PL intensity as a function of excitation wavelength for Ag thin film thickness of 5 and 10 nm and iodized at 60 min.

Finally, photoluminescence spectra show that the donor-accepter recombination rates, enhanced by thickness and particle size reduction give raise the exciton PL emission and shows formation of Intrinsic Frenkel defects and strong surface shallow traps. This strongly suggests silver ion interstitials and silver ion vacancies are the defects responsible for the D-A recombination. Photoluminescence of Ag films obtained by evaporation show upon iodization weak excitonic luminescence accompanied by weaker and broad shoulders due to Frenkel defects and stacking faults acting as surface traps. This could be identified as shallow donor-acceptor recombination centres existing in the forbidden gap.

3.7 Summary

Silver thin films in the thickness range 5-15 nm prepared by vacuum thermal evaporation onto glass substrates these films were systematically iodized and carefully characterized by XRD, AFM, UV/Visible optical absorption and Photoluminescence. While the un-iodized Ag films are X-ray quasi amorphous in keeping with their quasi-continuous nature and 2D islanded structure, briefly iodized (5-60 minutes) 5, 10, and 15 nm films showed characteristic of both γ (zincblende) and β (Wurtzite structure) perhaps due to local iodine excess [(Ag/I)<1] of silver iodide island nanoparticles. Most interestingly, DFM image of as deposited Ag films revealed uniform spherical shaped average particle 25 nm whose size and shape change appreciably upon iodization. Optical absorption spectra of uniodized Ag films show surface plasmon resonance (SPR) features with SPR peak maxima at 430, 435 and 457 nm for the films of thickness 5, 10 and15 nm respectively. Finally an interesting and unique Surface plasmon-exciton phase transition is observed as the ultra-thin films are progressively iodized at 60 minutes. Red shift observed with increasing iodization time and films thickness which could be the effect of increasing particle size thereby weak quantum confinement effects shows the decreases in the band gap. The photoluminescence studies shown the donor-accepter recombination rates, enhanced by thickness and particle size reduction give raise the exciton PL emission and shows formation of Intrinsic Frenkel defects.

References

1. Milton Ohring, *Material Science of Thin Films, deposition and structure*, second edition, Academic press, 1900, San Diego, California, USA-92101-4495.
2. D. L. Smith, *Thin films Deposition*. McGraw-Hill, New York, 1995.
3. J. L. Vossen and W. Kern, *Thin Films Process II.* Academic Press, New York, 1991.
4. L. Holland, *Vacuum Deposition of Thin Films,* Wiley, New York, 1956.
5. Z. H. Meiksin, *Physics of Thin Films*, **8**, (1975) 161.
6. M.Gnanavel, D. Bharathi Mohan, and C. S. Sunandana, *Thin Solid Films*, 517, 1058 (2008).
7. P. Senthil Kumar and C. S. Sunandana, *Nano Letters,* **2(4)**, 431-434 (2002).
8. D. Bharathi Mohan, K. Sreejith and C. S. Sunandana, *Appl. Phys.B*.**00**, 1-5 (2005).

9. D. Bharathi Mohan, V. Sivaji Reddy and C. S. Sunandana, *App. Phys. A*, **86,** 73 (2007).
10. D. Bharathi Mohan and C. S. Sunandana, *J. App. Phys*, **100**, 064314 (2006).
11. G. Safran, O.Geszti, G. Radnoczi, P. B. Barna, K. Toth, *Thin Solid Films*, **259**, 96 (1995).
12. T. B. Light and C. N. J. Wagner, "X-ray diffraction study of Vacuum Evaporated Silver films", *J. Vac. Sci. Technology*. **3**, 1-5 (1965).
13. V. G Dubrovskii and G, E. Cirlin, *Semiconductors*, **39(11)**, 1267 (2005).
14. Praveen Taneja and Pushan Ayyub, *Phys. Rev. B*, **65**, 245412 (2002).
15. H Han and T L Alford, *J. Phys. D: Appl. Phys*. **41**, 155306 (2008).
16. X. Sun, R. Hong, H. Hou, Z. Fan, J. Shao, *Thin Solid Films*, **515,** 6962 (2007).
17. T. N. Rhodin and P. W. Palmberg, *J. Vac. Sci. Technol*. **3(6)**, 611 (1969).
18. L. S. Palatnik, *J. Vac. Sci. Technol*. **2(6),** 610 (1969).
19. K. Maki, Y. Nakajima and K. Kinosita, J. *Vac. Sci. Technol*. **6(4)**, 623 (1969).
20. K. L. Jai, P. A. Targer and D. D. Bacon., *J. Vac. Sci. Technol*. **6(4)**, 687 (1969).
21. B.D. Cullity, *Elements of X-ray diffraction,* Addition-Wesley, Philippines, 1978.
22. S. Mochizuki and F. Fujishiro, *Phys. Stat. Sol. (c)*, **3(10)**, 3586 (2006).
23. G. Chumanov, Morgan S. Sibbald and T. M. Cotton, *J. Phys. Chem. B*, **102**, 10836 (1998).
24. H. Yamada, A. J. Bhattacharyya and J. Maier, *Adv. Funct. Mater*, **16,** 525, 2006.
25. C. Liang, K. Terabe, T. Hasegawa and M. Aono, *J. Appl. Phys*, **102,** 124308 (2007).
26. Jamese E. Manson, *J. Phys. Chem*, **60(6)**, 806 (1956).
27. Y. Li, H. Zhang, Z. Guo, J. Han, X. Zha, Q. Zha, and S. J. Kim, *Langmuir*, **24** 8351 (2008).
28. R. Khaton, S. Kashiwagi, T. Limori and N. Ohta, *Appl. Phys. Lett*, **93**, 234102 (2008).
29. M. Grzelczak, Ana sanchez-Lglesias, Bentio Rodriguez- Gonzalez, Ramon Alvarez-Puebla Jorge Perez-Justle and L M Liz- Marzain. *Adv. Funct. Mater*, **18**, 3780 (2008).
30. J. S. Lee, S. Adams, J. Maier, *J. Phys. Chem. Solids*, **61,** 1607 (2000).
31. R. Mu, Y. S. Tung, A. Ueda, and D. O. Henderson, *J. Phys. Chem*, **100**, 19927 (1996).
32. J. X. Fu, A. Collins, and Y. P. Zhao, *J. Phys. Chem. C*, **112**, 16784 (2008).

33. D. B. Pedersen and S. Wang, *J. Phys. Chem. C*, **111**, 1261 (2007).
34. S. Kapoor, R. Josi and T. Mukherjee, *Chem. Phys. Lett*. **354**, 443 (2002).
35. Choon Hwee Bernard and Wai Yip Fan, *J. Phys. Chem. C*, **111**, 2953 (2007).
36. Yu-Guo Guo, Jong-Sook Lee and J. Maier, Adv. Mater, 17, 2815 (2005).
37. C. F. Bohren and D. R. Huffman, *Absorption and Scattering of Light by Small Particles*, Wiley, New York (1983).
38. Stefan A. Maier, *"Plasmonics: Fundamentals and Applications"*, Springer, United Kingdom.
39. W. P. Halperin, *Rev. Mod. Phys*, **5**(3), 533-607 (1986).
40. Kreibig, U.; Vollmer, M. "*Optical properties of metal cluster*"; Springer: Berlin, 1995.
41. E. N. Economou, Phys. *Rev.* **182(2)**, 539 (1969).
42. A. Pinchuk, U. Kreibig, A. Hilger, *Surface Science*, **557**, 269 (2004).
43. G. Mie, *Ann. Phys.* **25**, 377 (1908).
44. Cecilia Noguez, *J. Phys. Chem. C.* **111**, 3806 (2007).
45. Cecilia Noguez, *Optical Materials*, **27**, 1204 (2005).
46. Stephan Link and Mostafa A. El-Sayed. *J. Phys. Chem. B*, **103**, 8410 (1999).
47. P. B. Johnson and R.W. Christy, *Phys. Rev. B*, **6(12)**, 4370 (1972).
48. Cecilia Noguez, *J. Phys. Chem. C.* **111**, 3806-3819(2007).
49. Prashant. K. Jain and Mostafa A. El-Sayed, *J. Phys. Chem. C*, **111**, 17451 (2007).
50. Jinlian Hu, Weiping cai, Haibo Zeng, Cuncheng Li and Fengqiang Sun. *J. Phys: Condens. Matter*. **18**, 5415 (2006).
51. U. Kreibig, G. Bour, A. Hilger, and M.Gartz, *Phys. Status. Solidi A*, **175**, 351 (1999).
52. H. Hovel, S. Dritz, U. Kreibig, and M. Vollmer. *Phys. Rev. B*. **48**, 18178 (1993).
53. B. N. J. Person, *Surface. Science.* **281**, 153 (1993).
54. R. Gupta, M. J. Dyer, and W. A. Weimer. *J. Appl. Phys.* **92(9)**, 5264 (2002).
55. Praveen Taneja and Pusham Ayyub, *Phys. Rev. B*. **65(24),** 245412 (2002).
56. P. Royer, J. P. Goudonnet, R. J. Warmack, and T. L. Ferrell, *Phys. Rev B* **35**(8), 3753 (1987).
57. P. Royer, J. P. Goudonnet, R. J. Warmack, and T. L. Ferrell, *Phys. Rev. B*, **32(8)**, 3753 (1987).
58. P. Orfanides, T. F. Buckner, and M. C. Buncick, *Am. J. Phys*. **68(10)**, 936 (2000).
59. G.W. Arnold, *J. App. Phys*. **46(10),** 4466 (1975).

60. G. Speranza, L. Minati, A. Chiasera, M. Ferrari, G. C. Righini, and G. Ischia, *J. Phys. Chem. C,* **113**, 4445 (2009).
61. H. T. Grahn, *Introduction to semiconductor physics,* World Scientific Publishing Co. Pte. Ltd., Singapore 912805.
62. Richard H. Bube, *Electrons in Solids*, 3rd Edition, Academic Press, INC, San Diego, New York.
63. A. D. Yoffe, *Advances in Physics*, **50(1)**, 1-208 (2001).
64. T. Trindade, *Chem. Mater*. **13**, 3843 (2001).
65. M. Cardona, *Phys. Rev*. **129** 69 (1963).
66. S. Kondo, T. Itoh, and T. Saito, *Phys. Rev B,* **57(20)**, 13235(1998).
67. Chester R. Berry, *Phys. Rev. B,* **161(3)**, 611 (1967).
68. Shosuke Mochizuki and Kouta Umezawa, *Physics Letters A,* **228**, 111(1997).
69. S. Mochizuki and Fumito Fujishiro, *J. Phys.: Condens. Matter,* **16**, 3239-3256 (2004).
70. S. Mochizuki, *Physica B,* **308–310**, 1042–1045 (2001).
71. Michal Ilana Freedhoff, Alfred P. Marchetti, George L. Mclendon, *J. Luminescence,* **70**, 400 (1996).
72. T. H. Wei, C. W. Chen, L.C. H. Wang, P. L. Tu, T, C. Wen, *Journal of Luminescence,* **128**, 161 (2008).
73. G. Mshvelidse, O. Gogolin, E. Tsitsishvili, Ch. MaÈrkle J.S. Chadha, A. Hepting, F. Gindele, W. Petri, W. Send, D. Gerthsen, U. Woggon, and C. Klingshirn, *Phys. Stat. Sol (b)*, **207**, 369 (1998).
74. L. E. Brus, *J. Chem. Phys*. **80(9)**, 4403 (1984).
75. A. P. Marchetti, J. C. Hansen, S. Chen, M. Irving, R. Baetzold and B. R. Sever, Phys. Rev. B, 69, 94107 (2004).
76. Bernard Valeur, *Molecular Fluorescence Principles and Applications*, Wiley-VCH, Weinheim, 2002.
77. Wei Chen, Zhanguo Wang, Zhaojun Lin, and Lanying Lin, Keming Fang and Yan Xu, Mianzeng Su and Jianhua Lin, *J. Appl. Phys*, **83**, 3811 (1998).
78. L. A. Swafford, L. A. Weigand, M. J. Bowers, J. R. McBride, J. L. Rapaport, T. L. Watt, K. Sriram, D. Leonard C. Feldman, and J. Sandra. Rosenthal, *J. Amer. Chem. Soc*. **128**, 12299-12306 (2006).

79. O. Scholps, N. Le Thomas, U. Woggon, and M. V. Artemyev, *J. Phys. Chem. B,* **110**, 2074 (2006).

80. S. A. Ivanov, A. Piryatinski, J. Nanda, S. Tretiak, K. R. Zavadil, D. Werder, and V. I. Klimov, *J. Am. Chem. Soc*. **129,** 11708 (2007).

Chapter IV

Thickness and composition dependent Plasmon-Exciton transition and Photoluminescence study of cation stabilized Co-Evaporated Ag-Cu nanostructured thin films iodized at ambient

4.1 Introduction

Plasmons are elementary excitations usually detected in metals that constitute quantized collective oscillations of conduction electrons. In silver/silver-alloy thin films conduction electrons arise from the 5*s* band with a non-negligible overlap with the *4d* band. Subtle effects of band structure variations depending upon particle size, thickness and alloying element composition can be reasonably expected to be observed in the UV/Visible optical absorption spectra of thin films [1-6]. It is interesting to investigate through the simple expedient of iodization of Ag films how the plasmons in the metal gradually give place to excitons of AgI whose signatures are sensitive to crystal structure of AgI (wurtzite or zincblende) and occur in the UV-visible too. Thus through a comprehensive and systematic optical monitoring of the iodization process of the Ag thin films one can hope to study 'plasmon-exciton transition' and expect to get valuable insights into the *ab initio* electronic band structure development in AgI [7-10].

In this chapter we discuss the formation of γ-AgI thin films deposited on fused silica substrates. Fused silica substrates offer (a) the required surface roughness (better than silicate glass substrates which are usually very smooth) to support surface plasmons (b) a dielectric constant higher than the silicate glass that ensures better electromagnetic coupling with the AgI and Cu-doped AgI thin films and (c) better morphology control of the growing Ag and AgI films.

The earlier investigations of Senthil Kumar et al [11] revealed that porous Ag foils obtained by etching offers as attractive a medium as an anodic alumina for the formation and growth of AgI particles. Also, the isovalent Cu substitution as a minor 'alloying' component to Ag precursor films yields, upon iodization, more stable AgI nanoparticles through island formation and particle growth [9]. In the present work, we have chosen Cu as a substitutional element for Ag, because both differ fundamentally in their dielectric

behavior especially in metal nanocluster glass composites. The random deposition of Cu atom presumably acts as nucleation centre for formation of Ag islands.

In view of the exceptional thermodynamic stability of the zincblende phase of CuI with easily formed CuI_4 and ICu_4 robust tetrahedra, randomly occupied Cu is expected to control nucleation and saturable growth of AgI nanoparticles better than Undoped AgI, resulting in size reduced AgI nanoparticles in Cu–reinforced zincblende AgI. The aim of our study is to investigate the nucleation and growth kinetics of nanoparticles of AgI by progressive iodization of the Cu-doped Ag thin films as revealed mainly by optical absorption and photoluminescence.

4.2 Deposition of Ag and Ag-Cu thin films

Thin $Ag_{1-x}Cu_x$ films were deposited on fused silica substrate by the vacuum co-evaporation method. The highly pure silver and copper powders (Aldrich, 99.999 %) of desired composition ratios of 0.05, 0.10 and 0.20% (by atomic weight) placed in the two separate evaporation sources (molybdenum boat) which was thermally co-evaporated on to the cleaned fused silica substrate kept at an ambient temperature at a pressure of $5x10^{-6}$ Torr. The base pressure of the vacuum chamber was maintained at ~$2.5x10^{-6}$ Torr throughout the evaporation process. Both evaporation sources were controlled individually and simultaneously. The substrates were kept at a distance of 20 cm from the source for deposition. A few batches of thin films of pure Ag and of $Ag_{0.95}Cu_{0.05}$, $Ag_{0.90}Cu_{0.10}$ and $Ag_{0.80}Cu_{0.20}$ composition with thickness of 5 and 15 nm deposited at room temperature and the rate of deposition was maintained constant (0.1 A^o/sec) during the entire depositions [12]. The above conditions were found favorable for the formation of homogeneous, amorphous alloy films, although the resulting composition ratio was not analyzed. The thickness of the films was determined by using AMBIOS XP-1 profilometer.

Iodization: Iodization of these thin films was done an hour-glass type chamber with dimension of 10 cm height x 6 cm diameter. Iodine kept at the bottom of the lower half of the chamber sublimates at room temperature and slowly (over durations ~ tens of minutes) deposits on the $Ag_{1-x}Cu_x$ alloys films kept at the top of the chamber kept in a dark room. Thus iodization was carried out for selected durations in the range of 15min to 6hr. The crystal structure of Ag-Cu and AgI films deposited on fused silica substrates as a function film thickness and Cu concentration were characterized using X-ray diffraction

(XRD) technique. Following the XRD measurement, Dynamic Force microscope (DFM) was employed to measure the surface morphology of the films, which provided high resolution images. The room mean square roughness (rms roughness) was also determined using DFM. Optical band gap (Eg) of cation stabilized AgI films deposited on fused silica substrates were determined from the spectral absorption data obtained from UV-Visible spectrophotometer. The band development of iodized Ag-Cu films was monitored by the photoluminescence a study using a Fluorolog@-3 Spectroflurometer has been used in the UV/Visible range 300 to 800 nm with scanning rate of 200 nm/min at different excitation levels. A correlation between the structural, microstructural and optical properties of AgI films is discussed.

4.3 Structural Characterization

4.3.1 Crystal Structure of γ and β-AgI, Vegard's Law and crystallites sizes

Ag-Cu is a unique binary system with the atomic size mismatch of Cu being 15% with respect to Ag i.e $2(a_{Ag} - a_{Cu})/ (a_{Ag}+a_{Cu}) = 15\%$. We have chosen the physical vapor deposition method to prepare quasi amorphous Ag-Cu thin films in which Cu promotes Stranski-Krastanov or Layer plus island type growth [9], thus providing an attractive platform for studying formation of γ-AgI nano particle growth. Although the Ag-Cu binary systems has only metastable solubility in view of their positive heat of mixing, the tendency of Cu to help stabilize small clusters and promote quasi-amorphous, discontinuous thin film growth in the precursor films is conductive for stabilization of quantum dot like structure in the iodized form even at ambient temperature in a matrix free manner on clean fused silica substrates. The formation of AgI thin films involve iodization of isolated Cu-stabilized Ag islands a process that simultaneously involves pre-crystallization which is very subtle and hard to detect easily [13-17].

The as-deposited films of pure Ag and Cu substituted films were found to be quasi-amorphous in nature as revealed by XRD patterns without any detectable Bragg peaks. These films were then iodized systematically to determine the structure of γ-AgI thin films and from a more fundamental point of view, to monitor the evolution of the crystal structure and the electronic band structure. The most interesting aspect of the Ag-Cu alloy/solid solution is the role played by Cu in stabilizing the γ-phase of AgI when iodized, as would be discussed [9,14-17]. Due to the availability of 30% vacancies in the fcc structure of Ag lattice, the doped Cu atoms could occupy the vacant interstitial

position in the Ag lattice, thereby arresting the random motion of the Ag^+ ions in the AgI lattice thus ensuring stability of the zincblende structure. As-deposited 5 and 15 nm Ag-Cu thin films are found to exhibit a quasi-amorphous nature with no detectable Bragg peaks in the XRD pattern. The amorphous Ag-Cu film to crystalline AgI transition of these films apparently depends strongly on the Cu concentration. The systematics of structure development of these Ag-Cu quasi-amorphous films upon iodization is shown in figure 4.1.

The thermally evaporated Ag_{1-x}-Cu_x films of thickness of 5 and 15 nm were subjected to velocity controlled iodine vapor flux for various intervals in the range 5–720 minutes to study the growth of γ-AgI (Zincblende) and β-AgI nanoparticles for 5, 10 and 20% Cu doped films respectively. Figure 4.1 and 4.2 (i)-(iii) shows the growth of γ-AgI nanoparticles upon iodization during different time period of 30-720 min of 5 and 15 nm Cu doped AgI thin films. γ-AgI is a metastable phase it forms even short time iodization of evaporated Ag films give rise the intense γ-AgI (111) plane which indicates the ease of two-dimensional growth of the zincblende phase of AgI with the more disordered ABCABC… stacking of atomic planes (compared to ABAB… stacking responsible for β-AgI development) [18,19]. Prolonged iodization AgI films caused development of two polymorphs, γ-AgI and β-AgI, with the same first neighbor coordination of Ag by I atoms (but different second neighbors) and the tendency of β-AgI to grow into big macroscopic crystal, thus offering a stiff competition to the nucleation and growth of γ-AgI nanoparticles, thereby making the particle growth process an attractive thin film growth challenge. The identification of β-AgI is through a triplet of low angle (100), (001) and (101) reflections as against the strong (111) low angle reflection and week (400) high angle reflection in γ-AgI [20-22]. Only subtle changes in the long range coulomb interaction observed in bulk γ-AgI makes its characterization difficult at the band structure level but its characteristic exciton signatures are most sensitive (XRD is quite insensitive-see later) to optical detection which is exploited in this work .

Figure 4.1 show the X-ray diffraction pattern of 5nm thickness of (i) $Ag_{0.95}Cu_{0.05}$ iodized for different time durations. Short time iodized films of all three compositions shows there is no signature of silver iodide peak development. After 30 min of iodization the γ-AgI (Zincblende) (111) peak starts growing slowly and there is no impurity phases present. Further 180 min iodization of Ag-Cu films clearly shows the predominant peak

(111) growing with very strong intensity. Even upon long time iodination only (111) intensity increases there is no trace of β- AgI formation. The reason could be evaporated films are quasi amorphous films it takes little iodine in the begin growth of γ-AgI (Ag rich) Zincblende structure. Significantly, the growth of the wurtzite phase of β-AgI is now completely suppressed, which suggests a rapid nucleation of γ-AgI crystallites aided by Cu.

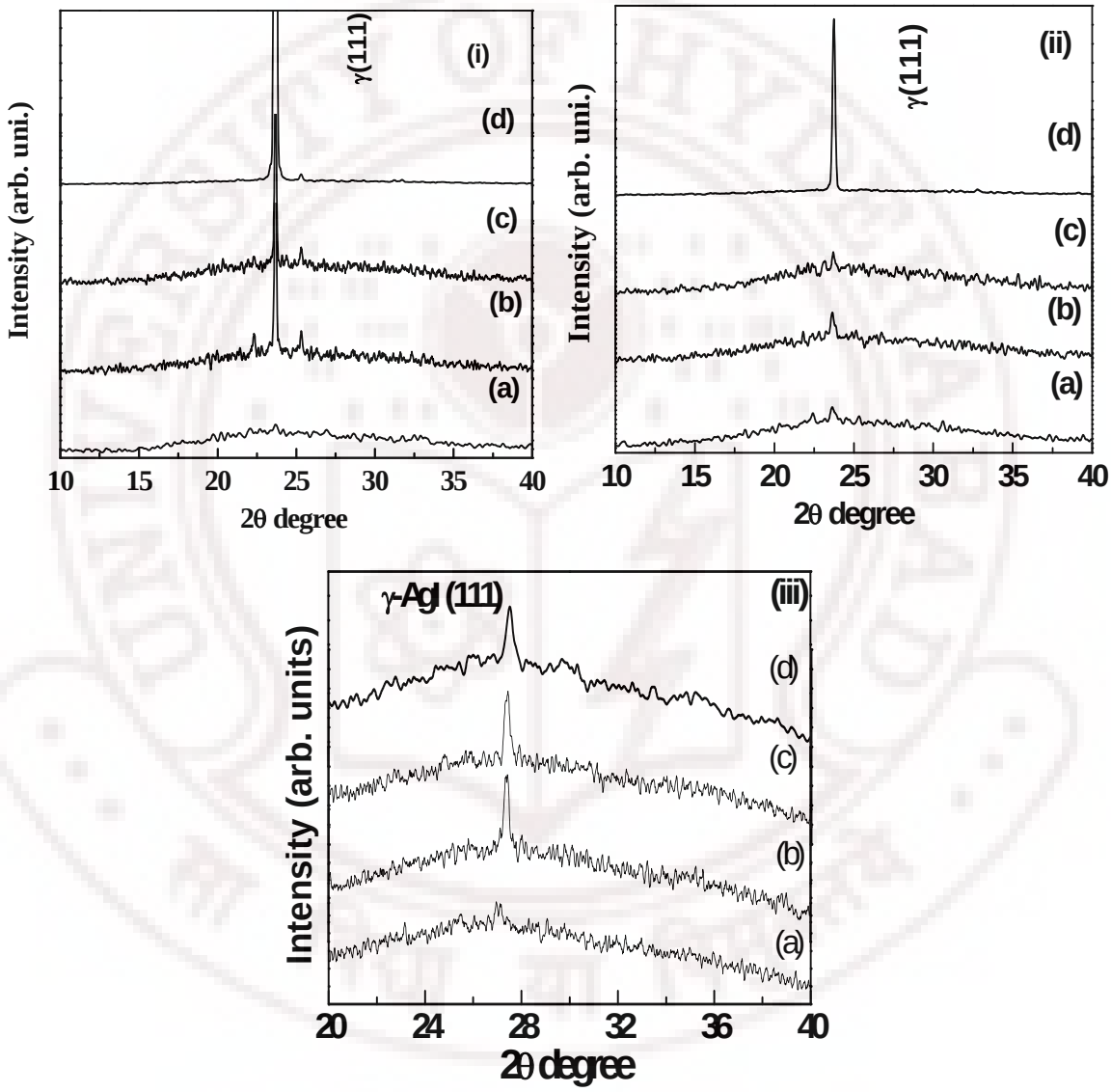

Figure 4.1: XRD Pattern of 5 nm thick (i) $Ag_{0.95}Cu_{0.05}$ (ii) $Ag_{0.90}Cu_{0.10}$ and (iii) $Ag_{0.80}$-$Cu_{0.20}$ iodized for (a) 15 min (b) 30min (c) 60 min and (d) 180 min.

XRD patterns clearly indicate the retarded nucleation and growth of AgI nanoclusters as well as the crystalline nature of the completely formed AgI films after 720 min of iodization. Even through a detailed structural characterization is lacking at present our optical spectra gives very strong evidence for mixture (γ + β) AgI phase formation. In

thick films 5% copper doped sample stabilizes γ-AgI (Zincblende) as a major phase along with small impurity β-AgI phase but in the case of 10 and 20% Cu doped AgI films clearly reveals evidence of formation of mixed phase of (γ+β) at 720 min iodized samples shown by XRD peaks (111) and the major β-AgI (Wurtzite structure) (110) and (101). $Ag_{0.90}Cu_{0.10}I$ and $Ag_{0.80}Cu_{0.20}I$ composition has only one γ-AgI line (100) with small intensity confirming the formation of the major zincblende phase of AgI stabilized by Cu. The Bragg diffraction pattern of $Ag_{0.90}Cu_{0.10}I$ sample shows a predominant peak corresponding to the zincblende structure of γ-AgI alone with no trace of β phase. We have observed that β-AgI phase was found on prolonging the iodization process. As we know that the excess concentration of iodine ions leads to the formation of β-AgI we have resorted to brief iodization as a strategy to stabilize the γ-AgI (with Ag/I >1) [23].

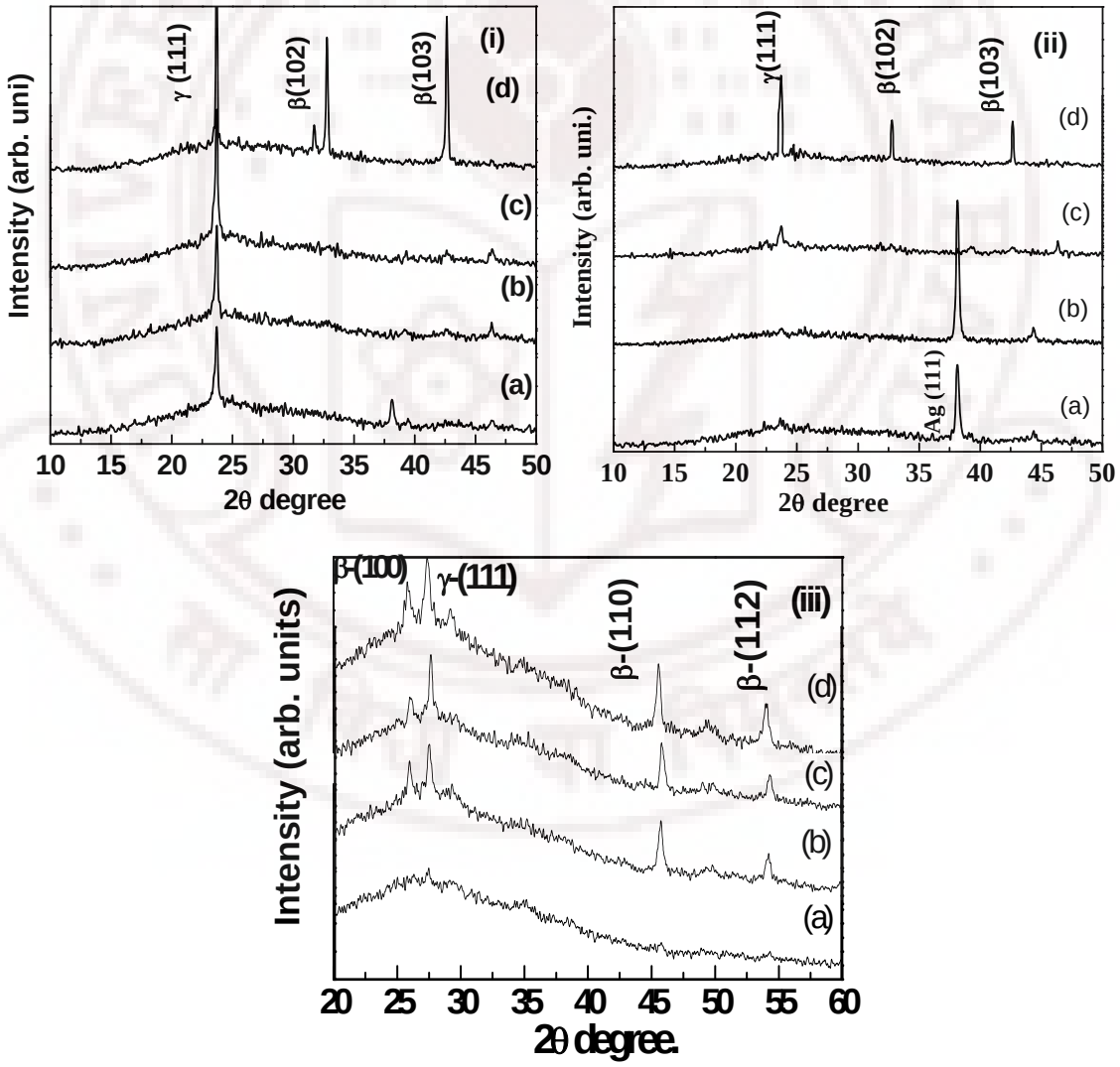

Figure 4.2: XRD Pattern of 15 nm thick (i) $Ag_{0.95}Cu_{0.05}$ (ii) $Ag_{0.90}Cu_{0.10}$ and (iii) $Ag_{0.80}Cu_{0.20}$ iodized for (a) 60 min (b) 180min (c) 360 min and (d) 720 min.

4.3.2 Strain Analysis

Figure 4.3 also shows an increase of all the Bragg angles accompanied by a broadening of the (111) peak upon progressive Cu addition. The lattice parameter of γ-AgI (111) peak 5 nm films is initially very high (6.50A^{o}) due to compressive residual stress but as Cu concentration goes more it decreases slowly and finally match with (JCPS) values. The lattice parameter (a in pm) decreases with increasing Cu substitution. The Bragg reflection of the intermediate (80:20) composition $Ag_{0.80}Cu_{0.20}I$ shows the changes in the 2θ of the first three prominent peaks. This indicates a continuous and uniform stabilization of static cation disorder in the zincblende AgI lattice brought about by the vacuum co-evaporation method. These significant observations corroborate our earlier XRD results on polycrystalline solid solutions $Ag_{1-x}Cu_xI$ [14,24]. From the peak shift in the XRD, the average strain (ε) can be calculated using the following relation

$\varepsilon = [(d_{observed} - d_{reference}) / d\ reference] \times 100\%$

where $d_{observed}$ and $d_{reference}$ are interplanar spacing of γ-AgI (111), β-AgI (110) and the reference from JCPDS. From figure 1 and 2 the calculated average strain (ε) of γ-AgI and β-AgI for two different thicknesses of 5 and 15 nm of Cu doped AgI films. The observed average strain (ε) is (1.95%) positive and its value depends up on iodization time, suggesting the existence of compressive stress at room temperature [8].

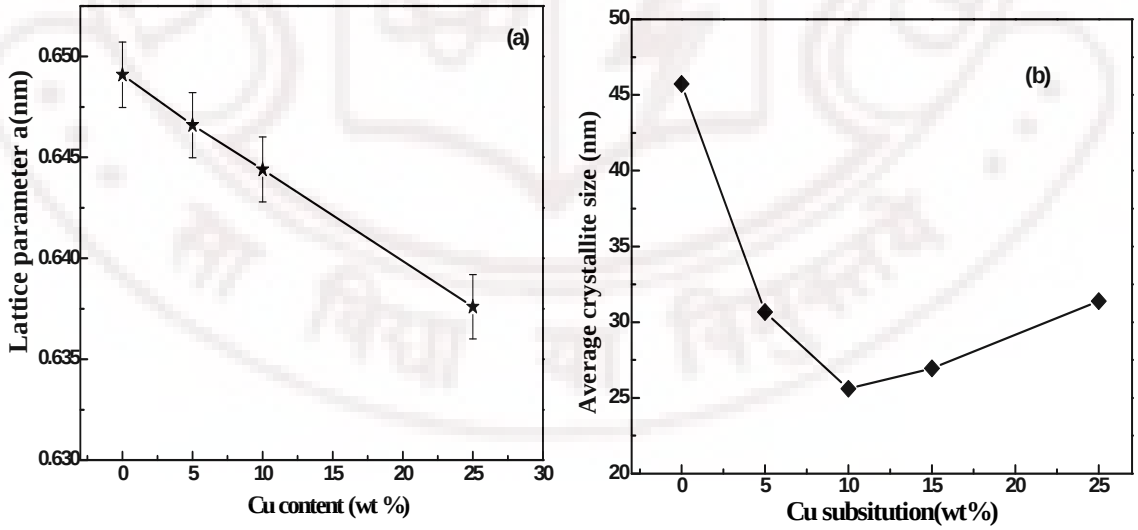

Figure 4.3: Evolution of the Zincblende AgI structure in (a) Cu doped Ag films upon progressive iodization of 360 min. There is a clear reduction in the lattice parameter of AgI upon Cu substitution evidencing the direct role of Cu in firming up the zincblende structure of AgI. (b) Cu substitution shown the clear evidence for crystallite size changes upon substituting Cu cation in to AgI matrix.

The average strain of 5 nm thick Ag film decreases slowly with increasing iodization time finally tending to zero (quasi free) for 3hr iodization. 15 nm thick Cu doped AgI shows tensile stress, the average strain value becoming negative for 12 hr iodization. Because of mixed phase formation, we may observe compressive stress if iodization is carried on for more than 24 hr due to formation of defects (in case of short time iodization we could not observe this). For the alloy compositions $x > 0.1$, the iodization process seems to be retarded possibly due to the formation of a large number of pure and mixed clusters during the films deposition itself. These clusters considerably reduce the number of active silver atoms and also defects that aid the adsorption and surface/bulk diffusion. Probably, both these processes are impeded upon progressive substitution of Cu. Comparison with the earlier results of Kuiry et al [25] on Cd-doped Ag, where only mixed ($\gamma+\beta$)-AgI films were formed, suggests that Cu-doping strongly favors the formation of γ-AgI, besides effectively controlling the iodization process so that the ($\gamma \rightarrow \beta$) phase transformation has been considerably and indefinitely delayed under optimized conditions.

4.3.3 Composition analysis

Energy dispersive x-ray (EDX) analysis was performed on an $Ag_{1-x}Cu_xI$(x=0.05, 0.1 and 0.20 atomic wt %) thin films coated on fused silica substrates. By considering the iodization time, copper concentration and thickness of the sample we have analyzed area contained Cu substituted AgI thin films of different thickness. However we were able to estimate the composition from the corresponding emission energy spectrum shown in figure 4.4. Copper ($L\alpha_{1,2}$ at 0.93 keV, $K\alpha_{1,2}$ at 8.04 keV and $K\beta$ at 8.90 keV), Silver ($L\alpha_1$ at 2.98 keV, $K\alpha_1$ at 22.16 KeV) and Iodine ($L\alpha_1$ at 3.93 keV, $K\alpha_1$ at 28.61 keV) emission energies were identified. Quantitative analysis resulted in the 95:5, 90:10 and 80:20 atomic weight % and fractions of iodine is kept 100%. The slight off-stiochiometry was attributed to the small quantity (film thickness) of the materials and also due to uncertainty in the analysis of bulk substrates element (Si).

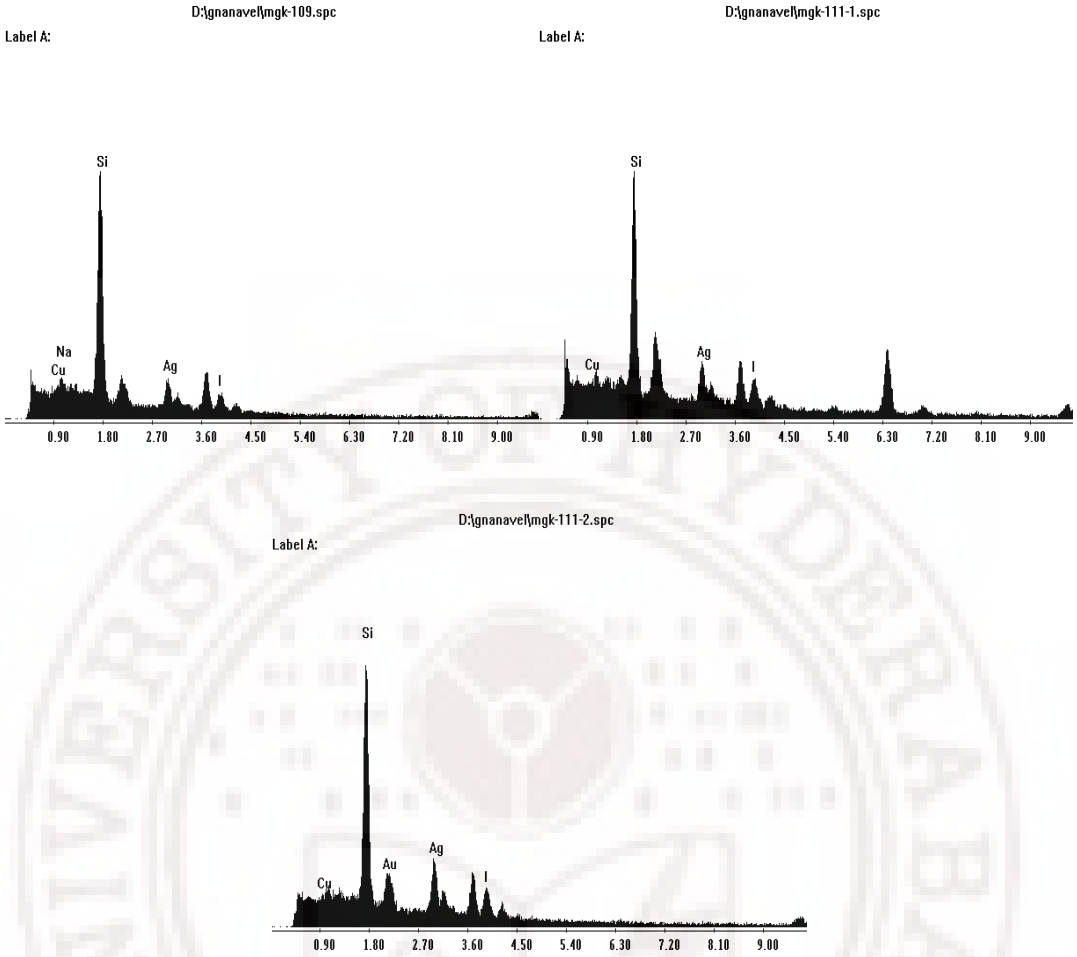

Figure 4.4: EDAX spectrum of 15 nm thin (a) $Ag_{0.95}Cu_{0.05}I$ (b) $Ag_{0.90}Cu_{0.10}I$ and $Ag_{0.80}Cu_{0.20}I$ formation of Cation (Cu) substituted AgI thin films.

4.4. Surface microstructure characterization of Cu doped AgI thin films

Figure 5 represents the two dimensional surface morphology (DFM images) of the Cu doped Ag thin films deposited on fused silica substrates as a function of copper substitution. Specifically figures 4.5(a), (b) and (c) show the surface morphologies of 5%, 10% and 20% Cu substituted Ag films 5 and 15 nm thick. 5 and 10% Cu substituted Ag films reveal well-shaped and uniform sized (~ 25 nm) spherical particles with surface roughness 1.5-2.5 nm (RMS) [26-28]. Generally Vacuum evaporated thin films form by island growth with loosely bound isolated particles due to high thermal strain and internal stress. This type of isolated metal particles favors for tuning the optical properties especially through surface plasmon-exciton transition. In contrast the 20% of Cu doped Ag microstructure show the anisotropic particle growth with different size and shape.

Essentially, the role of Cu is to qualitatively change the thin films growth mode from simple layered type of growth to a layered plus island type growth (S-K growth) mode via the formation of mixed Ag-Cu clusters. 20% Cu concentration shows increases in the particle size are seen in figure 4.5. This is probably a direct evidence for Cu substitution in the inorganic Ag matrix [10].

In order to understand the grain growth and AgI nanoparticle microstructure formation, these films were carefully iodized at different times, short time iodization at 30 min and long time at 12 hr shown in figures 4.6 and 4.7. The iodization process induces AgI grain growth leading to a significant increase in lateral grain size and a striking difference in the morphology between Ag-I bonds [29,30] depending upon iodization time. Copper substitution in to AgI matrix essentially helps control the particle growth, because Ag and Cu have fundamentally different dielectric properties in metal nanocluster glass composites as mentioned earlier. The random deposition of Cu atom presumably creates as nucleation centres for formation of Ag islands. Anisotropic particle growth with increasing surface roughness 5 nm due to the large particle size with different cluster size 150 nm is seen. Substituting Cu in to the Ag matrix it helps to form the confined clusters. An AgI nanoparticle thereafter grows by what may be called a delayed interfacial nucleation-cum-crystallization process evolving in time. Coalescence is avoided by the very nature of the quasi-amorphous precursor films. Decrease of Ag/Cu ratio with the aim of reducing the eventual size of AgI nanoparticles probably results in increased island density with decreased average size of the islands themselves [9,12].

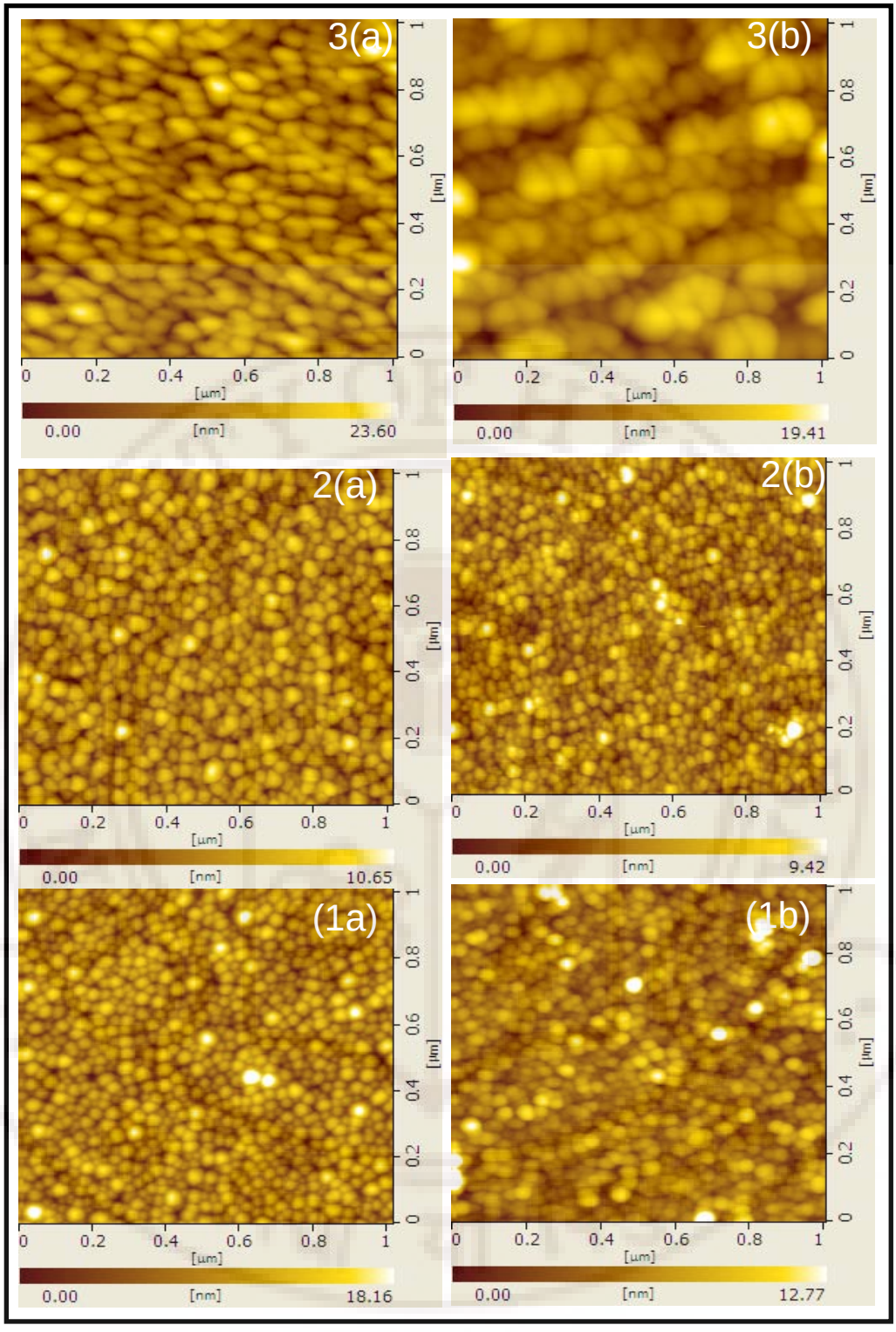

Figure 4.5: DFM image of Surface micro structure of as deposited (1) $Ag_{0.95}Cu_{0.05}$, (2) $Ag_{0.90}Cu_{0.10}$ and (3) $Ag_{0.80}Cu_{0.20}$ of Ag-Cu alloy thin film thickness of (a) 5 nm and (b) 15 nm. As deposited Ag-Cu film shows the uniform size (~ 25-45 nm) spherical nano particles function of Cu concentrations and average surface roughness increases function of film thickness.

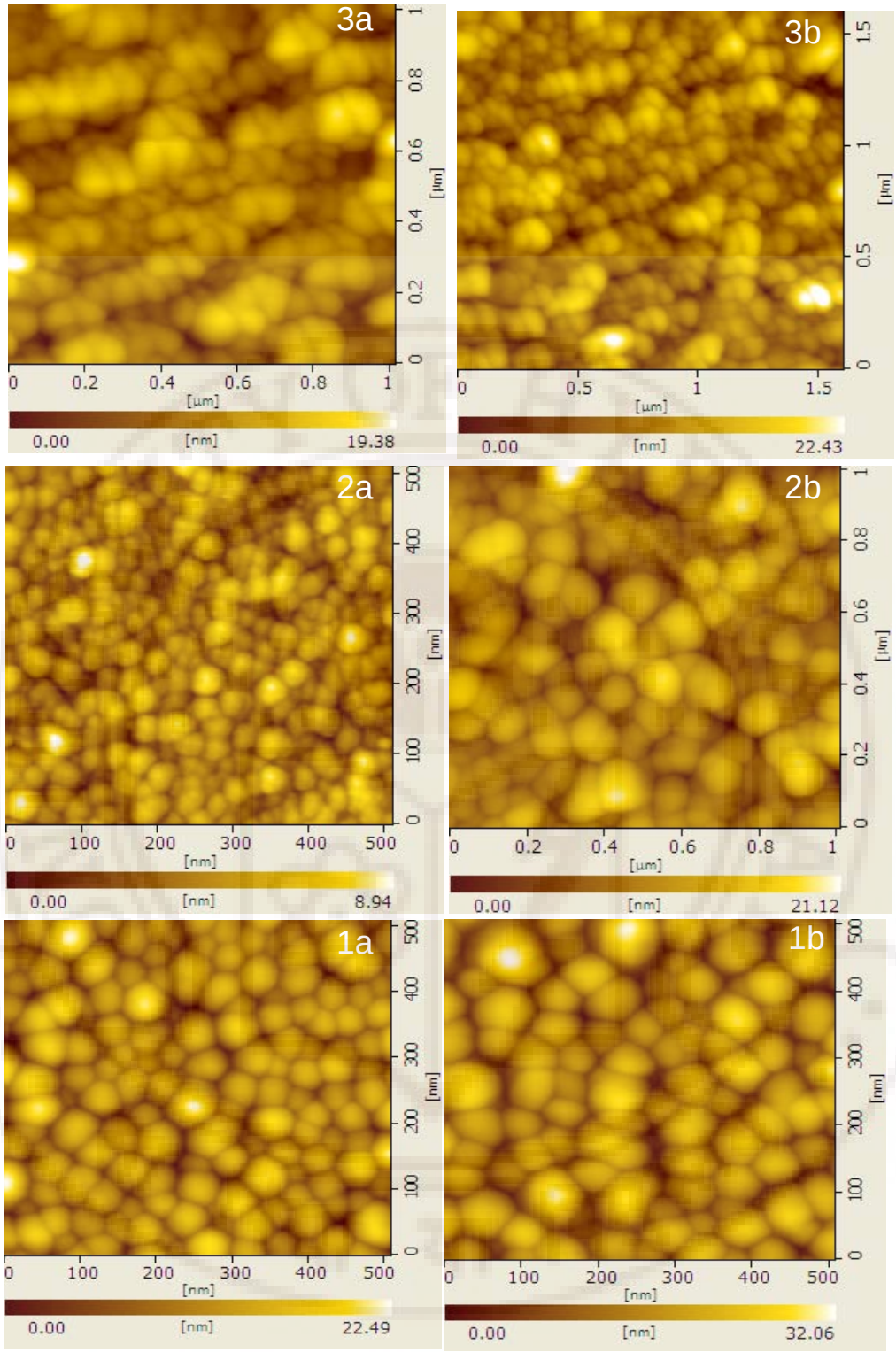

Figure 4.6: DFM image of Surface micro structure of 5 nm thick (1a) $Ag_{0.95}Cu_{0.05}$, (2a) $Ag_{0.90}Cu_{0.10}$ and (3a) $Ag_{0.80}Cu_{0.20}$ of Ag-Cu film iodized for 30 min and (1b) $Ag_{0.95}Cu_{0.05}$, (2b) $Ag_{0.90}Cu_{0.10}$ and (3b) $Ag_{0.80}Cu_{0.20}$ film iodized for 180 min. Short time iodized Ag-Cu film shows change in the surface morphology and surface roughness. The particle size varies with Cu concentration and iodization time.

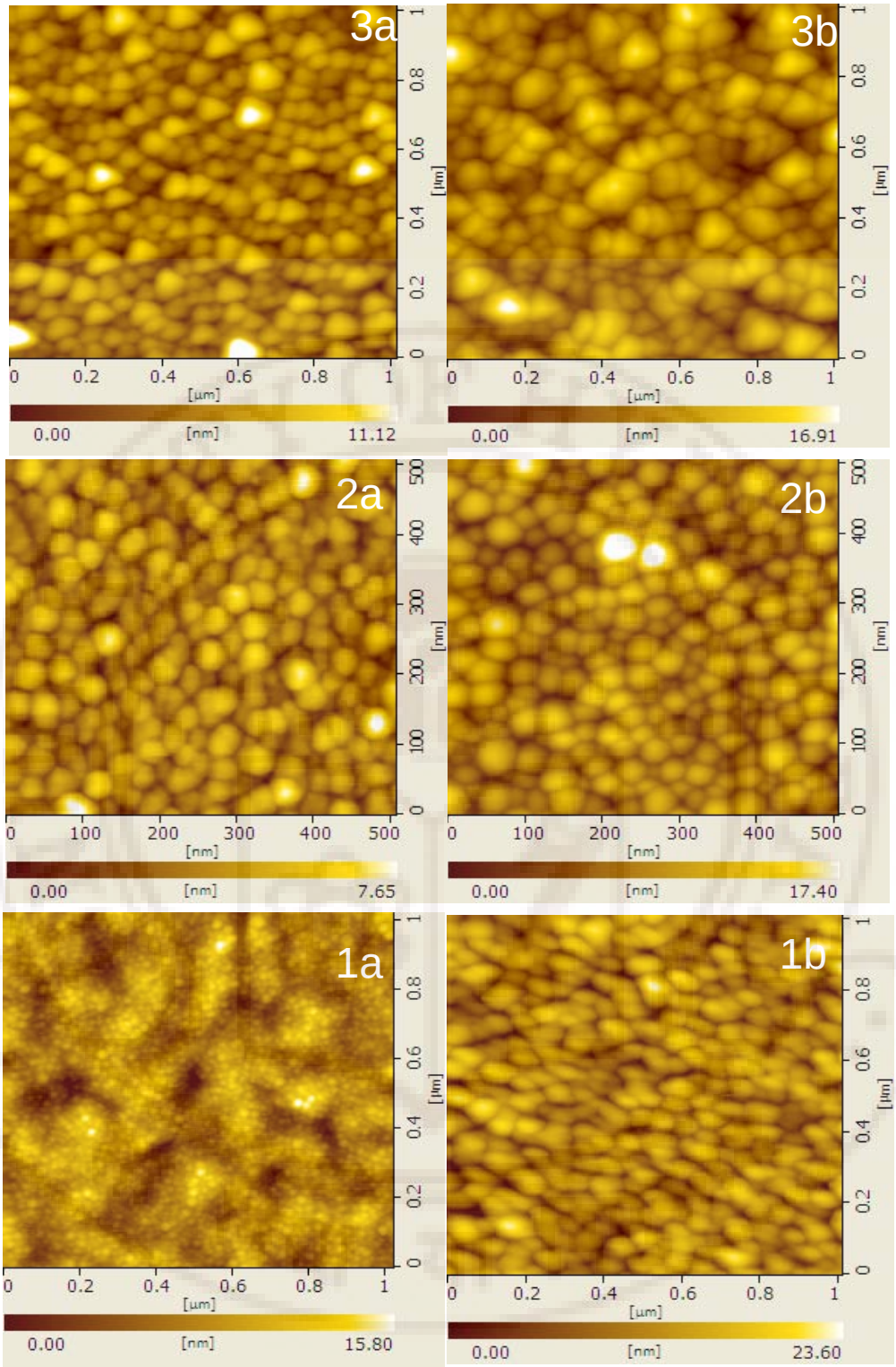

Figure 4.7: DFM image of surface micro structure of 15 nm thick (1a) $Ag_{0.95}Cu_{0.05}$, (2a) $Ag_{0.90}Cu_{0.10}$ and (3a) $Ag_{0.80}Cu_{0.20}$ of Ag-Cu film iodized for 30 min and (1b) $Ag_{0.95}Cu_{0.05}$, (2b) $Ag_{0.90}Cu_{0.10}$ and (3b) $Ag_{0.80}Cu_{0.20}$ compositions of Ag-Cu alloy thin film iodized for 360 min. Short time iodized Ag-Cu film shows changes in the surface morphology, surface roughness and increased particle sizes.

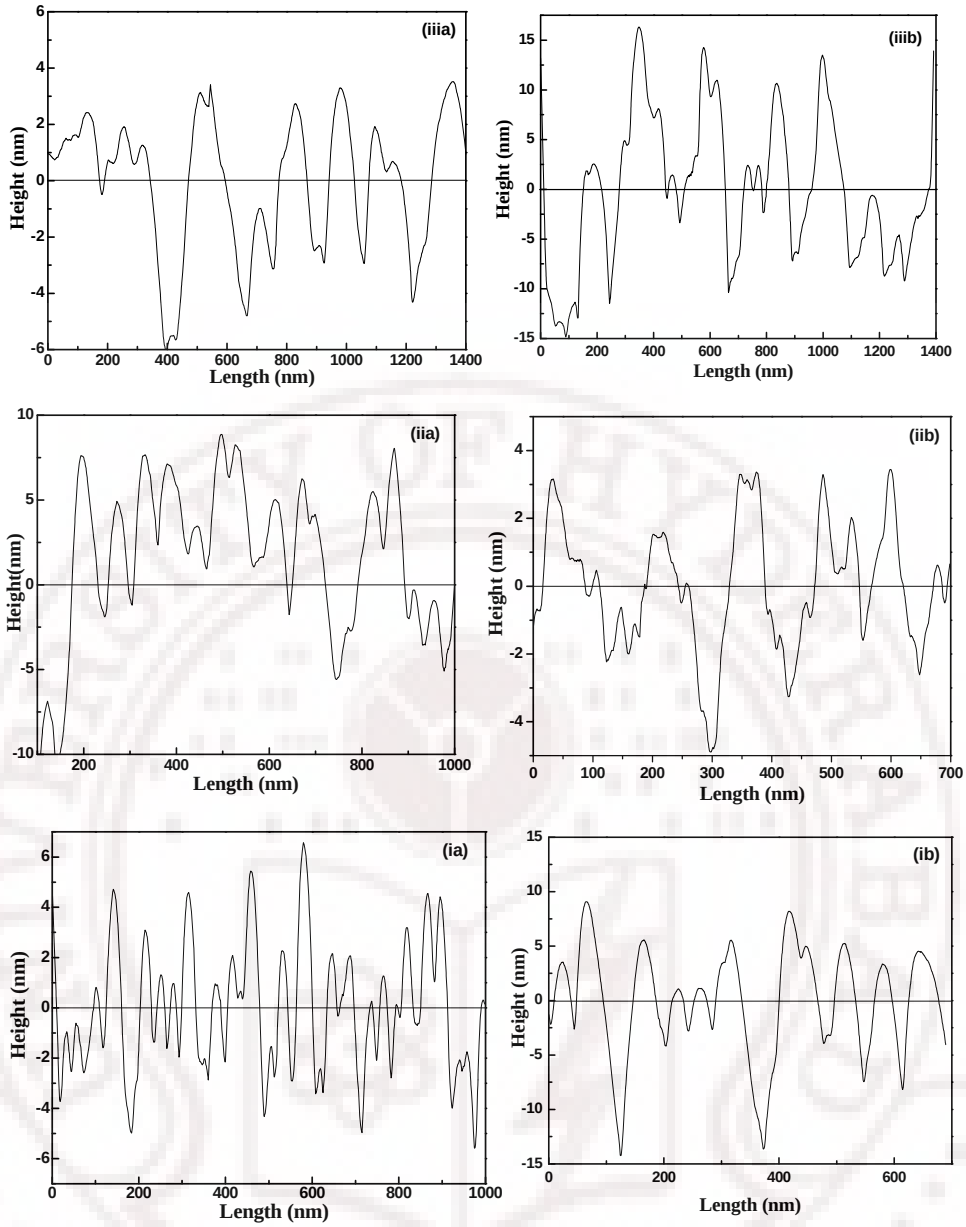

Figure 4.8: AFM Surface profile analysis of (ia) 5 nm thick Ag film (ib) 5 nm thick Ag film iodized for 360 min (iia) 5 % Cu doped 5 nm thick Ag film iodized for 30 min (iib) 5 % Cu doped 5 nm thick Ag film iodized for 360 min (iiia) 5 % Cu doped 15 nm thick Ag film iodized for 60 min (iiib) 5 % Cu doped 15 nm thick Ag film iodized for 360 min.

Figure 4.8 shows RMS roughness (height and length) derived from surface morphology of the Ag (Cu) and Ag sample as a function of the iodization times taken along the horizontal lines (derived from figures 4.6 and 4.7). It shows that surface profile in the vertical direction (height amplitude) decay to lateral scales for un-iodized and iodized samples and result in rough films surfaces when compared with as-deposited samples at both films 5 and 15 nm Ag and $Ag_{1-x}Cu_x$ (x=0.05, 0.10 and 0.20 atomic weight %). The grain boundary grooving width and depth are monitored with those of AFM cross-section topography analysis. Iodizing Ag-Cu films for durations above 60 min

initiates grain growth and shape changes which becomes wider and deeper with increased iodization times [8,29-31].

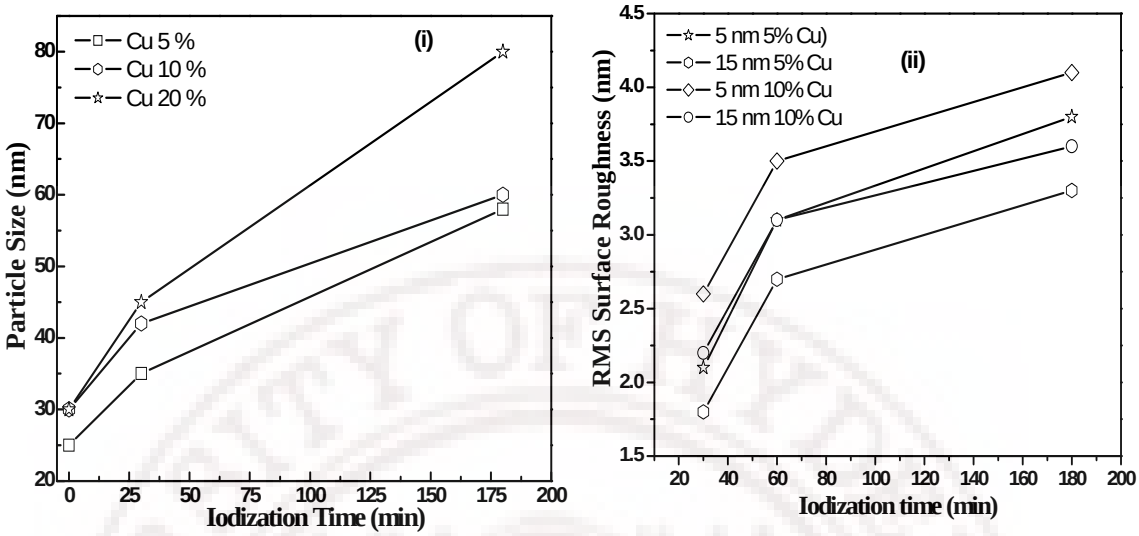

Figure 4.9: Variation of particle size and surface roughness as a function of Cu substitution and iodization time. (i) 5 nm thin $Ag_{1-x}Cu_x$ (x= 0.05, 0.10 and 0.20 wt %) films iodized at 0-180 min. (ii) 5 and 15 nm $Ag_{1-x}Cu_x$ (x= 0.05, 0.10 wt %) films iodized over 30-180 min.

Figure 4.9 shows the iodization time evolution of particle size and surface roughness of the three Cu-doped Ag thin film compositions. It is clear from these plots that while short time iodization produces a linear increase of these parameters long term iodization tends to produce a saturation indicating that the iodized films still support a Ag/I >1 stiochiometry demonstrating the role of Cu in stabilizing the γ-AgI structure.

4.5. Optical properties

4.5.1 Surface plasmon-exciton transition in progressively iodized Cu doped Ag thin films

The optical resonance absorption is observed in the UV-visible spectra of rough ultrathin films of Ag due to the collective oscillation of the 5s conductions with respect to the Ag^+ ionic background in the nanoscale silver particles. Since the electronic configuration of the silver atoms is [Kr] $4d^{10}5s^1$, the outermost ($5s^1$) energy band is only half filled, which is why silver is a metal. However, the immediately underlying d- band electron affects the optical and electronic properties much more markedly in silver than copper or gold [1-6].

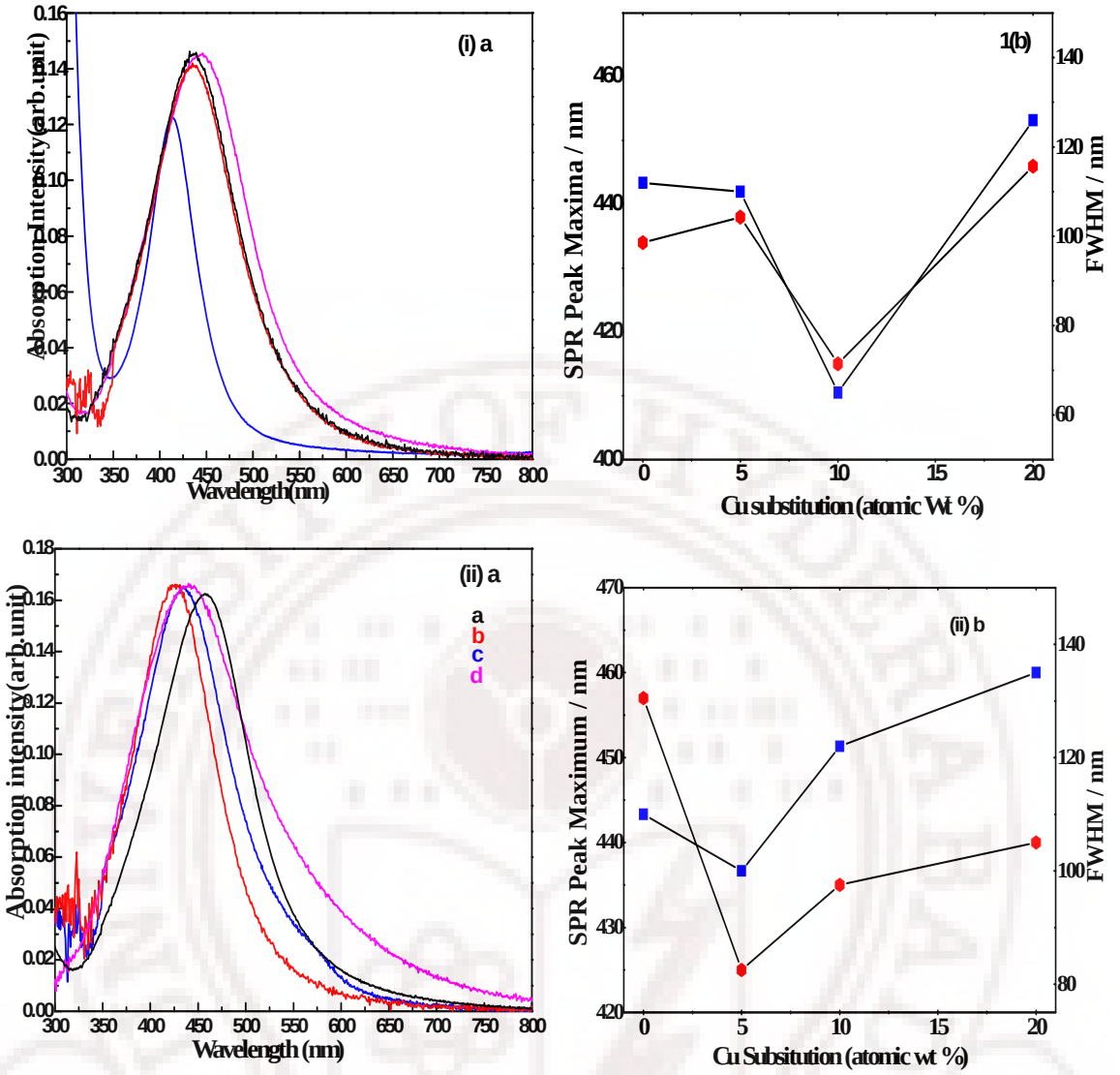

Figure 4.10: Thickness and Cu substitution dependent Surface plasmon resonance and FWHM. Figure (ia) 5 nm $Ag_{1-x}Cu_x$ (ii a) 15 nm $Ag_{1-x}Cu_x$ thin films(x= 0.05, 0.10 and 0.20 wt %). (a) Un-doped (b) 5 (c) 10 and (d) 20 % copper doped Ag films 5 and 15 nm thick.

Figure 4.10 shows the experimentally recorded optical absorption spectra of Cu doped Ag thin films of thickness of 5 and 15 nm. Figure (i)a and (ii)a. show the UV-Visible spectra of the pure Ag and $Ag_{1-x}Cu_x$ (x=0.05, 0.10 and 20 wt %) quasi-amorphous thin films, thickness of 5 and 15 nm. The Optical absorption as deposited un-doped pure Ag films show only one surface plasmon resonance peak (SPR) with peak maxima at 434 and 457 nm and corresponding FWHM of 112 and 110 nm for 5 and 15 nm films respectively, as shown in figure (i)b and (ii)b. These films deposited by vacuum thermal evaporation technique were formed via the S-K (mixture of island and layer) type growth which depends upon the deposition conditions and thickness. In 5 nm thin films formed by island type growth, the particle size distribution are not uniform, so that the

interparticle distance produces a broadening of SPR peaks seen through increased FWHM. Where as 15 nm thick films forms via S-K type film growth, resulting in very high filling factor and less interparticle distance leading to particle aggregation which eventually causes a red shift of SPR [32].

In figure 4.10(i) a and (ii) b are the Cu substituted (5, 10 and 20 wt %) Ag-Cu films show the blue shifts in the SPR peak maxima depends upon the Cu concentration. The 5% Cu concentration SPR appeared at 438 nm and 425 nm for 5 and 15 nm thick films, where as the in the case of 10% Cu concentration there is a strong blue shift of peak maxima. The principal cause for such a peak shift is that electronic conductivity is reduced by substituting Cu atoms for partial Ag ones in Ag phase with fcc structure. The solubility limit of Cu atoms for Ag phase has been known to be 14.1 at % and the Ag-Cu amorphous alloy having the Cu content of 14.1 at. % indicates lower electric conductivity than Ag and Cu. In 20% Cu doped 5 nm thin Ag film the peak maximum is observed at 446 nm (red shift) and the resonance is very broad (FWHM =126 nm) which could be due to the formation of Cu SPR. When Cu doping level is increased a shoulder at 570 nm can also be seen at the position of the metal copper plasmon peak which becomes stronger and appears as a clear peak with the increasing film thickness. It is known from the literature that the copper and silver exhibit very limited miscibility in the bulk [33-36].

The optical absorption spectra evolve systematically for progressively iodized island films with the maximum 20% Cu concentration. The islands with maximum copper content and thus with the least possible median island size behave like quantum dots [37-40], keeping in view the difference in the nature of confinement of the exciton in AgI and CuI. Figure 4.11 and 4.12 shows the room temperature UV/Visible absorption spectra of the progressively iodized metastable quasi-amorphous precursor Ag-Cu films thickness of 5 nm and 15 nm. A careful comparison of these optical spectra for isochronal iodization (up to 360 min) of the 5 nm thick Ag-Cu composite films reveals that the increasing Cu content progressively retards the AgI nucleation and growth thereby effectively controlling the resultant products particle size. The general feature of the absorption spectra in our iodized Ag-Cu films is the appearance of a strong exciton absorption peak edge around 422 nm characteristic of γ-AgI [9,12].

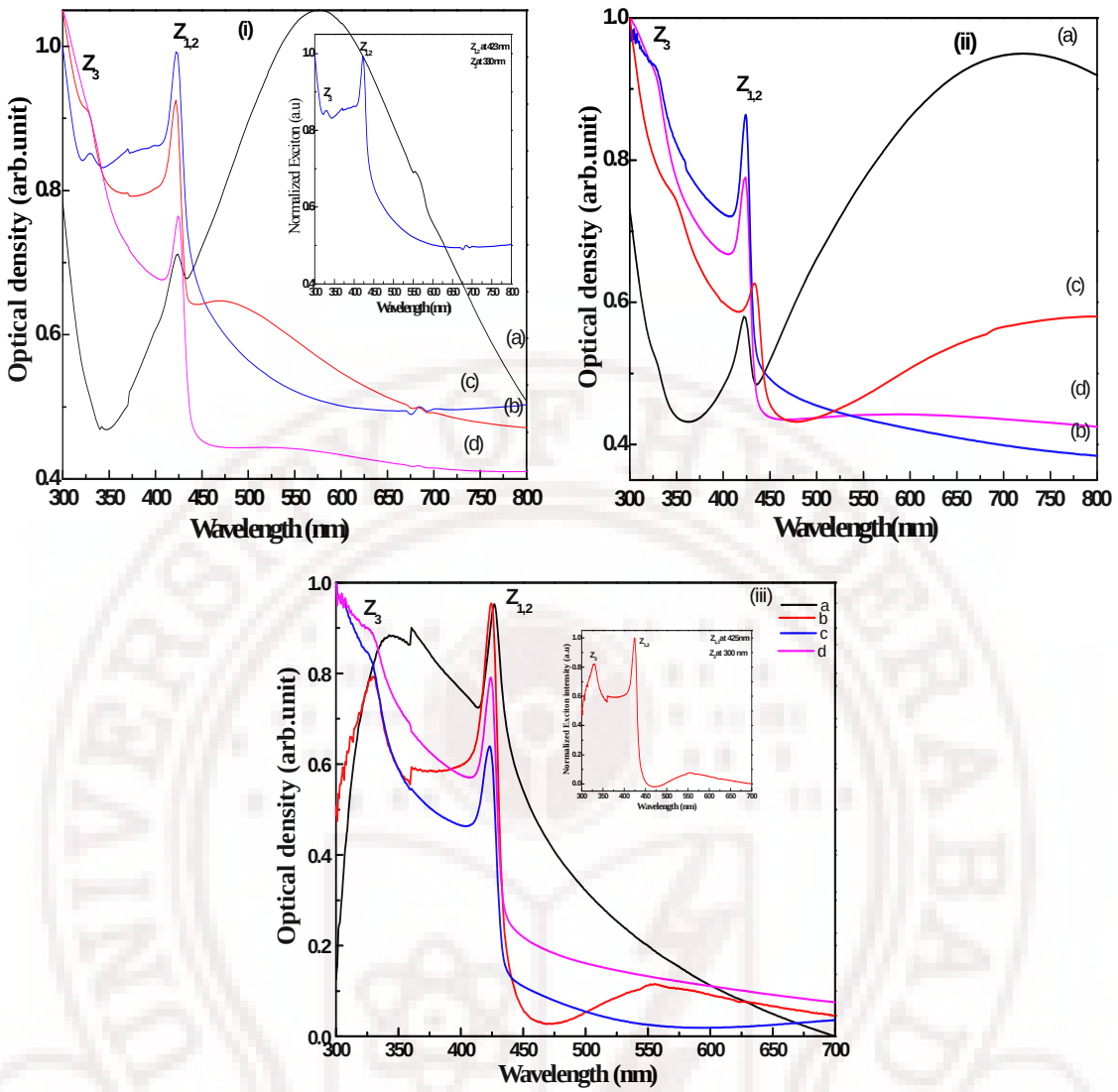

Figure 4.11: Optical absorption of spectra of 5 nm thickness of (i) $Ag_{0.95}Cu_{0.05}$ (ii) $Ag_{0.90}Cu_{0.10}$ and (iii) $Ag_{0.80}Cu_{0.20}$ thin films iodized at (a) 15, (b) 30, (c) 60 and (d) 180 min. These films show surface plasmon to exciton transition.

The evolution of $Z_{1,2}$ and Z_3 exciton absorption bands was observed at about 422 nm and about 330 nm which correspond to the two spin orbit components of exciton excitation in AgI as shown in figure 4.11(i), (ii) and (iii). The observation of these features is indicative of conversion of Ag to AgI upon exposure of the Ag nanoparticles to the I_2 vapor [41-43].

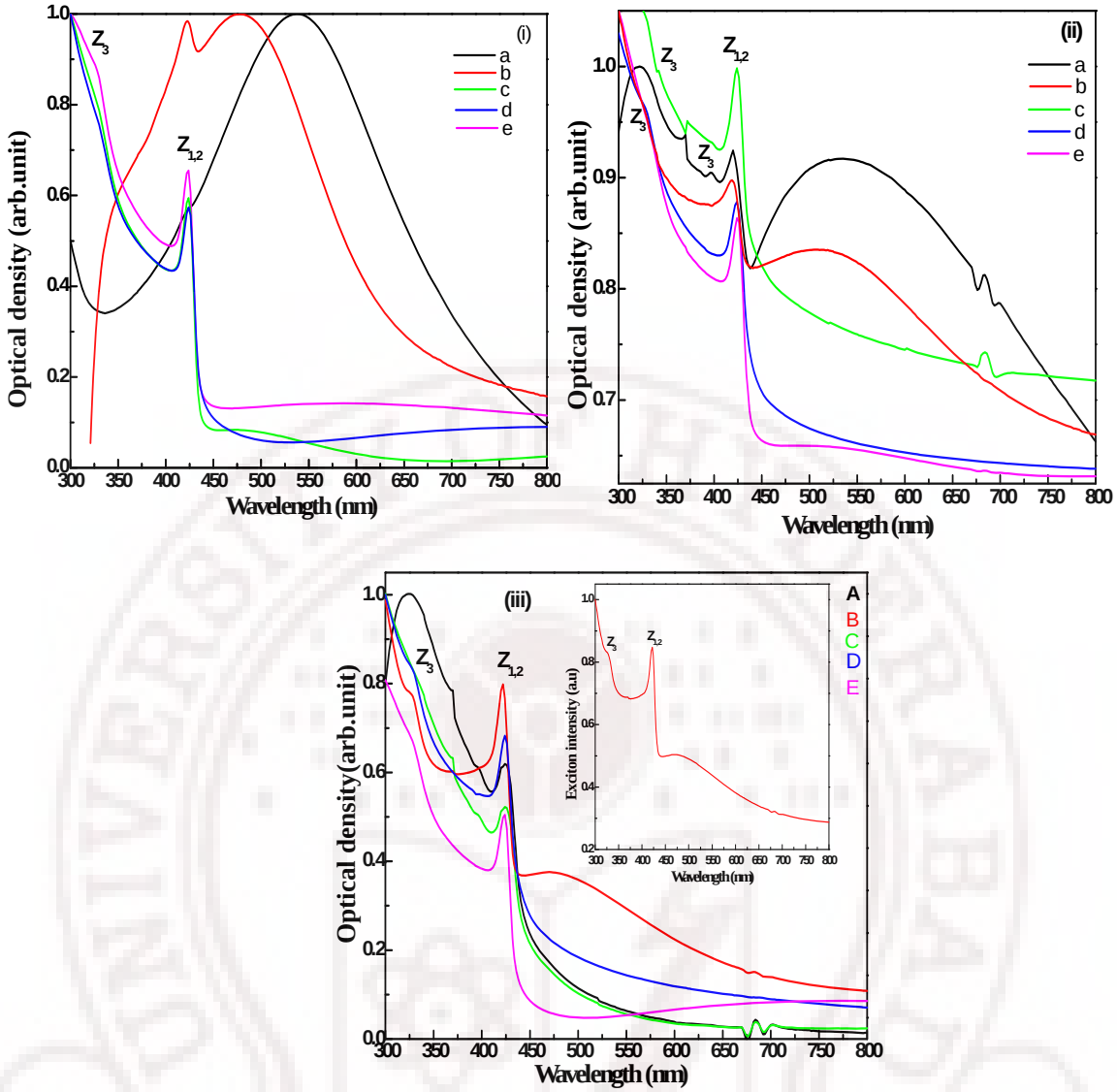

Figure 4.12: Evolution of the exciton absorption bands for 15 nm thickness Ag films after exposure to I_2 vapor. (i) $Ag_{0.95}Cu_{0.05}$ (ii) $Ag_{0.90}Cu_{0.10}$ and (iii) $Ag_{0.80}Cu_{0.20}$ thin films iodized at (a) 15(b) 30, (c) 60 (d) 180 and 360 min. The kinks at 700 nm are due to lamp change.

With gradual uptake of iodine, the SPR of the Ag nanoparticles, being sensitive to changes in the refractive index of the medium at or near the particle surface, shifts steadily to longer wavelengths as seen in the inset shown in figure 4.11. Simultaneously, figure 4.11(i) (a), (ii) a and (ii) a shows the short time (15 min) iodized 5 nm Ag film which exhibit a gradual development at 420 nm which is $Z_{1,2}$ exciton energy (2.919 eV) determined from the optical absorption spectrum of γ-AgI (Zincblende structure) [7-10,15]. The SPR peak maxima red shifted towards the higher wavelength at 550 nm due to the formation of core shell AgI nanoparticles. This type of mixed plasmon-exciton formation is called *'plexciton'* observed in short time iodized films [44]. Plexciton formation is the direct evidence of plasmon-exciton transition in iodized Ag thin films.

Thus the Ag/AgI interface forms during short time iodization where AgI acts as a dielectric matrix in which Ag particle embedded or aggregated on the surface shift the SPR to high wavelength redshift. During the initial stages of iodization the surface roughness (RMS) which eventually increases due to iodine molecule get diffused (lateral diffusion) in to the Ag surface and forms Ag-I bonds (physisorption) it causes the strain development in the structure as seen in XRD results.

Figure 4.11 (b-d) shown upon prolonged iodization of Ag films at (30-180 min) it clearly seen in strong peak development is observed at about 330 nm Z_3 exciton for 30 min iodized, which is close to the absorption peak wavelength of Z_3 exciton for γ-AgI zincblende crystal as well as redshift. At 60 min iodized sample, the $Z_{1,2}$ exciton absorption becomes very sharp and also band edge splits faintly into two bands. With progressing iodization the $Z_{1,2}$ exciton band grows to a single band with redshift and Z_3 band get faint due to the Frenkel defects [45,46] and strain present in the systems this causes the change in the exciton peak position and increase of absorption peak intensity. The exciton peak shift towards longer wavelength (425 nm) may be mainly due to the increase of particle size and aggregation of nanocrystals. Also, a splitting of the $Z_{1,2}$ exciton bands was clearly observed in the small crystallite region. The redshift arises from a decrease in the quantum confinement of exciton. The faint double peak structure arises from a splitting of the doubly-degenerate valence band Γ_8 with light and heavy hole masses due to the difference of quantum size effects, or some crystal-field change at the crystallite surface (for example, surface reconstruction or surface defects) or from the appearance of the wurtzite modification (β-AgI) in the small crystallite region. The β-AgI bulk crystal shows the $W_{1,2}$ and W_3 exciton lines at 420 nm and 414 nm, respectively. Since the observed exciton absorption peaks appear at longer wavelength than the W_3 exciton band in AgI bulk, the appearance of wurtzite structure can be ignored. The intensity of this peak gradually increases with increase in iodization time, the strong peak at 330 nm characteristic of γ-AgI in copper substituted films. In comparison with work of Cardona et al, [47] the evolution of 420 nm peak due to dipole forbidden $4d^{10}$-$4d^9 5s$ transition in Ag, allowed by the tetrahedral symmetry of Ag^+ ion in the zincblende AgI structure and the resultant p-d hybridization and the 320 nm peak due to spin- orbit splitting with increasing iodization time have been attributed to $Z_{1,2}$ and Z_3 excitons respectively. The top of the valance band (Γ_{15}, Γ referring to the centre of the Brillouin zone and the subscript 15 referring to the overall (orbital + spin) degeneracy) is triply degenerate without spin-orbit interaction in the zincblende structure. This degeneracy is

reduced by spin-orbit splitting to a double degenerate state (Γ_8) and a singlet (Γ_6). The Γ_8 doublet gives the $Z_{1,2}$ peaks whose degeneracy is lifted due to a strain field exchange at the crystallite surface due to surface reconstruction or surface defects.

Figure 4.12 (i), (ii) and (iii) show evolution of optical absorption and development of exciton spectra of the 5%, 10% and 20% copper substituted 15nm thick $Ag_{1-x}Cu_x$ films deposited on fused silica substrates. The short time iodized (30 min) Ag-Cu films have shown the immediate/rapid development of the $Z_{1,2}$ exciton peaks at 423 nm along with Surface plasmon peak and no evidence of 330 nm Z_3 band suggesting that the Cu substitution and higher thickness delay the Z_3 formation due to surrounding inorganic Ag-Cu matrix strongly restricting further aggregation during the formation of AgI crystallites. More interestingly, this saturation behavior clearly shows the strong particle size control particularly during the short-term iodization regime and exhibits the anisotropic growth. The exciton absorption observed even in the amorphous state points to a very small exciton radius of AgI (0.61 nm) so small that it could exist within the short range order itself. However, no trace of CuI exciton was observed even (80:20 wt ratio). Probably Cu^+ ions are dispersed as monomer in the amorphous environment, thus maintaining the electrical neutrality of the system each Ag^+ ion is replaced by Cu^+ ions. Figure 4.12 (ii) and (iii) (b-e) 30-360 min iodized sample shown a sharp peak at 424 nm (band gap) ascribed to the $Z_{1,2}$ excitonic absorption of AgI and a faint band at 260 nm (band gap) were observed in the bulk spectrum. The iodized AgI films show a number of intrinsic defects that should be expected to be formed in the grain at the grain boundaries, on the surface or at the interface, invariably leading to energy levels within the energetically forbidden gap. These separate defects levels can extend to form an energy band overlap with the conduction band or valance band of AgI, thus giving rise to band tail states. It is well known that a decrease in particle size generally results in the blue shift of this peak due to enhanced quantum confinement. However the red shift is not too surprising when the effect of lattice composition (figure 4.3) is taken into account. According to the bonding orbital theory [43,48] of band structure for covalent semiconductors, such as AgI (its band structure is characterized by strong p-d hybridization- even stronger in CuI), energy bands are derived from the extension of molecular orbitals in unit cells. As the lattice parameter decreases, the overlap between the MOs in adjacent cells increases, leading to broadening of the band leading to a decrease of band gap, as observed in many semiconductors and insulators. Moreover, a decrease in lattice parameter results in reduction of electron-hole distance in the exciton, leading to strong electron-hole

interaction and a larger binding energy of the exciton. These Cu^+ ions may also absorb light at their respective exciton energies, but this absorption might be irretrievably buried inside the strong absorption of the host Ag^+ ions, the small ionic radius of the Cu^+ ions being considered favorable for the substituting Ag in a unique manner. Thus the important role for Cu is in the rapid nucleation of the metal halide thus providing a new method for obtaining high densities of small nano clusters in a matrix free approach. These results clearly points to a thickness and composition induced transition from γ-AgI to β-AgI upon increasing iodization time. With increasing film thickness, the $Z_{1,2}$ exciton peaks becomes broad and red shifted, which could be a reflection of the decrease in the quantum confinement of excitons and a tendency towards formation of bulk band structure [9].

The plot of the exciton $Z_{1,2}$ and Z_3 peak maxima wavelength shift and band gap (Eg) vs iodination time for all Cu substitution as shown in figure 4.13. Figure 4.13(i) and (ii) reveal the AgI growth and saturation of excess peak wavelength below and above 60 min iodination suggesting that the surrounding inorganic Ag-Cu matrix strongly restricts the further aggregation and ripening of the as formed AgI crystallites. More interestingly this saturation behavior demonstrates strong particle size control particularly during the long time iodination regime and inhibits invariably the anisotropic growth and surface roughness increases as shown in figure 4.6 and 4.7. The exciton peak maxima of 5nm and 15nm thin films shows the non-linear behaviors with increasing Cu concentration and film thickness due to kinetics of short time iodination for all concentration. The 5% of Cu doped 5 and 15 nm Ag films exhibit exciton peak maxima at 420 nm upon 30 min iodization (called short time iodization) consist of the emerging exciton with broad Ag surface plasmon peak. As iodination time increases the exciton maxima also increases towards higher wavelength which gives rise evidence for AgI shell thickness increase and then finally exciton maxima get saturated when fully converted into AgI this transformation depending upon the Cu concentration. The exciton position is seen to vary by over 15 nm for different Cu concentrations. In view of the nanometer dimensions of the AgI shell in the Ag@AgI particles, most of the constituent of the AgI particles reside at or near the inner or outer surface of the AgI shell [29,31,37]. Accordingly, surface effects are generally accentuated and variability in the exciton peak position much higher than that observed in bulk AgI is not surprising. Thus the presence of Cu results in the renormalization of the static dielectric constant of AgI and thereby stabilizing the low-dimensional quasi-free nanoparticles in this matrix free approach.

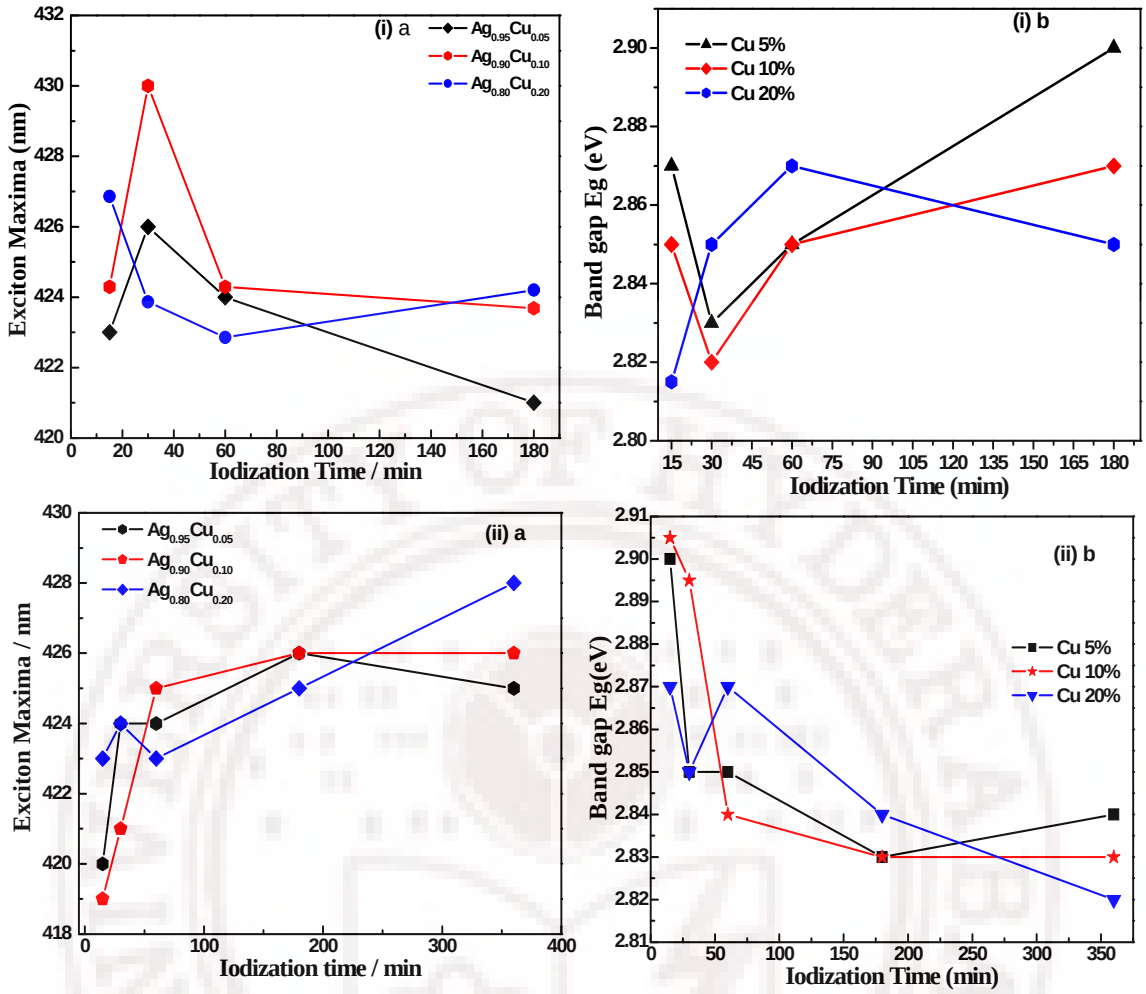

Figure 4.13: Band gap (Eg) and corresponding Exciton peak maxima as a function of Cu substitution and Iodization time (min) for Ag-Cu films (i a ,b) 5 nm and (ii a, b) 15 nm thick.

The band gap energy is determined from the expression of the semiconductor with a direct band gap, $(\alpha h\nu)^2 = B(h\nu - E_g)$, where α is the absorption coefficient, $h\nu$ is the energy of the incident light, B is the parameter that depends on the interband transition probability, and E_g is the energy gap. The plot of $(\alpha h\nu)^2$ *vs* incident photon energy $h\nu$ is found to be a straight line. The intercepts of the linear plots on the energy axis at $(\alpha h\nu)^2=0$ gave a band gap value determined for both $Z_{1,2}$ excitons. Initially the short time iodized AgI band gap shows a band gap 2.90 eV which is higher than bulk band gap of 2.82 eV for γ-AgI at 300 K [49]. When iodination time is increased the band gap exponentially decreases and upon further longer exposure to iodine vapours band gap asymptotically approaches a constant value due to increase of particle size as well as aggregation. The fluctuation of the band gap during the initial iodination period (30 min) reflects the presence of the partially iodized Ag-Cu island clusters. In 5 and 15nm thick AgI films band gap varies between 2.9eV to 2.82 eV for all Cu compositions which show strong

reduction in quantum confinement effect. The variation could arise from differences in the final shell thickness obtained and the overall diameter of the Ag@AgI nanoparticles. The exponential decrease in the energy is the trend expected of AgI nanoparticles whose diameter systematically increases, which is consistent with increasing AgI shell thickness as the Ag + I_2 reaction time.

Band gap fluctuations are a direct indication of local composition fluctuations and lattice parameter changes in AgI upon Cu substitution. The main reason for composition fluctuations could be the core-shell nature of the nanoparticles and the random positions of Cu in the AgI matrix. Semiconductor band gaps experience an analogous exponential-like decrease in band gap as the diameter of the quantum dot is increased. Accordingly systematically variation of shell thickness and core material or size over a larger range should afford an opportunity to tune the band gap of the AgI [50,51].

4.6. Photoluminescence study of Vacuum Evaporated nanostructured AgI thin films

4.6.1 Room temperature photoluminescence study of Cu doped AgI thin films

Figure 4.14 shows the room temperature photoluminescence (PL) spectra of 5 and 15 nm thick Cu doped AgI thin films deposited on fused silica substrates. A casual comparison of PL intensities with those observed by earlier workers [15,38,41.42,52] at liquid He temperatures at once reveals that the present PL is unusually intense-a feature attributable to the precursor preparative technique, film thickness and growth mode, dopant and the iodization technique employed in the present work. The emission peak appears at the same wavelength as that of the $Z_{1,\ 2}$ exciton bands as described in the optical absorption spectra. Thus the photo excited electron at the conduction band edge tends to recombine *directly* with holes at the valance band edge. This process results in the emission of a PL photon having energy *almost* equal to that of the band gap. For infinite separation between donor and acceptor the energy of the peak of the luminescence should be $E(\infty) = E_g - E_D - E_A$. It is well known that in silver halides interstitial silver atoms and clusters are produced under illumination. Such defects may act as shallow exciton traps and cause structure in the PL spectrum as observed [23,42,45,53]. The recombination rate is increased with increasing iodization time and Cu doping as seen from PL spectra figure 4.14. Even in direct band gap semiconductor materials such as AgI a typical electron-hole recombination takes place a few nano

seconds. The typical time for an electron or hole to undergo scattering with a photon is much shorter 0.1-10ps. Thus one normally sees effects of recombination but not of electron/hole-photon scattering in the observed PL spectra recorded in the continuous-wave mode.

Figure 4.14 (i) show the PL spectra of short time 30 min iodized $Ag_{1-x}Cu_x$ (x= 0.05, 0.10 and 0.20 wt %) thin film thickness of 5nm deposited on fused silica substrates at room temperature. The PL measurements have been performed by tuning of the emission energy in the tail of the absorption peak, ranging from 3.0 to 2.64 eV. The room temperature PL spectrum is characterized by an intense luminescence centered at 2.82, 2.83 and 2.85 eV for three different Cu concentrations. This luminescence is on a tail extending up to about 2.64 eV, and it is also accompanied by several shoulder components. The peak energy of 2.82 eV is corresponds to the $Z_{1,2}$ exciton energy determined from the optical absorption spectrum of γ-AgI (Zincblende structure) at room temperature. With increasing Cu concentration exciton luminescence intensity increases and corresponding band position increases from 2.82 to 2.85 eV towards blue region. This broad band may be assigned to radiative decay of γ-AgI excitons trapped by AgI/Ag surface or interface [9,12,15].

The observation of gradual evolution of the optical band gap and the corresponding emission spectra for γ-AgI the confinement effects in short time iodized AgI thin film. In particular, the higher energy portion of the tail overlaps in energy of the W_1 exciton absorption, polytype-related exciton absorption and Z_3 exciton absorption. Therefore, the higher energy portion (of which intensity is decreased by re-absorption) may arise from several kinds of free-excitons luminescence components and it may be assigned to radiative decay of these excitons. The corresponding free exciton luminescence decay within several nanoseconds, while the PL components below 2.9 eV remains after 30 ns. This suggests that the PL component below 2.919 eV arise from exciton trapped at Frenkel defects or impurities. Equally, nanoparticles of different size distributions could also account for the observed PL spectra especially for short-time iodization.

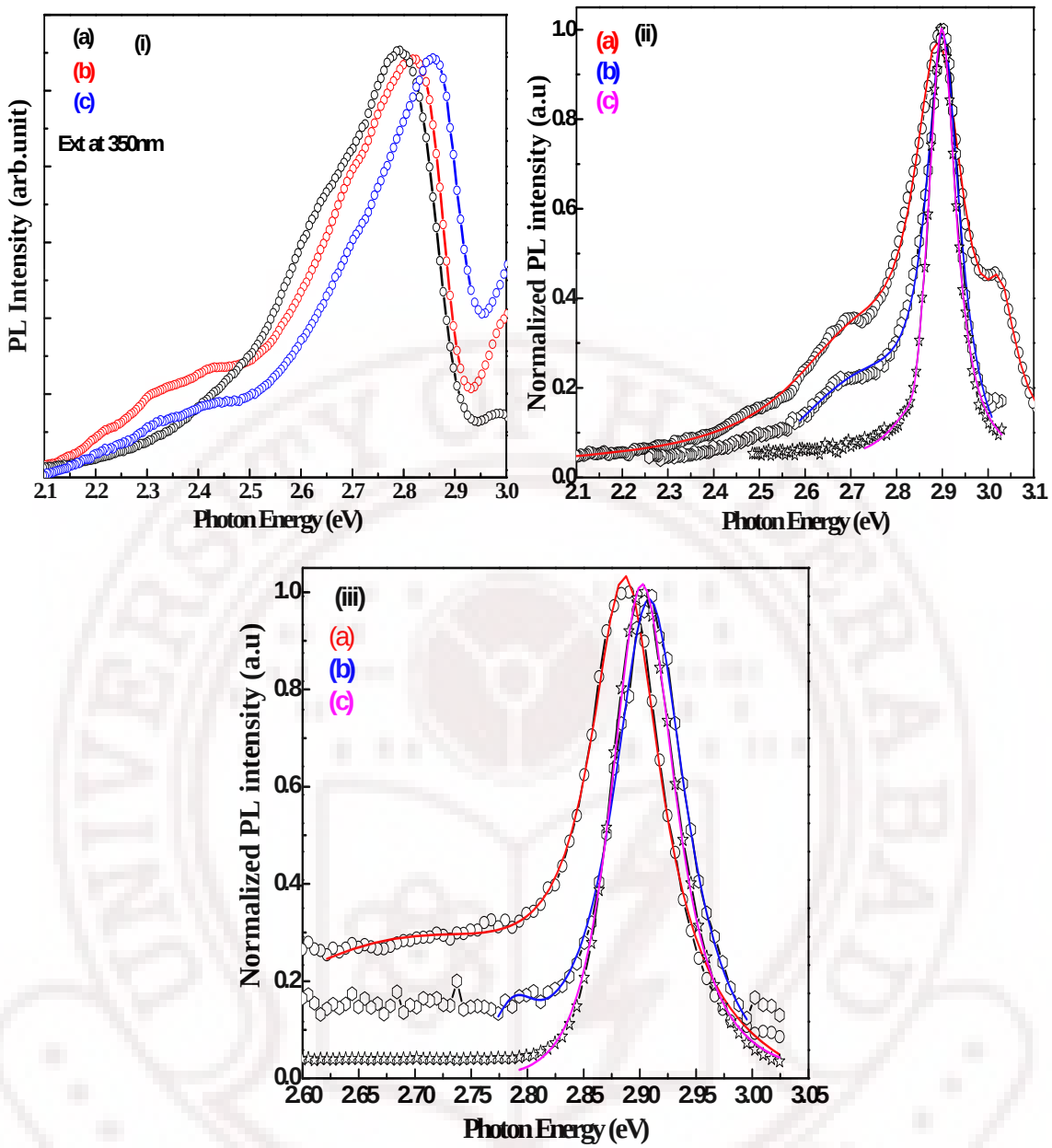

Figure 4.14: Emission spectra of 5 nm thick $Ag_{1-x}Cu_x$ thin films iodized for (i) 30 min iodized, (ii) 60 min iodized and (iii) 180 min. (a) Cu 5%, (b) Cu 10% and (c) Cu 20% (Cu substitution is atomic wt %). Excitation wavelength is 350 nm.

Figure 4.14(ii) show the PL spectra of 60 min iodized 5 nm Ag-Cu thin films, excited at 350 nm. The peak energy of 5% copper doped AgI shows at 3.01, 2.89 and 2.7 eV. In which the PL peak centre energy gap is 2.89 eV which is higher than 2.82 eV observed at RT. The energy gap shifts from 2.82 eV to 2.89 eV that is, a blue shift. Even after 60 min iodization tail remains same for 5% and 10% Cu concentrations. A sharp luminescence appears at 2.91 eV, which is slightly higher than the band gap obtained for 5 and 10% Cu doped AgI thin films. With increasing Cu concentration up to 20%, the PL line width (FWHM) is 75 meV where as in 5 and 10% Cu doped AgI PL line width

(FWHM) are 140 and 90 meV figure 4.15(iii). We observed the emission peak at 2.91 eV characteristic of free exciton formation in both films. The enhanced luminescence and spectral narrowing have been observed at high excitation wavelength (350 nm).

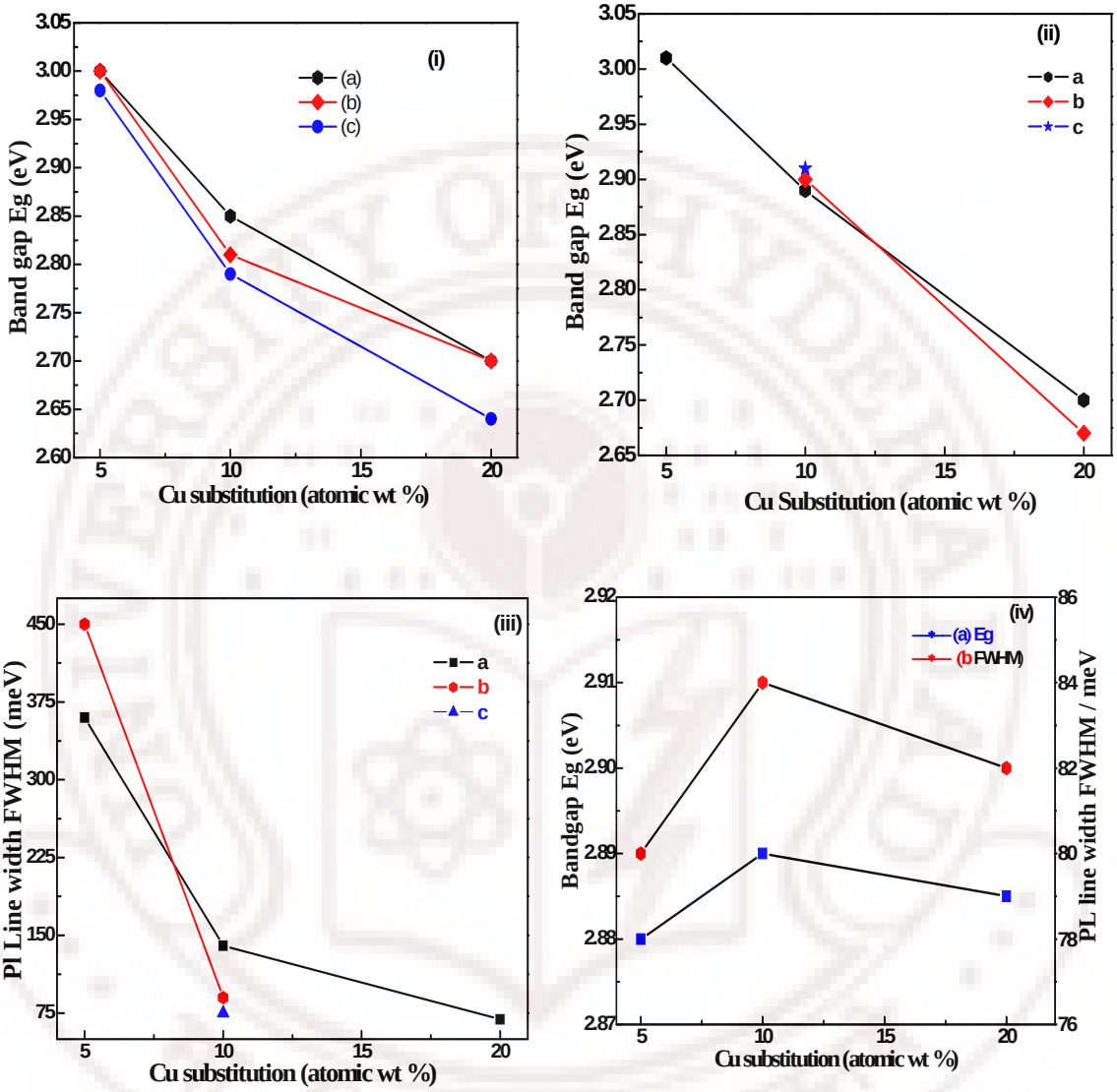

Figure 4.15: Cu concentration dependence of band gap (eV) and PL linewidth (eV) of 5nm thin $Ag_{1-x}Cu_x$ { x is (a) Cu 5%, (b) Cu 10% and (c) Cu 20% } films for different iodization times. **(i)** iodized for 30 min **(ii)** iodized for 60 min **(iii)** PL line width with different Cu doping $Ag_{1-x}Cu_x$ thin films iodized for 60 min **(iv)** 180 min iodized samples. Note that (ii), (iii) the number of PL peaks reduce from three to one upon progressive iodization suggesting the formation of AgI nanostructure.

Figure 4.14 (iii) traces the gradual evolution of the strong emission spectrum and corresponding optical band gap together with the development and disappearance of the phonon side bands. The corresponding emission spectra for AgI is very significant from

the point of view of particle growth and the associated quantum size effects in AgI semiconductor. Thus during PL of Cu-substituted AgI thin films, phonons form a minor non-radiative channel for energy transfer during recombination in sharp contrast to the results obtained earlier on iodized quasi-amorphous Ag-Cu films [13]. The enhanced trapping of the shallow and deep trap states and the limit of saturation can be visualized from the increase in the full width at half maximum (FWHM) of the in-homogeneously broadened sub-bands as shown in figure 4.15 (iv) Also the strain induced size control by Cu helps in the confinement of excitons in AgI nanoparticles and the in-homogeneity of the PL peak observed even at room temperature represents the particle size distribution as reflected by its FWHM.

The PL spectra of 15nm thick $Ag_{1-x}Cu_x$ (x=0.05,0.1and 0.2) iodized for 60 and 360 minutes show better resolved spectra with fewer components with the latter set showing a single sharp PL feature at 2.91 eV that shows concentration dependent blue shift. Seen in the context of microstructure revealed by AFM it can be said that the homogeneity of the films together with optimum interparticle separation is probably responsible for these observations. While the 5 nm films with islanded structure and strong interfacial strain leads to size distribution of nanoparticles with the possibility of energy distribution of exciton traps the 15 nm films seem to consist of uniform-sized nanoparticles resulting from relatively higher concentration of Cu modifying the growth process from islanded to layer type. The systematic blue shift (~0.1 eV) observed even at 300 K (as against earlier observations at 4 K) suggests weak confinement effect [41,42]. Thus optimally thick AgI films with Cu substitution to the extent of 0.05-0.2 have helped realize interesting optical properties that directly result from quantum-confined excitons. These interesting observations arise from the crucial role played by Cu in controlling Frenkel defect concentration in AgI besides reinforcing the Ag-I bond seen through a reduced zincblende lattice parameter and most importantly at the microscopic level causing a pressure effect on the electronic band structure thereby enhancing the oscillator strength for absorption and luminescence [9,15].

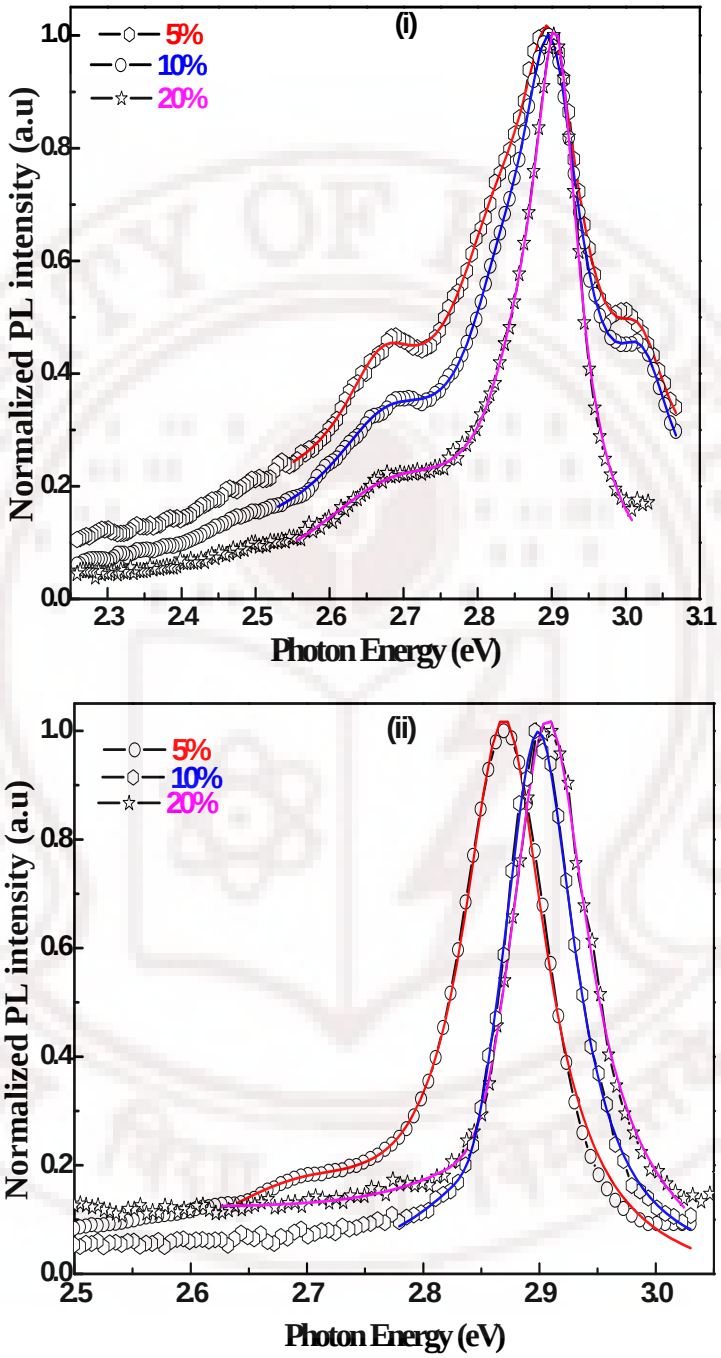

Figure 4.16: Photoluminescence spectra of (300 K) of the quasi free AgI nano particles formed during the iodization of Cu doped as deposited thin films (a) $Ag_{0.90}Cu_{0.05}$, (b) $Ag_{0.90}Cu_{0.10}$ and (c) $Ag_{0.80}Cu_{0.20}$ thickness of 15 nm.**(i)** iodized for 60 min and **(ii)** iodized for 360 min.

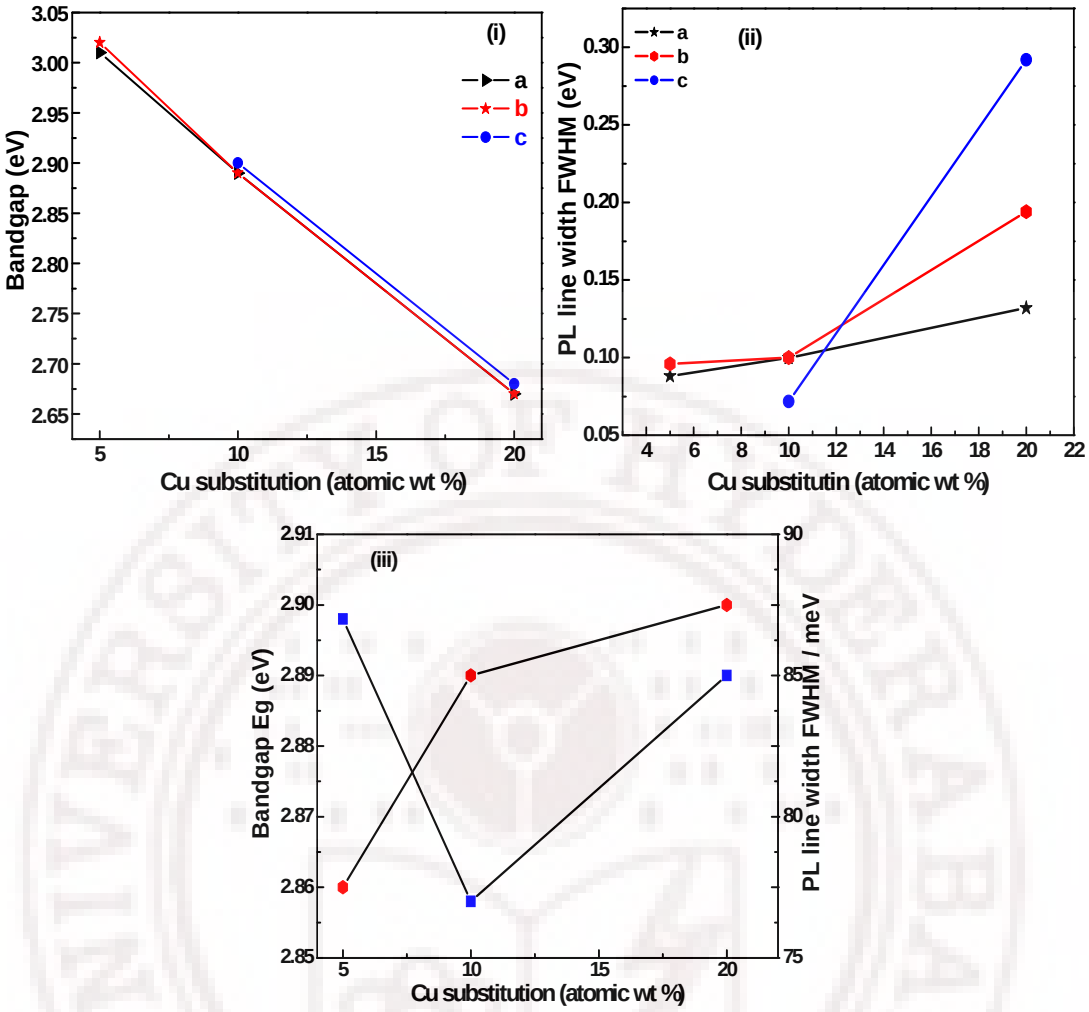

Figure 4.17: Show the 15nm AgI thin film observed band gap (Eg) and PL line width FWHM (eV) as a function of Cu concentration and iodization times. **(i)** (a) Cu 5% , (b) Cu10% and (c) 20% iodized at 30 min **(ii)** (a) Cu 5% , (b) Cu10% and (c) 20% iodized for 60 min **(iii)** 60 min iodized AgI PL line width with different Cu doping **(iv)** (a) 360 min iodized sample (a) band gap and (b) FWHM.

4.7 Summary

We have fabricated the co-deposited Cu substituted Ag films with thickness upto 15nm on fused silica substrate by co-evaporation method. The systematic iodization of Ag-Cu alloy films has apparently yields discontinuous films through island formation and shows the AgI particle growth leading to the long term stable γ-AgI phase. Optical absorption and PL characterization of all these AgI, Ag (Cu) I thin films have shown certain aspects of quantum confinement effect in AgI thin films. Cu substitution enhances the excitonic PL through quasi free AgI nanoparticles formation.

Although the co-evaporation method applied to Cu substituted Ag films upon iodization revealed the enhanced photoluminescence and band gap changes the long-term iodization creates locally iodine rich regions which readily favour formation of wurtzite impurity phase coexisting with the zincblende phase. To overcome this limitation in achieving the goal of stabilization of robust gamma AgI structures even upon long-term iodization we thought it appropriate to resort to co-sputtering technique to fabricate precursor Ag-Cu films and iodize them. These attempts and observations are described and discussed in Chapter 5.

References

1. C.F. Bohren, D.R. Huffman, *Absorption and Scattering of Light by Small particles*, John Wiley& Sons, New York, (1983).
2. Kreibig, U.; Vollmer, M. "*Optical properties of metal cluster*"; Springer: Berlin, 1995.
3. G. Mie, *Ann. Phys.* **25**, 377 (1908).
4. P. B. Johnson and R.W. Christy, *Phys. Rev. B*, **6(12)**, 4370 (1972).
5. Stephan Link and Mostafa A. El-Sayed. *J. Phys. Chem. B,* **103**, 8410 (1999).
6. Cecilia Noguez, *J. Phys. Chem. C.* **111**, 3806 (2007).
7. M.Gnanavel, D. Bharathi Mohan, C. S. Sunandana, *Thin Solid Films,* **517**, 1058 (2008).
8. D. Bharathi Mohan and C.S.Sunandana, *J. Appl. Phys,* **100**, 064314 (2006).
9. P. Senthil Kumar and C. S. Sunandana, *Nano Letters,* **2(4)**, 431-434 (2002).
10. D. B. Mohan, V. S. Reddy and C. S. Sunandana, *Appl. Phys. A,* **86**, 73 (2007).
11. P. Senthil Kumar and C. S. Sunandana, *Thin Solid Films*, **323**, 110-114 (1998).
12. M.Gnanavel and C. S. Sunandana, *Proc. SPIE*, 7394, **73942D** (2009).
13. S R. Galbadrakh, V. K. Miloslavskii, and U. Mayer, *J. Applied. Spectroscopy*, 59(1-2), 139 (1993).
14. D. Bharathi Mohan, C.S. Sunandana, *J. Phys. Chem. Solids*, **65**, 1669 (2004).
15. K. Suri and H. K. Henisch, *Phys, Stat. Sol. (b)* **44**, 627 (1971).
16. K. Shahi, W. Weppner and A. Rabenau, *Phys. Stat. Sol. A*, **93**, 171 (1985).
17. F. N. Rhines, Phase diagrams in Mattallurgy, McGraw-Hill, New York, p-54 (1956).
18. Stephen Hull, *Rep. Prog. Phys*, **67**, 1233 (2004).

19. C. Kittle. *Introduction to solid state physics*, 7th edition, *Wiley*, 1996.
20. D. Bharathi Mohan and C. S. Sunandana, *J. Naosci. Nanotech,* **5**, 1-5 (2005).
21. S. Mochizuki and F. Fujisshiro, J. Phys.: Condens. Mater, 15, 5057 (2003).
22. C. Liang, K. Terabe, T. Tsuruoka, M. Osada, T. Hasegawa, *Adv. Funct. Mater*, **17**, 1466 (2007).
23. S. Mochizuki and F. Fujisshiro, Phys. Stat. Sol. (c), 10, 3586 (2006).
24. P. Senthil Kumar, P. Babu Dayal and C.S. Sunandana, *Thin Solid Films,* **357**, 111 (1998).
25. S.C. Kuiry, "*Studies on Kinetics of Iodide Films Growth on Pb, Ag and their Doped Varieties in Iodine Atmosphere", Ph.D. Thesis,* IIT, Kharagpur, India, 1995.
26. Hao Chen and Jian-Min Zuo, Acta Materialia, 55, 1617 (2007).
27. H. Han and T. L. Alford, J. Phys. D: Appl. Phys. 41, 155306 (2008).
28. R. Guptha, M. J. Dyer and W. A. Weimer, J. Appl. Phys, 92, 5264 (2002).
29. S. Kapoor, R. Josi and T. Mukherjee, *Chem. Phys. Lett. 354*, 443 (2002).
30. M. Grzelczak, Ana sanchez-Lglesias, Bentio Rodriguez- Gonzalez, Ramon Alvarez-Puebla Jorge Perez-Justle and L M Liz- Marzain. *Adv. Funct. Mater*, **18**, 3780 (2008).
31. Choon Hwee Bernard and Wai Tip Fan, *J. Phys. Chem. C*, **111**, 2953 (2007).
32. Cecilia Noguez, *Optical Materials,* **27**, 1204 (2005).
33. J. Gonzalo, D. babonneau and C. N. Afonso, *J. Appl. Phys*, **96**, 5163 (2004).
34. Soumya Nag. C. Kristopher. Mahdak. D. Arun. G. Smita. Pushan Ayyub. R. Banerjee, J. Mater. Sci, 44, 3393 (2004).
35. M. Hirai and Ashok Kumar, J. Appl. Phys, 100, 014309 (2006).
36. Ganesh Suyal, *Thin Sold Films*, **426**, 53-61 (2003).
37. T. H. Wei, C. W. Chen, L.C. H. Wang, P. L. Tu, T, C. Wen, *Journal of Luminescence,* **128**, 161-165 (2008).
38. G. Mshvelidse, O. Gogolin, E. Tsitsishvili, Ch. MaÈrkle J.S. Chadha, A. Hepting, F. Gindele, W. Petri, W. Send, D. Gerthsen, U. Woggon, and C. Klingshirn, *Phys. Stat. Sol (b)*, **207**,369 (1998).
39. Sihai Chen, Takashi Ida and Keissaku Kimura, *J. Phys. Chem. B*, **102**, 6169 (1998).
40. Takenari Goto and Yoshihiro Sasaki, *J. Phys. Soc. Japan*, **53 (12)**, 4432 (1984).

41. S. Mochizuki and K. Umezawa, *Physics Letters A*, **228**, 111 (1997).
42. S. Mochizuki and Fumito Fujishiro, *J. Phys.: Condens. Matter*. **16**, 3239 (2004).
43. S. Kondo, T. Itoh, and T. Saito, *Phys. Rev B,* **57(20),** 13235 (1998).
44. Nche T. Fofang, Tae-Ho Park, Oara Neumann, Nikolay A. Mirin, Peter Nordlander, and Naomi J. Halas, *Nano Letter,* 8(10), 3481 (2008).
45. S. Mochizuki, Stacking faults and excitons in AgI, *Physica. B,* **308**, 1042 (2001).
46. O. Gogolin, G. Mshvelize, M. Schmidt, E. Tsitsishvili, O. Bakradze, A. Hepting and C. Klingshirn, *J. Lumin*, **102-103**, 451 (2003).
47. Manuel Caradona, *Phys. Rev,* **129(1)**, 69 (1963).
48. S. Ona, M. Kobayashi, H. Iyetomi and T. Tomoyose, *Solid State Ionics*, **139**, 249 (2001).
49. A. P. Marchetti, J. C. Hansen, S. Chen, M. Irving, R. Baetzold, and B. R. Sever, *Phys. Rev B,* **69**, 094107 (2004).
50. Q. Dai, Y. Wang, X. Li, Y. Zhang, J. Donald. Pellegrino, M. Zhao, B. Zou, J. T. Seo, Y. Wang, and W. William, Yu, *ACS Nano*, **3(8)**, 1518 (2009).
51. L. A. Swafford, L. A. Weigand, M. J. Bowers, J. R. McBride, J. L. Rapaport, T. L. Watt, K. Sriram, D. Leonard C. Feldman, and J. Sandra.Rosenthal, *J. Amer. Chem. Soc*. **128**, 12299-12306 (2006).
52. O. Husberg, H. Vogelsang, W. Von der Osten, *J. Luminescence,* **96**, 155 (2002).
53. S. Mochizuki and F. Fujishiro, *Phys. Stat. Sol. C*, **4**, 763, (2003).
54. T. Fujii, *Appl. Phys. Lett*, **84**, 855 (2004).

Chapter V

Cu enhanced quasi–free excitonic photoluminescence in Co-Sputtered $Ag_{1-x}Cu_X$ (x= 0.05, 0.1 and 0.2) thin films grown on fused quartz substrates iodized at ambient

5.1 Introduction

The Ag-Cu binary system is quite interesting because its alloys are classic examples of relative ineffectiveness of alloying and thus has the possibility of existing as metastable solid solutions over the entire range of compositions [1,2]. Earlier studies on Su-substituted AgI thin films by Senthil Kumar [3,4] and on nano/micropowders by Bharathi Mohan [5,6] and Shahi [7,8] have recognized the unusual effect of Cu on the physics of AgI. The most interesting aspect of these Ag-Cu solid solutions is the crucial role played by Cu in stabilizing the γ-phase of AgI when iodized and favourably enhancing the optical properties, as would be demonstrated in this chapter. As 30% vacancies in the fcc structure of Ag lattice, are available for the smaller Cu atoms the latter would control the motion of Ag^+ ions in the AgI lattice upon iodization thus ensuring stability of the zincblende structure reinforced at the Ag-I band level, with Cu induced reduction in lattice parameter.

In present study we have chosen the RF magnetron sputtering technique to prepare quasi amorphous Ag-Cu thin films in which Cu promotes layer type growth. The RF sputtered films will have more disorder and display stain-induced thin films growth depending upon the plasmon environment. This helps us to slow down the growth kinetics, thus providing an attractive controllable platform for studying formation of γ-AgI nano particle growth through structural, microscopic and optical probes. Relative to the sputtering of Undoped Ag and the evaporation of cu-doped Ag, the inherent disorder associated with sputtering coupled with the Cu-advantage are expected to result in delayed formation of gamma AgI upon iodization reducing the possibility of wurtzite formation even in thicker films. A dramatic consequence of these development is the observation of Cu-enhanced quasi-free excitonic photoluminescence in the blue region at 300K.

5.2 Deposition of Ag-Cu thin films

Thin Ag-Cu alloy (at wt % 5, 10 and 20 Cu) films thickness of 5 and 15 nm were deposited on fused silica substrates by RF Co-Sputtering method. The highly pure silver and copper metal targets (Aldrich, 99.999) are used for thin films depositions. The desired composition ratios of 5, 10 and 20 % (by atomic weight %) were obtained by placing appropriate size of Cu metal pieces placed on the top of the 2 inch Silver target(cathode dia: 2inch). This target was placed on the RF cathode for prior deposition. Here we have used up sputtering or sputter-up process to deposit Ag-Cu alloy films. Initially, the sputtering chamber was evacuated to a base pressure of $2x10^{-6}$ Torr after loading the cleaned substrates on to the substrate holder placed inside the vacuum chamber. All the films were deposited at a fixed RF power 15 W. A working pressure of 10 mTorr was constantly maintained using high pure argon (purity: 99.999%). The argon pressure was 10 sccm to achieve uniform rate of deposition. The target to substrate distance was fixed at 15 cm. It was observed that without any heating, the un-cooled substrate temperature increased to about 50-80^{o}C during the deposition, presumably due to ion bombardment. To avoid this undesirable substrate heating the substrate was kept at distances greater than 15 cm (even though scattering will be more). A few batches of thin films of pure Ag and of Ag-Cu (5, 10 and 20%) composition with thickness of 5 and 15 nm were deposited at room temperature and the rate of deposition was maintained constant during the entire depositions. The above conditions were found favorable for the formation of homogeneous, amorphous alloy films, and the actual composition ratio of coated films was analyzed using EDAX. The average thickness of the films was determined by using AMBIOS XP-1 profilometer.

Iodization: Iodization of these thin films was done an hour-glass type chamber. Iodine kept at the bottom of the lower half of the chamber sublimates at room temperature and slowly (over durations ~ tens of minutes) deposits on the $Ag_{1-x}Cu_x$ alloys films kept at the top of the chamber kept in a dark room [9-11]. Thus iodization was carried out for selected durations in the range of 30 to 720 min.

Substrate clean: Fused silica substrates were cleaned with piranha solution for 30 minutes (1:3 ratios: 30% hydrogen peroxide/concentrated sulfuric acid). *(Caution piranha solution reacts violently with most organic materials and should be handled with extreme care).*

Following the deposition of Ag-Cu thin films, a series of characterization techniques probing the structural, microstructure and optical properties of the films were performed. The stiochiometry of the films was established by Energy dispersive X-ray analysis (EDAX) analysis as *described in chapter 2*. The crystal structure of Ag, Ag-Cu and AgI films deposited on fused silica substrates as a function film thickness and Cu concentration were characterized using X-ray diffraction (XRD) technique. Following the XRD measurement, Dynamic Force microscope (DFM) was employed to measure the surface morphology of the films, which provided high resolution images. The room mean square roughness (rms roughness) was also determined using DFM. Optical band gap (Eg) of cation stabilized AgI films deposited on fused silica substrates were determined from the spectral absorption data obtained from UV-Visible spectrophotometer. The band development of iodized Ag-Cu films was monitored by the photoluminescence a study using a Fluorolog@-3 Spectroflurometer has been used in the UV/Visible range 300 to 800 nm with scanning rate of 200 nm/min at different excitation levels. A correlation between the structural, microstructural and optical properties of AgI films is discussed.

Table 5.1 Sputter deposition parameters of Ag and Ag-Cu thin films

Parameter	Value
Power density (W/cm2)	15 W
Substrate to target distance (cms)	15 cms
Working pressure (mTorr)	10 mTorr
Ar pressure (sccm)	10 sccm
Substrate types	Fused silica substrates.
Substrate temperature	RT

5.3 Structural characterization of γ-AgI films deposited on fused silica substrates

5.3.1 Lattice parameter and iodization time dependent strain measurement

The crystal structure of γ-AgI thin films grown at two different film thickness which is 5 and 15 nm with 5, 10 and 20% Cu concentrations on fused silica substrates were analyzed by XRD θ–2θ scans using Cu Kα radiation (λ=1.54Å) and are shown in figure 5.1,5.2. The as-deposited Ag and Ag-Cu alloy films were found to be quasi-amorphous in nature as revealed by XRD patterns without any detectable Bragg peaks [12-17]. Without any further post deposition treatment, these films were then iodized systematically to determine whether the disordered structure would yield stable γ-AgI thin films and offer a more fundamental platform to monitor the evolution of the crystal structure and electronic band structure (It is pertinent to think of nanostructure development as a nucleation and growth phenomenon from a frozen liquid). XRD pattern of 5nm Ag films iodized at 30 to 360 min shows figure 1 the gradual AgI structure development. Over short time iodization up to 30 min there is no evidence for AgI structure development observed because of RF sputtered Ag films will have more disorder and strain because of low thermal energy arresting surface diffusion on sputtered Ag particles and therefore it delays the formation of AgI which is favorable for stabilizing metastable γ-AgI structure [10,11]. After 30 min iodization, there is small peak development absorbed around 2θ=27.54 which is characteristic of γ-AgI. As iodization time is further increased from 30 to 180 min there is a gradual increase in the (111) plane intensity. The enhancement of intensity is due to increase of crystallinity suggesting that the rate of generation of γ-AgI nanoparticles in these 5 nm Cu doped Ag films is relatively higher than in 5 nm Undoped Ag films [9-11,17-20]. Upon further iodization for 180 to 360 min the (111) reflection intensity starts to decrease slowly, possibly due to small impurity phase formation which is wurtzite β (100) and β (101) at low Bragg angles. Figure 5.1 (ii) shows the structure of 15 nm Ag films iodized at up to 24 hr. Iodization of 15 nm thick Ag films shows amorphous nature an-indication of lack of development of long range order. Nano-crystallization begins after 60 min iodization of thick Ag films. After a prolonged iodization up to 360 min we could see only stable γ-AgI (111) plane with very high intensity Thereby the expected goal of delayed and disorder controlled fabrication of zincblende AgI films is achieved. In the case of long time iodization 24 hr mixed phase of minor wurtzite β-AgI phase with (100), (102) and (103)

planes and major zincblende phase (111) structures of AgI were observed for *thicker* films [10,11].

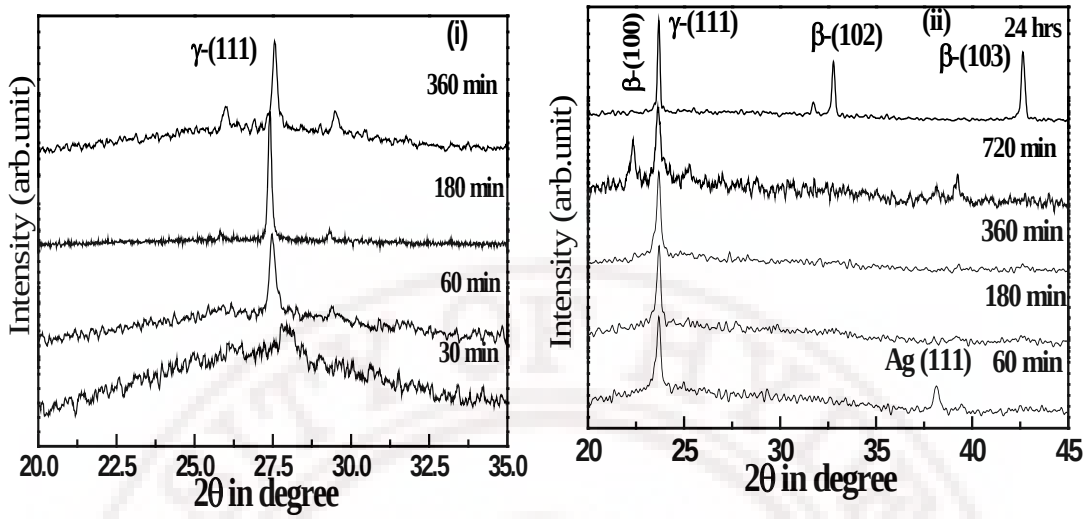

Figure 5.1: XRD pattern of **(i)** 5 nm **(ii)** 15 nm Ag thick films iodized for different times.

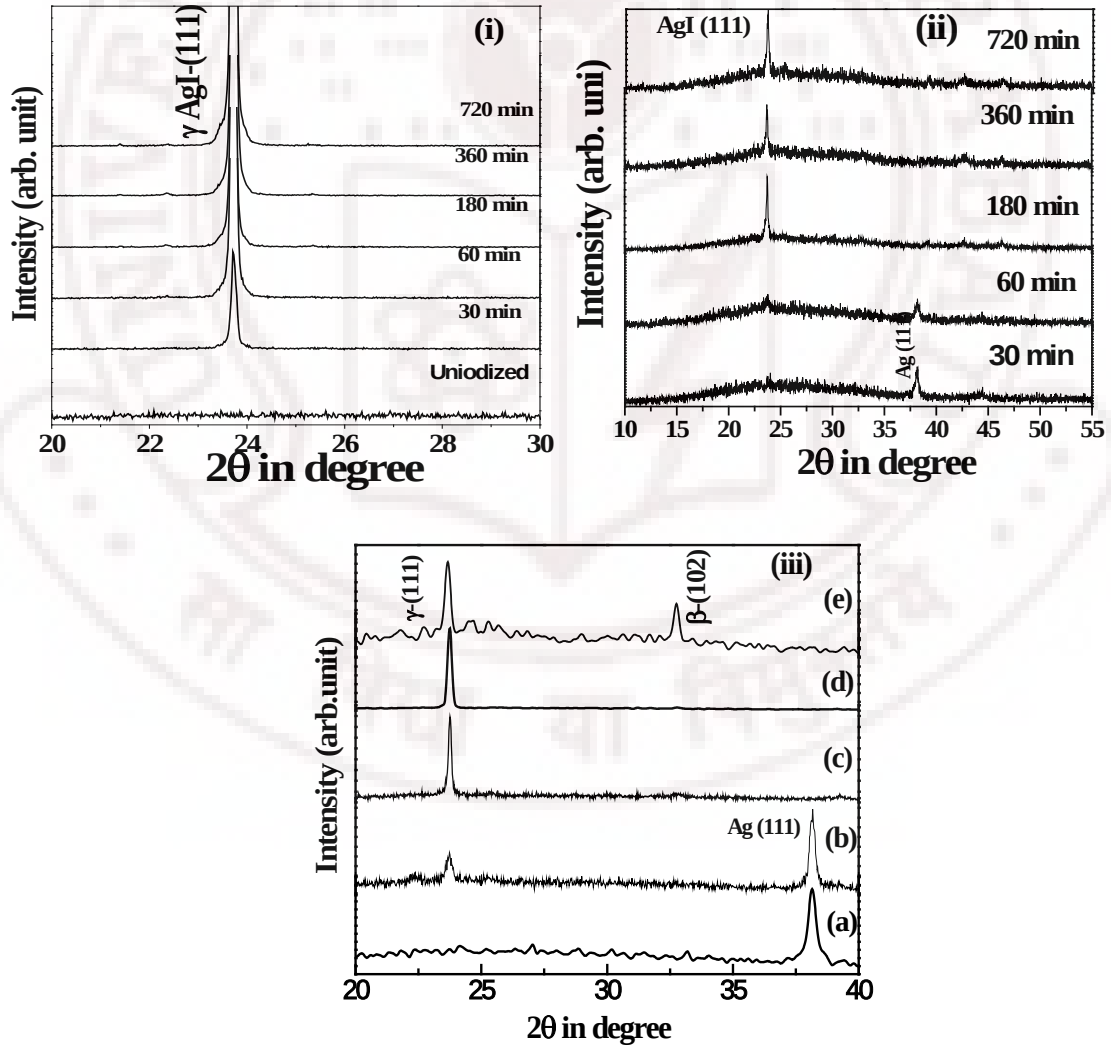

Figure 5.2: XRD pattern of 5 nm thick (i) $Ag_{0.95}Cu_{0.05}$ (ii) $Ag_{0.90}Cu_{0.10}$ and (iii) $Ag_{0.80}$-$Cu_{0.20}$ Ag-Cu films iodized for different times (a) 30 min (b) 60min (c) 180 min and (d) 360 min (e) 720 and (f) 24 hr.

The ratio R of the relative percentage of β and γ-AgI could be determined by using the relation

$R= [I (111)_{\gamma}+I(002)_{\beta}]/ [I(100)_{\beta}+ I (101)_{\beta}]$

Figure 5.2 (i), (ii) and (iii) shows the structure evolution in Cu doped (5, 10 and 20 %) Ag-Cu thin films 5nm thick. The γ-AgI nanoparticles were clearly seen upon progressively iodized Ag-Cu metastable alloy thin films under ambient condition (300K and ~760 mm pressure). Cu induced disorder in Ag films (initially upto 60 min iodized) enables growth of γ-AgI nanoparticles. After 180 min iodization around $2\theta=23.75^0$ the γ-AgI (111) zincblende structure pattern observed with very small intensity. As iodization time is increased to 360 min the intensity of the (111) plane increased with no impurity phase (β-AgI) being observed. But in the case of un doped AgI films after 180 min iodization there is strong overlapping between β and γ AgI structures co-existing in the iodide film. The Cu substitution thus stabilizes the metastable zincblende structure of γ-AgI besides assisting in particle size reduction due to the possibility of reinforcing the Ag sublattice in AgI aided by enhanced covalency of the Ag-I bond. Doped Cu ions could either occupy the vacant interstitial position in the Ag lattice or substitute Ag ions thereby depleting Frenkel defects in the AgI lattice and arresting the random motion of the Ag^+ ions. Although the Ag-Cu binary system has only metastable solubility in view of their positive heat of mixing, there is a natural tendency for Cu to stabilize γ-AgI zincblende structure especially because zincblende CuI is the most stable phase.

Figure 5.3 (i), (ii) and (iii) shows the XRD of Cu doped (5, 10 and 20 atomic wt %) Ag-Cu thin films thickness of 15 nm. Short time iodization (60 min) of 5% Cu doped Ag films shows the there is a strong Ag (111) plane: there is no evidence for AgI formation due to film thickness as well as Cu induced disorder nature. Prolonged iodization of Ag-Cu alloy shows the strong Ag crystalline fcc structure with only two diffraction peaks appearing in the spectra, namely the (111), (200). The low angle (111) Ag peak is the most intense in the pattern, which implies a slight preferential orientation of the Ag grain along the (111) crystallographic direction [21-26].

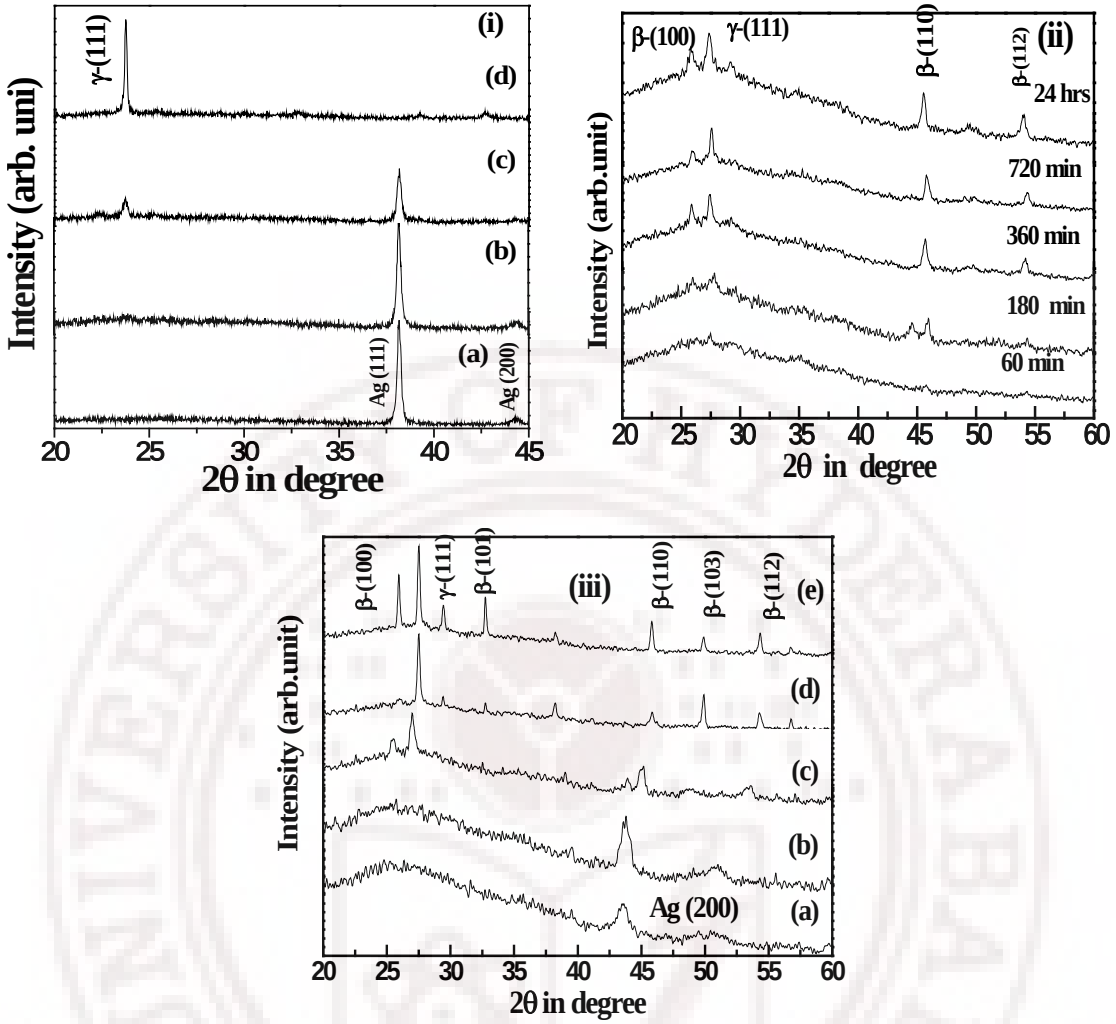

Figure 5.3: XRD pattern of 15 nm thick (i) $Ag_{0.95}Cu_{0.05}$ (ii) $Ag_{0.90}Cu_{0.10}$ and (iii) $Ag_{0.80}$-$Cu_{0.20}$ iodized for different times (a) 60 min (b) 180min (c) 360 min and (d) 720 min and (e) 24 hr.

In figure (ii) and (iii) the iodization time increased to 3 to 24 hr shows the β-AgI phase observed for 15 nm thicker films and proportions of which increases with increasing iodization time reflecting the iodine-rich regions in these films favor that the condition, (Ag/I)≤1. The wurtzite structure of β-AgI (2H) and zincblende structure of the metastable γ-AgI (3C) [27] differ in the stacking sequences, and they can be regarded as different polytypes so called γ-AgI films shown in figure 5.3. γ-AgI film contains more or less stacking disorder, exhibiting only traces of the β (100) and β (111) line. This is evidence of γ-phase being stabilized by non-stiochiometry and strain due to a difference in the thermal expansion coefficients between the AgI film and substrates. The 5 nm Ag films iodized at 360 min show reddish colour, suggesting iodine deficiency, while the 15 nm Ag film iodized at 24 hr exhibit pale yellow colour. These stacking faults are usually associated with (111) planes of crystallites, which are prone to *'ABABAB'* type of

hexagonal close packing instead of *'BCABCABC'* type of cubic close packing the existence of two polymorphs [28], γ-AgI and β-AgI, with the same fist neighbor coordination of Ag by I atoms and propensity of β-AgI to grow into big micro crystal, thus offering a stiff competition to the nucleation and growth of γ-AgI nanoparticles making the study of nanoparticle structure growth process an attractive challenge.

However, the peaks become intense and narrow with increase in iodization time, which indicates that crystallinity improves with increase in iodization time. Interestingly it was observed that the iodization influences the direction of preferred orientation of γ-AgI films on fused silica substrates. Perhaps the Si-O tetrahedral banding in SiO_2 substrate encourages this. The evolution of preferrd orientation in polycrystalline thin films can be analyzed from the viewpoint of energy minimization. The total energy in any film deposited on a substrate is the sum of three components: (1) the surface energy of the film, (2) the film–substrate interface energy, and (3) the strain energy in the film [25].

Figure 5.4 clearly shows the qualitative analysis of thickness and iodization time dependent of changes in γ-AgI lattice parameter (a) and average stain (ε) calculate from XRD pattern. Lattice parameter of γ-AgI (111) peak for 5 nm thin film is initially, short time iodization shows very high ($6.61A^o$) which shows the there is the compressive residual stress present in the initial iodization time [10]. Upon prolonged iodization the lattice parameter starts decreasing slowly and finally matching with $6.495A^o$ JCPDS standard value for γ-AgI. This means Cu progressively substitutes Ag ions thereby depleting Frenkel defects in the AgI lattice, thus arresting the random motion of the Ag^+ ions and internal stress gets relaxed in the AgI matrix. However, for 15 nm thick films the lattice parameter decreases crosses the JCPDS value during short time iodization finally $6.641A^o$ after 24 hrs iodization due to defects and multiphase AgI (γ and β) phase [23].

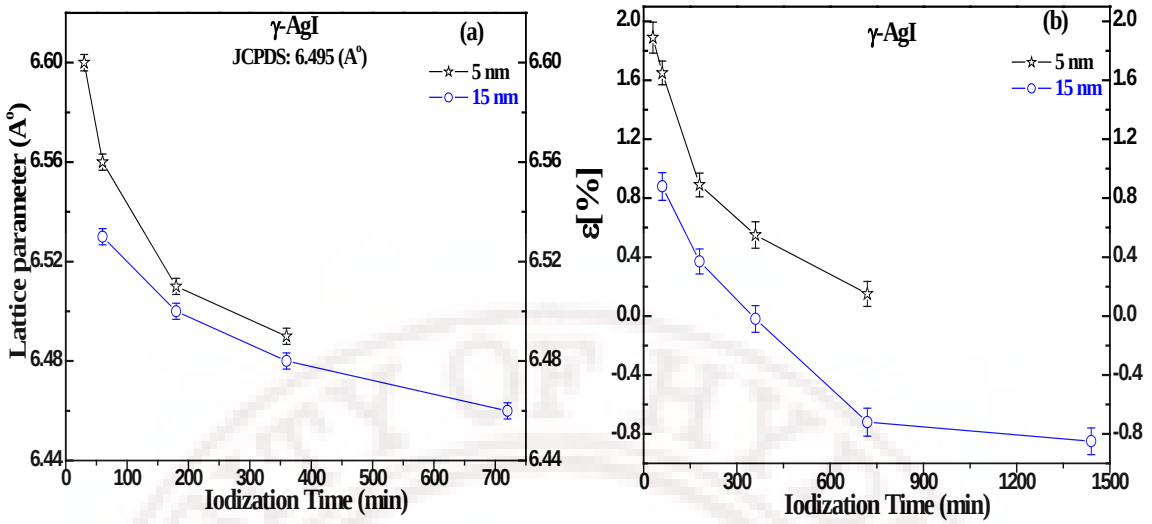

Figure 5.4: Thickness and iodization time dependent of lattice parameter (A°) variation for γ-AgI (zincblende) thin film structure.

From the peak shift in the XRD pattern, average strain (ε) was calculated using the following relation $(\varepsilon) = [d_{observed} - d_{reference})/ d_{reference}] \times 100\%$ where d observed and reference are the interplanar spacing of γ-(111) and reference from JCPDS respectively. Figure 5.4(b) shows calculate average strains of γ-AgI for two different thickness 5 and 15 nm. The short time iodized 5 nm AgI films shows the average strain is positive and it is very high (1.89 %) at 30 minutes iodization suggesting the presence of compressive stress at room temperature. On prolonged iodization the average strain decreases slowly and finally approaches zero strain or free strain state at 720 minutes. It clearly shows the strain relaxation in defects free film realized by iodization. In 15 nm thick Ag films iodized at (1 -24 hr) show that the compressive stress becomes the tensile stress (the calculated values of strain is negative) for 24 hr iodization time while compressive stress (strain is positive) increases with the increasing iodization time 24 hr resulting in the production of more β-AgI. This strain arises possibly due to the formation of Frenkel defects.

5.4 Surface microstructure characterization of AgI thin films grown on fused silica substrates

The two dimensional and its corresponding three-dimensional, DFM image of AgI and Cu doped AgI films deposited on fused silica substrates at two different film thickness (5 and 15 nm) and different iodization time shown in figure 5.5 to 5.10. Figures

5.5 and 5.6 show the microstructure of as deposited 5 nm and 15 nm thick Ag films. The surface morphology of as deposited Ag film consists of uniform spherical size particles with average particle sizes of 25 and 35 nm [10,11,17,29]. Surface roughness (rms) of the as deposited films is 1.23 and 3.26 nm as shown in figure 5.11. With increasing the film thickness the surface to volume ratio decreases and in turn grain size and surface roughness increases. The iodization process induces AgI grain growth leading to a significant increase in lateral grain growth and a striking difference in the morphology between Ag-I bonds depending upon iodization time. Figure 5.5 and 5.6 (b) and (c) all show Ag to be passivated at the top by a thin I_2 layer and at the bottom by the unconsumed Ag layer (core-shell) after the 60, 360 and 720 minutes iodization of 5 and 15 nm Ag films [30-33].

In short time iodization initially favours core-shell type grain growth the core being Ag while shell is AgI (to be discussed exhaustively in the chapter 6). Depending upon the iodization time, the iodine will diffuse (lateral diffusion) in to the Ag surface and stabilizes the Ag-I bond formation [30-31]. When iodization time increased to 360 minutes the shell thickness increases which shows the development of γ-AgI zincblende structure. Upon prolonged iodization grain size increases from 24 nm to 55nm and from 35 to 83 nm for 5 and 15 nm films. Surface roughness of the films increased which are 1.23 to 3.2 nm and 3.26 to 6.46 nm for 5 and 15 nm films as clearly shown in figure 5.11. In short time iodization when the iodine flux is exposed to Ag surface the Ag grains start slowly growing and once the formation of Ag-I bond is complete the grain size and roughness of the films get stabilized which implies the uptake of iodine molecules is just enough to form Ag-I bond and AgI_4 tetrahedra. Further more 24 hr iodization shows the iodine rich regions in the system which would allow the formation of β-AgI wurtzite structure seen in XRD pattern [9-11,30].

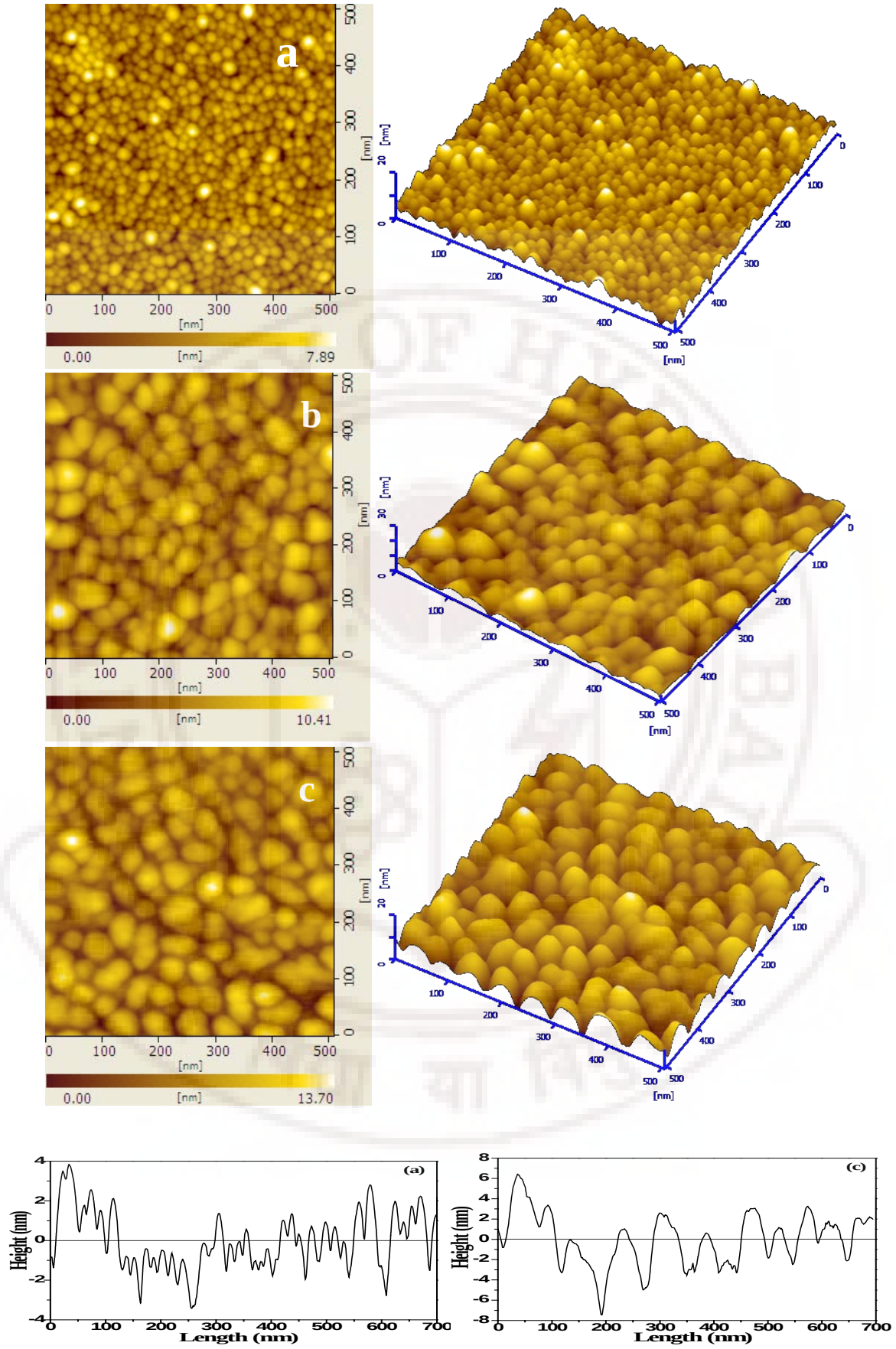

Figure 5.5: DFM Surface micro structure (0.5 μm x 0.5 μm) of 5 nm thin Ag films (a) As deposited (b) 30 min (c) 360 minutes iodized.

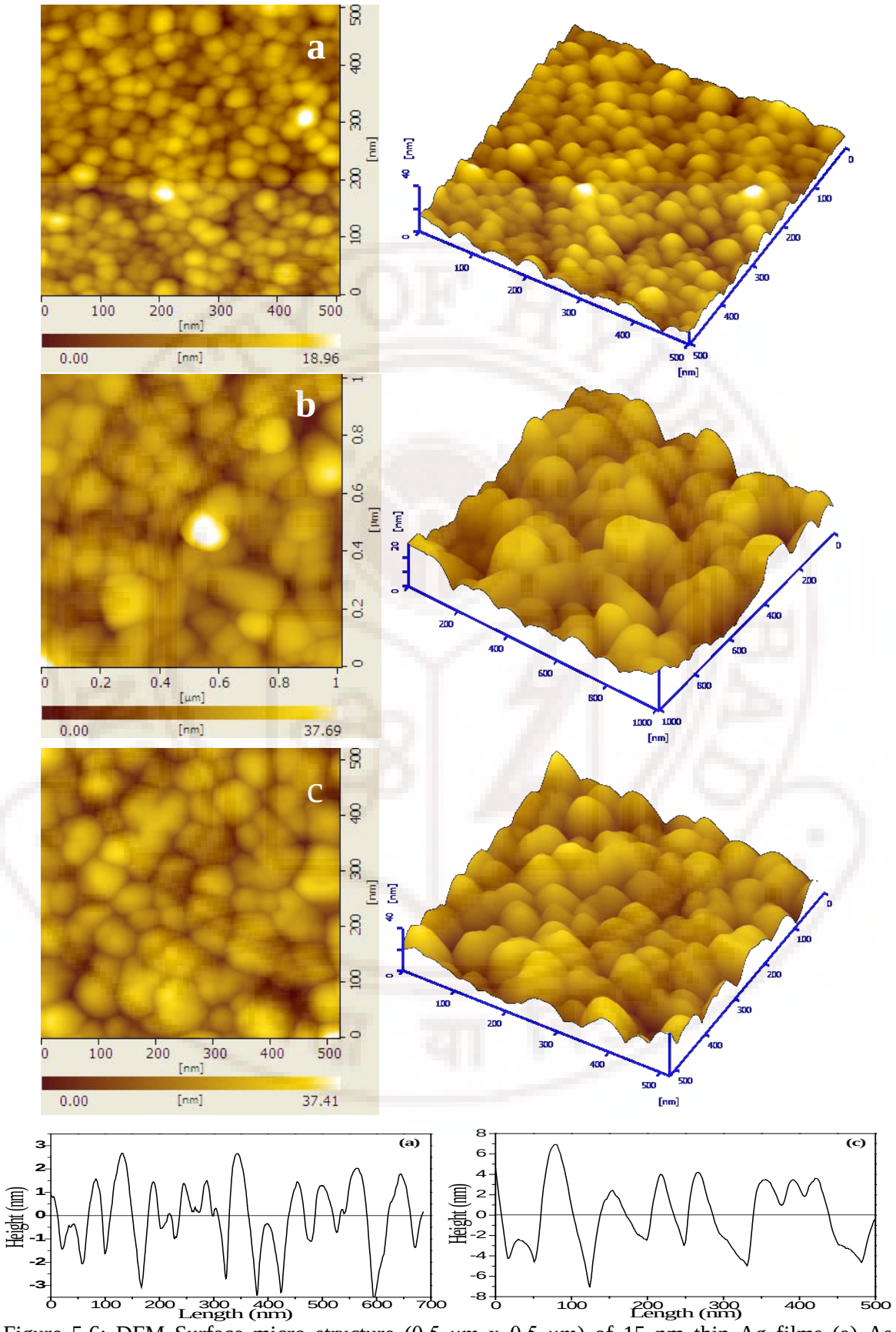

Figure 5.6: DFM Surface micro structure (0.5 µm x 0.5 µm) of 15 nm thin Ag films (a) As deposited (b) 60 min (c) 720 minutes iodized.

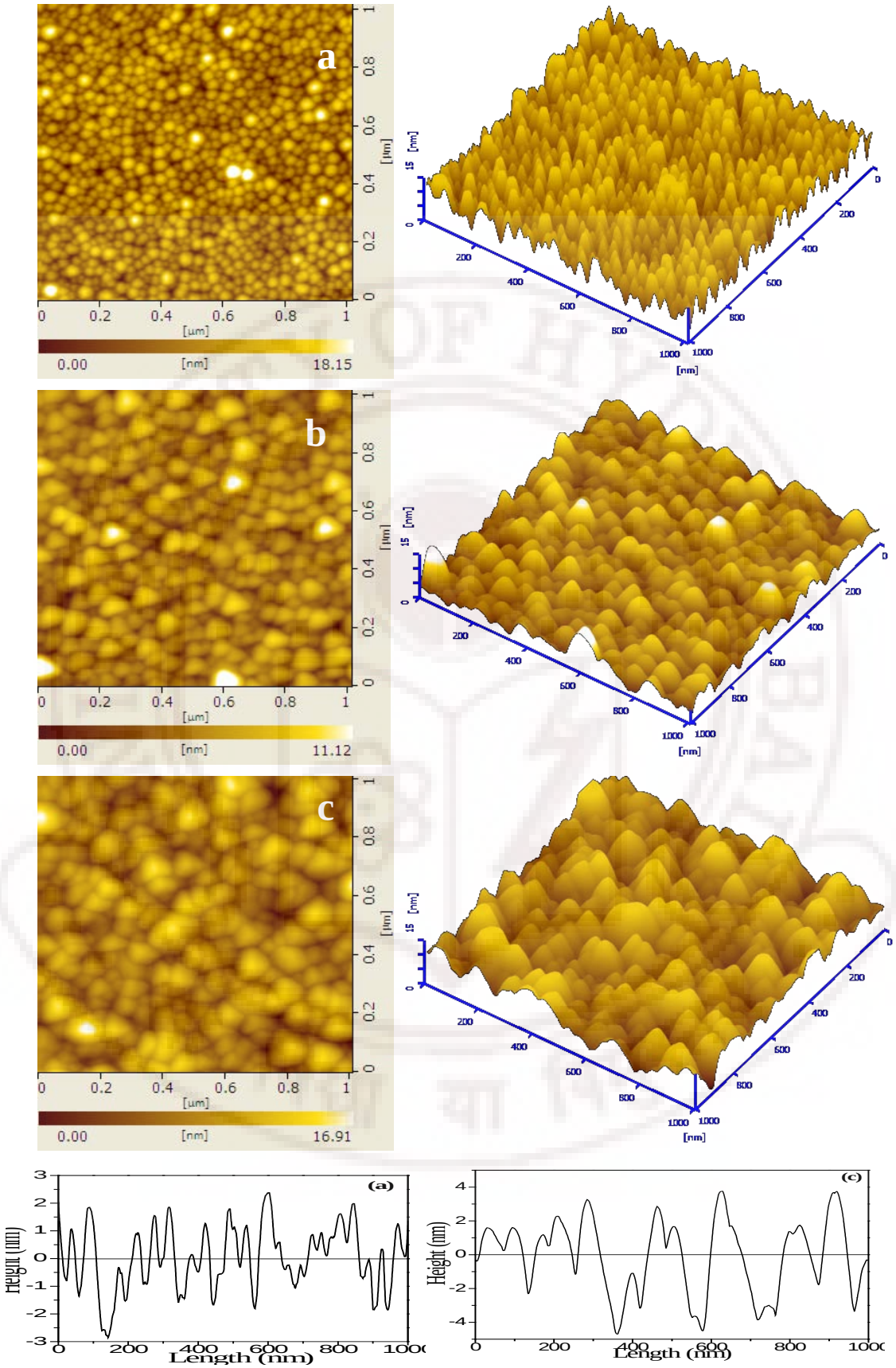

Figure 5.7: DFM Surface micro structure (1 µm x 1 µm) of 5 % Cu doped 5 nm thick Ag films (a) As deposited Ag (b) 60 min (c) 720 minutes iodized.

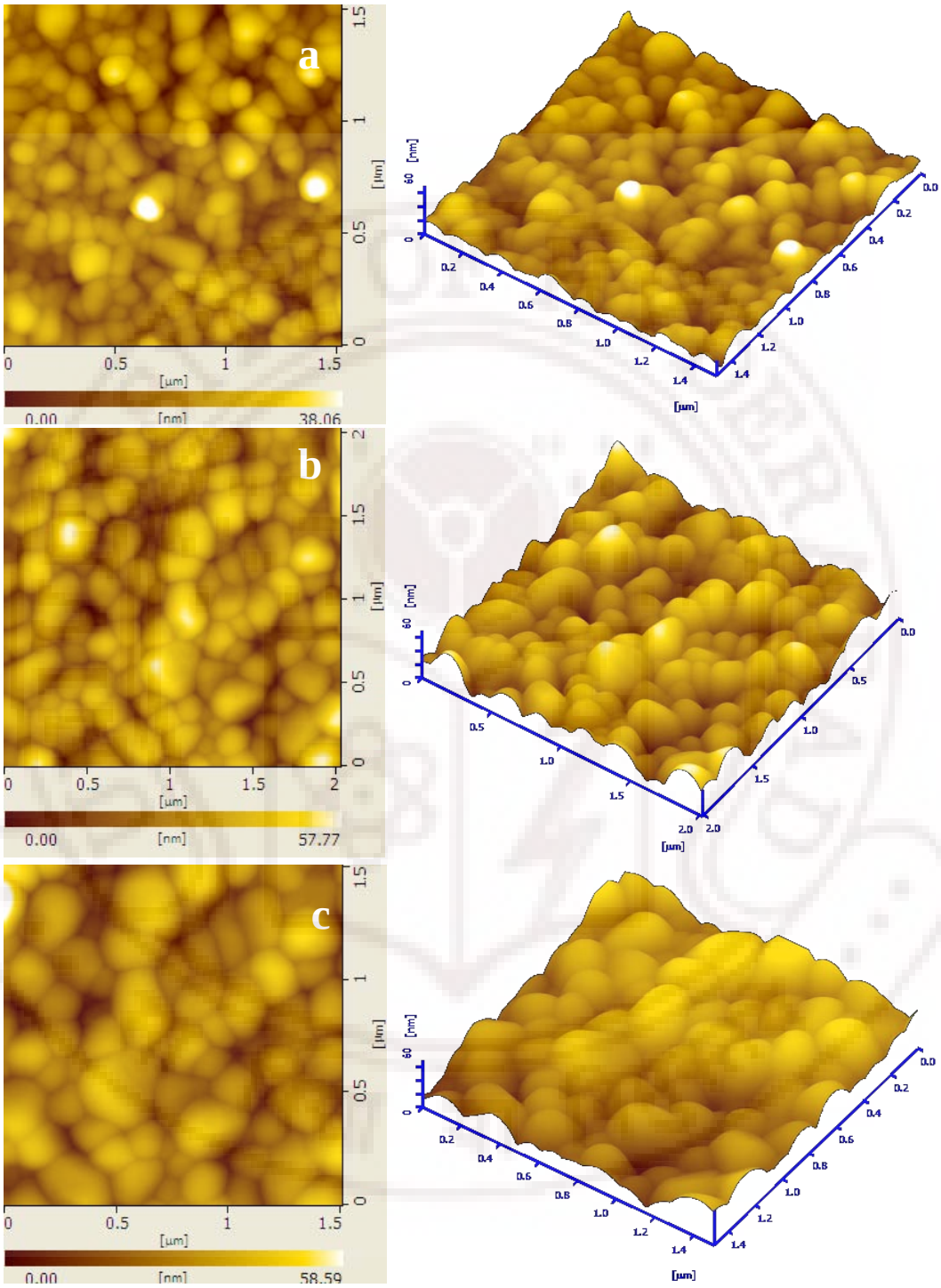

Figure 5.8: DFM Surface micro structure (1.5 µm x 1.5 µm) of 10 % Cu doped 5 nm thick Ag films (a) As deposited Ag (b) 60 min (c) 720 minutes iodized.

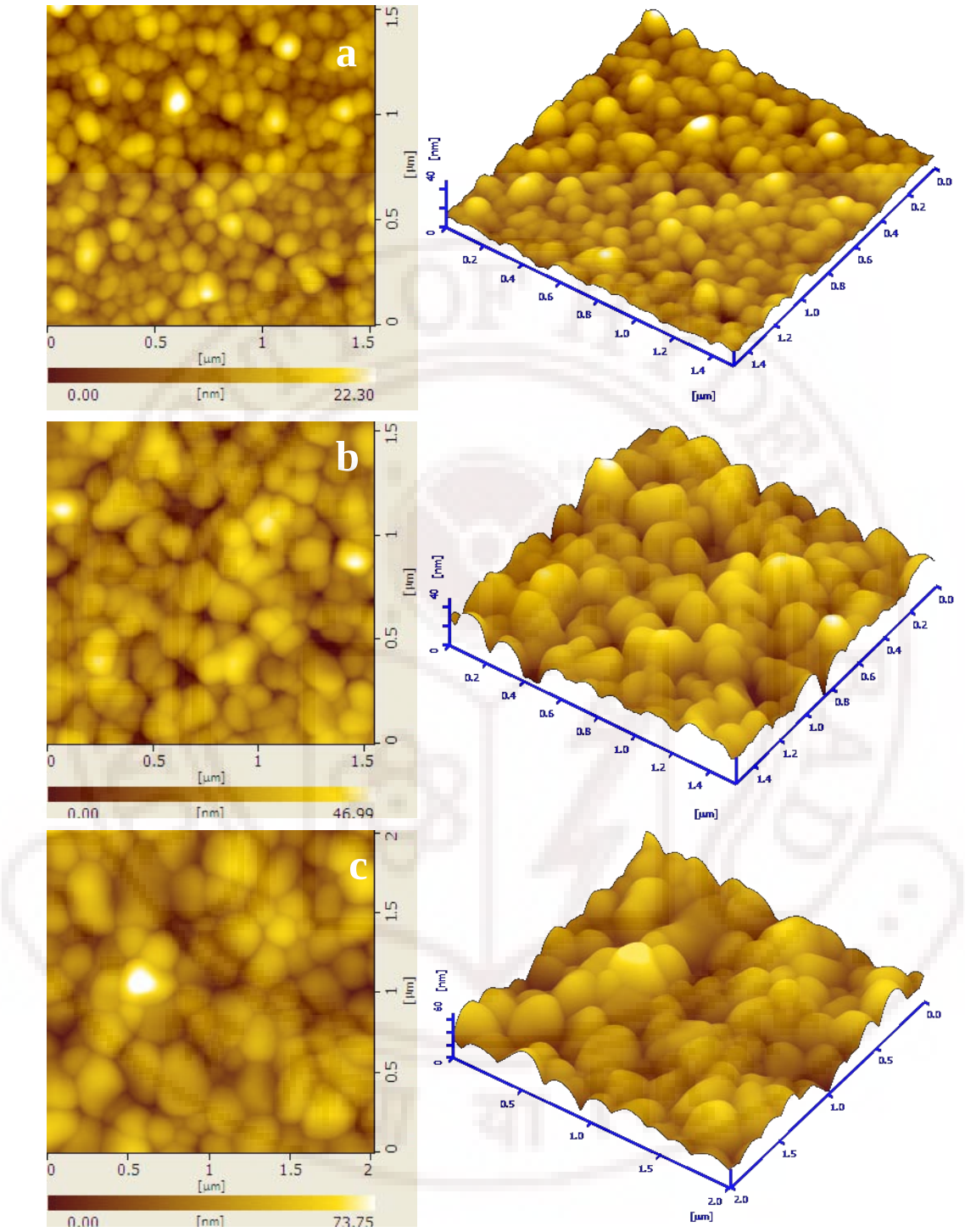

Figure 5.9: Surface micro structure of 5 % Cu doped 15 nm thick Ag films (a) As deposited Ag (b) 180 min (c) 24 hr iodized.

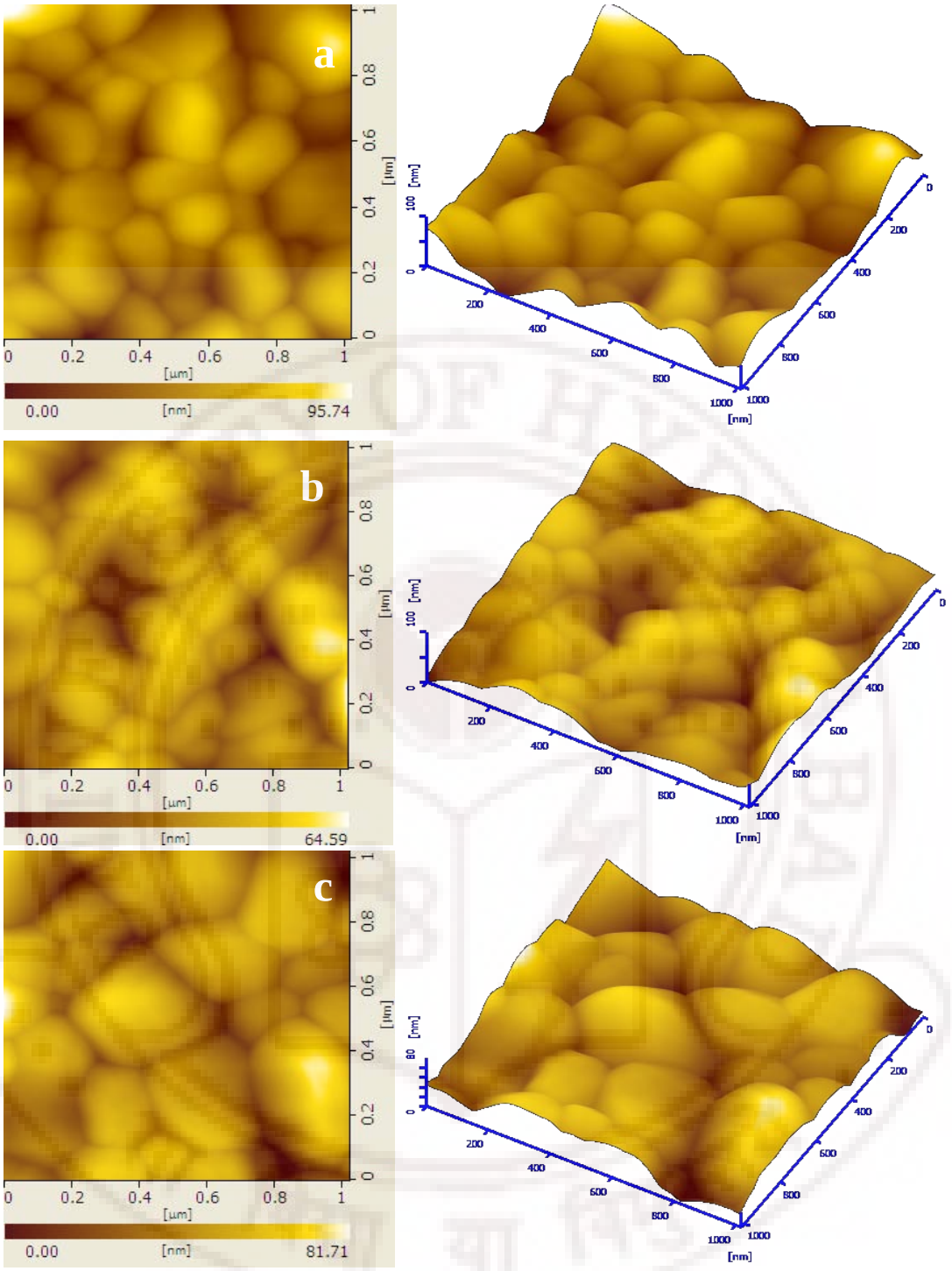

Figure 5.10: DFM Surface micro structure (1 µm x 1 µm) of 10 % Cu doped 15 nm thick Ag films (a) As deposited Ag (b) 180 min (c) 24 hr iodized.

Figure 5.7 and 5.8 show DFM micrographs of 5, 10 and 20 % Cu doped 5 nm thin Ag-Cu alloy films iodized at different times. The purpose of Cu doping is to stabilize zincblende structure of γ-AgI besides assisting particle size reduction and control the growth assisted by sputter disorder. The surface morphology of the as deposited Ag-Cu

alloy film shows the well defined uniform spherical shaped nanoparticles with average grain sizes of 30 and 40 nm [13-15,34-38]. Significantly Cu arrests agglomeration in nanoclusters of Ag-Cu alloy systems. Because of lower atomic radius of Cu relative to that of Ag the amount Cu ions that go into silver sub lattice controls the grain growth. The short time iodization of Cu doped AgI shows the triangular shaped grain growth which provides direct evidence for Cu induced shape transformation shown in figure 5.7. As the Cu^{+} ions are the reinforcing cations in to the sublattice of these Ag rich zincblende solid solutions, the identity of the phase that evolve thermally depends on the changes in the Cu^{+} occupancies relative to the initial Zincblende lattice. The γ-AgI grain growth is clearly seen in progressively iodized Ag-Cu metastable alloy films under ambient condition. As more and more Cu atoms substitute Ag in AgI, the Ag-I bond progressively shortens and strengthen due to enhanced p-d hybridization, there by stabilizing robust γ-AgI grain growth.

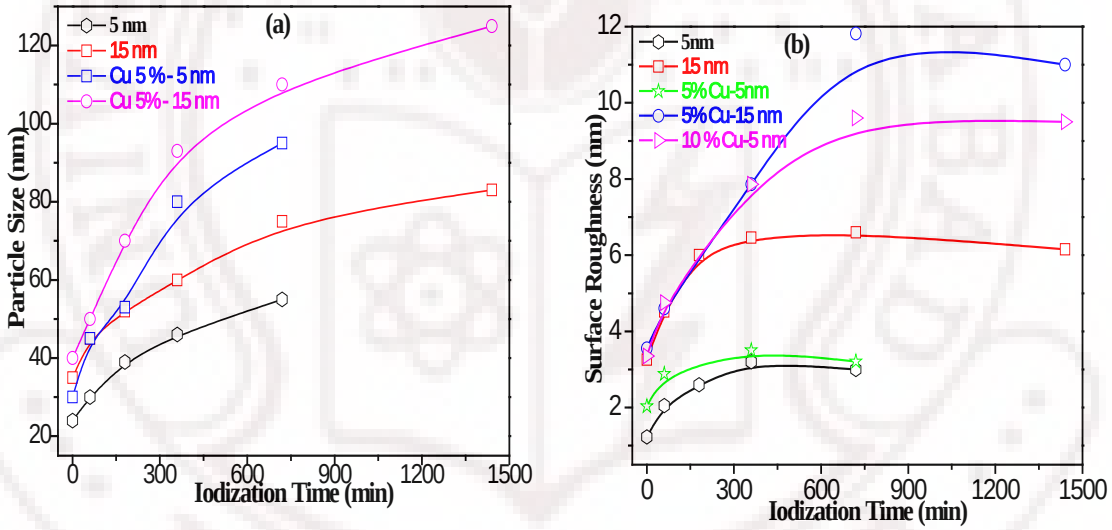

Figure 5.11: Thickness and iodization time dependent (a) particle size and (b) surface roughness changes in Ag and 5 and 10% Cu doped 5 and 15 nm thick Ag-Cu thin films.

5.5 Optical properties of RF Sputtered Ag and AgI thin films

5.5.1 Surface plasmon resonance of Ag and Ag-Cu alloy films

Figure 5.12 shows the UV-visible optical absorption spectrum of 3-15 nm thick Ag films. Figure 5.12(a-d) shows thickness dependent surface plasmon resonance (SPR) of Ag thin films deposited on fused silica substrates [39-49]. 3 nm thin Ag film shows the SPR band maximum (λ_{max}) at 413 nm. Where as 5, 8, 10 and 15 nm thick films show the

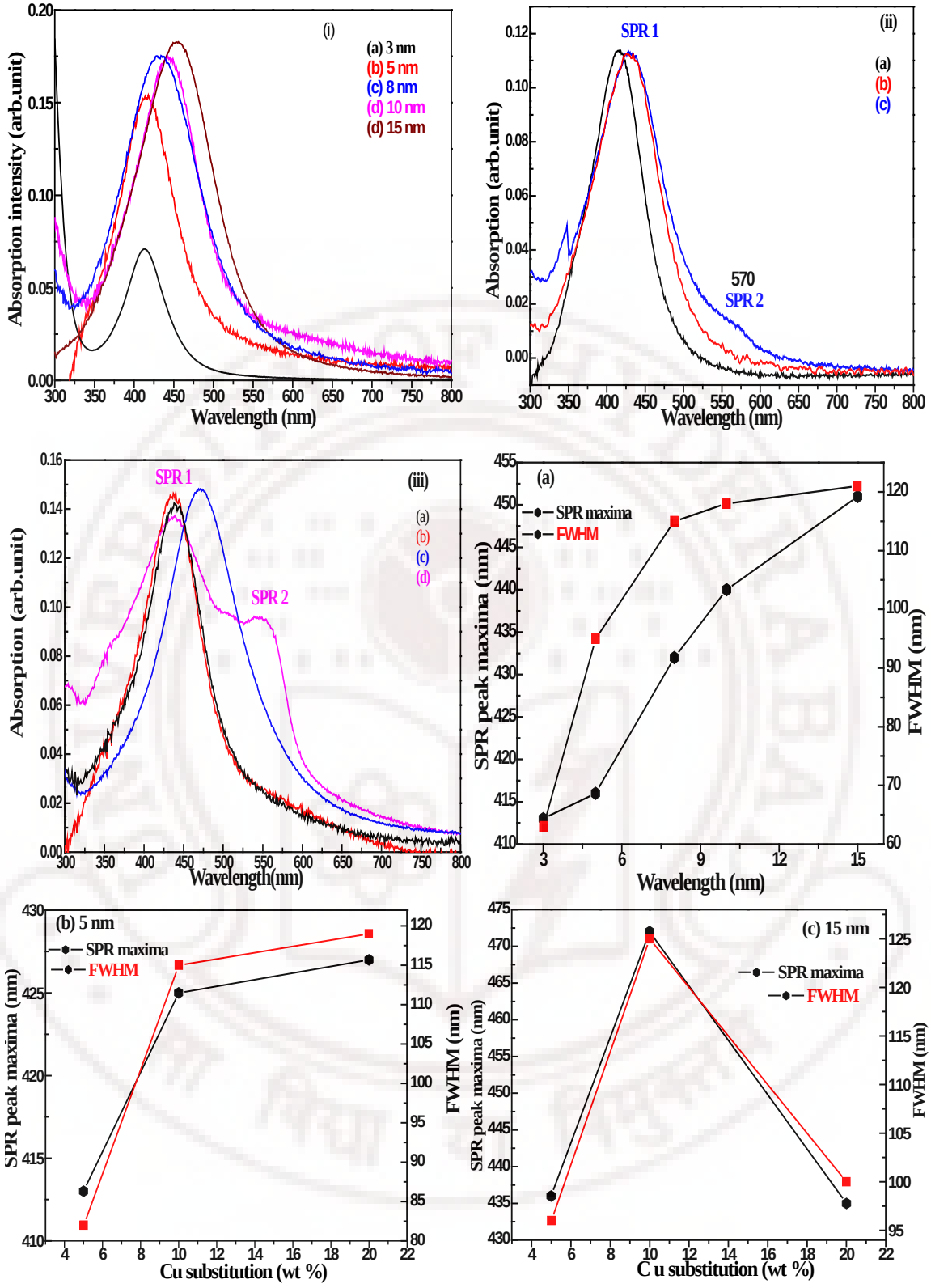

Figure 5.12: Surface plasmon resonance spectra of (i) pure Ag films thickness of 3-15 nm (ii) 5, 10, 20 % Cu doped Ag films thickness of 5 nm (ii) 5, 10, 20 % Cu doped Ag films thickness of 15 nm. Figure 5.12 (a), (b) and (c) SPR peak maxima and FWHM (a) un doped (b) 5, 10, 20 % Cu doped Ag films thickness of 5 nm (c) 5, 10, 20 % Cu doped Ag film thickness of 15 nm. Thickness dependent SPR show shifts in the plasmon peak position towards red but Cu doped Ag films show shifts towards blue in the SPR.

SPR at 466, 432, 440 and 451 nm. Increase in absorbance value and shifting of SPR peak position in the higher wavelength region is in proportion to increase of Ag films thickness and subsequent formation of larger sized grains [50-54]. The full width and half maximum (FWHM) of the SPR of 3 nm thin Ag film is 63 nm. The shape of the SPR peak is very sharp an evidence for uniform distribution of Ag nano particles size of 25 nm. A systematic increase of SPR peak broadening with FWHM of 95, 115, 118 and 121 nm observed with increasing Ag films thickness merits explanation from Mie's theory [39,40].

According to Mie's theory, only a single SPR band is expected in the optical absorption spectra of spherical nanoparticles (NPs), whereas anisotropic particles can give rise to two or more SPR bands depending on the shape of the particles [41-43]. The λ_{max} value shifted gradually towards the red region with the increasing of Ag film thickness due to decrease of interparticle distance and increase of volume fraction which causes the aggregation of Ag nano particles [51].

Figure 5.12 (ii) and (iii) shows the UV-visible optical absorption spectra attributed to surface plasmon resonance of 5, 10 and 20% Cu doped 5 nm thin Ag thin film. 5% Cu doped Ag films show a single peak in the visible blue range SPR band λ_{max} at 413 nm [38,58-62]. The FWHM of the SPR line width is 82 nm which again gives evidence for uniform particle distribution and controlled grain growth. With increasing copper concentration up to 10% the SPR peak shifts to longer wavelengths side shown in figure 5.12(iib). The peak position of Ag-Cu films typically show the formation of two distinct resonance peaks due to the anisotropic particles growth which gives the dipole and quadrupole resonance with redshifted broad resonance [38]. The SPR for pure silver and copper occur at 400 nm and 570 nm respectively. For Ag-Cu alloy films, in our study these resonances move to 424 and 572 nm for the pure metals. For bimetallic nanoparticles with 10% Cu substitution, an absorption peak is seen between 427 and 570 nm. With increasing Cu content, the SPR exhibits redshift, the existence of a single broad resonance peak is evidence of an alloyed particle rather than a phase-segregated system. Further increasing Cu content to 20% there is no change in Ag SPR λ_{max} position but intensity of the second resonance increases. This result confirms that the nanoparticles are a bimetallic form of silver and copper and not just a physical mixture of silver

nanoparticles and copper nanoparticles. The red-shifts of the SPR peaks with increasing copper concentration are attributed to the decrease in conductivity [55,56].

Figure 5.12 (iii) shows the Surface plasmon resonance of 5, 10 and 20 % Cu doped Ag film thickness of 15 nm. The 5% Cu doped Ag films showed the SPR maxima at 436 nm single resonance with line width FWHM of 96 nm. Undoped 15 nm Ag films shown the SPR λ_{max} at 451 nm where Cu doped Ag film 436 nm the peak shift is observed 15 nm towards blue shifts. In the Cu doped 15 nm thick Ag films grain growth is controlled by doping Cu is seen clearly. On 20% Cu doping SPR peak shifts slightly towards higher wavelength, and an additional resonance can also be seen at the position of copper plasmon peak which becomes stronger and appears as a clear resonance with increasing concentration of Cu [55,56,60]. It is known from literature that the copper and silver exhibit very limited miscibility in the bulk. Therefore the optical absorption of 15 nm thick Ag films with some un-reacted copper shows the presence of free copper nanoparticles [61-62].

5.6 Exciton formation in Undoped and Cu doped AgI thin films

5.6.1 Exciton formation in AgI thin films

Figure 5.13 shows UV-visible optical absorption spectra of 5 and 15 nm thin Ag films deposited on fused silica substrates and these films were iodized at different time. Upon controlled iodization, flux-controlled iodine vapor is slowly deposited on the Ag surface and diffuse into silver lattice and replaces the interstitial atom by the action of several processes initiated by surface diffusion (lateral surface diffusion) at the gas-solid interface, and silver nanoparticles surface are eventually iodized [9-11]. RF sputtered silver iodide begins to grow on the surface at the ‘early’ stage of iodization (30 minutes) the core still remaining as silver constituting at Ag/AgI core-shell type of growth [34-33,63]. This type of growth chiefly depends on the surface morphology and surface roughness of the Ag film. The AgI formation delay depends on the preparation techniques and is thus a kinetically controlled process, determined by iodization time. In case of evaporated Ag films exciton formation took 15 min as has been observed because evaporated films are quasi amorphous due to thermal strain where as in the RF sputtered films formation took 30 min to begin AgI formation due to stress [10,11].

Short time iodization (15 minutes) of 5 nm Ag films shows the formation of exciton peak at 426 nm $Z_{1,2}$ zincblende AgI structure. Short time iodization shifts the SPR peak towards longer wavelength at 492 nm are shown in figure 5.13(ia). In short time iodization AgI nanoparticles grow on the surface of Ag films, where as bottom of the films remains as unconsumed layer of silver nanoparticles the two constituting an Ag @ AgI core shell type structure. Thus an Ag/AgI interface is formed during short time iodization where AgI acts as a dielectric matrix in which Ag particles embedded or aggregated on the surface, which shifts the plasmon to the higher wavelength side and become close enough to interact electromagnetically with each other this makes the onset of plasmon-exciton transition. Moreover AgI films possess a large concentration of Frenkel defects, and stacking faults at the grain boundaries as a result of iodization process [64-67]. On prolonged iodization (at 30 minutes) SPR peak broadens and AgI exciton band intensity increases with peak position observed to shift from their initial λ_{max} 419 nm and intensity of the absorption spectrum increased. The core–shell structures in which the AgI shell is forming gradually and engulfing the core Ag nanoparticle on its way to being converted fully into its iodide form and it can be seen that the size of the silver core is larger during the higher time iodization. The formation of the exciton peak at 426 nm ($Z_{1,2}$) is due to the dipole forbidden $4d^{10}$-$4d^9$ 5s transition in Ag allowed by the tetrahedral symmetry of Ag^+ ion in the Zincblende AgI structure and the resultant p-d hybridization [68-71]. The weak peak at 330 nm Z_3 is due to spin- orbit split I^- valence of the spin orbit interaction, so that the growth of $Z_{1,2}$ and Z_3 exciton, respectively is seen in figure 5.13(i). When iodization time is further increased to 180 min the exciton peak position shifts to 435 nm (higher wavelength side) as also the intensity of the exciton peak increases and the absorption edge becomes very sharp [10,11]. Increase of exciton peak maximum gives evidence for increase in the crystallinity (as seen in XRD) which decreases the band gap energy. It must be mentioned that the growth and development of $Z_{1,2}$ and Z_3 excitons strongly reflects the valence band development in AgI upon progressive iodization, the corresponding energies and energy difference quantitatively determining the band structure. This is because the electrons in the exciton are essentially differing from the developing/developed valence band.

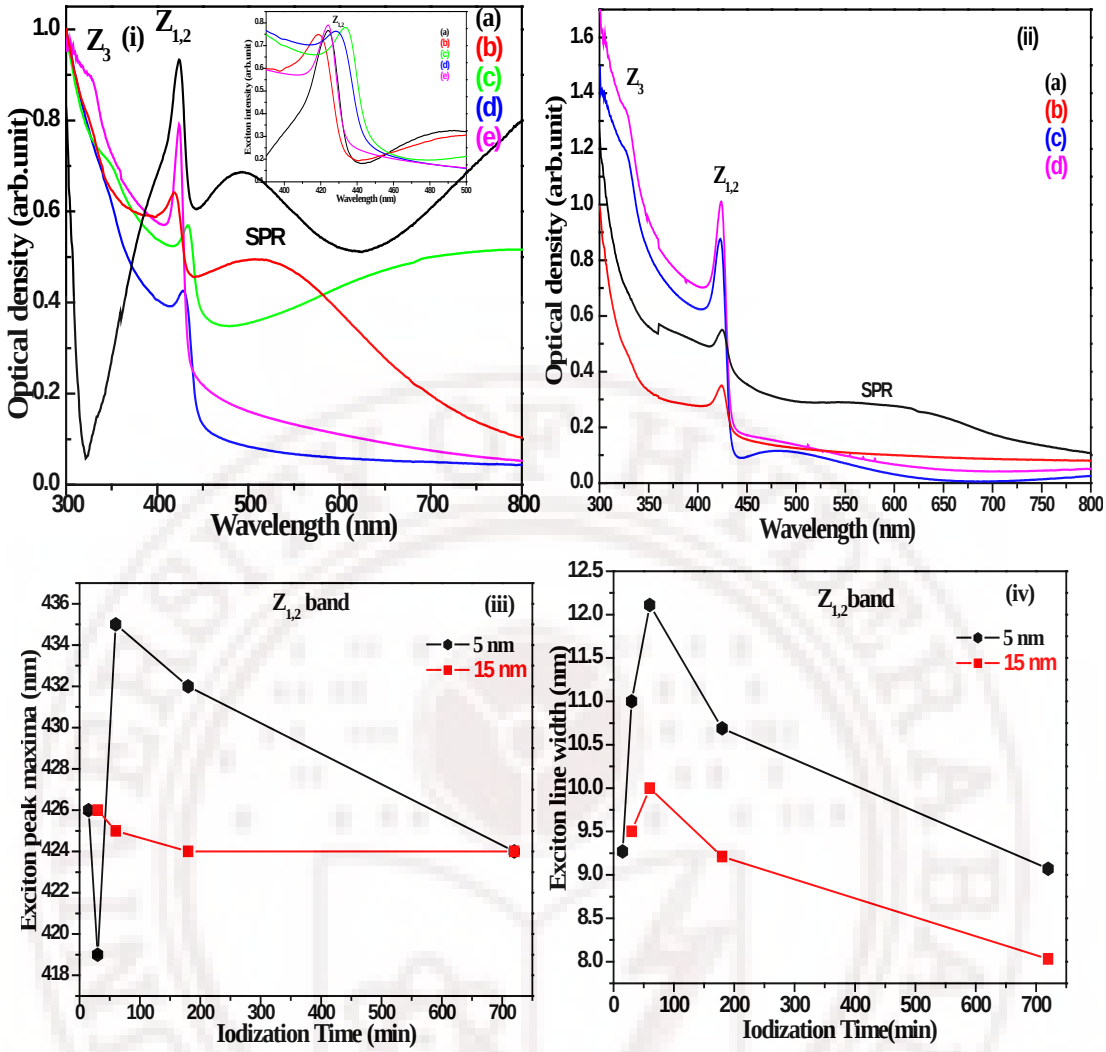

Figure 5.13: Thickness and iodization time dependent exciton formation in Ag films thickness of (i) 5nm (ii) 15 nm iodized for (i) (a) 15 (b) 30 (c) 60 (d) 180 and (d) 360 minutes and (ii) (a) 30 (b) 60 (c) 360 (d) 720 minutes. (iii) and (iv) Thickness and iodization time dependent exciton peak maxima and line width of 5 and 15 nm thick Ag films.

Upon iodization at 360 min the exciton peak shits towards the blue region at 424 nm which shows strong quantum confinement effects in AgI thin film [72-75]. 5 nm thick Ag films iodized upto 360 minutes showed the fully developed γ-AgI structure. Upon long time iodization (720 minutes) shows the formation of the mixed phase β and γ- AgI due to iodine rich region in the film. The exciton peaks $Z_{1,2}$ and Z_3 belong to the γ-AgI phase since they are very strong in the 5 nm AgI with high γ-AgI content. All these observations systematically characterize the very basic process of the band structure formation of AgI. 15 nm Ag films iodized at different time (same as 5 nm Ag films) shown in figure 5.13 (ii). The thick 15 Ag films for long time iodization do not favor stabilizing γ-AgI zincblende structure. While doing iodination of Ag films the AgI band

structure forms as follows: the top of the valance band (Γ^{15}) is triply degenerate without spin orbit interaction in the zincblende structure. This degeneracy is reduced by spin-orbit splitting to a doubly degenerate states (Γ^{8}) and a singlet (Γ^{6}). The Γ^{8} doublet gives the $Z_{1,2}$ peaks whose degeneracy is lifted due to some strain field changes at the crystalline surface (surface reconstruction or surface defects). With increasing film thickness, the saturation behavior of optical absorption unequivocally demonstrates strong particle size control particularly during the long term iodization regime and inhibits invariably the anisotropic growth and coalescence of the special crystal plane of the crystallites through Ostwald ripening process. This exciton spectrum can be interpreted along the same line as the absorption edges of other materials with wurtzite and zincblende structures. The strength of the exciton spectrum suggests direct allowed transition which by analogy with the other zincblende and wurtzite materials should occur at k=0 in the E *vs* k plot. These results are to be compared with the work of Cardona et al [68], Kondo et al [69] and Mochizuki et al [71] who measured optical absorption of AgI at temperature from 7K; through the superionic phase transition point Tc at 419K to 472K. The results obtained in the present case are at room temperature with is very rare and unusual because so far there are no studies so far on optical absorption of pure γ-AgI, the valance band degeneracy of which is lifted at room temperature.

Figure 5.13(iii) and (iv) shows the thickness and iodization time dependent exciton peak maxima and line width (FWHM). The iodization time dependent exciton band broadening makes it difficult to separate it form the interzonal absorption edge. To determine the $Z_{1,2}$ band parameter these peaks were fitted with Gaussian function. The iodization time dependent exciton peak maxima and line width of 5 and 15 nm thick Ag films shows of Ag@AgI nanostructure core-shell formation. Upon prolonged iodization peak position slowly decreases towards blue region with increasing iodization time, which is indication of quantum confinement effects decreasing upon iodization. In thick films intensity increases linearly with increasing iodization time. These results clearly indicate a thickness induced transition from γ-AgI to β-AgI upon increasing iodization time. With increasing film thickness, in short iodization initially forms the $Z_{1,2}$ exciton and prolonged iodization initiates the formation of bound exciton due to formation of Frenkel defects in the Zincblende AgI structure. Long time iodization (720 minutes) shows the bound exciton becoming quasi free exciton which is an indication of the formation of strain free stable γ-AgI zincblende structure. Where as in thickness induced

long term iodization Z_3 exciton get merged with W_3 exciton as seen in figure 5.13 (ii). Iodine rich areas show an exciton peak close to bulk value, which could be a reflection of the increase in the particle size decrease in the quantum confinement effect and a tendency towards formation of bulk band structure.

5.6.2 Cation stabilized exciton formation of Cu doped AgI thin films

In the previous chapter, we have employed XRD, UV-visible optical absorption and photoluminescence as monitors for AgI particle growth of Cu doped AgI thin films thickness of 5 and 15 nm by vacuum evaporation method. Presently optical absorption spectroscopy is used to study the evolution of AgI in the quasi amorphous Ag-Cu matrix upon progressive iodization for the period of 15 to 720 minutes using RF sputtered thin films. The crucial role of Cu in the formation of crystalline thin films is being ascertained. As the precursor films are quasi-amorphous, the rate of crystallization possibly controls the particle growth rate triggering changes in the exciton spectral feature and the development and stabilization of the energy band gap. For all three compositions (5, 10 and 20%) UV-visible optical absorption measurements were done at room temperature.

Figure 5.14 shows the room temperature optical absorption spectra of the progressively iodized metastable quasi amorphous precursor Ag-Cu films. Figure 5.14 (ia)a, (ib)a and (ic)a shows the 5, 10 and 20 % Cu doped Ag films. Short time (15 min) iodized 5 nm Ag film which exhibit a gradual development of features at 423 nm and 331 nm which is $Z_{1,2}$ and Z_3 exciton energy (2.931 eV) respectively as determined from the optical absorption spectrum of γ-AgI (Zincblende structure) [79]. These results have been observed for the first time in sputtered AgI films. These results clearly point to a thickness and Cu substitution induced stabilization of a robust γ-AgI zincblende structure. With increase of iodization time, the $Z_{1,2}$ exciton peaks intensity increases and SPR peak position shift at 458 nm towards the red region, which could be a AgI band structure development. This type of mixed plasmon-exciton formation could be termed '*plexciton*' [80] observed in short time iodized films. Plexciton formation is the direct evidence of plasmon-exciton transition in iodized Ag films [12,13]. When iodization time increased, the optical density saturates and the degree of saturation depends on refractive index (n). In thin films, the optical density is expected to decrease linearly with increasing iodization time; since the filling factor becomes smaller. Careful comparison of these

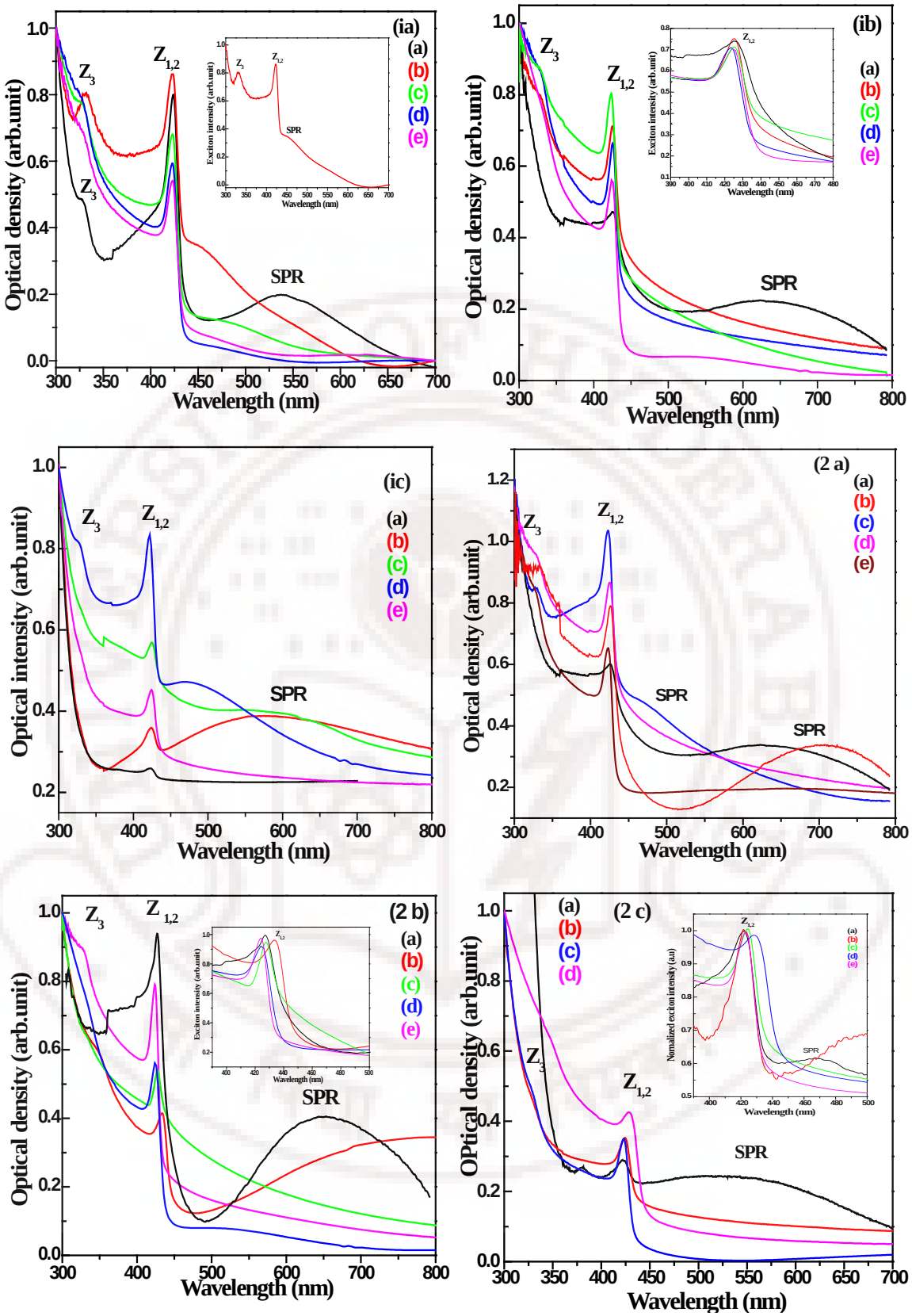

Figure 5.14: Evolution of exciton absorption band at 422 nm during the progressive iodization of the Ag-Cu thin films thickness of 5 and 15 nm of various compositions of 5, 10 and 20 %. Figure (i) a, b and c. shows the data for 5 nm thin Ag film iodized for (a) 15 (b) 30 (c) 60 (d) 180 and (e) 360 minutes. Figure (2) a, b and c. shows the data for 15 nm Ag films iodized at thick Ag films iodized for (a) 30 (b) 60 (c) 180 (d) 360 (e) 720 minutes.

optical spectra for isochronal iodization up to 360 minutes of the three Ag-Cu composite films of 5 nm thickness reveals that the increasing Cu content farms facile AgI nucleation and saturable growth thereby effectively controlling resultant product particle size.

A general feature of the absorption spectra in our iodized Ag-Cu films is the appearance of strong exciton absorption peak edge around 422 nm ($Z_{1,2}$) and 330 nm (Z_3) characteristic of γ-AgI zincblende structure. This feature persists even upon a substantial increase of the Ag/Cu ratio, signaling the fact that Cu acts only as a catalyst for controlled particle growth and stabilization of defect free structure γ-AgI and thus does not evolve itself as CuI giving its own characteristic exciton bands. The optical property of AgI is enhanced by partial Cu substitution [4,79]. The intensity of the peak increases with the increasing iodization time. The evolution of $Z_{1,2}$ and Z_3 exciton absorption bands was observed at about 422 nm and about 330 nm which correspond to the two spin orbit components of exciton excitation in AgI. This absorption edge corresponding to unresolved excitons is due to the forbidden transition in the Ag^+ ions, which becomes resolved because of the tetrahedral symmetry caused by the p-d hybridization in the electronic structure of AgI. Besides, there is a strong UV band at around 330 nm characteristic of γ-AgI in copper substituted films. With increasing iodization time, the SPR of the Ag nanoparticles, being sensitive to changes in the refractive index of the medium at or near the particle surface, shifts steadily to longer wavelengths as seen in the inset shown in figure 5.14.

Prolonged iodization of Cu doped Ag films iodized at 60 and 180 minutes shows clearly $Z_{1,2}$ band formations. The width of the exciton peak decreases to 162 meV which evidences the development of strong Ag-I bond. The $Z_{1,2}$ exciton absorption becomes very sharp and band edge splits faintly into two bands for 60 minutes iodization. With progressive iodization the $Z_{1,2}$ exciton band grows to a single band shifting towards blue region and Z_3 band gets faint due to the Frenkel defects but the 330 nm Z_3 exciton peak intensity decreases which means 360 minutes iodized films are fully iodized [68,81]. In comparison with work of Cardona et al and Kondo et al increasing iodization time provides clear evidence of a 'phase transition' from amorphous to crystalline state in the 5 nm thick AgI film. The faint double peak structure arises from a splitting of the doubly-degenerate valence band Γ_8 with light and heavy hole masses due to the difference of

quantum size effects, or some crystal-field change at the crystallite surface (for example, surface reconstruction or surface defects).

From the work of Kondo et al, it is clear that the thin films surface have the effect to lower the nucleation activation barrier and grain growth activation barrier. It is interesting to note that the iodization induces the amorphous films to crystallize into the γ-AgI phase at room temperature *without passing through the β-AgI phase.* As is well known the valence and conduction bands in semiconductor retain their meaning (in a broad sense) even in the amorphous state, and the density of states (DOS) of the bands is almost unaltered by amorphous since the gross feature of electronic states is determined by the short range order. But the lack of the long range order in the amorphous states leads to the relaxation of the k-conserving and/or symmetry-imposed selection rule. Such a relaxation sometimes gives rise to a significant result, particularly in the case of indirect band gap semiconductors. In the case of AgI, where the amorphous AgI films transform to the γ- phase crystalline films, the situation seems to be somewhat different. γ-AgI is known to have a direct band gap at the Γ points with the allowed types of optical transition matrix element the band edges.

The exciton bands in the nanocrystals (NCs) are characterized by a blue shift and inhomogeneous broadening that are caused by the relatively weak spatial confinement of the exciton in the small particles and by the (NC) size distribution and Cu impurity respectively [75-78]. While in un-doped 5 and 15 nm thick AgI films FWHM of the $Z_{1,2}$ exciton in γ-AgI NCs between 102 and 155 meV shown in figure 5.13 in the 5 % Cu doped AgI exciton line width varies with iodization time 139, 162 and 137 meV corresponding iodization time 15, 60 and 360 minutes respectively. The data reveal the internal structure of the 422 and 430 nm exciton states that is interpreted in terms of the electron–hole exchange interactions as well as a possible non spherical shape of the NCs. With increased Cu concentration the β-phase impurity decreases and it disappears at x= 10%. At room temperature the broadened exciton peak is isolated against the background of interzonal absorption shown in figure 5.14. The exciton band broadening causes definite difficulties in separating it from the interzonal absorption edge. As in bulk material, in NCs of γ-AgI, the lowest energy state ($Z_{1,2}$) is a ($1S_{3/2}$, $1S_e$) pair-state composed of a hole from the uppermost J=3/2 valence band and an s-type conduction band electron. By reduction of symmetry through the crystal field, in β-AgI the eightfold

degeneracy of this state is removed resulting in exciton states 330 nm four-fold degenerate. In bulk crystals, the ($Z_{1,2}$) exciton is split further by short- and long-range exchange interactions caused by the spatial overlap of the electron and hole wave functions [71-73].

Figure 5.14 (2a), (2b) and (2c) show optical absorption of the 5%, 10% and 20% copper substituted 15nm thick Ag-Cu films deposited on fused silica substrates with a dielectric constant different (larger) than glass substrate and thus expected to exercise better control over nanostructure formation and resulting properties. The short time iodized (30 min) Ag-Cu films have shown the immediate/rapid development of the $Z_{1,2}$ exciton peaks at 423 nm along with Surface plasmon peak and no evidence of 330 nm Z_3 band suggesting that the Cu substitution and higher thickness delay the Z_3 formation due to surrounding inorganic Ag-Cu matrix strongly restricting further aggregation during the formation of AgI crystallites. More interestingly, this saturation behavior clearly shows the strong particle size control particularly during the short-term iodination regime and exhibits the anisotropic growth. The exciton absorption observed even in the amorphous state points to a very small exciton radius of AgI (0.61 nm) so small that it could exist within the short range order itself. However, no trace of CuI exciton was observed even (80:20 wt ratio). Probably Cu^+ ions are dispersed as monomers in the amorphous environment, thus maintaining the electrical neutrality of the system each Ag^+ ion is replaced by Cu^+ ions [4,77].

The iodized AgI films show a number of intrinsic defects that are expected to be formed in the grain at the grain boundaries, on the surface or at the interface, leading to creation of energy levels within the energetically forbidden gap [82-84]. These separate defects levels can extend to form an energy band overlapping with the conduction band or valance band of AgI, thus giving rise to band tail states. It is well known that a decrease in particle size generally results in the blue shift of this peak due to enhanced quantum confinement. However the red shift is not too surprising when the effect of lattice composition (XRD figure) is taken into account. According to the bonding orbital theory of band structure for covalent semiconductors, such as AgI (its band structure is characterized by strong p-d hybridization-even stronger in CuI), energy bands are derived from the extension of molecular orbitals in unit cells. As the lattice parameter decreases, the overlap between the MOs in adjacent cells increases, leading to broadening of the band.

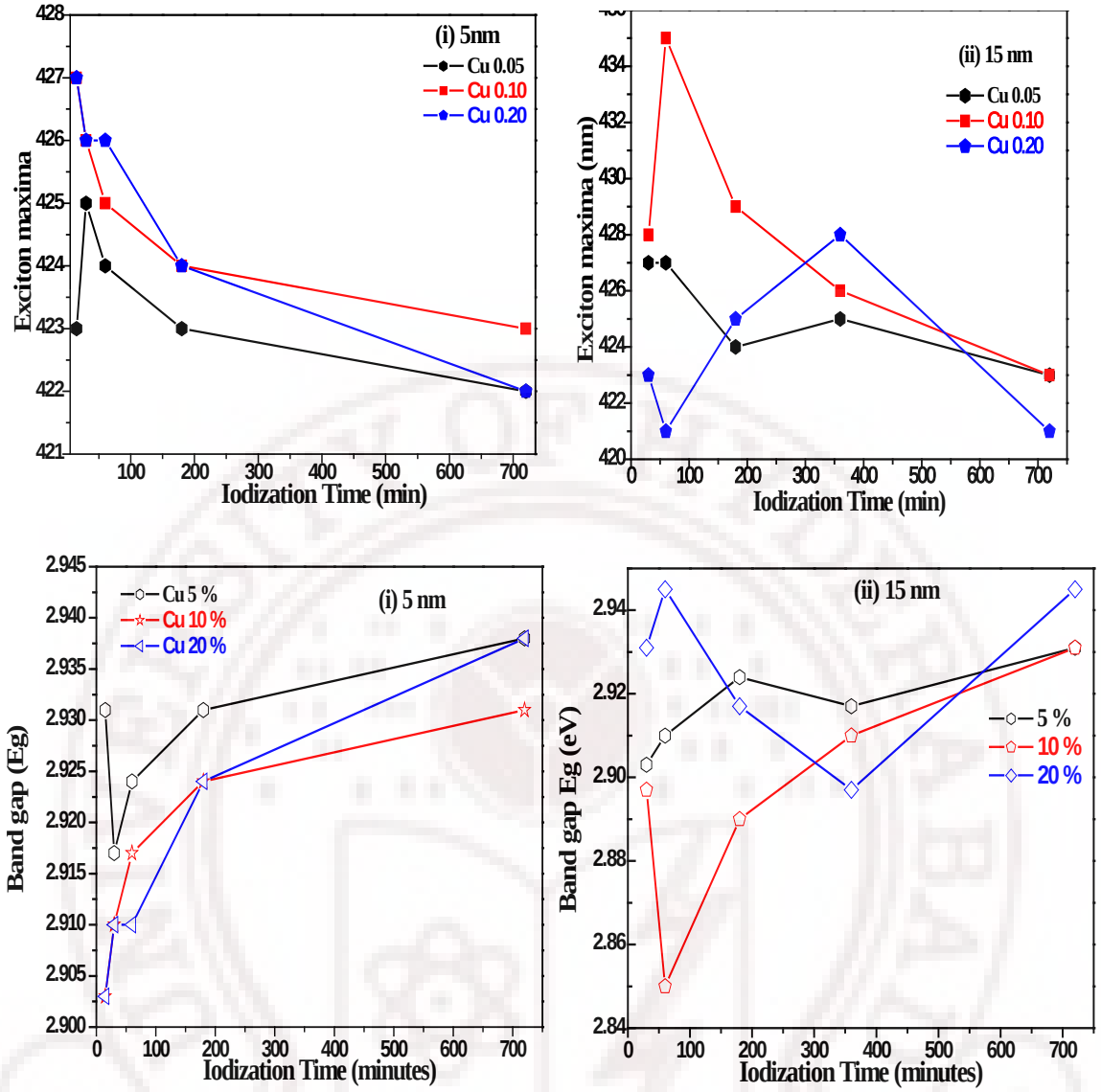

Figure 5.15: Band gap and exciton peak maxima of Cu doped (5, 10 and 20%) AgI thin films (i) 5 nm and (ii) 15 nm thick.

This generally results in a decrease of band gap, as observed in many semiconductors and insulators. Moreover, a decrease in lattice parameter results in reduction of electron-hole distance in the exciton, leading to strong electron-hole interaction and a larger binding energy of the exciton (the exciton binding energies in AgI eV). These Cu^{+} ions may also absorb light at their respective exciton energies, but this absorption might be irretrievably submerged by the strong absorption of the host Ag^{+} ions, the small ionic radius of the Cu^{+} ions is considered favorable for the substituting in a unique manner. This observation shows the important role for Cu in the rapid nucleation of the metal halide thus providing a new method for obtaining nanostructures for basic and applied research [4].

5.7 Photoluminescence study of nanostructured Silver iodide thin films

5.7.1 Thickness and iodization time dependent band structure development of AgI thin films

Figure 5.16 (i) and (ii) shows room temperature photoluminescence (PL) spectra of 5 and 15 nm thick Ag films grown on fused silica substrates by RF magnetron sputtering technique and these films were iodized at different times. Further, these iodized 5 and 15 nm Ag films are excited at 355 nm which is higher than the AgI band gap (bulk AgI 2.82 eV) to study band structure formation of γ-AgI zincblende structure [79-81]. As a source of the excitation the momochromatized light of a high pressure Xenon lamp was used.

Figure 5.16 (i) show the room temperature emission spectra of 5 nm thin Ag films iodized at 15 to 720 minutes, the iodized Ag films shown emission at 2.90 eV which is from $Z_{1,2}$ exciton. AgI (zincblende structure) and two sub-bands which is appears around at 3.03 eV and 2.70 eV [11,26,27,71-74,68,82,83]. In the direct band semiconductor the emission will appear at same in excitation wavelength. The emission spectra display an intense three-finger pattern with three prominent emission bands probably seen for the first time at room temperature. The first weak emission band at around 2.90 eV arises from the excitonic absorption peak but does not appear to be from the bottom of the conduction band, thus possibly corresponding to a shallow trap state or intrinsic near band edge state slightly below the conduction band [27,84]. The intensity of the emission peak associated with this weak luminescence is low in short time iodized films; the PL line is very broad. The assignment of the broader emission line with small energy shifts remains uncertain.

Upon increasing iodization time (i.e increase nanocrystals radius) the energy shift varies from 2.90 eV to 2.79 eV (290 meV). Besides, from the excitation/ emission scheme one would expect a resonance behavior parallel to that of the lower energy line, whereas that is not in the case. For these reasons a different origin may have to be considered, e.g. strain splitting of the states A_T and/or A_F. Assuming bimodal nanocrystals size distribution, the two processes could also be due to the short-range electron-hole exchange interaction in each of the two distributions. Since in that case the excited states A_T and the emitting states A_F each are different, this interpretation would qualitatively explain both the different emissions and different PL line widths. As prolonged iodization shows the strong intensity enhancement in strong emission band at 2.90 eV and also emission band shifts towards blue region this could be due to increase in the crystallinity

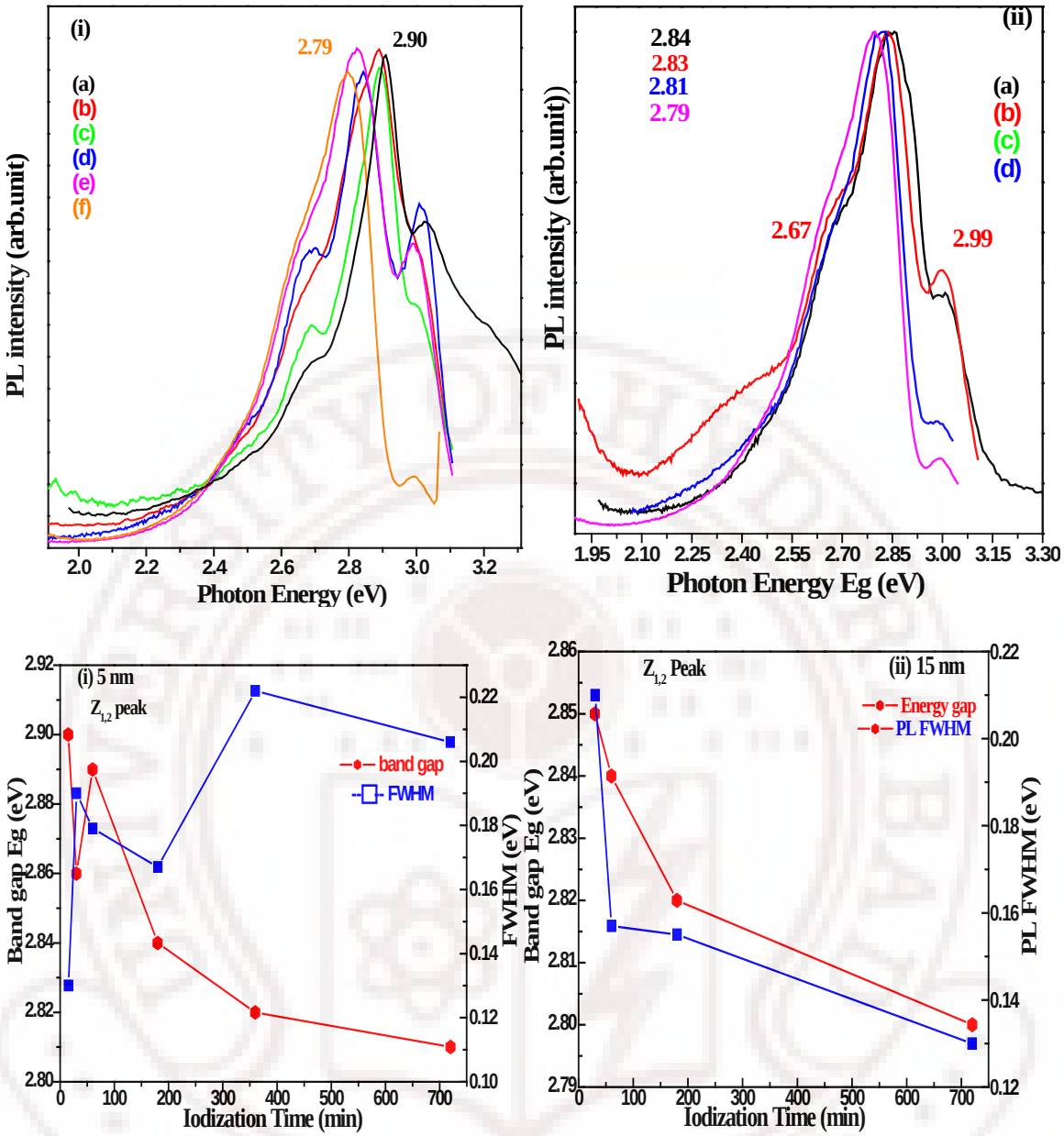

Figure 5.16: Room temperature PL spectra of as deposited (i) 5 nm Ag and (ii) 15 nm Ag thin film iodized for (a) 15 (b) 30 (c) 60 (d) 180 (e) 360 (f) 720 min. The non- linearity in the band gap show the changes in lattice parameter due to the Cu atoms going in to the sub-lattice position.

as well as quantum confinement effects (seen in XRD patterns). The band edge emission is red-shifted from the band edge absorption peak by 24 to 55 nm, with smaller nanocrystals showing larger shifts. Likewise, the relative intensity of deep trap emission varies from zero in large nanocrystals to peak intensity on the order of the intensity of the band edge emission for small nanocrystals [72-74,85].

Even after 720 minutes of iodization the single emission band remains unresolved which is supposed to appear at 2.82 eV at room temperature. This observation implies

that the majority of the charge carriers i.e electron hole pairs decay primarily via non-radiative pathways (shown by the remaining sub- bands appeared at 3.03 eV and 2.70 eV. Due to strong binding of the electron- hole pair the non radiative decay is attributed to fast electron- hole (D-A) recombination mediated by high density of deep trap states involving exciton- phonon interaction or some crystalline defects or impurities. Also as these are very thin films the grain sizes are in the nanometer range (seen in figure 5.11) the surface area to volume will be high. Thus there is a possibility of unsaturated dangling bonds, which act at shallow surface traps to effectively enhanced the PL properties.

Coulomb interactions between donors and acceptors in a semiconductor cause the recombination energy to be distance dependent. The recombination energy of a distant donor-acceptor (D-A) pair is given by $E = E_g - (E_D + E_A) e^2/\varepsilon_r$ where E_g is the band gap energy, ED and EA are the binding energies of the donor and acceptor and the last term is the Coulombic interaction of the D-A pair separated by r. This gives rise to discrete line spectra in semiconductors where the electron-phonon coupling is weak. In the case of AgI with strong electron-phonon coupling the peak of the resultant broad emission should shift to lower energies with time after excitation. The broad emission observed in room temperature photoluminescence (PL) from AgI is reasonably expected to result from D-A recombination. The intent of this investigation is to establish the nature of this broad emission and to explore to what extent it is affected by quantum confinement. The long time iodization induced redshift of the emission peaks following increased excitation energy is indicative of a coulombic interaction between the donor and accepter sites and long time iodization increases the grain size from 24 nm to 55 nm, the increase in particle size decreases the quantum confinement effect in γ-AgI due to decrease of confinement effect the energy shift will be towards the redshift shown in figure 5.16 [72-74,85-87]. The intrinsic Frenkel defects such as interstitial silver ions (Ag_i) and silver ion vacancies (V_{Ag}) would have the proper coulombic interaction.

In figure 5.16 (ii) the PL spectra of the 15 nm γ-AgI film on a fused silica at room temperature. The iodization time dependent emission intensity peaks for the γ-AgI films are observed at 2.85, 2.84, 2.82 and 2.80 eV corresponding to iodization times of 30, 60, 180 and 720 minutes respectively. The bands are accompanied by at least two shoulders at 3.01 eV and 2.67 eV shown in figure 5.16 (ii). The 2.85 eV band is close to the $Z_{1,2}$ and 2.80 eV emission band is closed to W_1 exciton absorption peaks. Other shoulders and low intensity peaks arise from excitons trapped by exciton-phonon interactions, or some

crystalline defects or long time iodization induced β-AgI impurities as seen in thick films. With increasing iodization time the low intensity peaks shift toward longer wavelength and, passing through Tc (crystallization temperature) it shifts abruptly to about 2.80 eV which is slightly shorter than the absorption trace of γ-AgI band position. This suggests that some luminescence states are above free exciton band in β-AgI. We suspect that the two emission bands on the low energy side of the $Z_{1,2}$ emission (around 2.80 eV in figure 5.16(a)) is due to electron–hole recombination at point defects or to smaller aggregates that have formed besides the NCs during longer time iodization. Except for the low energy region of the $Z_{1,2}$ band, this dependence does not show a clear correlation with the exciton absorption peaks demonstrating that energy transfer processes in the sample actually are important.

The compositional behavior of the structure of Cu doped AgI is characterized by Vegard's Law, which states that, lattice constant changes linearly with composition, as seen in figure 5.4a. Other physical properties such as band gap often vary nonlinearly as seen in figure 5.16. To a first approximation, the variation is quadratic: The sources of nonlinearity are threefold: (i) the changing lattice constant alters the band structure; (ii) the atoms in the alloy have different electro-negativities, deforming the electron distribution; and (iii) anion-cation bond lengths and angles must relax in order to accommodate the differently sized constituents [88,89].

5.7.2 Room temperature photoluminescence study of Cu doped AgI thin films deposited on fused silica substrates

Figure 5.17 shows the PL emission spectra of 5, 10 and 20 % Cu-doped 5 nm thin Ag films. The emission bands centered at 2.82 and 2.91 eV are likely to be caused by the radiative recombination associated with the Cu^{+} states replacing the Ag^{+} lattice sites(which is mandatory for reducing the Ag-I lattice parameter upon Cu-substitution[*] [6], which could be formed during the systematic iodization of Ag films [6,23]. The strong direct gap semiconductor AgI emission feature has been shown to be blue shifted. In smaller NCs, the luminescence arising from the direct recombination of exciton is absent, and this is attributed to surface effect [85]. In contrast the radiative excitonic recombination in AgI is dramatically reduced in the smaller size particles. While the surface of AgI is to play an important role in exciton recombination dynamic at smaller size [71-73].

Figure 5.17 (i) shows the PL spectra of 5% Cu doped Ag films displaying a broad emission band that ranges from 410 nm to 550nm (3.05 eV to 2.4 eV). The broad peak centered at 2.82 eV and 2.89 eV for 15 and 360 min iodization. The short time iodized 5 % Cu doped Ag films shows the broad emission peak and shoulders at 3.02 and 2.67 eV at energies greater than the emission energies of both the bulk γ and β-AgI excitons. When silver iodide clusters are excited, not only the emission of silver iodide clusters, but also the emissions of Ag clusters were observed. Similarly, when Ag clusters are excited, both the emission of AgI and Ag clusters were detected. This demonstrates that energy or charge carriers can transfer from Ag clusters to AgI clusters and vice versa. It is interesting to find that the emission of AgI clusters is stronger than that of Ag clusters when excitation is at the absorption band of Ag clusters. Similarly the emission of Ag clusters is stronger by indirect excitation into the excited states of AgI clusters than that by direct excitation into the excited states of Ag clusters. These phenomena indicate that energy transfer or carrier migration between AgI and Ag clusters is a dominant process in photo excitation.

** This is different from the possibility of interstitial occupation of Cu in the fcc lattice of Ag*

Details about the interaction and energy transfer between the two clusters are not very clear now, but they are probably related to the structure of the two clusters [90]. Thus a type of composite clusters i.e., clusters each containing some Ag as well as AgI, may be formed upon partial iodization. Each of these composite clusters may have two domains with a sharp boundary separating the Ag from AgI. The structure of the composite AgI-Ag clusters is probably similar to that of mixed CdS-CdSe and ZnO nanoparticles [88,89].

Upon prolonged iodization the emission peak is due to exciton emission (but broad with a low energy tail) at 3.02 eV, redshifted by 70 meV. This red shift is a clear evidence of donor-acceptor recombination [10,11,92-95]. The red shifted PL peak also suggests a Coulombic interaction among the defects. Thus silver ion interstitials and silver ion vacancies could be the defects responsible for the D-A recombination. In particular, the intensity of this blue emission (centered at 440 nm (2.82 eV)) is enhanced by doping of Cu. This luminescence can be explained tentatively as follows.

During photo-excitation of AgI films it is likely that free electrons can be shallowly trapped at the bottom of the conduction band and in addition be coulombically attracted by the interstitial species (e.g., Ag^+ [i]). On the other hand, because the degree of

covalency in AgI is already sufficient to prevent hole self-trapping even at the room temperature and because silver iodide exhibits a relatively stronger covalent tendency as compared to AgBr (e.g. ionicity values of AgI (0.77) < AgBr (0.85) [13]), the self-trapped holes such as those of AgI_6 may be eliminated. Therefore, holes are probably trapped at the vacancy-compensated divalent cations (i.e., Ag^{2+} [Vac] and Cu^{2+} [vac]). The extra holes provided by the charge transfer reaction between Cu^{2+} and Cu^{+} ions are also considered. The Cu^{2+} ions can be formed as a result of the trapping of photo holes by the Cu+ ions; subsequently, under a light energy hν ≥ 2.2eVeV (≤ 564nm), the reverse of this reaction will release a free hole according to the reaction: $Cu^{2+} \rightarrow Cu^{+} + h^{+}$.

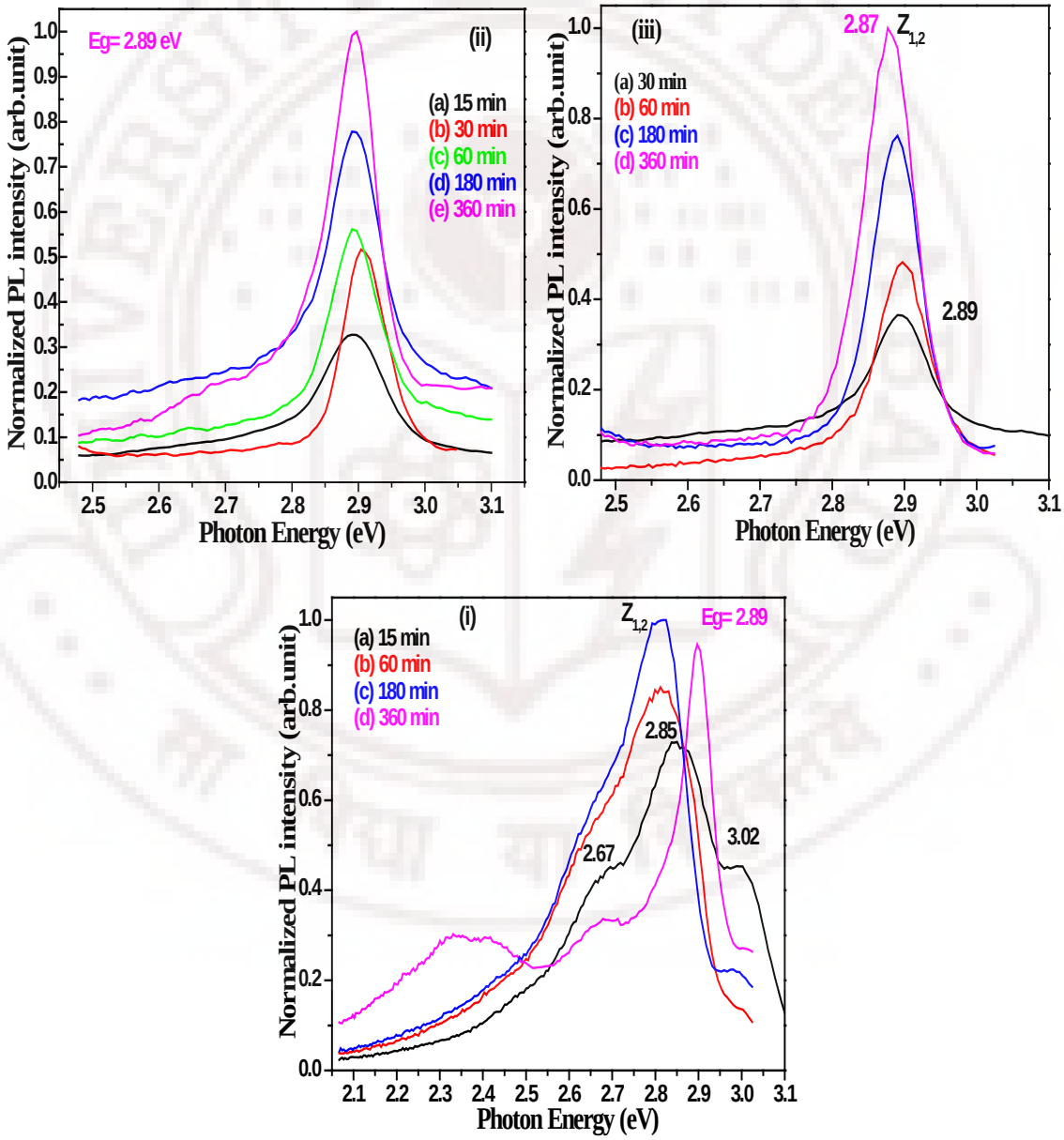

Figure 5.17: Room temperature PL spectra of 5 nm thick (i) $Ag_{0.95}Cu_{0.5}$, (ii) $Ag_{90}Cu_{10}$ and (iii) $Ag_{80}Cu_{20}$ films iodized for (a) 15 (b) 30 (c) 60 (d) 180 (d) 360 min. As the Cu concentration is increased there is a strong intensity enhancement as well as the exciton luminescence peak shift from 2.82 to 2.90 eV due to the confinement effects.

Finally, we suggest that an increase in the concentrations of Cu may increase the amount of AgI: Cu^{+} species in our samples. Therefore, the possible mechanisms for the 440 nm emission can be attributed to the DA radiative recombination from the electron-trapped donor site (e.g., Ag^{+} [i]: e^{-}) to the hole-trapped acceptor site such as Cu^{3+} [vac] and Ag^{3+} [Vac]. Other processes such as the DA recombination from an electron trapped Ag_n^{+} bulk species to an acceptor site such as Cu^{3+} [vac] should also be considered.

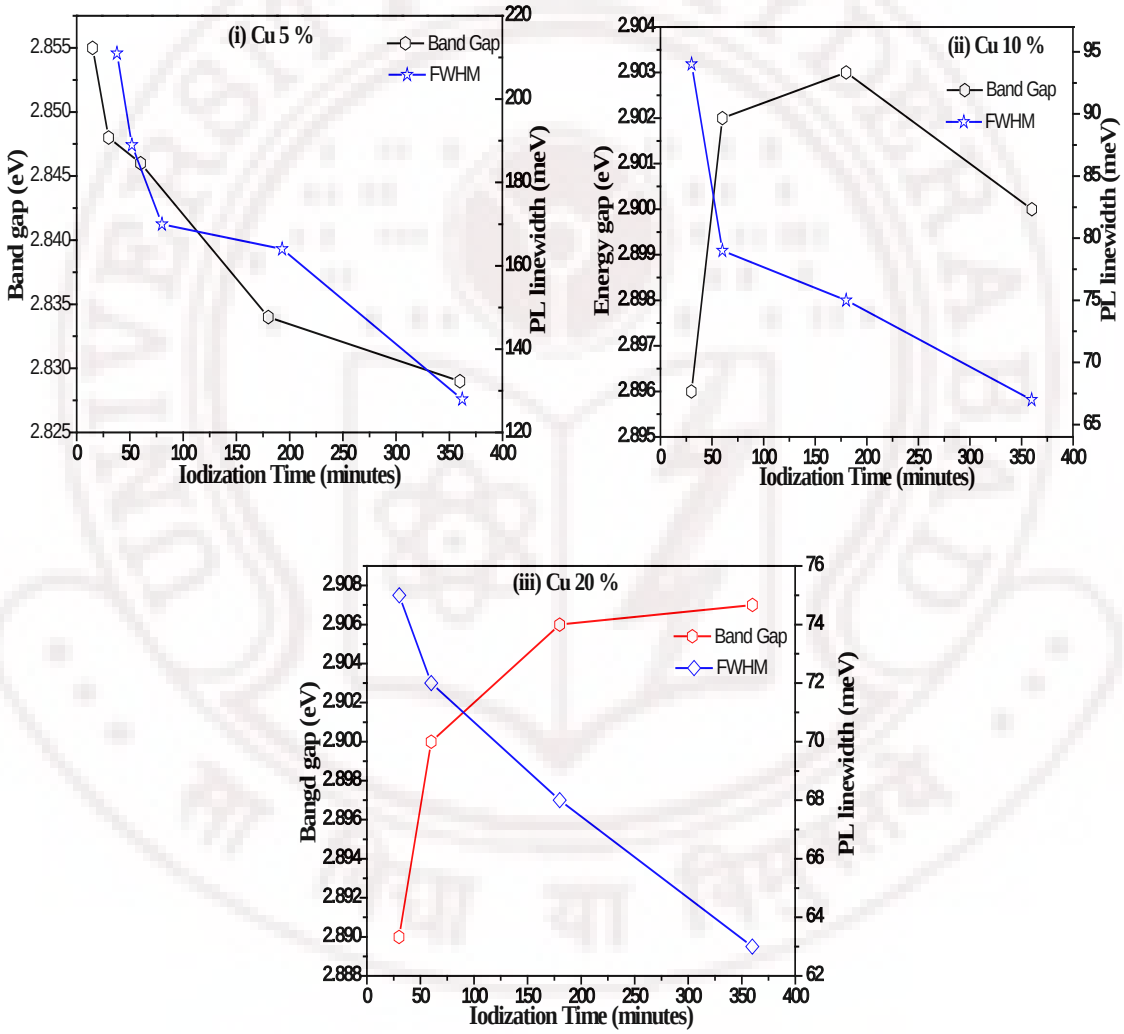

Figure 5.18: Fluctuations in the energy gap and PL line width (FWHM) observed in 5, 10 and 20 % Cu doped 5 nm thick Ag-Cu films iodized at different times. The peak shift is due to Cu^{+} in lattice substitutional position also their may be some kind of compositional fluctuations.

Figure.5.17 shows the normalized emission spectra of 10 and 20 % Cu doped 5 nm Ag thin films iodized at different durations in the range 15-360 min. The 10% Cu substitution into AgI, produces a single intense band 427 nm assigned to the radiative recombination of $Z_{1,2}$ excitons This is the most important change brought about by Cu substitution that too at room temperature-not seen in the literature so far. The spectral structure of the 429 nm peak assigned to D-A recombination of $Z_{1,2}$ excitons changes with iodization time as shown in the inset. The shift in band indicates that there are several shallowly trapped exciton states. In such cases, the lower energy trapped excitons tend to populate higher energy trapped exciton states with increasing Cu content.

The short time (15 min) iodized films shows the broad band at 2.89 eV (427 nm) further iodization at 30 min the broad band becomes narrowed and blue-shifted 2.89 eV, which is close to the intensity maximum (427 nm) of pristine AgI. Therefore, it should be interpreted that the Cu doping delays the iodization as well as controls the surface trapped exciton seen clearly. The narrow peak of the γ-AgI luminescence spectrum on figure 5.18 (ii) shifted by the same amount in the presence of copper and this shift also corresponds to change of effective band gap. The observation of gradual evolution of the optical band gap together with the development of the step like absorption and the corresponding luminescence spectra for AgI is very significant from the point of view of particle growth and associated quantum confinement effect in γ-AgI. We believe that copper is executing an extremely important role in the stabilization of the quantum confinement effect in the I-VII semiconductor. The very small thickness of the films, the extended metastable solubility of Cu in Ag and the condition for the growth of quasi amorphous film have all helped in the stabilization of γ-AgI quantum dot structure at room temperature.

The absence of any characteristic feature of γ-CuI or of β-AgI in the optical spectra of Ag(Cu)I films quite significant, this reflects the fact that the amorphous AgI formed at the initial stage of iodization relaxes to achieve much better defined short-range order than that in CuI before the crystallization process takes place and a complete nanocrystalline film is obtained at 360 minutes iodization. Essentially the role of Cu is to qualitatively change the thin film growth mode from a simple layered type growth to a layered plus island type growth mode after all these film thickness is 5 nm via formation of mixed Ag-Cu cluster as evidence from the optical spectra figure 5.14. Thus the strain-induced size control by Cu helps in the confinement of exciton in γ-AgI nanoparticles and inhomogenity of the PL peak observed even at room temperature represents the particle size distribution as reflected by its FWHM shown in figure 5.18. The PL lineshape

analysis was done by fitting all the PL spectrum using Gaussian functions. The FWHM of the luminescence peak decreases with increasing iodization time but there is not much change in PL line shape as shown in figure 5.18. The nonlinearity in the band gap points to the presence of Cu^{+} in lattice substitutional position also suggests some kind of compositional fluctuations present in the systems [88,89]. However, precise characterization of the exciton energy levels and wave function and the identification of the traps responsible for luminescence must await low-temperature measurements and also time resolved PL investigations.

5.8 Summary

In summary, structural, microstructural exciton and photoluminescence properties of Cu substituted metastable γ-AgI films with thickness of 5 and 15nm on fused silica substrates by RF magnetron sputtering have been studied. The systematic iodization of Ag-Cu alloy films has apparently yields continuous γ-AgI films through 5, 10, and 20 % Cu substitution. Cu stabilized γ-AgI formation shows the AgI particle growth leading to the long term stable γ-AgI phase. The lattice parameter of the γ-AgI zincblende structure systematically reduces upon Cu substitution in accord with our earlier work on $Ag_{1-x}Cu_xI$ ($0<x<1$) nanopowders [6] which gives the evidence of changing the phase transition temperature upon Cu substitution.

The Cu doped γ-AgI films reveals $Z_{1,2}$ and Z_3 exciton transitions with increased broadening of γ-AgI nanoparticles due to the effect of disorder produced during the course of iodization in 5 and 15 nm AgI thin films. The Cu doped AgI films have shown blue shift in the exciton maxima which could be effect of decreasing particle size and thus shown increasing the band gap 2.91 eV at RT (2.82 bulk γ-AgI at RT). The exciton energy blue shift upon Cu substitution due to Cu^{+} in lattice substitutional position.

PL characterization of Cu doped AgI thin films thickness of 5 and 15 nm shown the very strong emission peak at 2.91 eV. The strain induced size control by Cu helps in the confinement of exciton in AgI nanoparticles and the inhomogenity of the PL peak observed even at room temperature represents the particle size distribution as reflected by its fwhm narrowing upon iodization. Thickness and Cu doping favors the quasi free AgI nanoparticles formation which enhances PL emission intensity at RT and more

importantly a drastic reduction in shallow-trap luminescence. Quantum confinement results in the loss of the longer lived components of the D-A emission.

Taking cue from the quartz-substrate induced results described and discussed above it would be fascinating to consider the effects of using a soft substrate such as poly-vinyl alcohol on the nature of Ag nanostructure formation and AgI nanoparticle shape/size evolution upon iodization. Results of such an investigation form the basis of the next chapter.

References

1. M. Hansen, *Constitution of binary Alloy*, pp. 48-49, McGraw Hill, New York, 1958.
2. R. Galbadrakh, V. K. Miloslavsii and U. Mayer, *J. Appl. Phys*, **59**, 571 (1993).
3. P. Senthil Kumar, *"Ionic and Mesoscopic Aspects of Cation Stabilized Silver Iodide"*, Ph.D Thesis, University of Hyderabad, Hyderabad, (2002), India.
4. P. Senthil Kumar and C. S. Sunandana, *Nano Letters*, **2(4)**, 431-434(2002).
5. D. Bharathi Mohan, "*Synthesis and Studies of Cation and Disorder stabilized AgI nanostructured Materials"*, Ph.D Thesis, University of Hyderabad, (2002), Hyderabad, India.
6. D. Bharathi Mohan, C.S. Sunandana, *J. Phys. Chem. Solids*, **65**, 1669(2004).
7. K. Shahi, *Phys. Stat. Sol. A*, **41**, 1144 (1917).
8. K. Shahi, W. Weppner and A. Rabenau, *Phys. Stat. Sol. A*, **93**, 171 (1985).
9. M.Gnanavel, D. Bharathi Mohan, C. S. Sunandana, *Thin Solid Films*, **517**, 1058(2008).
10. D. Bharathi Mohan and C.S.Sunandana, *J, Appl. Phys*, **100**, 064314 (2006).
11. D. B. Mohan, V. S. Reddy and C. S. Sunandana, *Appl. Phys. A*, **86**, 73(2007).
12. S. Fujime, *Jap. J. Appl. Phys*, **5**, 643 (1996).
13. H. Han and T L Alford, *J. Phys. D: Appl. Phys*, **41**, 155306 (2008).
14. Hao Chen and Jian-Min Zuo, *Acta Materialia*, **55**, 1617 (2007).
15. G. De, L. Tapfer, M. Catalano, G. Battagin, F. Caccavale, F. Ganella, P. Mazzolod and R.F. Haglund, *Appl. Phys, Lett*. **68**, 3820 (1996).
16. R.K. Line, *J. Appl. Phys*. **37**, 934 (1996).

17. Xilian Sun, Ruijin Hong, Haihong Hou, Zhengxiu Fan, Jianda Shao, *Thin Solid Films*, **515,** 6962 (2007).
18. P.Senthil Kumar and C. S. Sunandana, *Nano Letters*, **2(4)**, 975(2002).
19. P. Senthil Kumar and C. S. Sunandana, *Thin Solid Films*, **323**, 110-114 (1998).
20. P. Senthil Kumar, P. Babu Dayal and C.S. Sunandana, *Thin Solid Films*, **357**, 111 (1998).
21. L.E. Brady, J. W. Castle and J.F. Hamilton, *Appl. Phys. Lett*, **13(2)**, 76 (1968).
22. G. Sagran, O. Geszti, G. Radnoczi, P.B. Barna and K. Toth, *Thin Solid Films*, **259**, 96 (1995).
23. P. Senthil Kumar, A.K. Tyagi and C. S. Sunandana, *J. Phys. Chem. Solids*, **67**, 1809 (2006).
24. C. Liang, K. Terabe, T. Hasegawa and M. Aono, *J. Appl. Phys*, **102**, 124308 (2007).
25. G. R. Robb, A. Harrison and A. G. Whittaker, *Phys. Chem. Chom*, **5(19)**, 135 (2002).
26. S. Mochizuki and F. Finisher, *J .Phys: Condens. Matter*, **15**, 5057 (2003).
27. S. Mochizuki and F. Fujishiro, *Phys. Stat. Sol. (c)*, **3(10)**, 3586 (2006).
28. C. Kittle. Introduction to solid state physics, 7th edition, *Wiley*, 1996.
29. J. X. Fu, A. Collins, and Y. P. Zhao, *J. Phys. Chem. C*, **112**, 16784 (2008).
30. G. Chumannov, M. S. Sibbald and T. M. Cotton, *J. Phys. Chem. B.*, 102, 10836 (1998).
31. D. B. Pedersen and S. Wang., *J. Phys. Chem. C*, **111**, 1261 (2007).
32. S. Kapoor, R. Josi and T. Mukherjee, *Chem. Phys. Lett*. 354, 443 (2002).
33. M. Grzelczak, Ana sanchez-Lglesias, Bentio Rodriguez- Gonzalez, Ramon Alvarez-Puebla Jorge Perez-Justle and L M Liz- Marzain. *Adv. Funct. Mater*, **18**, 3780 (2008).
34. K. C. Kim, N. D. Theodore and T. L. Alford, *J. Appl. Phys*. **95**, 5180 (2004).
35. Makoto Hirai and Ashok Kumar, J. Appl. Phys, **100**, 014309 (2006).
36. H. Han, Yeong Seok Zoo, J. W. Mayer and T. L. Alford, *J. Appl. Phys*. 102, 0361101 (2007).
37. J. Gonzala, D. Babonneau and C.N. Afonso, *J. Appl. Phys*, **96**, 5163 (2004).
38. S. Chowdhury, V. R. Bhethanabotla and Rajan Sen, *J. Phys. Chem. C*, **113**, 13016 (2009).

39. C. F. Bohren and D. R. Huffman, *Absorption and Scattering of Light by Small Particles*, Wiley, New York (1983).

40. G. Mie, *Ann. Phys*, **25**, (1908) 377.

41. Cecilia Noguez, *Optical Materials*, **27,** 1204-1211 (2005).

42. Cecilia Noguez, *J. Phys. Chem. C,* **111**, 3806 (2007).

43. Stephan Link and Mostafa A. El-Sayed. *J. Phys. Chem. B* **103**, 8410-8426 (1999).

44. P. B. Johnson and R.W. Christy, *Phys. Rev. B,* **6(12)**, (1972) 4370.

45. W. P. Halperin, *Rev. Mod. Phys*, **5(3)**, 533-607 (1986).

46. Kreibig, U.; Vollmer, M. "Optical properties of metal cluster"; Springer: Berlin, 1995.

47. E. N. Economou, *Phys. Rev.* **182(2)**, 539-554 (1969).

48. J. M. Pitarke, V.M. Silkin, E.V Chulkov and P M Echenique, *J. Opt. A: Pure Appl. Opt*, 7, S73-S84 (2005).

49. Josette Rivory, *Phys. Rev B,* **15(6)**, 3119(1977).

50. P. Royer, J. P. Goudonnet, R.J. Warmack and T. L. Ferrell, *Phys. Rev. B,* **36**, 3753 (1987).

51. Tolga Atay, Jung-hoon Song, and Arto V. Nurmikko, *Nano. Lett*, **4**, 1627 (2004).

52. W.A. Weimer and M. J. Dyer, *Appl. Phys. Lett,* **79**, 3164 (2001).

53. W. E. Vargas, D.E. Azofeifa, N. Clark and Marquez, *J. Phys. D: Appl. Phys*, **41**, 02309(2008).

54. R. Guptha, M. J. Dyer and W.A. Weimer, *J. Appl. Phys*, **92**, 5264 (2002).

55. Ganesh Suyal, *Thin Sold Films*, **426**, 53-61 (2003).

56. Y. H. Wang. C. Z. Jiang F. Ren. Q. Q. Wang. D. J. Chen. D. J. Fu. *J. Mater. Sci,* **42**, 7294 (2007).

57. Praveen Taneja and Pusham Ayyub, *Phys. Rev. B.* **65(24)**, 245412 (2002).

58. J. Gonzalo, D. Babonneau, and C. N. Afonso, *J. Appl. Phys*, **96(9)**, 5163 (2004).

59. Ved Varum Agarwall, P. M. Mahalashmi, G. U. Kaulkarni and C. N. R. Rao, *Langmuir*, **22**, 1846 (2006),

60. Jianhui Zhang, Huaiyong Liu, Zhenlin Wang, Naiben Ming, *Journal of Solid State Chemistry*, **180**, 291–1297 (2007).

61. Hao Chen, J.M. Zuo, *Microsc Microanal,* **10**, 817, 2004.

62. Soumya Nag , Kristopher C. Mahdak , Arun Devaraj. Smita Gohil, P. Ayyub, and R. Banerjee, *J. Mater. Sci,* **44**, 3393 (2009).
63. Choon Hwee Bernard Ng and Wai Yip Fan, *J. Phys, Chem. C,* **111**, 29553 (2007).
64. Yu. Ya Gurevich and A.K Ivanov-shits. *Semiconductor properties of Sperionic Materials, Semiconductor and semi metals,* Academic Press, New York, 1988.
65. S. Mochizuki, *Physica B,* **308–310**, 1042–1045 (2001).
66. J. S, Lee, St. Adams and J. Maier, *J. Phys. Chem. Solids*, **61**, 1607 (2000).
67. S.C. Kuirty, S.K. Roy and S.K. Bose, 'Influence of short circuiting on the kinetics and mechanism of iodide films growth on the Ag and Cd-doped Ag, *Met. & Mat. Trans. B,* **28**, 1189 (1997).
68. Manuel Caradona, *Phys. Rev,* **129(1)**, 69(1963).
69. S. Kondo, T. Itoh, and T. Saito, *Phys. Rev B,* **57(20)**, 13235(1998).
70. Chester R. Berry, *Phys. Rev. B,* **161(3)**, 611 (1967).
71. Shosuke Mochizuki and Kouta Umezawa, *Physics Letters A,* **228**, 111(1997).
72. O. Husberg, H. Vogelsang, W. Von der Osten, *J. Luminescence*, **96**, 155 (2002).
73. Michal Ilana Freedhoff, Alfred P. Marchetti, George L. Mclendon *J. Luminescence*, **70**, 400 (1996).
74. T. H. Wei, C. W. Chen, L.C. H. Wang, P. L. Tu, T, C. Wen, *Journal of Luminescence,* **128**, 161-165 (2008).
75. G. Mshvelidse, O. Gogolin, E. Tsitsishvili, Ch. MaÈrkle J.S. Chadha, A. Hepting, F. Gindele, W. Petri, W. Send, D. Gerthsen, U. Woggon, and C. Klingshirn, *Phys. Stat. Sol (b),* **207**,369 (1998).
76. S.K. Suri and H. K. Henisch, *Phys, Stat. Sol. (b),* **44**, 627 (1971).
77. Nche T. Fofang, Tae-Ho Park, Oara Neumann, Nikolay A. Mirin, Peter Nordlander, and Naomi J. Halas, *Nano Letter,* **8(10),** 3481 (2008).
78. O. Golin, G. Mshvelidze, M. Sxhmidt, E. Tsitsishvili, O. Bakradze, A. Hepting, C. Klingshirn, *J. Luminescence*, **102-103**, 451 (2003).
79. A. N. Pikhtin and H. H. Hegazy, *Semiconductors*, **43(10)**, 1259 (2009).
80. H. T. Grahn, "*Introduction to semiconductor physics"* World Scientific Publishing Co. Pte. Ltd, Singapore, 1999.
81. A.P. Marchetti, J. C. Hansen, S. Chen, M. Irving, R. Baetzold, and B. R. Sever, *Phys. Rev. B,* **69**, 094107 (2004).
82. Chaghao Liang, Kazuya Terabe, Tohru Tsuruoka, Minoru Osada, Tsuyoshi Hasegwa, *Adv. Funct. Mater*, **17**, 1466 (2007).

83. S. Mochizuki and Fumito Fujishiro, *J. Phys.: Condens. Matter,* **16**, 3239-3256 (2004).
84. S. Mochizuki and F. Fujishiro, *Phys. Sat. Sol. (c)*, **2**, 763 (2003).
85. H. Vogelsang, O. Husberg, W. Von der Osten, *J. Lumin*, **86**, 87-94 (2000).
86. L. E. Brus, *J. Chem. Phys*. **80(9)**, 4403 (1984).
87. Tito Trindade, Paul O'Brien and Nigel L. Pickett, *Chem. Mater*. **13**, 3843 (2001).
88. L. A. Swafford, L. A. Weigand, M. J. Bowers, J. R. McBride, J. L. Rapaport, T. L. Watt, K. Sriram, D. Leonard C. Feldman, and J. Sandra.Rosenthal, *J. Amer. Chem. Soc*. **128**, 12299-12306 (2006).
89. Keigo Suzuki, Hiroyuki Kondo, Masashi Inoguchi, Nobuhiko Tanaka, Keisuke Kageyama, and Hiroshi Takagi, *Appl. Phys. Lett*, **94**, 223103 (2009).
90. A. Ben Fredi, M. Debbichi, M. Said, *Microelectronics Journal,* **38**, 860–870 (2007).
91. Wei Chen, Zhanguo Wang, Zhaojun Lin, and Lanying Lin, Keming Fang and Yan Xu, Mianzeng Su and Jianhua Lin, *J. Appl. Phys*, **83**, 3811(1998).
92. O. Schops, N. Le Thomas, U. Wagon, and M. V. Artemyev, *J. Phys. Chem. B,* **110,** 2074 (2006).
93. F. O Lucas, A Mitra, P. J McNally, S. Daniels, A. L Bradley, D. M Taylor, Y. Y Proskuryakov, K. Durose and D. C. Cameron, *J. Phys. D: Appl. Phys*, **40,** 3461(2007).
94. C. Y. Wong, Jeongho Kim, P. Sreekumari Nair, M. C. Nagy, and G. D. Scholes, *J. Phys. Chem. C*, **113,** 795 (2009).
95. R. S. Bauer and W.E. Spicer, *Phys. Rev. B,* **14**, 4359 (1976).

Chapter VI

Iodization time dependent Surface plasmon to exciton transition and Photoluminescence study of Core shell Silver Iodide thin films sputtered On PVA substrates

6.1 Introduction

The noble metal nanoparticles embedded in thin polymer films are versatile composite materials combining the unique properties of nanoparticles and polymers, a contemporary area of research with much application. We have fabricated Ag and AgI thin films on poly (vinyl alcohol) PVA substrates by RF magnetron sputtering technique. The fabrication technique adopted here provides free-standing and supported films with a range of applications. We visualized that the Ex *situ* growth of metal nanoparticles in thin polymer films constitutes a unique platform to nurture the growth of nanostructures. These films were systematically iodized and carefully characterized. The uniodized Ag films are quasi-amorphous while briefly iodized films show characteristic γ-AgI structure is vividly revealed by selected area electron diffraction (SAED). Most interestingly TEM scan of Ag and AgI films enable us to see the uniform spherical shaped nanoparticles whose shape evolves spectacularly upon iodization. Optical absorption spectra of uniodized Ag films show intense SPR features with maxima at 415, 417 and 420 nm for the films of thickness 3, 5 and 10 nm respectively. Finally an interesting and unique SPR-exciton phase transition is observed as the ultrathin films are progressively iodized. The transition typically begins after 15 minutes iodization and complete 360 minutes iodization. Blue shift is observed as a result of decreasing particle size thereby increasing the quantum confinement effects is seen as a increase in the band gap. The photoluminescence studies show that the donor-accepter recombination rate enhanced by thickness and particle size reduction give rise to the enhanced PL emission.

6.2 Experimental details

6.2.1 AgI thin film fabrication

Thin Ag films with thicknesses of 5 and 10 nm were deposited at room temperature on 100 nm thick poly (vinyl alcohol) PVA coated glass substrates by RF magnetron sputtering. The highly pure silver metal targets (Aldrich, 99.999 %) are used for thin films depositions. Here we have used "up sputtering" (target at bottom and substrate at top) to deposit silver metal film. Initially, the sputtering chamber was evacuated to a base pressure of $2x10^{-6}$ Torr after loading the PVA coated glass substrates on to the substrate holder placed inside the vacuum chamber. All of the films were deposited at a fixed RF power of 10 W. A working pressure of 10 mTorr was constantly maintained using high pure argon (purity: 99.999%). The argon pressure was 10 sccm to get uniform rate of deposition. The target to substrate distance was fixed at 15 cm. It was observed that even without any substrate heating, the un-cooled substrate temperature increased to about 50-80^{o}C during the deposition, presumably due to ion bombardment. To avoid this substrate heating substrate was kept at distances higher than usual (through scattering will be more). The rate of deposition was maintained constant during the entire depositions. The above conditions were found favorable for the formation of homogeneous metal thin films. Thickness of the films was determined by using AMBIOS XP-1 profilometer.

6.2.2 PVA substrate preparation: 3.5 gm of PVA powder (Aldrich, average molecular weight = 1,300 kDa) was dissolved in 16 ml de-ionized water under constant string, until becomes a transparent solution. In order to prepare PVA thin film, the above solution was diluted by adding water. The solution was stirred for 5 min at ambient temperature (~ 25^{0}C), always protecting it from light. Subsequently the PVA solution was spin coated directly on top of a glass substrate using a Laurell Technologies Corporation Model WS-400B-6NPP/LITE/8K Photoresist Spinner at 500 RPM for 10 sec followed by 4000 RPM for 10 sec.

6.2.3 TEM sample preparation: In order to prepare AgI thin films for TEM imaging, the substrate was prepared as follows. A few drops of a solution of polystyrene, PS (average molecular weight = 280 kDa) in toluene (1 g in 8 ml) was spin-coated on glass substrate at 1,000 RPM for 10 sec and dried in a hot air oven at 90°C for 10 - 15 min. The PVA solution was spin-coated on the polystyrene layer and dried under dry nitrogen gas for 3 min. These substrates were used for Ag metal films deposition. Finally Ag/PVA films

were iodized systematically at different times ranging from 5 min to 180 min. Finally dipping this plate in toluene, the PS layer was dissolved and the AgI-PVA film that becomes free which was collected on a 200-mesh copper grid for TEM imaging [1-3].

6.3 Spectroscopic and TEM Monitoring of Growth process

As discussed earlier nanoparticles of noble metals (Au, Ag, and Cu) display very interesting optical properties due to so-called surface plasmon resonances, which involve the collective oscillation of conduction electrons in resonance with the alternating electric field of incident electromagnetic radiation. The frequency of the surface plasmon mainly depends on the nature (dielectric function) of the metal, but is largely affected by the size and shape of the nanoparticles, or by their dielectric environment, among other parameters. Such resonances result in bright colours, as well as large enhancements of the local electric fields around the particles. The optical response of anisotropic shape and size typically involves two surface plasmon modes, associated with the oscillation of conduction electrons, either parallel (longitudinal surface plasmon, LSP) or perpendicular (transverse surface plasmon, TSP) to the long axis [4-15]. The influence of substrate on the tunability of the localized surface plasmon resonance wavelength, λ_{SPR} of silver island films was investigated by magnetron sputtering the films on PVA coated glass substrates [16-21]. It reveals that increasing refractive index of the substrate, n_{sub}, not only leads to redshift, but also an extension of the tunable range in λ_{SPR}. Such effects can be greatly enhanced by increasing the mass thickness of the metallic islands. The resonance wavelength of an island film can be readily adjusted from the visible to the near infrared region of the electromagnetic spectrum. The presence of distinct halide ions and their molar ratios in this reaction condition resulted in the formation of diverse morphologies, i.e., spheroid, triangular (or irregularly circular) nanoplates [22-25]. In particular, a minuscule amount of iodide ion (a few mg I_2) was crucial for the formation of a triangular disk (and a circular disk at higher concentration) instead of a nanorod. In spite of the minimal amount of iodide, the resulting dramatic change of the nanocrystals morphology is largely attributed to the adsorption of iodide on low-indexed silver surfaces, allowing for a distinct growth rate of the present redox pair Ag-PVA on each facet.

In figure 6.1 spectrum shows the experimental UV–vis spectrum of silver thin films on PVA substrates. As deposited 3 and 5nm Ag film shows a symmetric absorption band whose maximum absorption occurs at 413 and 417 nm. When thickness was

increased to 8 and 10 nm spectrum shows a single peak, but asymmetric, whose maximum absorbance occurs at 435 and 438 nm respectively and that arise from the longitudinal surface plasmon resonance of Ag films. The LSPR absorption peak intensity and FWHM increases with increasing film thickness. 3 and 5nm thick Ag films show typically spherical Ag nanoparticle shape and exhibit more intense and sharper LSPR spectra and narrower LSPR bandwidth found in Ag-PVA thin films predicts a much more precise quantification of the LSPR spectrum variations in response to refractive index changes in the surrounding medium of the Ag NPs. With increasing film thickness, the volume fraction will increase and the interparticle distance decreases which causes the aggregation NPs. This effect can be attributed to an increase in the average size of the NPs growing by the Ostwald ripening mechanism.

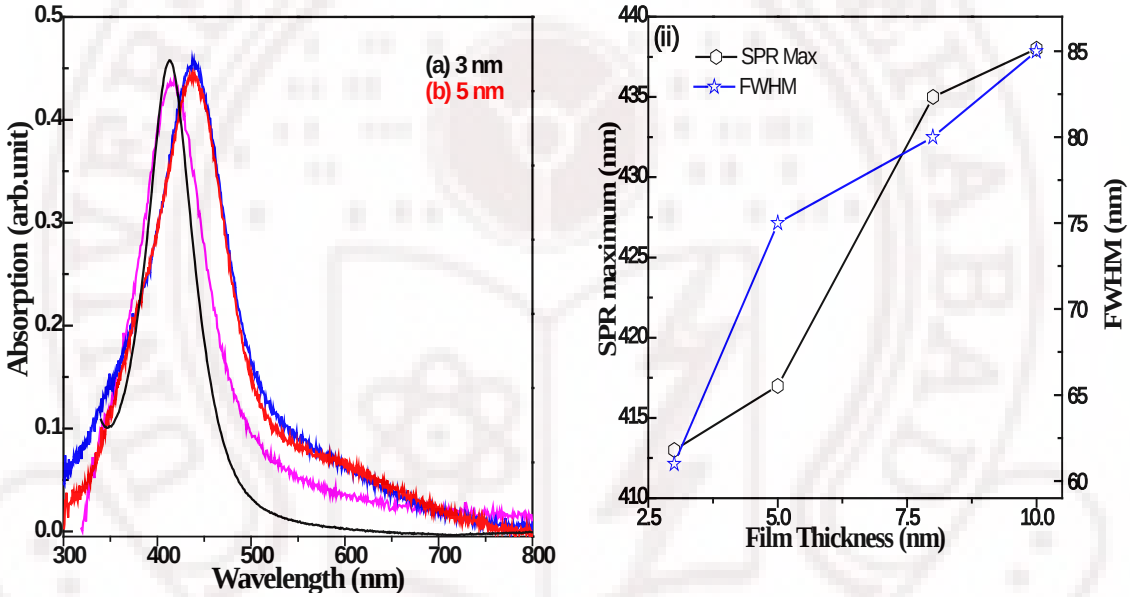

Figure 6.1: (i) Surface plasmon resonance of ultra thin Ag films thickness of 3 and 5 nm deposited on 100 nm thick PVA coated glass substrates. (ii) Thickness dependence of SPR peak maxima and line width.

The position of the surface plasmon absorption peak of widely separated spherical silver particles depends on the refractive index of the surrounding medium, particle size and substances adsorbed on their surfaces. If one considers that the true position of the SPR of spherical silver nanoparticles (particle diameter 10 nm) in water predicted to be 382±1nm [17] as predicted then the redshift observed for the absorption peak of silver particles in PVA must be due to the larger refractive index of polymeric matrix. This experimental result agrees with theoretical predictions, which indicate that the position of the surface plasmon absorption band of silver particles embedded in solid polymer matrix

shifts to longer wavelengths [15,16]. As a result, a notable wavelength shift of SPR is expected to occur as predicted by simple Mie theory.

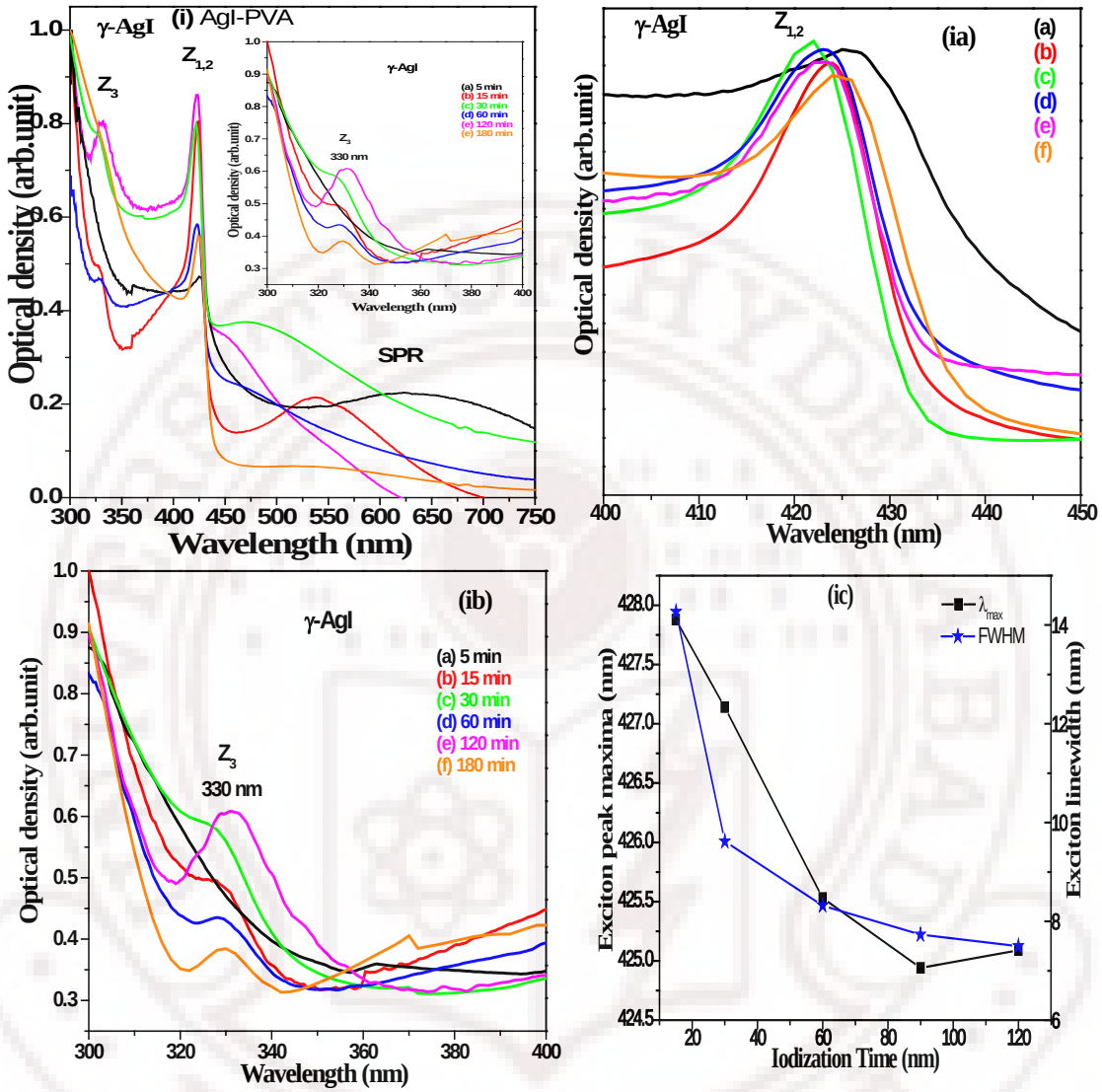

Figure 6.2: Evolution of the exciton absorption bands in PVA backed Ag films upon iodization. Figure 6.2 (ia) and (ib) shows the systematic development of $Z_{1,2}$ and Z_3 zincblende AgI structure. (ic) exciton peak ($Z_{1,2}$) maxima and line width as a function of iodization time which increases the exciton maxima with reduced FWHM due to formation of AgI.

The sharpness of SPR observed here compared to the rather broad SPR found in vacuum thermal evaporated Ag films on glass substrates indicates the extent of particle size and even growth mode control exercised by the PVA film. Indeed, the PVA surface offers an electrostatically charged medium whose (local) electric field could influence film formation and particle growth (to be explained later in this chapter).

Figure 6.2 shows the UV/visible optical absorption spectra of 5 nm thin Ag films deposited on PVA coated glass substrates and systematically iodized for duration from 5 to 180 minutes. In short time (5 min) iodized Ag films the exciton peak at 428 nm which is characteristic of ($Z_{1,2}$) γ-AgI zincblende structure besides the SPR features co-existing in such films. Exciton peaks observed near at 330 and 424 nm correspond to the two spin orbit components of exciton excitation in AgI. The observation of these features is indicative of conversion of Ag to AgI upon iodization of Ag film to the I_2 vapor (interface effects). With uptake of iodine, the SPR of the Ag nanoparticles, which is sensitive to change in the refractive index of the medium at or near the particle size, shifts steadily to longer wavelengths as seen in the inset shown in figure 6.2 loss of the SPR band, or more specifically a loss of the low wavelength component and growth at longer wavelength, occurs whenever the refractive index of the medium surrounding nanoparticles increases and is therefore by itself, not characteristic of chemical reaction. It can be caused by physisorption of I_2 on the surface of the particles [26-32]. In figure 6.2 the position of the SPR band of the Ag is shown as a function of the iodization time. The SPR shifts smoothly to longer wavelength as the silver nanoparticles converted to AgI, which is most consistent with an AgI shell or islands of AgI forming on the Ag nanoparticle surfaces. Due to the small size of these particles (15 nm) the decrease of Ag core size due to conversion to AgI is not expected to shift SPR of lower wavelengths significantly. The SPR peak position is relatively size independent for nanoparticles with diameters less than ~ 20 nm. Upon prolonged iodization (30 minutes) the $Z_{1,2}$ and Z_3 exciton peaks at 424 nm and 330 nm appear in the absorption spectra. Formation of the Ag @ AgI core shell and change in shell thickness were observed systematically as a function of iodization time shown as in figure 6.4. During reaction of the Ag/PVA nanoparticles with I_2, the AgI formed cannot be leaving the Ag nanoparticle surface as such a reaction mechanism would not lead to a shift of the SPR to longer wavelengths. Similarly, the appearance of the exciton absorption of AgI in the spectra as the reaction proceeds is evidence of formation of increased particle size of AgI this size being large enough to have a band gap (exciton) near 424 nm. The long time iodization decreases the confinement effect due to increase of particle size when their effective particle diameter decreases. These results are most compatible with Ag @ AgI core-shell formation. The magnitude of SPR shifts, by as much as 150 nm as seen in short time iodized Ag films shown in figure 6.2. The 424 nm exciton peak, the sharp rise in absorption at 330 nm and the long wavelength tail due to the intrinsic Frenkel disorder completely characterize the

excitons derived from as plasmon through the plasmon exciton transition. Upon prolonged iodization upto 180 min the $Z_{1,2}$ peak becomes progressively sharper, with the peak position shifting towards blue region confirming the formation of nanocrystalline γ-AgI structure [32-36]. The exciton peak is considerably sharp indicating a single median size of particles. Exciton line width (FWHM) varies from 14 to 7.5 nm as a function of iodization time shown in figure 6.2. Even at 180 min iodization the Z_3 peaks is very stable which shows the strong evidence of quasi free exciton formation and no indication of any β-AgI (wurtzite) phase. AgI coated on polymer matrix clearly reveals the controlled growth of γ-AgI $Z_{1,2}$ and Z_3 exciton (where as in previous chapter we have seen as iodization time increases the Z_3 peak intensity slowly decreases) which stabilizes the γ-AgI even upon long time iodization. (Significantly the PVA matrix is seen to effectively prevent the nucleation and growth of beta AgI.) This spectrum can be interpreted along the same lines as the absorption edge of other materials with zincblende structure. The strength of the exciton spectrum suggests direct allowed transitions which, by analogy with the other zincblende materials should occur at k=0, the top of the valence band (Γ_{15}) is triply degenerate without spin orbit interaction in the zincblende structure. This degeneracy is reduced by spin orbit splitting to a doubly degenerate state (Γ_8) and a singlet (Γ_6). The (Γ_8) doublet favours the formation of $Z_{1,2}$ peaks whose degeneracy is lifted in AgI /PVA films probably as a result of interfacial strain [33].

6.4 Quantum Confinement Effect

AgI was the one of the first materials in which quantum confinement effects on the exciton were observed [34]. Upon iodization of 5 nm Ag films the conversion of the surface of Ag nanoparticles to AgI manifests as the growth of an AgI shell from an initial thickness of near zero to a thickness of a most 15 nm (conversion of Ag to AgI). In this regime, confinement effects impact the energetics of exciton excitation in direct band gap materials. By fitting Gaussian functions to the exciton peak in the derivative spectrum, the peak position was determined for a series of spectra and results are shown in figure 6.2 (1a). At different time of iodization, the peak position and roughness changes which reflect variability in the Ag nanoparticle sizes and extent of aggregate formation due to slightly different source and deposition conditions as well as to differences in the roughness of the PVA substrates on which the nanoparticles were deposited. In short time iodization initially, the exciton peak maxima show up at 428 nm while upon prolonged iodization peak maxima shift to lower energies with increased I_2 exposure time; at the

longer exposure times (~180 min) they asymptotically approach a constant value. Bulk AgI can assume zinc-blend structure with a band gap of 2.82 eV at room temperature. The variance could be due to differences in the final shell thickness obtained and the overall diameter distribution of the Ag@AgI nanoparticles. It may also reflect difference in the crystalline structure that the AgI shell assumes due to variations in interfacial structure, in the overall polycrystalline matrix. The confinement energy was calculated by using Brus equation (eq 1) as follows [37]:

$$E_x \cong E_g + \frac{\hbar^2\pi^2}{2R^2}\left[\frac{1}{m^*_e} + \frac{1}{m^*_h}\right] - \frac{1.8e^2}{4\pi\varepsilon\varepsilon_o R} \qquad (6.1)$$

where $E_g \approx 2.82$eV; R is the cluster radius; m^*_e and m^*_h, the electron and hole effective masses, respectively; and εεo, the dielectric constant. $m_e^* = 0.26m_e$, $m_h^* = 0.7m_e$ and $\varepsilon\varepsilon_o = 4.0 \times (8.85\times10^{-12} C^2 J^{-1} m^{-1})$ were used.

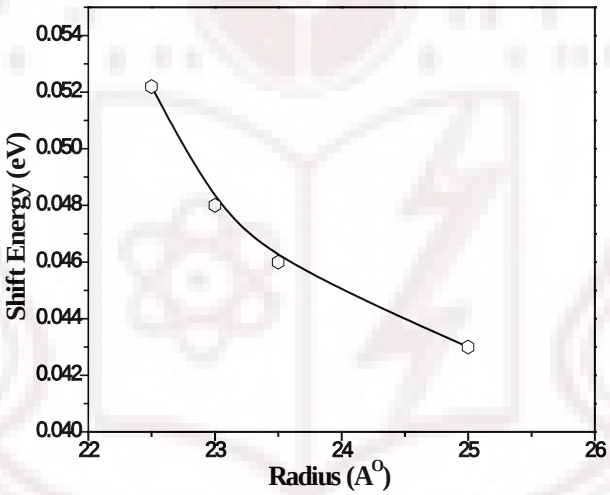

Figure 6.3: A plot of the theoretically computed change in peak position *vs* experimental results

Figure 6.3 shows the nonlinear decrease in energy as the trend expected of direct band gap nano materials whose dimensions are systematically being increased as a function of iodization time. There is decrease in the energy gap as the diameter of the quantum dot is increased. This trend is attributable to difference in the final shell thickness obtained and the overall diameter of the AgI nanoparticles. The band gap obtained corresponds to that of AgI nanoparticles with a diameter of between 2 to 3 A^o. As the excitons generated in the AgI shell are free to travel over the entire surface of the nanoparticles; the effective diameter should be close to that of the original Ag nanoparticles shown in TEM results. The difference between the effective diameter and

the actual particle diameter may be attributed to confinement and/or variations in the interfacial energy of the AgI shell on the Ag core (figure 4 and 5). The second spin-orbit component of the AgI exciton appearing at ~330 nm in the γ-AgI nanoparticles indicates that the wave function associated with the hole generated upon creation of the exciton is poorly shielded from the AgI surface. As the two spin orbit components of the exciton have different symmetries, it is reasonable to assume that the spatial extent of one, and the strength of its interaction with the AgI surface, is greater than the other as shown in figure 6.2. That the surface effects are generally accentuated and variability in the exciton peak position is much higher than that of observed in bulk AgI is not surprising.

6.5 Grain growth and structural analysis of AgI nanoparticle

Ultra thin (< 5nm) Ag films sputter- deposited on PVA matrix consist of some particles likely to diffuse inside the polymer matrix which nucleate and grow into nanocrystals. Studies of ex-situ reduction of Ag^+ inside PVA film have shown that the oxygen atoms of the polymer are coordinated to the precursor Ag^+ ions. Since the molecular level interactions of PVA with the Ag atoms are likely to be weaker than that with the Ag+ ions, an effective increase in volume may be expected to occur in the vicinity of emerging nanoparticles. The dynamic processes occurring inside the polymer could then lead to fluctuations of the surface profile, but eventually a net growth will be manifested. PVA is most popular as a stabilizer for nanoparticles; however it can also act as a reducing agent in the formation of metal nanoparticles. Interestingly, we found that Ag^+ undergoes facile reduction to Ag inside the PVA coated glass substrates, even under ambient conditions [1-3].

TEM monitoring of the iodization progress, revealed the formation of Ag and AgI core-shell nano particles as a function of iodization time. TEM images show that the particles are characterized by multiple *twin planes* [17,22] development upon iodization as shown in figure 6.4, 6.5, during the short and long time iodization of 5 nm Ag films. The AgI nanoparticles formed from the initial ambient oxidation of Ag^0 atoms followed by the reaction of Ag^+ with I^-, which grew via atomic addition and/or aggregation. It may be initially puzzling how Ag^0 may be oxidized in a reducing PVA environment. TEM analysis of uniodized 5 nm Ag thin films deposited on PVA substrates revealed that a large proportion of the nanocrystals exhibits spherical shape morphology, with the average particle size of 15 nm. Short time (5 min) iodized Ag films have also shown spherical particles with Ag@AgI core-shell AgI nanoparticle growth. It is important to

point out that AgI decomposes rapidly under the intense electron beam and thus the samples were viewed under low magnifications and electron beam intensities. All images were acquired of the nanocrystals in less than one minute exposure to the electron beam to minimize decomposition. The selected area electron diffraction (SAED) of the short time iodized Ag films show rings that could be indexed to Miller planes of Ag and zincblende γ-AgI core shell nanoparticle growth. The prolonged iodization of Ag films clearly indicated that shell thickness increases which indicates the iodine diffuse the via Ag surface to form full-fledged AgI nanoparticles which were systematically monitored by TEM analysis

6.6 Iodine induces AgI nano particle growth

Iodization time dependent Ag nanoparticle growth mechanism has been essentially explained. However, the kinetics of nucleation and the growth mechanism have drawn much attention, in addition to thermodynamics or physical restrictions imposed by the surface stabilizing agent. The addition of Cl^-, Br^-, or Fe^{3+} leads to the formation of single-crystalline, single-twinned, and multiple-twinned Ag seeds which grow to produce triangles, pyramids, cubes, hexagonal, wires and rods of silver particles. This phenomenon was explained by the influence of the additives on the extent of oxidative dissolution of the Ag nuclei. They found that nanoparticles with twin defects are preferentially etched in the presence of Cl^-, Br^-, and air, leading to high yields of single-crystal and single-twinned seeds [10,15,24,28-29,38].

In this work, we have studied substrates and iodization time dependent anisotropic AgI nanoparticle formation using 5 nm thin Ag films deposited on PVA coated glass substrates by RF magnetron sputtering. The simple iodization process lies in the use of I^- as an oxidative etching regulator for the selective nucleation of twinned seeds and subsequently as a reactant to effect a tandem reaction to form AgI nanoparticles. Furthermore, the ability of I^- to serve as a stabilizing agent overcomes the need for the introduction of an external capping agent, which greatly reduces the complexity of the reaction. The twins (stacking faults) are commonly formed for Ag and Au due to their low stacking fault energy. The formations of twin planes were observed during the TEM imaging of the AgI nanoparticles, which shows single and multi-twinned structures. The formation of many single and triple-twinned particles may be due to I^- ion during the iodization process. Hence, I^- ion enables sufficient etching to eliminate the seeds with multiple twin defects but not so much as to form single-crystalline seeds. The twinning

observed in the Ag seeds could have directed the formation of AgI nano triangles in a manner similar to previously reported formation mechanisms of metallic nanoplates [10,24].

Upon prolonged iodization of Ag films showed the *dumbbell* shape nanoparticle growth. Iodization time dependent shape transformation which observed in the system might be explained as nucleation of triangular platelets whose growth is inhibited due to the depletion of iodine while the nanorods/wires (figure 6a) could have grown from the small amounts of twinned seeds that survive the iodization induced I^- catalyzed oxidative etching. To consolidate the fundamental influence of the Ag nanoparticle growth in directing the formation of AgI triangular nanoparticles, we observed the morphology of the Ag nanocrystals by simply iodizing Ag films as shown in figure 6.7. The systematic iodization of Ag films resulted in the formation AgI clusters with no definite morphology/geometry [39]. In a general sense, the reaction of preformed metallic nanoparticle with other reactive species (e.g., halides, chalcogenides) might provide a convenient channel for the shape-controlled production of semiconductor nanostructures, with the final shapes being determined by the structure (twinning) of the seed.

Prolonged iodization (24 hr) of 5 nm thin Ag films shows the development of anisotropic AgI nanoparticles, suggesting that iodine rich β-AgI structure get stabilized. The β-AgI is more stable at room temperature whereas γ-AgI may be present as impurity. The long time iodization of thin Ag films favours stabilization of β-AgI through interesting changes in particle shape and size. However, it is observed that nanocrystals size increase correlates with the formation of larger nano triangles and bi-pyramids. Iodization of Ag films is likely to be the limiting process (due to multiple role of I_2) and an increase in its local concentration would lead to enhanced growth as well as phase transition [10,24]. Long time iodization has shown the formation of triangular platelets but in case of structural stabilization it favors for β-AgI which is unavoidable.

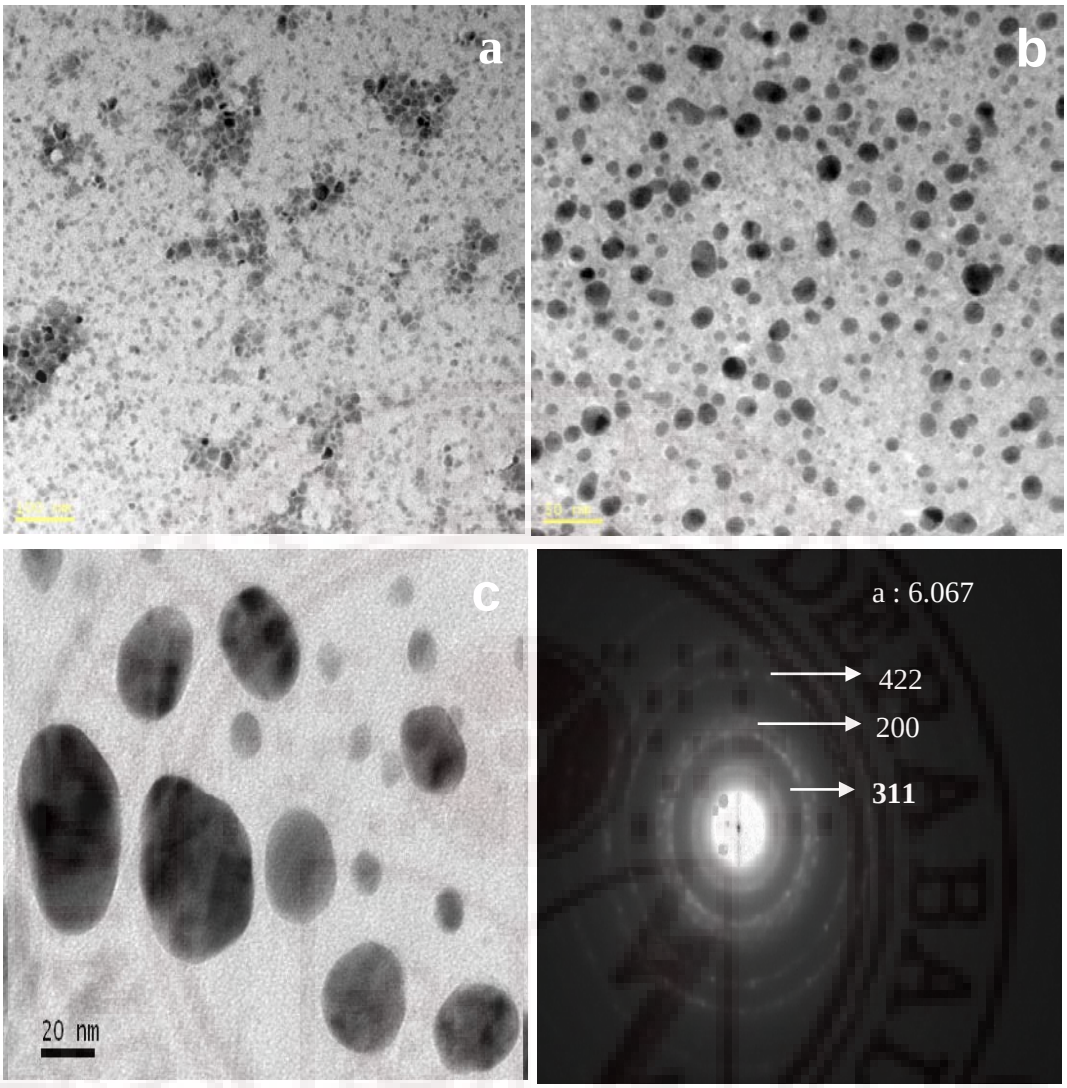

Figure 6.4: TEM image of 5 nm thin Ag film deposited on PVA coated glass substrates and iodized at different times. (a), (b) and (c) short time (30 min), iodized Ag film shows the self assembled AgI core-shell (Ag @ AgI) nanoparticle formation. Selected area electron diffraction pattern (SAED) of figure 6.4. (c) 30 min iodized 5 nm thin Ag films shown formation of γ-AgI zincblende structure.

We have carried out selected area electron diffraction (SAED) by using TEM investigations on partly and completely iodized Ag films. Figure 6.4 (d) show the SAED patterns taken at normal position of a sample relative to the electron beam, respectively. This predicts the development of a preferred orientation (111) of AgI nano crystals by the reaction of randomly oriented polycrystalline Ag films and iodine, since the films certainly contain a large number of Ag grains having the above orientations. In the present study we tried to confirm or exclude the coexistence of hexagonal and face centered cubic phases of AgI, which is widely discussed in the literature [40]. As the

SAED patterns of (111) planes in cubic AgI cannot be distinguished from the patterns of hexagonal AgI, it is hard to confirm the presence of face centered cubic AgI.

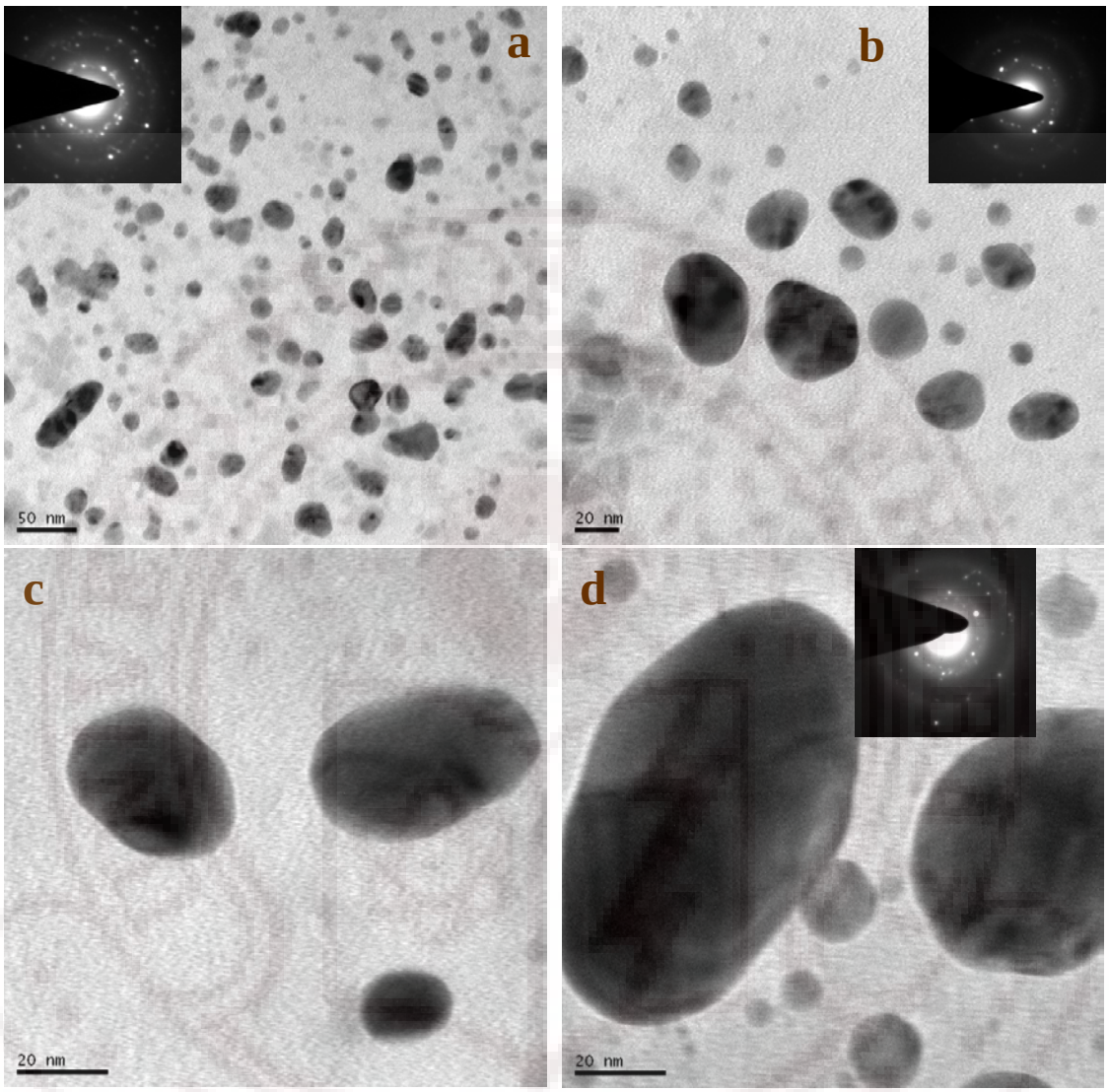

Figure 6.5: TEM images of 60 min iodized 5 nm Ag film showing the iodine induced growth of Ag seeds converted into anisotropic shape and size AgI nanoparticles growth in PVA matrix upon iodization. Figure 6.5 (c) and (d) show the core-shell type growth, where shell thickness increases as a function of iodization time. SAED pattern of 60 minutes iodized sample shows the twin crystal formation which increases crystallinity.

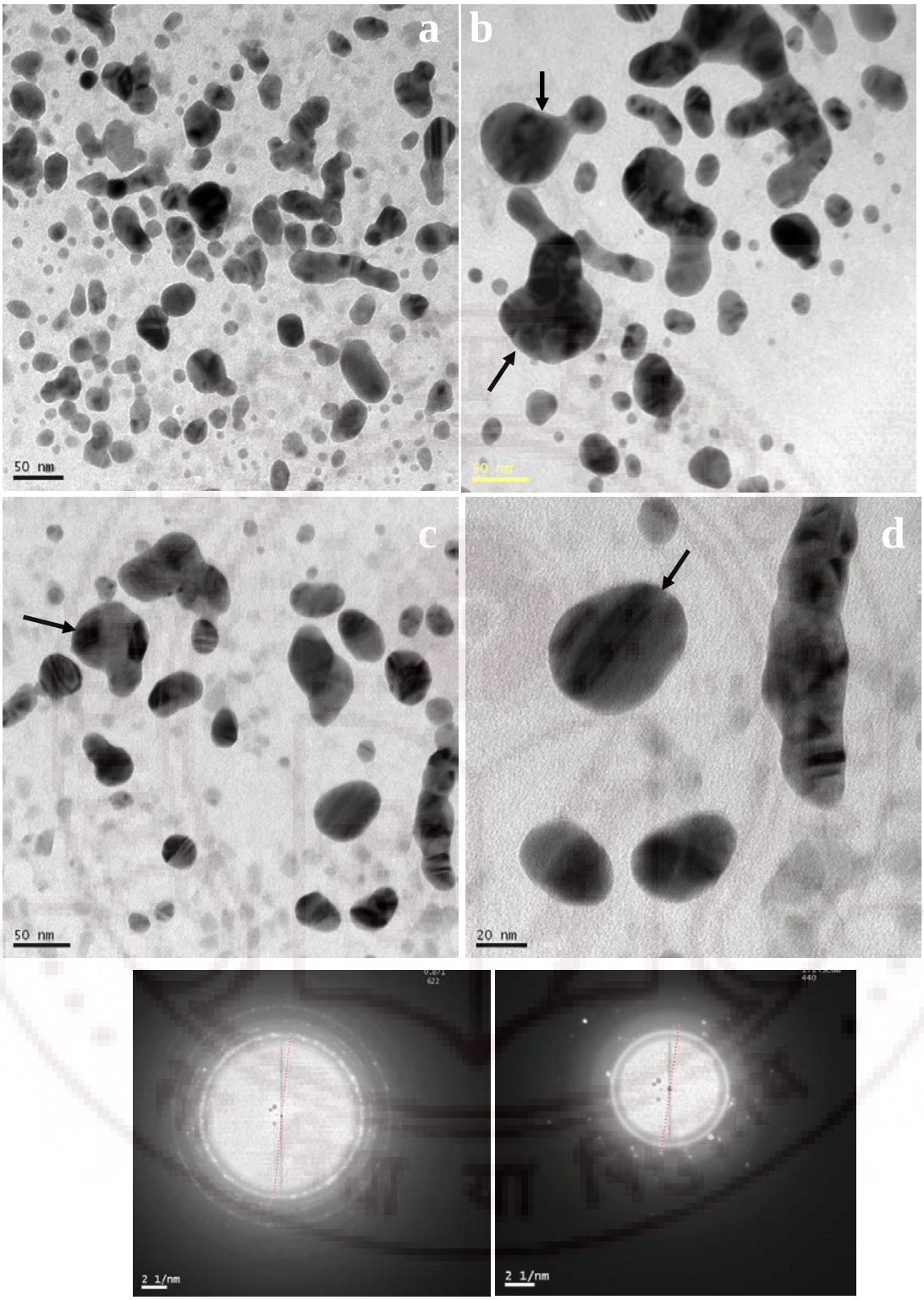

Figure 6.6: showing the TEM and SAED of 180 min iodized 5 nm Ag films. TEM images depict the dumbbell and rod like anisotropic growth of AgI nanocrystals. The twinned dumbbell and nano rods are containing single and multiple twins are also present. SAED pattern show direct evidence of highly polycrystalline γ-AgI zincblende structure.

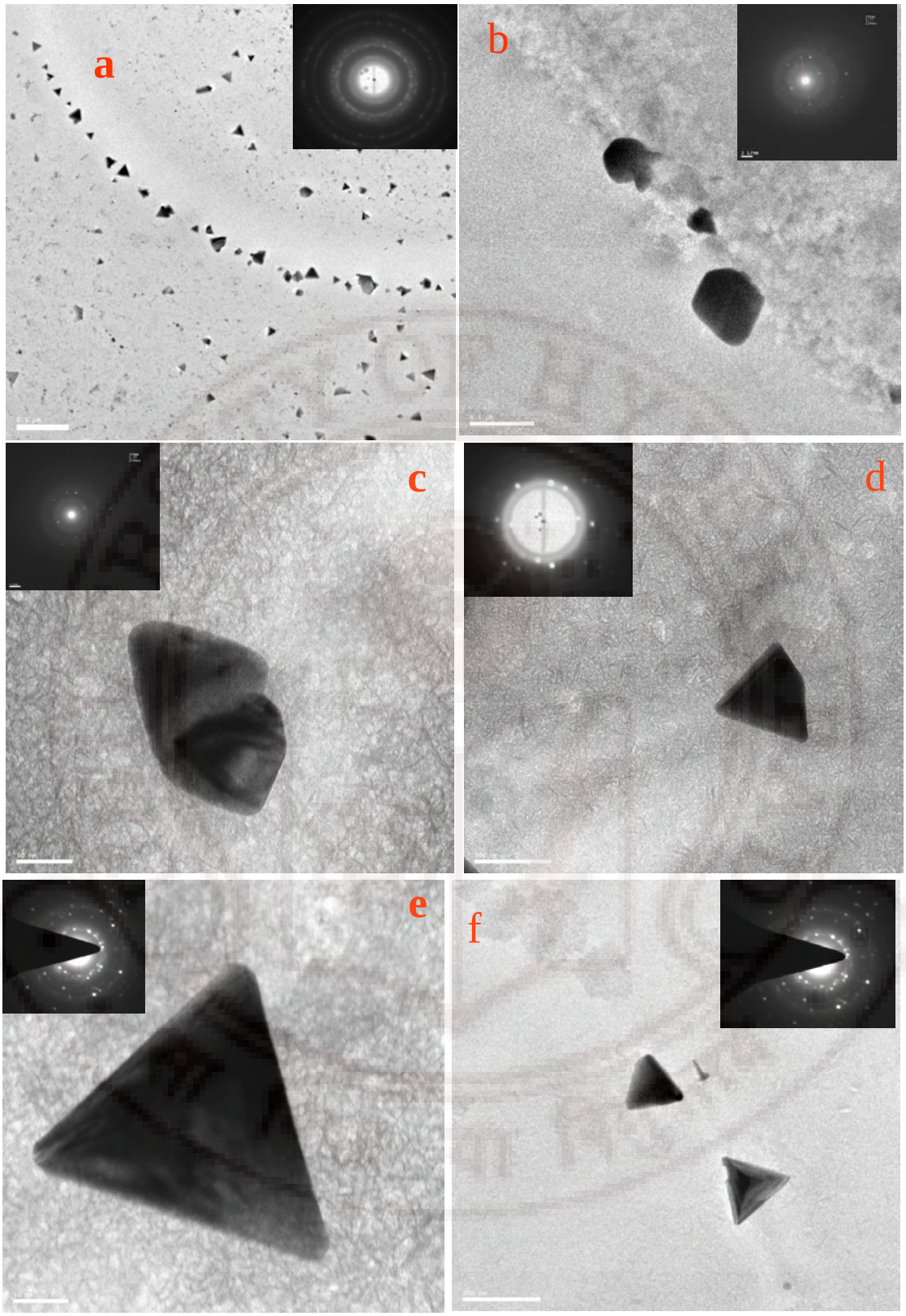

Figure 6.7: TEM images of 24 hrs iodized 5 nm Ag thin films. The long time iodization of Ag films stabilizes the iodine rich β-AgI wurtzite structure and also it favours anisotropic grain growth with a mixture of hexagonal, triangles and bi-pyramids of twinned AgI nanoparticles.

The partially iodized Ag films exhibits the (111), (220), (200) and (222) reflections which are correspond to planes of cubic AgI. But upon long time iodization (at 360 minutes) of Ag films we observe highly crystalline iodine rich hexagonal (200), (220), (440), (422) and (600) β-AgI reflections are shown figure 6.7. As both the completely iodized samples (gamma and beta AgI) decompose rapidly under the electron beam, the time consuming tilting studies could not be carried out on these samples. A higher sensitivity against the incident electron beam was found in fully iodized than those of partially iodized Ag films. The presence of metastable cubic γ-AgI phase is seen in samples iodized at 60 minutes while in samples iodized at 360 min the existence of γ-AgI could be neither proved nor excluded because of the rapid decomposition of the AgI phases under electron beam irradiation. As the formation of the γ-AgI is also possible, we can consider its orientational relationship to the parent Ag crystal on the basis, that the (111) planes of the f.c.c. crystal are equivalent to the (0001) in the h.c.p. structure. The azimuthal positions could also be understood on the same basis, since atomic matching in the interface remains the same, only the stacking sequence of the AgI crystal will be different in f.c.c. and hcp structure [40].

6.7 Photoluminescence studies of Partially iodized Ag thin films

Figure 6.8 (i) show the room temperature (300K) PL spectra of 5 nm thin Ag films iodized at different times. Short time (15 minutes) iodized Ag films excited at 355 nm shows a very strong visible emission band at 426 nm (2.91 eV) shown in figure 6.8. The formation of quasi free excitonic emission band at 2.91 eV is due to confined AgI (average particle diameter 15 nm) nanocrystals stabilized by PVA matrix [41-44]. When an Ag thin film is iodized, all of its 5s electrons go into the formation of AgI which has Ag^+ lattice ions and Ag^+ interstitials. These 5s electron get involved in the formation of the valence band (VB) of the AgI semiconductor, and, out of these valence band electrons, a fraction of them when excited through visible (blue) light from electron–hole pairs bands (weakly) by coulomb interaction to form excitons. When during short time iodization a small blip appears in the optical absorption spectrum by way of exciton formation, it means that the VB is already formed at nanoscale and a fraction of these electrons are already forming excitons.

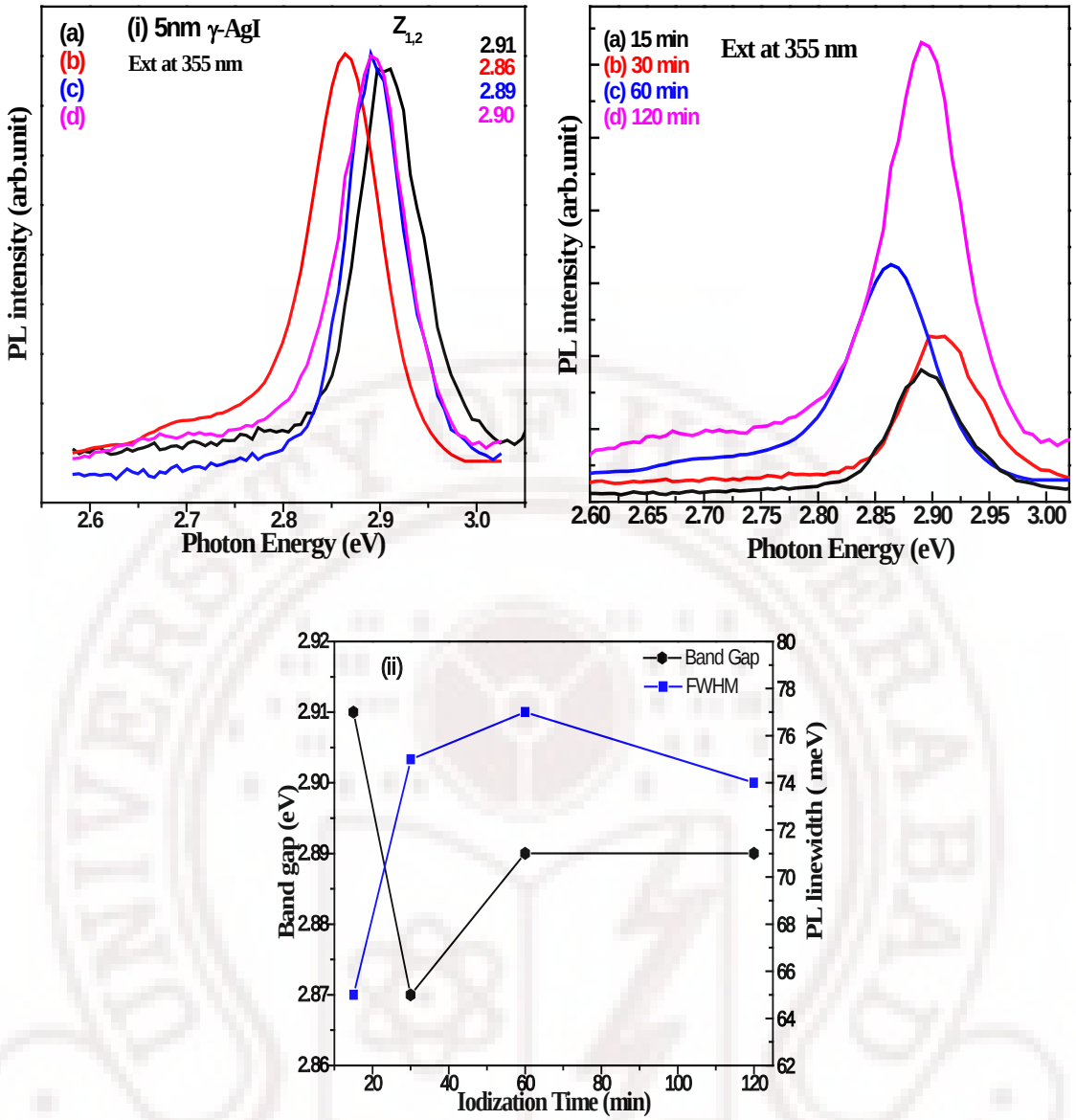

Figure 6.8: Room temperature photoluminescence spectra of 5 nm thin Ag/PVA films showing signatures of AgI core-shell nanoparticles as function of iodization time. (a) 15 min (b) 30 min (c) 60 min (d) 120 min of iodization. (ii) Non-linearity in band gap and PL line width give evidence of formation of Ag-I bond upon iodization, after 60 min of iodization band gap and FWHM get stabilized which is evidence of formation of γ-AgI stabilized by PVA matrix.

The core-shell formation (Ag plasmon-AgI exciton 'transition') implies AgI valence band formation and for valence band formation to begin, the nanocrystals must be formed, which means 3D ordering of AgI_4 clusters into a zincblende structure. This is stable because initially during iodization, the AgI ratio is >1. In partially iodized Ag films zincblende AgI formation is assured with zincblende exciton signature. One of the ways this structure is stabilized is through Ag core-AgI shell composite formation. In short time iodized (15 minutes) silver films are excited, not only the emission of silver iodide clusters, but also the emissions of Ag clusters as observed. Similarly, when Ag clusters

are excited, both the emission of AgI and Ag clusters were detected. This demonstrates that energy or charge carriers can transfer from Ag clusters to AgI clusters and vice versa. It is interesting to find that the emission of AgI clusters is stronger than that of Ag clusters when excitation is at the absorption band of Ag clusters. Similarly the emission of Ag clusters is stronger by indirect excitation into the excited states of AgI clusters than that by direct excitation into the excited states of Ag clusters. These possibilities indicate that energy transfer or carrier migration between AgI and Ag clusters is a dominant process in photo excitation. Details about the interaction and energy transfer between the two clusters are not very clear now, but they are probably related to the structure of the two clusters. Thus a type of composite clusters i.e., clusters each containing some Ag as well as AgI, may be formed upon partial iodization. Such complementary paramagnetic clusters. We realized and detected by EPR in mechanochemical reaction synthesized AgI and AgI-CuI nanopowder [42]. This is also similar to the result observed in the coupled composite CdS-CdSe and in the core-shell type mixed (CdS) CdSe and (CdSe) CdS nanoparticles [43-45].

Upon prolonged iodization at 30 minutes the intense luminescence peak centred at 2.86 eV shows the red shifted (50 meV) emission band. The formation of core-shell nanoparticles were interface play important role while doing photo excitation. Upon iodization the shell thickness increases core thickness decreases which affect the changes in band gap. Non-linearity in the band gap gives evidence for changes in γ-AgI lattice parameter (a) upon iodization (discussed in previous chapter 5). The change in lattice parameter is due to local composition disorder (Ag/I ratio). This red shift is a clear evidence of donor-acceptor recombination. Red shifted emission band indicate the Coulombic interaction among the defects. This strongly suggests silver ion interstitials and silver ion vacancies are the defects responsible for the D-A recombination.

Further prolonged iodization of 5 nm Ag film iodized at 120 minutes shows the very strong intense emission peak at 427 nm (2.9 eV). This shows the fully converted confined AgI nanoparticles formation. The AgI films in PVA matrix exhibited strong luminescence in blue region at 2.91 eV while short time iodization results a weakly luminescence. Upon iodization the emission peak shifts towards the red region due to increase of particle size which shown the decrease in quantum confinement effects. The PL peak for AgI on PVA matrix shown at 427 nm (2.91 eV) which is higher than the $Z_{1,2}$

exciton band gap for zincblende γ-AgI (E_g= 2.82 eV) and les than the band gap for pure wurtzite β-AgI (E_g= 2.94 eV). The essentially iodine deficient γ-AgI can be visualized as an n-type direct band gap semiconductor with a large electron concentration than beta AgI. Therefore, the observed continuous wave study-state PL is a manifestation of the substrate-enhanced donor-accepter recombination which yields an unusually large excitonic emission intensity which could be exploited for optoelectronic applications. This recombination seems to be a linear process in as much as there is apparently a rough linear correlation between the intensity of luminescence and particle size. The FWHM of the most intense (120 min iodized) luminescence peak is ~75 meV thus corresponds to a particle size of ~25A^0. Eventually, the photoluminescence saturates as the particle size crosses the nanometer regime. The upper state responsible for emission involves trap states located below the conduction band edge.

6.8 Summary

We have fabricated Ag and AgI thin films on poly (vinyl alcohol) PVA coated glass substrates by RF magnetron sputtering technique. We have attempts that the Ex *situ* growth of metal nanoparticles in thin polymer films which has offered a unique opportunity to 'see' the growth of nanostructures. These films were systematically iodized and carefully characterized. The PVA substrate not only acts as a reducing agent but more importantly stabilizes the gamma AgI nanoparticles even for long term exposure of Ag films to iodine. The Ag- core AgI- shell nanoparticles stabilized in the PVA matrix help realize the plasmon-exciton transition and most importantly follow *ab-initio* the formation of the zincblende AgI valence band, $Z_{1,2}$ and Z_3 exciton growth and finally the evolution of the band gap. While the uniodized Ag films shown quasi-amorphous nature briefly iodized films showed characteristic γ-AgI structure examined by selected area electron diffraction (SAED). Most interestingly TEM of Ag films revealed uniform spherical shaped nanoparticles whose shape changes appreciably upon iodization. Optical absorption spectra of uniodized Ag films show intense SRP features with maxima at 415, 417 and 420 nm for the films of thickness 3, 5 and 10 nm respectively. Finally an interesting and unique SPR-exciton phase transition is observed as the ultrathin films are progressively iodized. Blue shift observed with effect of decreasing particle size thereby increasing the quantum confinement effects shows the increase in the band gab. The photoluminescence studies show that the donor-accepter recombination rates, enhanced by thickness and particle size reduction give raise the substrate (or matrix)-enhanced PL

emission which has potential applications in optoelectronics especially where flexible devices are required. Such investigation should also be carried out with other polymeric substrates to optimize the PL efficiency for device applications.

References

1. Hiroshi Endo, Masaya Mitsuishi and Tokuji Miyashita, *J. Mater. Chem.,* **18**, 1302–1308 (2008).
2. Shatabdi Porel, Shashi Singh, S. Sree Harsha, D. Narayana Rao and T.P. Radhakrishnan, *Chem. Mater.,* **17**, 9-12 (2005).
3. J. P. Juste, B. R. Gonzalez, P. Mulvaney and L.M. Liz-Marzan, *Adv. Funct. Mater*, **15**, 1065 (2005).
4. Stephan Link and Mostafa A. El-Sayed. *J. Phys. Chem. B.*, **103**, 8410-8426 (1999).
5. Cecilia Noguez, *J. Phys. Chem. C.* **111**, 3806-3819(2007).
6. K. Lance Kelly, Eduardo Coronado, Lin Lin Zhao, and George C. Schatz, *J. Phys. Chem. B.*,**107**, 668 (2003).
7. Prashant. K. Jain and Mostafa A. El-Sayed, *J. Phys. Chem. C*, **111**, 17451 (2007).
8. Catherine J. Murphy, Tapan K. Sau, Anand M. Gole, Christopher J. Orendorff, Jinxin Gao, Linfeng Gou, Simona E. Hunyadi, and Tan Li, *J. Phys. Chem. B, **109**,* 13857(2005).
9. Deirdre M. Ledwith, Aine M. Whelan and John M. Kelly, *J. Mater. Chem,* **17**, 2459 (2007).
10. Tai Hwan Ha, Hee-Joon Koo, and Bong Hyun Chung, *J. Phys. Chem. C*, **111**, 1123 (2007).
11. Tolga Atay, Jung-Hoon Song, and Arto V. Nurmikko, *Nano.Lett*, **4(9**), 1627 (2004).
12. A. Callegari, D. Tonti and M. Chergui, *Nano.Lett*, **3(11)**, 1565 (2003).
13. G. H. Chen, Jing Zhao, Erin M. Hicks, George C. Schatz and R.P. Van Duyne, *Nano.Lett.*, **7(7)**, 1947 (2007).
14. W.A. Weimer and M. J. Dyer, *J. Appl. Lett*. **79**, 3164 (2001).
15. Jose Luis Elechiguerra, Jose Reyes-Gasga and Miguel Jose Yacaman, J. *Mater. Chem*, **16**, 3906–3919 (2006).

16. H. Takele, H. Greve, C. Pochstein, V. Zaporojtchenko and F. Faupel, *Nanotecnology*, **17**, 3499 (2006).
17. R. Gradess, R. Abargues, A. Habbou, Josep Canet-Ferrer, Esteban Pedrueza, A Russell, J. L Valdes and J P. martinez-Pastor, *J. Mater, chem*, **19**, 9233 (2009).
18. Lin-Bao Luo, Shu-Hong Yu, Hai-Sheng Qian and Tao Zhou, *J. Am. Chem. Soc*, **127**, 2822 (2005).
19. H. Takele, U. Schurmann, H. Greve, D. Paretkar, V. Zaporojchenko, and F. Faupel, Eur. Phys. *J. Appl. Phys*, **33**, 83-89 (2006).
20. T. G. Fitzgerald, Francesca Borsetto, J. M. O'Callaghan, Barbara Kosmala Justin D. Holmes and M.A. Morris, *Soft Matter*, **3**, 916-921 (2007).
21. Z. H. Mbhele, M. G. Salemane, C. G. C. E. van Sittert, J. M. Nedeljkovi, V. Djokovi, and A. S. Luyt, Chem. *Mater,* **15**, 5019 (2003).
22. Benjamin Wiley, Thurston Herricks, Yugang Sun, and Younan Xia, *Nano Lett.*, **4(9)**, 1733, (2004).
23. Pastoriza-Santos and L. M. Liz-Marzan, *Nano Lett*., **2**, 903 (2002).
24. Marek Grezelczak, Ana Sanchez-Iglesias, Benito Rodriguez-Gonzalez, Ramon Alvarez-Puebla Jorge Perez-Juste and Luis M. Liz-Marzan, *Adv. Funct. Mater*, **18**, 3780 (2008).
25. Xianluo Hu, Jimmy, C. Yu, Jingming Gong, and Quan Li, *Crystal Growth & Design,* **7(2)**, 262 (2007).
26. D. B. Pedersen and S. Wang, *J. Phys. Chem. C*, **111**, 1261 (2007).
27. S. Kapoor, R. Josi and T. Mukherjee, *Chem. Phys. Lett*. **354**, 443 (2002).
28. Choon Hwee Bernard Ng and Wai Yip Fan, *J. Phys. Chem. C,* **111**, 2953 (2007).
29. D. B. Mohan, V. S. Reddy and C. S. Sunandana, *Appl. Phys. A,* **86**, 73(2007).
30. P. Senthil Kumar and C. S. Sunandana, *Nano Letters*, **2(4)**, 431-434(2002).
31. D. Bharathi Mohan and C.S.Sunandana, *J, Appl. Phys,* **100**, 064314 (2006).
32. Manuel Caradona, *Phys. Rev,* **129(1)**, 69(1963).
33. S. Kondo, T. Itoh, and T. Saito, *Phys. Rev B,* **57(20)**, 13235(1998).
34. Chester R. Berry, *Phys. Rev. B,* **161(3)**, 611 (1967).
35. Shosuke Mochizuki and Kouta Umezawa, *Physics Letters A,* **228**, 111(1997).
36. S. Mochizuki and Fumito Fujishiro, *J. Phys.: Condens. Matter,* **16**, 3239-3256 (2004).
37. Tito Trindade, Paul O'Brien and Nigel L. Pickett, *Chem. Mater*. **13**, 3843 (2001).

38. S-Hong Ciou, Yi-Wei Cao, H. C. Huang, De-yan Su, and C.L. Huang, *J. Phys. Chem. C*, **113**, 9520 (2009).
39. V. S. Gurin, *Int. J. Qunt. Chem*, **71**, 337 (1999).
40. G. Safran, O. Geszti, G. Radnoczi, P. B. Barna, K. Toth, *Thin Solid Films*, **259**, 96 (1995).
41. C. Liang, K. Terabe, T. Tsuruoka, M. Osada, T. Hasegawa, *Adv. Funct. Mater*, **17**, 1466 (2007).
42. D. B. Mohan and C. S. Sunandana, *J. Phys. Chem. B,* **110**, 4569 (2006).
43. L. A. Swafford, L. A. Weigand, M. J. Bowers, J. R. McBride, J. L. Rapaport, T. L. Watt, K. Sriram, D. Leonard C. Feldman, and J. Sandra. Rosenthal, *J. Amer. Chem. Soc*. **128**, 12299-12306 (2006).
44. O. Scholps, N. Le Thomas, U. Woggon, and M. V. Artemyev, *J. Phys. Chem. B*, **110**, 2074 (2006).
45. S. A. Ivanov, A. Piryatinski, J. Nanda, S. Tretiak, K. R. Zavadil, D. Werder, and V. I. Klimov, *J. Am. Chem. Soc*. **129,** 11708 (2007).

Chapter VII

Superionic phase transition in AgI and (Ag-Cu) I thin films: A Preliminary Impedance Spectral Study

7.1 Introduction

Iodized Ag, $Ag_{0.90}Cu_{0.10}$ and $Ag_{0.80}Cu_{0.20}$ thin films-especially the partially iodized ones are interesting mixed conductors (ionic and electronic) besides being important for elucidating the role of interfaces in conductivity enhancement and ion transport in two-dimensional ionic conductors. Although there are many investigations of ionic conductivity on bulk AgI monocrystal/ploycrystalline samples[1-9] and there are only very few previous electrical studies on thin films [10-14] that emphasize the above aspects and thus a preliminary attempt was made (basically to complement our studies on microstructural and optical properties reported in previous chapters) to look at the superionic phase transition through DC conductivity derived from impedance measurements at selected temperatures and frequencies in the range 300 to 470K and 40 Hz to 1 MHz on 40 nm thick AgI, $Ag_{0.85}Cu_{0.15}I$ and $Ag_{0.80}Cu_{0.20}I$ films deposited on Pt/Si single crystal substrates. With respect to the AgI nanopowders [15-17] we have observed a ~ 3 order enhanced conductivity in the low temperature phase. Further the structural phase transition to alpha AgI is observed at 420 K. In Cu doped AgI films there is a lowering of conductivity throughout the temperature range besides an absence of phase transition in the same temperature as expected. The conductivity of Cu doped AgI is diminished compared with that of undoped AgI thin film.

7.2 Deposition of Ag and Ag-Cu films on Pt/Si single crystal substrates

Thin Ag and Ag-Cu alloy thin films thickness of 40 nm were deposited on (111) oriented Pt/Si single crystal substrates by RF co-sputtering method. The pure silver and copper metal targets (Aldrich, 99.999 %) are used for thin films depositions. The desired composition ratios of pure Ag, $Ag_{0.90}Cu_{0.10}$ and $Ag_{0.80}Cu_{0.20}$ (by atomic weight %) alloy films were obtained by placing appropriate size of Cu metal pieces placed on the top of the 2 inch Silver target (cathode dia: 2inch). This target was placed on the RF cathode for prior deposition. Here we have used up sputtering or sputter-up process to deposit Ag-Cu alloy film. Initially, the sputtering chamber was evacuated to a base pressure of $2x10^{-6}$ Torr after loading the cleaned Pt/Si substrates on to the substrate holder placed inside the vacuum chamber. All the films were deposited at a 15 W RF power. A working pressure of 10 mTorr was constantly maintained using high pure argon (purity: 99.999%). The argon pressure was 10 sccm to achieve uniform rate of deposition. The target to substrate distance was fixed at 15 cm. The rate of deposition was maintained constant during the entire depositions. The above conditions were found favorable for the formation of homogeneous, alloy films, although the resulting composition ratio was analyzed using EDAX. The thickness of the films was determined by using AMBIOS XP-1 profilometer. These films were characterized by XRD using a wide angled X-ray powder diffractometer (INEL Model CPS120) and a position sensitive detector with Co Kα ($1.7889A^{o}$) radiation. The surface micros structures of the films were examined by SPA 400 Atomic Force Microscopy (AFM) operated in the non contact dynamic force mode.

Iodization: Iodization of these thin films was done an hour-glass type chamber with dimension of 10 cm height x 6 cm diameter. Iodine kept at the bottom of the lower half of the chamber sublimates at room temperature and slowly deposits on the $Ag_{1-x}Cu_x$ alloys films kept at the top of the chamber kept in a dark room. Thus iodization was carried out for selected durations in the range of 180 to 720 min.

7.3 Structural characterization of Ag and Ag-Cu alloy films deposited on Pt/Si substrates

Figure 7.1 shows the XRD pattern of as deposited 40 nm thick Ag and Ag-Cu alloy films deposited on Pt/Si substrates. These films were systematically iodized at different times for determination of structural characteristic. Uniodized 40 nm thick Ag films consist of two strong prominent peak (111) and (220) reflections which is

characteristic of *fcc c*ubic Ag structure. Further systematic iodization at 720 min of these films shows the development of mixed phase of γ and β-AgI structure in which γ-AgI zincblende structure as a major phase. This diffraction pattern consists of number of prominent peaks characteristic of a substantial amount of β-AgI minor phase and γ-AgI is a major phase [5,9]. The presence of additional weak reflection, which are attributed to the co-existence of two phases. In thick films stabilizing γ-AgI zincblende single phase structure cannot be stabilized easily at room temperature (discussed in previous chapters) 10 and 20 % of Cu substitution on to Ag film stabilizes the zincblende phase co-existing with the wurtzite possibly due to the fact that the films are not ultrathin(<10 nm). Even at 40 nm thick films the Cu substitution apparently helps to stabilize the zincblende phase as a major phase by reinforcing the cation sublattice of γ-AgI which has the smaller unit cell than of the wurtzite or β-AgI [7]. However 40 nm thicknesses is found to be quite suitable for electrical measurements because they are continuous [10,11].

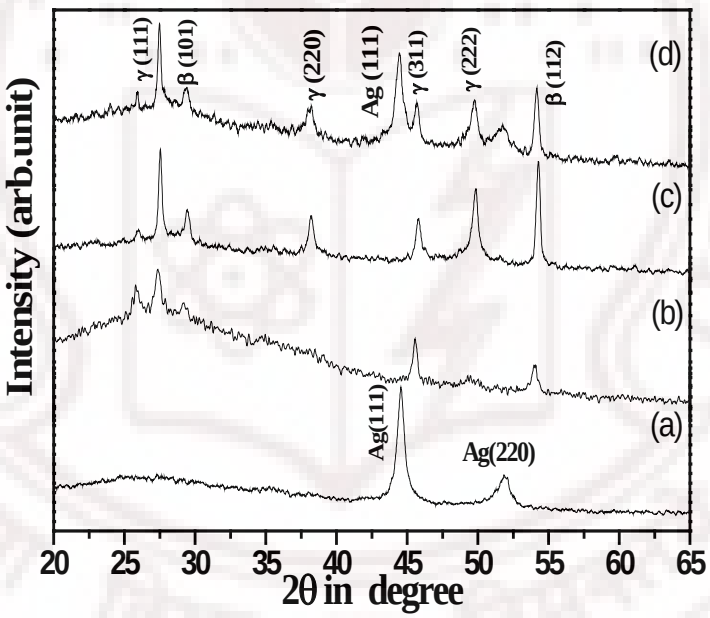

Figure 7.1: XRD pattern of 40 nm thick (a) as deposited Ag (b) Ag film iodized for 720 min (c) $Ag_{0.90}Cu_{0.10}$ alloy film iodized for 720 min (d) $Ag_{0.80}Cu_{0.20}$ film iodized for 720 min deposited on Pt/Si substrates.

7.4 Surface morphology

The surface morphology of the 40 nm thick Ag and Cu doped Ag films iodized at 720 min shown in figure 7.2. Undoped AgI films shown the uniform smaller grains with average grain size ~50 nm with RMS of the iodized film is 3.5 nm. In 10 and 20 % Cu doped AgI films are shown anisotropic grain growth with average grain size 80 and 150

nm for 10 and 20 % Cu substitution. Surface roughness increase the as function of iodization time and Cu substitution.

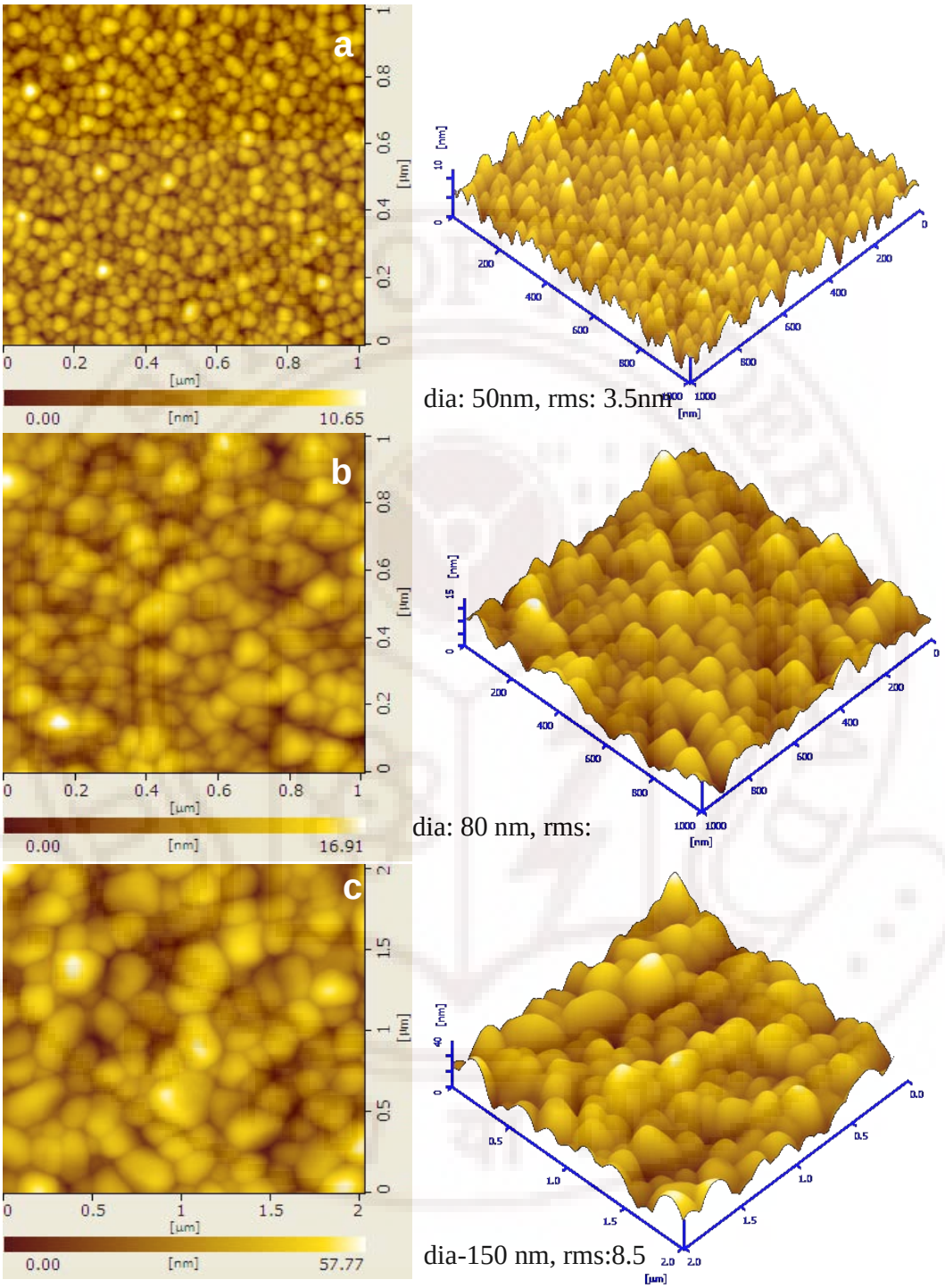

Figure 7.2: DFM images of 40 nm thick (a) Ag (b) $Ag_{0.90}Cu_{0.10}$ (c) $Ag_{0.80}Cu_{0.20}$ films iodized for 720 minutes. These films were deposited on Pt/Si single crystal substrates.

7.5 Impedance measurement

7.5.1 Fabrication of M-I-M structure

The frequency and temperature dependent impedance measurement of 40 nm thick AgI and Cu doped AgI films grown on Pt/Si substrates were characterized at low frequencies (≤ 1 MHz) using the MIM structure. The top electrode of 300μm^2 area of the MIM structure was fabricated using the shadow mask techniques. The measurement were carried out from 40 Hz to 1 MHz using Agilent 4294A impedance analyzer (shown in chapter 2)

The schematic cross section and top view of the M-I-M structure fabricated is shown in figure 7.3.

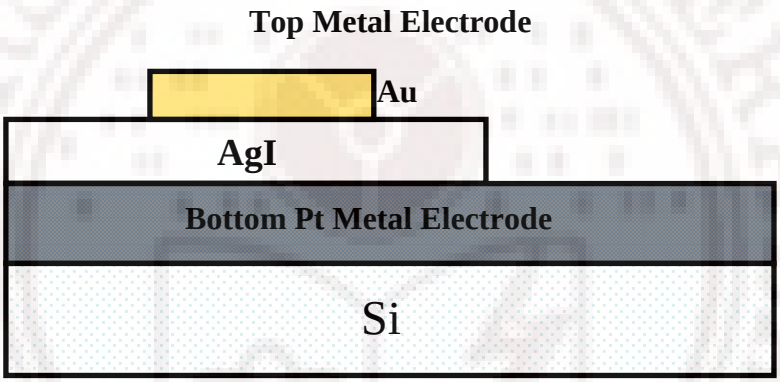

Figure 7.3: Cross-section view of the MIM structure

The top and bottom electrodes of the M-I-M (Au/AgI/Pt) structures were connected to the impedance analyzer through two tungsten needles mounted on their respective micropositioners in a custom made probe station with heating and cooling base. The modulus of impedance |Z| and phase constant θ were measured from impedance analyzer. The real and imaginary part of the complex impedance were calculated using the following equations

$$Z' = |Z| Cos(\theta) \quad (7.1)$$

$$Z'' = |Z| Sin(\theta) \quad (7.2)$$

The bulk resistance of the sample is determined from the Z', Z'' plot by extrapolating the curve to the Z' axis at the low frequency side. The DC conductivity of the samples was determined from these bulk resistance.

Figure 7.4(a) shows the complex impedance plots as Z' vs Z" plotted at various frequencies at selected temperatures. A general feature of this family of plots is the presence of a single semi-circle followed by an almost linear rise in impedance at higher frequencies. This represents a Debye-type relaxation [1]. The three low-temperature plots ($T<T_c$) form a closely spaced group widely separated from the two high-temperature ($T>T_c$) plots (after the phase transition). Figure 7.4(b) represents the temperature dependence of the real part of impedance and figure 5c shows the temperature-dependence of the imaginary part of Z figure 7.4(c) reflects the trend of impedance plot of figure 7.4(a) with clearly separated groups for high and low temperature regions [6].

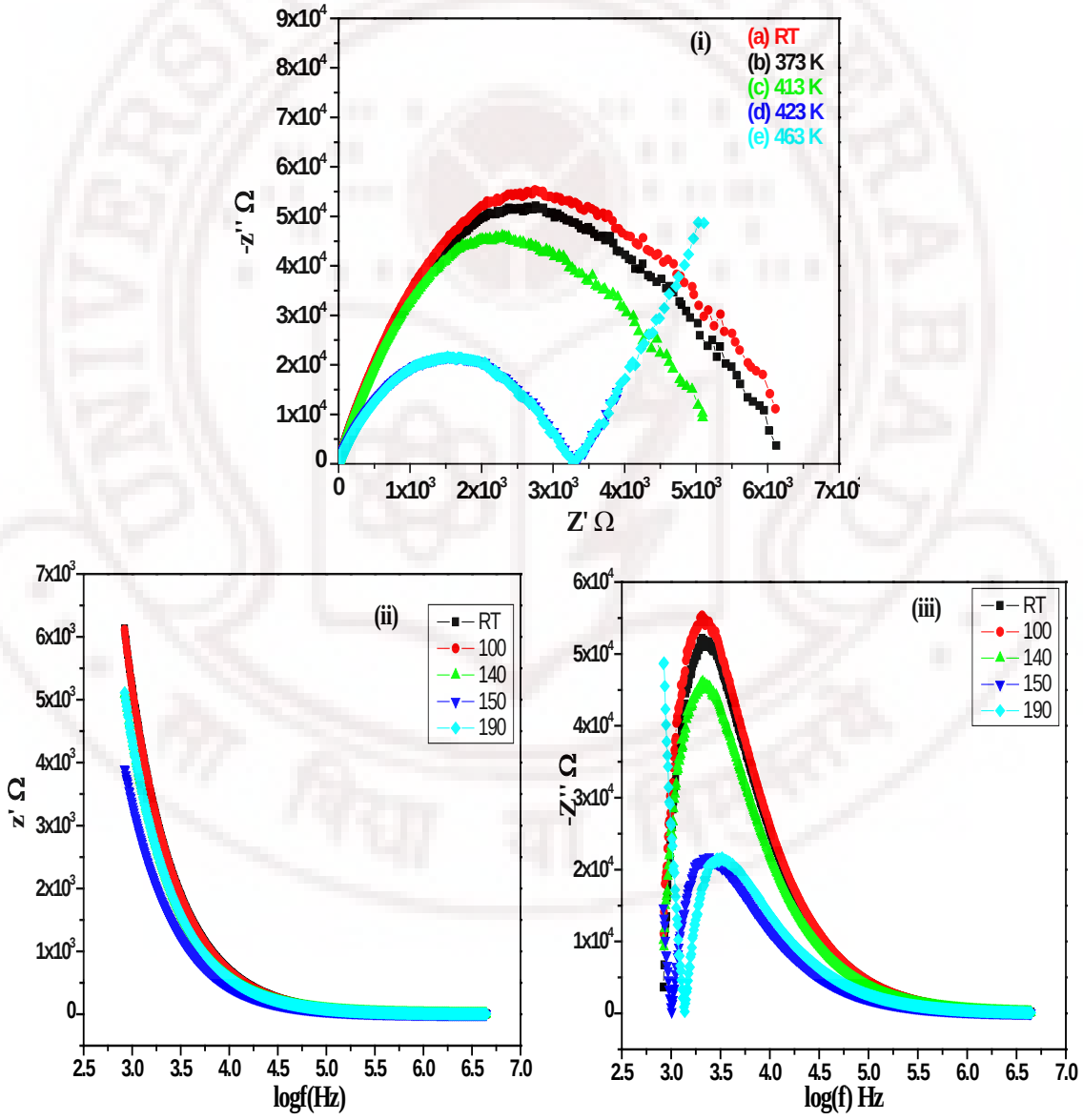

Figure 7.4: (i), (ii) and (iii) shows the complex impedance spectra for the LT and HT (inset) phase of 40 nm thick Ag film deposited on Pt/Si substrates and iodized for 720 min.

The plots of figure 7.4 (a) were analyzed by extracting the real part of impedance value at point where the semi-circle intersects the Z' axis. This latter value represents the true impedance which is usually used to obtain DC conductivity. A plot of log sigma dc *vs* 1000/T may now be drawn to get the conductivity profile of the AgI thin film sample.

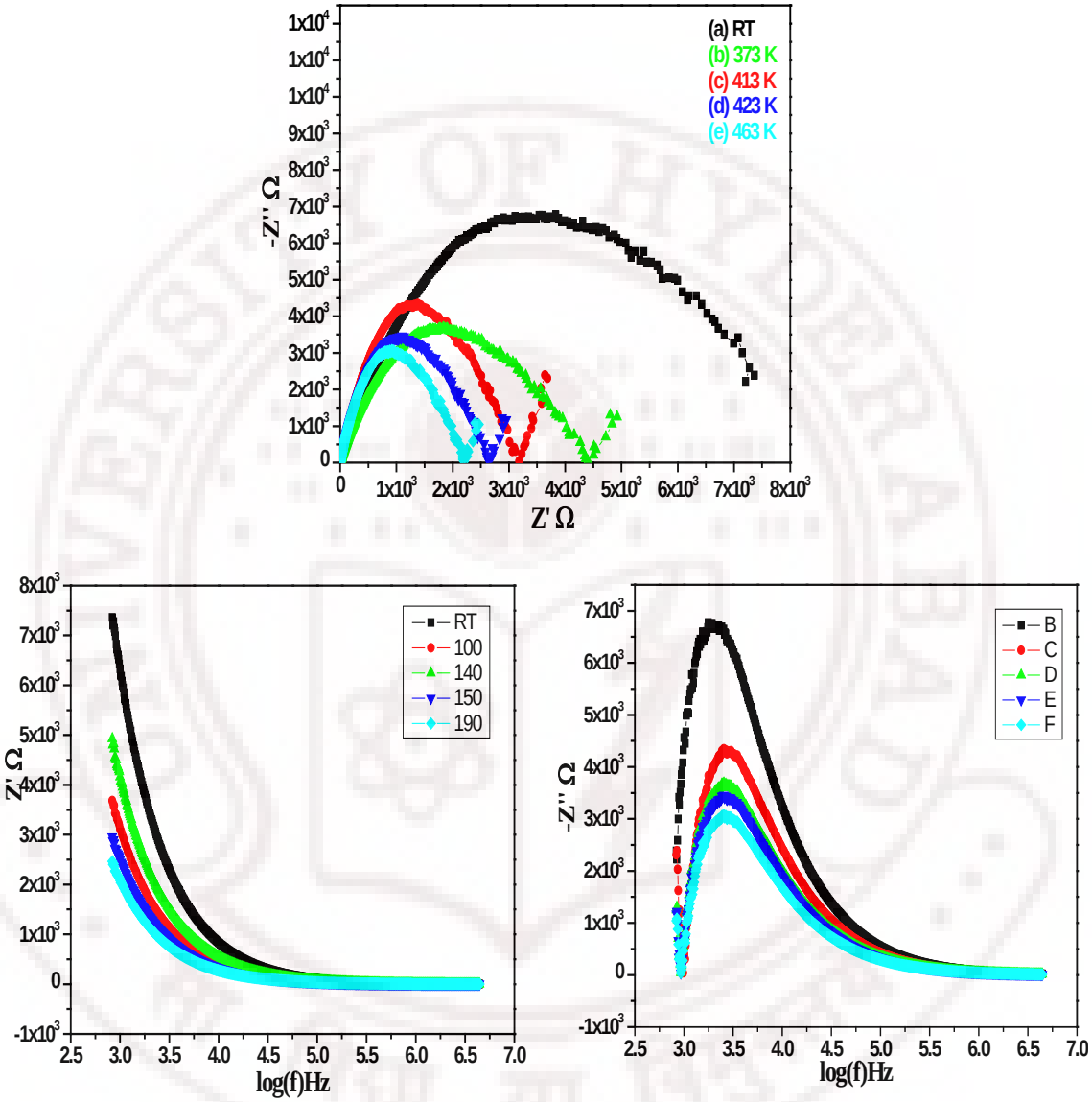

Figure 7.5: Complex impedance spectra for the LT and HT (inset) phase of 40 nm thick $Ag_{0.90}Cu_{0.10}$ alloy film deposited on Pt/Si substrates and iodized for720 min.

Figure 7.5 (a-c) and 7.6 (a-c) show real and imaginary components impedances, $Z^{'}$ and $Z^{''}$ ($Z^{*} = Z^{'} + i\,Z^{''}$) as functions of frequency and temperature, for 10% and 20% Cu doped AgI films respectively. A comparison to figure 7.4 shows qualitative changes upon Cu doping. Mainly conductivity changes marginally with temperature with no conductivity phase transition anomaly in the impedance plots [18,19]. A similar

conductivity vs temperature graph was drawn which reflects the effect of doping and the absence of anomaly as expected. The 300 K impedance plot of figure 7.5 (a) is very interesting as it is widely separated plots for T > 300 K w.r.t. the 300K plot. This plot is very similar to the impedance plot obtained by Watts et al [12] for Ag-AgCl mixed conductor films obtained by co-sputtering as in our case. This feature could arise from interfacial (substrate-thin film) contribution to conductivity which is characteristic of thin films [10-11].

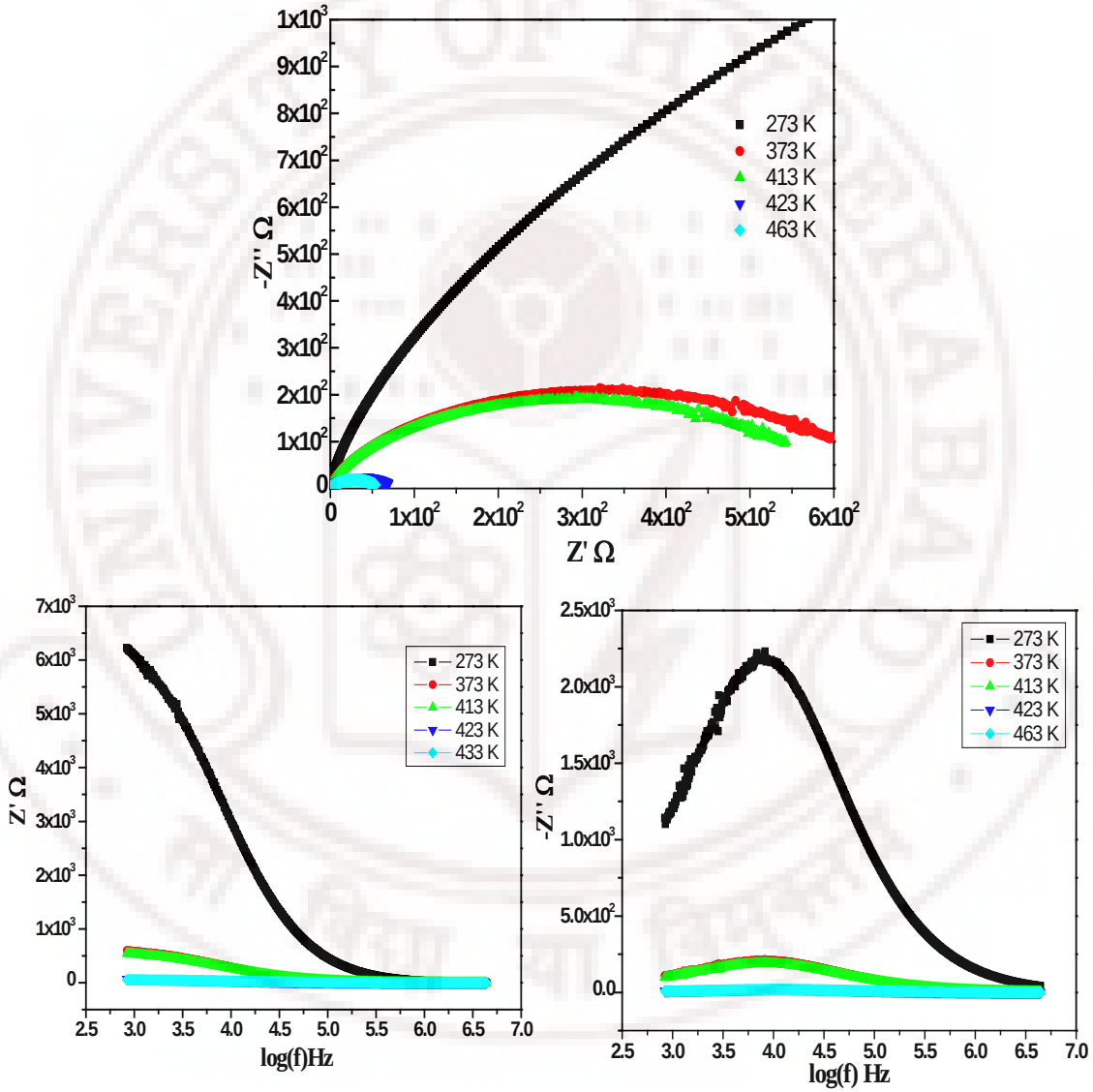

Figure 7.6: Complex impedance spectra for the LT and HT (inset) phase of 40 nm thick $Ag_{0.80}Cu_{0.20}$ alloy film deposited on Pt/Si substrates and iodized for 720 min.

7.6 DC Conductivity

Figure 7.7 show the conductivity profiles of AgI and Cu-doped AgI thin films as log sigma *vs* 1000/T plots with sigma derived from figure 7.4, 7.5 and 7.6. There is an abrupt jump in conductivity at the superionic phase transition temperature in undoped AgI (420K) but the low temperature conductivity is considerably enhanced by ~ three orders of magnitude relative to the bulk emphasizing the effect of dimensionality on conductivity especially the possible role of interfaces in enhancing ion diffusion. Another important feature is the considerably reduced slope (0.1eV) relative to bulk which strongly suggests facile ion motion in the films although the exact mechanism is yet to be ascertained. A tentative explanation is that there exist preferred conducting channels along the interface region, with a high concentration of defects (vacancies) around the insulator/conductor boundary or space charge region that may favor the faster migration of Ag^+ ions.

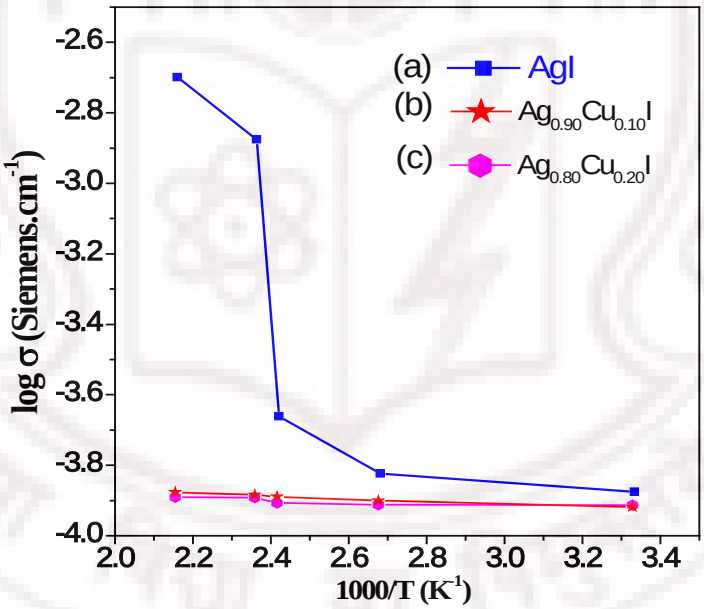

Figure 7.7: Arrhenius plot of the temperature dependent of the dc conductivity of 40 nm thick (a) undoped Ag film (b) $Ag_{0.90}Cu_{0.10}$ (c) $Ag_{0.80}Cu_{0.20}$ films iodized for 720 min.

Doping of Cu into AgI reduces the transport number for Ag^+ because CuI is not an ionic conductor in this temperature range 300-580 K. In fact it is a p-type semiconductor in the temperature range. Therefore one expects to observe a reduced conductivity in the low temperature region as is observed. Equally importantly, Cu-doping shifts the phase transition temperature to T>>420 K due to reduction in lattice parameter and the

strengthened AgI bond which becomes more covalent than in Undoped AgI. However measurement of actual transition temperatures is deferred until a high temperature measuring set up is designed and developed [20].

These results which involve defects and interfaces are broadly relate to and supplement the earlier work on EPR of nanopowders of AgI and AgI-CuI solid solutions [21] and the present work on structural and optical properties of AgI and Ag-CuI thin films discussed in earlier chapters.

A detailed investigation of conductivity of AgI and $Ag_{1-x}Cu_xI$ ($0<x<1$) films as function of thickness and different substrates is expected to throw more light on conduction mechanism besides helping to optimize the film properties for thin film battery and sensor applications.

References

1. S. Chandra, *Superionic Solids: Principle and Applications*, Amsterdam, North Holland, 1981.
2. J. S, Lee, St. Adams and J. Maier, *J. Phys. Chem. Solids*, **61**, 1607 (2000).
3. K. Shahi and J. B. Wagner, *Appl. Phys. Lett*, **37**, 757-759 (1980).
4. Richard P. Buck, *Electrochemical. Acta,* **42 (20-22)**, 3375-3384 (1997).
5. P. Senthil Kumar, A.K. Tyagi and C. S. Sunandana., *J. Phys. Chem. Solids*., **67**, 1809 (2006).
6. P.S. Kumar, P. Balaya, P.S. Goyal, C.S.Sunandana, *J. Phys. Chem. Solids*, **64**, 961 (2003).
7. D. Bharathi Mohan, C.S. Sunandana, *J. Phys. Chem. Solids* **65**, 1669(2004)
8. J. Rogez, A. Garmier and P. Kanuth, *J. Phys. Chem. Solids*, **63**, 9-14 (2002).
9. Hirotoshi Yamada, Aninda J. Bhattacharyya, and Joachim Maier, *Adv. Funct. Mater*, **16**, 525-530 (2006).
10. Shin-ichi Furusawa and Takashi Kawaguchi, *J. Phys. Soc. Jpn.* **70**, 3585-3590 (2001).
11. Shin-ichi Furusawa and Yuichi Sakai, *J. Phys. Soc. Jpn.* **68**, 976-980 (1999).
12. Paul C P Watts, Simmon J Henley, Ernest Mendoza, S Ravi P Silva, June K Irvine and Eric T McAdams, *Nanotechnology*, **18**, 205502 (2007).

13. Chaghao Liang, Kazuya Terabe, Tohru Tsuruoka, Minoru Osada, Tsuyoshi Hasegawa and Masakazu Aono, *Adv, Funct. Mater*, **17**, 1466-1472 (2007).
14. C. Liang, K. Terabe, T. Hasegawa, and M. Aono, *J. Appl. Phys*, **102**, 124308 (2007).
15. R. Makiura, T. Yonemura, T. Yamada, M. Yamauchi, R. lkeda, H. Kitagawa, K. Kato and M. Takata, *Nature Mater*, **8**, 476 (2009).
16. Yu-Guo Guo, Jong-Sook Lee amd Joachim Maier, *Adv. Mater*, **17**, 2815 (2005).
17. Chaok Seok and David W. Oxtoby, *Phys. Rev. B*, **56** (18), 11485 (1997).
18. J.S. Lee, St. Adams and J. Maier, *Solid State Ionic*s, **136-137**, 1261 (2000).
19. J.S. Lee, St. Adams and J. Maier, *J. Electrochem. Soc*, **147**, 2407 (2000).
20. D. Bharathi Mohan and C. S. Sunandana, *Pramana*, **67,** 331 (2006).
21. D. Bharathi Mohan, C.S. Sunandana, *J. Phys. Chem. B*, **110**, 4569 (2006).

Chapter VIII

Conclusions and Suggestions for Future Work:

Before stating the conclusions and pointing to directions for future research, it would be appropriate to mention that the major gain of this thesis effort is an insight into quasiparticle (plasmons and excitons) production and their transformation through a systematic oxidation of a two-dimensional noble metal nanostructure, witnessing in the process an *ab initio* development of the electronic band structure of a direct gap I-VII semiconductor.

Based on the experimental research work reported in the present thesis -essentially focused on the optical and electrical behaviour of ultrathin nanostructured films of the I-VII semiconductor and Ag^{+} superionic conductor gamma AgI the following conclusions emerge:

1. (a) short term (15 minutes) and (b) long term (360 minutes) iodization of vacuum evaporated 5 nm and 15 nm thick Ag films to Iodine vapours in the in-house developed iodization reactor yields nanostructured AgI films with zincblende (gamma) (case (a)), and zincblende (major) and wurtzite (beta) minor phases (case (b) as characterized by XRD, AFM and TEM supplemented by SAED. Extended (12 hr) iodization destabilizes the gamma phase and brings about a interpolytypic transition to beta AgI.
2. RF magnetron sputtering technique was applied to fabricate quasi amorphous Ag-Cu alloy thin films in which Cu promotes layer type growth with more disorder and in built strain-induced due to the plasmon environment, enabling retarded growth kinetics, thus providing an attractive controllable platform for studying formation of γ-AgI nano particle growth.
3. Surface plasmons are readily detected in ultrathin rough Ag films whose properties show dramatic thickness dependence.
4. Short-term iodization of evaporated pristine Ag films 5 and 15 nm thick exhibit the co existing plasmonic and excitonic absorption characteristic of zincblende phase AgI shell-Ag core nanoparticles.
5. Long-term iodization of evaporated pristine Ag films 5 and 15 nm thick results in the formation of zincblende phase AgI with characteristic ($Z_{1,2}$ and Z_3) excitons formed form the complete consumption of Ag plasmonic electrons. This could

be called 'plasmon-exciton transition' indicating the conversion of core-shell nanoparticles to full-fledged AgI nanoparticles.

6. Sputtered Ag pristine thin films 5 and 15 nm exhibit considerably delayed iodization kinetics so that one always gets a minor wurtzite AgI phase along with the major zincblende phase. The natural roughness of these Ag films result in intense blue-shifted SPR which gradually get converted to zincblende excitons in 5 nm films and both zincblende and wurtzite excitons in 15 nm films due to enhanced thickness. Such films could be used in molecular detection using SERS technique.
7. Photoluminescence of Ag films obtained by evaporation and sputtering show upon iodization weak excitonic luminescence accompanied by weaker and broad shoulders due to Frenkel defects and stacking faults acting as surface traps. This could be identified as shallow donor-acceptor recombination centres existing in the forbidden gap. The shoulders are much weaker in sputtered films indicating lower defect concentrations than in evaporated films.
8. (a) Thermally evaporated Cu-doped (5, 10 and 20 at %) Ag films 5 nm thick exhibits upon iodization zincblende structure and sharper and more intense blue shifted SPR than pristine Ag films. Upon iodization they exhibit $Z_{1,2}$ and Z_3 excitons- the latter with enhanced intensity. Most interestingly the room temperature photoluminescence spectra of these films (with 5, 10% Cu) show a single sharp and intense peak due to Cu-enhanced excitonic photoluminescence with negligible concentration of defect raps.

   (b) Sputtered films exhibit these same features with even sharper excitonic PL. These changes are accompanied by reduction in the band gap. Optical absorption of 20% Cu doped Ag films show both Ag and Cu SPRs and upon iodization exhibit exciton features of both zincblende and wurtzite structures-the latter one a minor phase probably arising from composition fluctuations. Cu substitutionally doped into AgI enhances the excitonic PL by drastic reduction of Frenkel defects and increasing the oscillator strength for absorption by strengthening Ag-I bond which is also responsible for nonlinearity in band gap with respect to iodization time.
9. Ag films (5 nm thick) sputtered onto PVA substrates show enhanced SPR (with respect to films on glass and fused silica substrates). Also PVA supports Ag particles with different sizes and shapes (spherical in uniodized Ag and

triangular, trapezoidal and bypyramidal in iodized Ag films. TEM and SAED have helped visualization of shape evolution and characterization of zincblende structure respectively. Enhanced–intensity single sharp PL characteristic of defect-free excitonic luminescence is observed. These γ-AgI/PVA films could be used to develop flexible devices.

10. Impedance spectra of iodized (a) Ag and (b) Ag-Cu thin films (which show mixed conduction and thus make true DC ionic conductivity measurements very difficult) give (a) enhanced Ag^+ ionic conductivity relative to bulk and show the anomaly at superionic phase transition (as in the well known bulk AgI) and (b) reduced ionic conductivity and absence of the conductivity anomaly in Ag-Cu due to the reduced defect concentration and off-critical ionicity of the Ag-I bond.

Suggestions for future work

1. Low temperature PL of all the sputtered and evaporated, and, iodized AgI thin films investigated in this thesis would enable temperature dependence of excitonic intensities and linewidths to be obtained providing insights on exciton dynamics.
2. Nonlinear optical properties of AgI and Cu-doped AgI thin films could be investigated using Z-scan for evaluation of these films for optical limiting and SHG applications.
3. Extending the impedance spectroscopy measurements to the study of conductivity phase transitions in Ag-Cu I thin films would provide motivation to look at AC conductivity relaxation and develop models for ion diffusion in thin films.
4. Development of optoelectronic and flexible microbattery elements based on gamma AgI and composite Ag-AgI thin films on PVA substrates could be a worthwhile project.
5. Mechanisms of (a) thin film formation (b) plasmon-exciton phase transition and (c) *ab initio* band structure development in gamma AgI could be explored in a semi-quantitative approach. This could also involve elucidation of thin film formation and microstructure development –crucial inputs to physical property enhancement.

Research Publications: (*In refereed international journals***)**

1. M. Gnanavel, D. Bharathi Mohan and C. S. Sunandana, 'Optics of quasi- particle phase transition in nanostructure Ag thin films', ***Thin Solid Films,*** 517, 1058 (2008).

2. M.Gnanavel and C. S. Sunandana, 'Iodization time dependent Surface plasmon to exciton transition and Photoluminescence study of Core shell Silver Iodide thin films sputtered on PVA Substrates. (accepted for ***Journal of Nano science***).

3. M. Gnanavel and C. S. Sunandana, ''*Optics of triangular Mie particles in ultrathin Ag films'***. *SPIE Proceedings*. 1, 6901-50 (2007).

4. M.Gnanavel and C. S. Sunandana, '*Optical absorption and Photoluminescence in ultra thin silver and silver iodide films*'. ***IEEE Proceedings***. Page-(s) 1-4, 2008.

5. Gnanavel and C. S. Sunandana, 'Plasmon –Exciton transition in Iodized Ag-Cu nanostructured films'. ***SPIE Proceedings***. v- 7894, (1-8) 2009.

Manuscripts (to be communicated)

1. **M.Gnanavel and C. S. Sunandana,** Surface plasmon-exciton transition in ultra thin silver and silver iodide films deposited on glass substrates by vacuum thermal evaporation.

2. **M.Gnanavel and C.S. Sunandana,** Thickness and composition dependent plasmon-exciton transition and photoluminescence study of cation stabilized Co-Evaporated Ag-Cu nanostructured thin films iodized at ambient.

3. **M. Gnanavel and C. S. Sunandana,** Cu enhanced quasi–free excitonic photoluminescence in Co-Sputtered $Ag_{1-x}Cu_X$ (x= 0.05, 0.1 and 0.2) thin films grown on fused quartz substrates iodized at ambient.

4. **M. Gnanavel and C. S. Sunandana,** Iodine induced Ex-situ growth and photoluminescence study of Core shell Silver Iodide thin films sputtered On PVA substrates.

5. **M. Gnanavel and C. S. Sunandana,** Impedance Spectroscopic studies of Superionic phase transition in AgI and (Ag-Cu) I thin films.

International conferences

1. Gnanavel M and C S Sunandana**,** *'Optics of triangular Mie particles in ultrathin Ag films',* ***OPTO-2007*** *USA* (poster presentation)

2. Gnanavel and C S Sunandana**, '**Substrate dependent Surface Plasmon Resonance and Optics of triangular Mie Particles in ultra thin Ag films'**,** *International Conference on Nano science and Nano Technology (* ***ICONSAT-2008****)*
Chennai, India (poster presentations).

3. M.Gnanavel and C. S. Sunandana**,** 35th **ICMCTF** (American Vacuum society international conference at San Diego USA, April 28-May 2008 *(Oral presentation).*

4. M. Gnanavel and C. S. Sunandana, *Optical absorption and Photoluminescence in ultra thin silver and silver iodide films*, International conference on **Photonics Global-2008** at Singapore *(oral presentation).*

5 M. Gnanavel and C. S. Sunandana, Thickness dependent Surface plasmon-Exaction transition in ultra thin silver/silver iodide films. Inter national on Fiber Optics and Photonics (**PHOTONICS-2008**) at IIT Delhi, Delhi, India ***(****Oral presentation).*

6. M. Gnanavel and C. S. Sunandana**,** Plasmon –Exciton transition in Iodized Ag-Cu Nanostructured films. ***SPIE Plasmonics.*** V-7894, p-1-8 (2009) *(poster).*

7. M.Gnanavel and C S Sunandana. Iodization time dependent Surface plasmon to exciton transition and Photoluminescence study of Core shell Silver Iodide thin films sputtered on PVA Substrates. International Conference on Nano science and Nano Technology ***(ICONSAT-2010)*** IIT Bombay**,** India *(poster presentations).*

ACRHEM: work presented at (*National and International Conferences*)*****

1. M.Gnanavel and C. S. Sunandana, '*Mechnochemical Synthesis of* MoO_3 *Nanoparticles*, International conference on **Nano-2005**, July 13-15, 225 (2005), at Verdu Nagar, Tamil Nadu, India. ***(****Oral presentation****).***

2. M. Gnanavel and C S Sunandana, *Energy Release Characteristics of the Nano Scale Al-* MoO_3 *Metastable Intermolecular Composite*. **HEMCE-2007**, 13-15 Dec 2007 Chennai, India. ***(****Poster presentation****)***.

3. M. Gnanavel M and C S Sunandana, *Combustion Energy Release Characteristics of Nano Scale Al-*WO_3 *Metastable Intermolecular Composite (MIC),* Bangalore **Nano-2007**, Dec 6-7, 2007 at Bangalore, India. *(Poster presentations).*

4. M. Gnanavel and C. S Sunandana, *Synthesis and Characterization of Nano Size* Fe_3O_4 *powder for Pyrolent applications,* International Conference on Magnetic Materials, Oct-21st -23rd 2008, at NPL, New Delhi, India. *(Poster presentation)*.

5. M.Gnanavel and C S Sunandana, *Combustion Energy Release Characteristics of Nano Scale Al-*Fe_2O_3 *metastable Intermolecular Composite (MIC),* India-Russia international conference "HEDPI'' Technologies and Industry Applications, at pune 19-21st Dec, 2008, India. (Poster)

*Does not form part of the PhD Thesis.